Physics-Based Modeling of Failure of Novel Light-Weight Materials: Applications to Computational Design of Materials

by

Benhour Amirian

A thesis submitted in partial fulfillment of the requirements for the degree of

Doctor of Philosophy

Department of Mechanical Engineering
University of Alberta

© Benhour Amirian, 2021

Abstract

Advanced physics-based computational models have been developed in this thesis to study dynamic failure in novel light-weight materials used in impact applications, focusing on applying different computational techniques to study three material systems: 1. novel self-propagating high-temperature synthesized ($\gamma + \alpha_2$)-TiAl/Ti_3Al-Al_2O_3 ceramic-metal composites, 2. single crystal magnesium, and 3. nano-grained boron carbide. For the ($\gamma + \alpha_2$)-TiAl/Ti_3Al-Al_2O_3 cermet, a progressive study has been carried out by developing a three-dimensional microstructure-based finite element model. The models have been developed to investigate the rate-dependent mechanical response features (e.g., compressive strength, flow stress hardening, and energy absorbing efficiency) and predominant failure mechanisms (e.g., void deformation and growth, particle cracking, and interface decohesion), and have been validated with high fidelity experimental data. Validating the numerical model has enabled predicting the material response outside of the experimentally-accessible conditions. To date, few studies have been made to bridge ceramic-metal material models under different loading conditions with experimental inputs, such as porosity, particle volume fraction, elastic modulus of the constitutions, and void clusters. To address this, a modified variational formulation of the Gurson model has been used to allow for the damage caused by the voids. The strain hardening components, as one of the most unknown material properties, have been calibrated by matching the modeling results with experimental data. Following validation, the effects and implications of different parameters such as particle volume fraction, porosity, unit cell size ratio, and the variability of the inclusions have been presented and discussed. After that, the model

was extended to explore the response of the $\alpha_2(Ti_3Al) + \gamma(TiAl)-$submicron grained alumina cermet by considering high particle volume fraction and under high strain-rate loading applications. In this part of the study, the energy absorbing efficiency, as one of the important factors in using the ceramic-metal composites in high-rate applications, has been studied. The results have indicated that the particle shapes and void volume fraction play an important role on energy absorption capabilities of the $(\gamma + \alpha_2)$-TiAl/Ti_3Al-Al_2O_3 cermets' damage tolerant design. These new understandings have informed the fabrication and refinement of new generations of the cermet variant for commercial use in protection products by industry partners.

In the second thrust of my research involving magnesium and boron carbide, I have developed an advanced physics-based time-dependent phase-field model to predict deformation and failure mechanisms (e.g., fracture and twinning) in these anisotropic materials. Computationally, a monolithic scheme has been used as a powerful technique to increase the accuracy of the solver and high-performance computer clusters have been employed to solve large-scale problems associated with the research. The coupled differential equations have been implemented in an open-source high-level Python interface, FEniCS. First, the model is extensively validated for an intrinsically brittle material, magnesium. Comparing with molecular dynamics simulation, the twin interface velocity is explored in order to obtain the kinetic coefficient. Finding this velocity-related parameter is important as one of the main factors for determining the driving force of twinning for magnesium. In addition, the spatial distribution of the shear stress field in the parent and twinned phases is investigated. The result provides insights into the effect of twin's thickness on further twin nucleation and growth. Next, the critical strain and initial twin embryo size required for propagation and growth of a single twin embryo in magnesium are predicted by the current phase-field approach. After that, the effect of twin-twin and twin-defect interactions is explored because this may increase the likelihood for crack and failure leading to reduction of material lifetime. Then, the phase-field approach is extended

to predict various deformation mechanisms in nano-grained B_4C (e.g., fracture and twinning). In addition, the crack propagation under compressive loading is treated by using a new decomposition for the strain energy density, which represents a valuable contribution to the literature.

Overall, this thesis consists mainly of three parts adapted from the two published and the two submitted journal articles:

1. A physics-based model to capture the mechanical response of $(\gamma+\alpha_2)$-TiAl/Ti_3Al-Al_2O_3 cermet under quasi-static and dynamic loading,

2. An advanced phase-field approach to evolution and interaction of twins to unravel time-evolved twinning behavior in magnesium at nanoscale, and

3. A comprehensive calibrated and validated phase-field model for studying the deformation mechanisms of nanocrystalline Mg and B_4C in order to provide guidance for material refinement via tailoring their mechanical properties and microstructure.

Preface

- Chapter 2 of this thesis has been published in *Materials Science and Engineering: A (744), 570-580* as **B. Amirian**, H.Y. Li, and J.D. Hogan, "An experimental and numerical study of novel nano-grained $(\gamma + \alpha_2) - \mathrm{TiAl}/\mathrm{Al_2O_3}$ cermets". I, the first author of this publication, was responsible for developing the model, writing the code, designing and performing all the numerical simulations, and writing the original draft. H.Y. Li performed the experiments and contributed to manuscript edits. J.D. Hogan was the supervisory author and was involved with concept formation and manuscript composition.

- Chapter 3 of this thesis has been published in *Acta Materialia (181), 291-308* as **B. Amirian**, H.Y. Li, and J.D. Hogan, "The mechanical response of a $\alpha_2(\mathrm{Ti_3Al}) + \gamma(\mathrm{TiAl})-$submicron grained $\mathrm{Al_2O_3}$ cermet under dynamic compression: modeling and experiment". I, the first author of this publication, was responsible for developing the model, writing the code, designing and performing all the numerical simulations, and writing the original draft. H.Y. Li performed the experiments and contributed to manuscript edits. J.D. Hogan was the supervisory author and was involved with concept formation and manuscript composition.

- Chapter 4 of this thesis has been submitted to *Acta Materialia* as **B. Amirian**, H. Jafarzadeh, B.E. Abali, A. Reali, and J.D. Hogan, "An advanced phase-field approach to evolution and interaction of twins in single crystal magnesium". I, the first author of this submission, developed the model, wrote the code,

designed and performed all simulations, analyzed results, and wrote the original draft. H. Jafarzadeh analyzed results, reviewed, and edited the submitted journal article. B.E. Abali helped with the code, allocated the computational resources, reviewed and edited the submitted journal article. A. Reali reviewed and edited the submitted journal article. J.D. Hogan supervised the research, acquired funding, reviewed, and edited the submitted journal article. All authors discussed the results.

- Chapter 5 of this thesis has been submitted to *Journal of the Mechanics and Physics of Solids* as **B. Amirian**, H. Jafarzadeh, B.E. Abali, A. Reali, and J.D. Hogan, "Time-evolved phase-field model for capturing twinning, fracture-induced twinning, and fracture at large strains in anisotropic brittle materials". I, the first author of this submission, developed the model, wrote the code, designed and performed all simulations, analyzed results, and wrote the original draft. H. Jafarzadeh analyzed results, reviewed, and edited the submitted journal article. B.E. Abali helped with the code, allocated the computational resources, reviewed and edited the submitted journal article. A. Reali reviewed and edited the submitted journal article. J.D. Hogan supervised the research, acquired funding, reviewed, and edited the submitted journal article. All authors discussed the results.

"Our virtues and our failures are inseparable, like force and matter. When they separate, man is no more"

-Nikola Tesla

This thesis is wholeheartedly dedicated to my parents (Mehri and Eliyas) and my beloved wife (Leila), for their great support, motivations, and true loves. Words can not express how grateful I am to them. Specially, I dedicate this dissertation to my father that pushed me forward to finish my PhD journey that I had started with his help and support. I will always remember him as my hero and will love him.

I would also like to dedicate this work to my brilliant sister, Bita, and my affectionate brothers, Benjamin and Davood, for all of their supports and kindness during my study since the beginning until my PhD.

I also dedicate this thesis and give special thanks to my dear father- and gracious mother-in-law for their endless help and pray.

Acknowledgements

First, I would like to thank my supervisor, Dr. James Hogan, for his mentorship and guidance throughout my graduate degree. I am so honored to study under his supervision, truly appreciative for the trust he has placed in me, and blessed for all of the great opportunities he has provided for being a great human being.

I am grateful to Professor Zengtao Chen, Professor Chong-Qing Ru, Professor Xiaodong Wang, Professor Mustafa Gul, and Professor Kaan Inal for serving on my dissertation and preliminary exam committee. They have provided me a number of valuable suggestions on my thesis by putting their valuable time and effort in reviewing my work.

I also want to thank Professor Valery I. Levitas for his supports throughout my first two years as a graduate student at the Iowa State University.

Next, I would like to express my thanks to Haoyang Li for teaching me valuable knowledge on material experiments.

I would also like to extend my appreciation to Dr. Bilen Emek Abali, Dr. Hossein Jafarzadeh, and Professor Alessandro Reali for the support during my model development, where numerous mistakes could have happen without their helps.

Lastly, I would like to thank my groupmates, especially Calvin Lo, Dr. Brendan Koch, and Dr. Kapil Bhagavathula, for their countless helps and supports. We made a great team together.

Above all, I owe immense thanks to my parents and wife for giving me unconditional love, support and encouragement.

Table of Contents

List of Tables

List of Figures

Chapter 1

Introduction

1.1 Motivation

This thesis explores the dynamic failure of novel light-weight materials that are used in impact applications [1]. Subsequently, we provide brief motivations for the study of the three primary materials of interest in this thesis: TiAl-Al_2O_3 ceramic-metal composites, single crystal magnesium, and nano-grained boron carbide, with additional details on motivations found for these materials in the individual chapters.

1.1.1 An Introduction to Two-Phase TiAl-Al_2O_3 Ceramic-Metal Composites

Due to its excellent corrosion resistance, high specific strength, sufficient creep resistance at elevated temperatures, and relatively low density, the two-phase titanium aluminide alloys are a potential candidate for aerospace and automotive structural applications [2–4]. These alloys can exhibit preferable mechanical performance as a result of containing multilayer phases with smaller interlayer thickness [5, 6]. However, drawbacks such as poor fracture toughness, low ductility at room temperature, and insufficient strength at high temperatures put a strict limit on their use in some applications [7]. To remedy this, introducing second phase particle reinforcements, termed intermetallic matrix composites (IMCs), can improve the toughness, creep resistance, and heat-resistance stability of the titanium aluminide material systems

[8, 9]. This class of ceramic-metal materials can be categorized as either metal matrix composites (MMCs) ($\geq$ 50 vol.% metal) [10] or cermets ($\geq$ 50 vol.% ceramic) [11]. With higher ceramic contents and associated greater strengths of cermets in comparison with MMCs, cermets are expected to be more effective as strike-face materials in aerospace and defense applications [12, 13]. Among compatible and thermochemically stable strengthening phases for intermetallic TiAl, such as SiC [14], TiB_2 [15], Ti_2AlC [16], Ti_5Si_3 [17], Al_2O_3 [18], and their combination [19, 20], this thesis is focused on a $\alpha_2(Ti_3Al) + \gamma(TiAl)$-submicron grained alumina cermet due to its high temperature strength [21], excellent oxidation resistance [22], exemplary wear resistance [23], relatively low cost [24], and similarities between the coefficients of thermal expansion of the constituents [25]. In addition, the submicrometer alumina grain size of the material under study here can lead to improved hardness, strength, and optical performance in comparison to bulk alumina [26, 27], which makes submicron grained advanced cermets more favorable for a wide range of applications, from light-weight ballistic armor [28] to electronic packaging substrates and medical applications [29].

In the literature, researchers have developed various methods such as reactive hot processing [30], mechanical alloying [31], and sintering [32] for fabricating intermetallic TiAl-submicron grained Al_2O_3 materials. To date, there has been a number of published papers detailing the microstructure features and low strain-rate mechanical properties of two-phase $TiAl/Al_2O_3$ (see [18, 33]); however, limited studies have been devoted to the mechanical response of these unique materials under high strain-rate loading. A limited number of research has attempted to explore the deformation mechanisms of γ(TiAl)-based alloys [34, 35], and dynamic fracture of nano-grained transparent alumina [36, 37]. No coupled numerical and experimental studies have investigated the dynamic mechanical behaviors (e.g., stress-strain response), microstructure parameters (e.g., inclusion shape, size, and aspect ratio), and damage mechanisms (e.g., void deformation and growth) of an intermetallic TiAl-Al_2O_3 cermet; these are addressed in the present thesis.

1.1.2 An Introduction to Single Crystal Magnesium

Due to their excellent strength-to-weight ratios, magnesium and magnesium-based alloys have gained a lot of interests for transportation [38] and defense applications [39]. However, limited number of dislocation slip systems in hexagonal close-packed structure makes magnesium a comparable low ductile material at low temperature [40]. Consequently, the successful implementation of Mg-based materials hinges upon an accurate model to predict the complex material response (e.g., plasticity mechanisms), where twinning is a common mechanism that manifests in magnesium [41–43], especially under high strain-rate loading [44]. A variety of techniques operating on different length scales, including in-situ synchrotron X-ray diffraction (XRD) [45], transmission electron microscopy (TEM) [46], nanoindentation [47], and molecular dynamics (MD) simulation [48] have been proposed to bridge the gap between macroscopic observations and microstructural mechanisms in magnesium. Recent approaches have been supported by numerical simulations, performing a finite element method within the framework of crystal plasticity [49] and time-independent phase-field approach [50] . In the present thesis, the research focuses on the twin morphology in magnesium at the propagation stage which is associated with the formation and migration of twin tips and twin boundaries. This is important for understanding the mechanical behavior dominated by the twinning process and interactions [51] as will be explored in this thesis.

1.1.3 An Introduction to Nano-Grained Boron Carbide

As a result of having high elastic stiffness, relatively low mass density ($2.52\,\frac{\mathrm{g}}{\mathrm{cm}^3}$), and a high Hugoniot elastic limit (HEL) of 14 - 19 GPa, boron carbide (B_4C) has received considerable attention in ballistic impact applications [52]. In boron carbide, twinning is believed to occur under high pressure and high temperature conditions during manufacturing processing [53], and can serve as the preferred cleavage planes [54]. Studying twinning phenomena in boron carbide is primarily motivated by its link

to subsequent amorphization and phase transformation [55, 56], limiting B_4C from performing to its full potential in ballistic applications [57, 58]. Developing next-generation boron-based materials with controlled twinning behaviors offers promising opportunities for improved mechanical properties [59, 60] and performance in engineering applications (e.g., gas turbine engines) [61]. This motivates the current research for nano-grained boron carbide.

For nano-grained boron carbide, limited literature data has primarily focused on processing [62], the effect of grain size on hardness and elastic modulus [63], and rate-dependent mechanical behavior [64]. More recently, state-of-the-art real-time visualization techniques such as ultra-high-speed-imaging have been coupled with experimental setups to explore the in-situ fracture behaviors of boron carbide during quasi-static and dynamic loading [65, 66]; however, no in-situ measurements exists on time-resolved twin evolution and growth in boron carbide, which is likely a result of the limitations in available diagnostics to capture growth and evolution behaviors at sufficient length and time scales [67]. Computationally, modeling sub-nanometer scale behavior of boron carbide have been pursued using molecular dynamics simulations [68] and time-independent phase field approaches [69], with focus on hardening and toughening mechanisms and twinning. While new understandings have been gained by using molecular dynamics simulations to study plastic deformation and fracture behaviors in boron carbide [70], atomistic simulations are limited in their ability to simulate twinning behaviors at relevant length and time scales needed for practical implementation in materials design. These limitations and gaps are addressed in this thesis by studying growth mechanisms of twin tips and twin boundaries in single crystalline boron carbide at the nanoscale. Specifically, a generalized constitutive model for fracture and twinning as a failure mode for a novel nano-grained B_4C is developed based on the phase-field concept [71], expanding on previous work in the literature involving continuum nonlinear elastic and elastic-plastic models [69].

1.2 Thesis Objectives

Understanding and predicting dynamic deformation and damage evolution in anisotropic brittle materials (e.g., ceramics and ceramic-metal composites) is needed for industries to refine the materials' design. To address this, the objective of this thesis is to develop physics-based multi-scale computational models that describe the behavior of novel light-weight brittle material systems: 1. a $\alpha_2(Ti_3Al) + \gamma(TiAl)$-submicron grained alumina cermet, 2. single crystal magnesium, and 3. nano-grained boron carbide. The models can be used for studying the boundary value problems involving more complicated geometries and boundary conditions. The computational models make use of the most recent advancements in constitutive model formulation, parallel computing, and numerical scheme. The models are informed and validated with high fidelity experimental tests and molecular dynamics simulations developed in the group and from literature. The applied methods are described in the subsequent chapters in detail. The outcomes of this thesis will be important to:

1. Offer promising avenues for qualitative and quantitative understanding of light-weight materials using in impact applications, and serving as a foundation for further material design and optimization such as increasing the confidence limits of these materials.

2. Provide insights into the factors that control the dynamic behavior of light-weight materials by connecting their deformation and fracture mechanisms to the microstructural features.

3. Understand the physics of the main plastic deformation in nanoscale magnesium for tailoring their ductility at room temperatures by capturing detailed microstructural characteristics, such as twin interface evolution, to shed light on the early stages of twin growth.

4. Guide the design, manufacturing, and testing of next-generation nano-grained

brittle materials used in armor solutions by exploring favorable mechanical properties and microstructures for improved performance.

1.3 Thesis Goals

The objectives of this thesis will be accomplished by completing the following research goals:

- ✓ Obtaining some of the critical microstructure parameters of two-phase TiAl-Al_2O_3 ceramic-metal composites (e.g., shape, distribution, and volume fraction of each constituent phases) via scanning electron microscopy (SEM), along with obtaining elastic stiffness of the matrix and inclusions from an ultra-nanoindentation tester from Anton Paar. These parameters are considered as inputs to the numerical framework.

- ✓ Implementing a microstructure-dependent physics-based model for predicting the behavior of $\alpha_2(Ti_3Al) + \gamma(TiAl)$-submicron grained alumina cermet under both strain-rate dependent compression loading. As a result of having a porous matrix with high particle volume fraction (up to 65 %), a three dimensional face centered cubic (FCC) unit cell with a uniform monodisperse distribution of voids is considered as the geometry in this study. The fracture behavior of the cermet is modeled using the modified variational formulation of the Gurson model (MVAR), in which the main damage variable is the existing voids. The void rotation as a result of subjecting the material to high stress values is taken into account in the model. For the first time, the MVAR model is used for the dynamic failure of realistic cermets rather than idealised ones.

- ✓ Conducting strain-rate dependent uniaxial compression experiments using MTS machine (quasi-static strain rates) and split-Hopkinson Pressure Bar apparatus (dynamic strain rates). Experiments are coupled with ultra-high-speed imaging

and digital image correlation to evaluate stress-strain, lateral vs. axial strain, and failure responses. This information serves to validate the model.

✓ Solving more than 30 simulations for both quasi-static and dynamic loading conditions in terms of different particle shapes (icosahedron, sphere, platelet, and prism), inclusion volume fraction (60%, 65%, and 70%), void volume fraction (0.5%, 1.5%, and 3%), and elastic stiffness for both particles and matrix in order to account for the experimental variability and to achieve realistic matching with experiments.

✓ Taking field emission (FE) SEM micrographs on the fracture surface of the recovered fragments in a dynamic experiment for post-mortem analysis of failure mechanisms (e.g., void deformation and growth, particle micro-cracking, and interface decohesion). These are used to compare with simulation results. To model observed fracture behaviors at the matrix-patricle interface, a polynomial cohesive zone model is incorporated into our numerical model. The proposed model is shown to provide a good agreement with experimental data and is then used to explore the material response outside of the experimentally accessible conditions.

✓ Using an advanced physics-based model of deformation and nano-twinning to predict the failure in magnesium nanoscale single crystals. The results confirm that our model is able to describe the early stages of twinning deformation.

✓ Generalizing a robust multi-scale micromechanical model for magnesium and nano-grained boron carbide (B_4C) under various loading conditions, which can bridge the gap between lower scale deformation mechanisms (e.g., amorphization, dislocation, and twinning) to macroscopic material behaviors such as fracture, fragmentation, and granular flow. A fully nonlinear continuum-based phase-field approach which enables regularization of localization zones is used.

The problem formulations are derived in both small and large strains with consideration of anisotropic elasticity and surface energy, making the study comprehensive.

✓ Focusing on twinning and fracture as the key deformation mechanisms in single crystal magnesium and boron carbide at the nanoscale, an open-source Python-based finite element package FEniCS is implemented to solve the governing equations by a monolithic scheme algorithm to improve the computational accuracy. The simulation has been performed with the help of high performing clusters to study the multi-length scale material response, enabling new insights in twin growth and interaction to be determined.

✓ The obtained results are finally compared, both qualitatively and quantitatively, with the available experimental data for boron carbide and recent molecular dynamics simulation results for magnesium from the literature.

1.4 Contributions

The contributions of this thesis are summarized as follows:

- Providing guidance to our partners in the USA and Canadian government for material refinement to enhance their mechanical properties and performance.
- Augmenting our understanding of dynamic failure in structural ceramic-based materials driven by advancements in multi-scale physics-based modeling and experimental validation coupled with state-of-the-art imaging and diagnostics during experimentation.
- Presenting a detailed finite element method for two separate order parameters at both small and large strains with anisotropic elasticity and surface energy which can be developed easily for describing other deformation mechanisms, including dislocation, amorphization, phase transformation, fragmentation, etc.

- Solving the coupled governing equations by implementing a highly accurate monolithic algorithm in an open-source Python-based platform, which is compatible with parallel computing using high-performance clusters.

- Predicting the crack path in anisotropic brittle materials (e.g., boron carbide) for the first time by considering a new decomposition for the strain energy density for specimen under biaxial compressive loading.

- Tracking complex crack and failure trajectories induced by the spatial variation of microstructure features across a heterogeneous material that are difficult to capture with conventional numerical methods.

- Determining the sequence of fracture and twinning in anisotropic brittle materials that are almost impossible from analysis of post-mortem material characterization in dynamic experiments.

1.5 Thesis Structure

This thesis is organized as follows:

- Chapter 1: Introduction of this thesis, including motivations for studying $\alpha_2(Ti_3Al)+\gamma(TiAl)$-submicron grained alumina, magnesium, and nano-grained B_4C, and outlining the thesis objectives, thesis goals, contributions, and thesis structure.

- Chapter 2: Proposes a microstructure-based finite element model for a novel nano-grained ceramic-metal composites. This study, titled "An experimental and numerical study of novel nano-grained $(\gamma+\alpha_2)-TiAl/Al_2O_3$ cermets", was published in *Materials Science and Engineering: A* in December 2018 [72].

- Chapter 3: Develops a microstructure and strain-dependent constitutive model for $\alpha_2(Ti_3Al+\gamma(TiAl)$-submicron grained Al_2O_3 cermet under dynamic compression. This study, titled "The mechanical response of a $\alpha_2(Ti_3Al+\gamma(TiAl)$-

submicron grained Al_2O_3 cermet under dynamic compression: modeling and experiment", was published in *Acta Materialia* in September 2019 [73].

- Chapter 4: Utilizes a first-of-its-kind time-resolved phase-field model to study the growth and interactions of twins in single crystal magnesium. This chapter is a prelude to use the model for investigating the deformation mechanisms of B_4C under various loading conditions. This study, titled "An advanced phase-field approach to evolution and interaction of twins in single crystal magnesium", has been submitted to *Acta Materialia* in August 2021.

- Chapter 5: Extends the phase-field approach to predict various deformation mechanisms (e.g., twinning and fracture) in single crystal Mg and B_4C by implementing the monolithic solver in an open-source finite element platform. This study, titled "Time-evolved phase-field model for capturing twinning, fracture-induced twinning, and fracture at large strains in anisotropic brittle materials", has been submitted to *Journal of the Mechanics and Physics of Solids* in August 2021.

Chapter 2

An Experimental and Numerical Study of Novel Nano-Grained $(\gamma + \alpha_2)$-TiAl/Al_2O_3 Cermets

Published in Materials Science and Engineering: A

B. Amirian[a], H.Y. Li[a], James D. Hogan[a]

[a]*Department of Mechanical Engineering, University of Alberta, Edmonton AB T6G 2R3, Canada*

Abstract

In this study, a microstructure-based finite element model for nano-grained $(\gamma + \alpha_2)$-TiAl/Al_2O_3 cermets is proposed based on a modified variational formulation of the Gurson model for an elastic-plastic porous material. In the modeling approach, the high volume fraction of alumina, variability in material characteristics, and microstructural features (e.g., inclusion size) are considered. Mechanical properties and microstructure inputs are derived from nanoindentation and microscopy analysis performed for this study, as well as using available information in the literature. Once developed, modeling results are validated against experimental quasi-static compressive stress-strain measurements using digital image correlation techniques. The validation is extended by comparing

experimental observations and computational outputs of the ratio of the lateral to axial strain (as a measure of deformation), and reasonable agreement is found. Once the model is validated for an experimentally known condition, the effect of varying the mechanical properties (e.g., strain hardening parameters and elastic modulus) and microstructure variables (e.g., alumina volume fraction and porosity) on material responses are then explored. These results serve as a foundation for future microstructure optimization.

Keywords: Finite element models; Modified variational formulation; Cermet; Uniaxial compression test; Digital image correlation

---

2.1 Introduction

Structural ceramics have properties necessary to allow them to serve as structural components subjected to mechanical stress. Many of these ceramics also exhibit other attractive properties, such as resistance to deformation at high temperature [21], high hardness [22], and high wear resistance [23]. Taken together, these properties make many structural ceramics suitable for application in light-weight ballistic armor [28], and as medical applications and dental implants [29, 74]. In these and many other applications, the monolithic form of these ceramics are susceptiple to catastrophic brittle fracture. To remedy this, researchers have attempted to improve the ductility and fracture toughness of ceramics by combining the high toughness of metals with the high hardness, strength, and stiffness of the ceramics [75–77]. In the ceramic-metal materials, one can classify materials containing more than 50 vol.% metal as metal matrix composites (MMCs) [10, 78], and those containing more than 50 vol.% ceramic as cermets [11, 79]. In this study, we investigate the elastic characteristics and strength of cermets.

Cermets typically have strengths that range between 2 and 7 times the strength of the metal matrix composites, and this allows them to be a potential candidate for aerospace and defense applications [79, 12, 13]. Compared with structural ceramics, cermets have higher fracture toughness and higher flexural strength [80]. To further the use of ceramic-metal materials in industrial applications, this study focuses on understanding the linkages between mechanical responses (e.g., stress-strain behavior), and microstructure characteristics (e.g., inclusion size and porosity). This is studied both experimentally and computationally for $(\gamma + \alpha_2)$-TiAl/Al_2O_3 cermets.

Achieving more favorable engineering properties in TiAl (e.g., high ductility and toughness) can be obtained by incorporating $(\gamma + \alpha_2)$ phase in the TiAl material [3]. The $(\gamma + \alpha_2)$-TiAl is believed to exhibit improved mechanical properties over its monolithic constituents as a result of greater volume fractions of lamellar grains, which

are the result of the $\alpha \rightarrow \gamma$ phase transformation and eutectoid reactions [81]. Prior studies of $(\gamma + \alpha_2)$-TiAl family of materials include the processing and fabrication of dense alumina-TiAl-Ti_3Al [82], the oxidation behavior of in-situ $TiAl/Al_2O_3$ [83], and microstructure characteristics of synthesized $TiAl/Al_2O_3$ [84–86]. Altogether, these studies have advanced our understanding of the material science of these material systems. To date, no studies have focused on the mechanical behavior and numerical modeling of these materials, which is addressed in this study.

There are numerous predictive models that are used to desribe the mechanical properties of cermets [87–89]. In earlier studies, the limiting state of plastic collapse was used to relate the hardness of cermet to its microstructure [90]. Later, Engqvist et al. [91] proposed empirical models for hardness of cemented carbide by studying the interactions between the binder and the carbide. Among other modeling approaches, microstructural models such as unit cell models [92] and dislocation based models [93] have generated interest in predicting the strength of cermets. For example, in a study by Legarth [94], the non-monotonical effect of a material length scale parameter on the failure strain of MMCs was adopted using a unit cell approach. In a separate study, Bao et al. [95] carried out the combination of continuum plasticity theory with unit cell modeling to study the non-deforming particles in reinforcing ductile matrix materials. Other microstructure-independent approaches, such as the self-consistent models, were developed for composites, however, their usefulness are limited to materials with a low particle volume fraction [96]. In some commercial cermets, the particle volume fraction can reach up to 80% [97]. To date, the majority of the modeling efforts have concentrated on idealised microstructure configurations in conceptual ceramic-metal materials. Limited efforts have been made to bridge these models with experimental inputs [**christman1989experimental**, 98, 99]. In this present study, contributions are made towards these efforts by employing microstructural data as model inputs, and then using experimental data to validate the model.

Building on these previous works, the aim of this study is to develop a three-dimensional face centered cubic (FCC) unit cell model of $(\gamma + \alpha_2)$-TiAl/Al_2O_3 commercial cermet. A modified variational formulation of the Gurson model (MVAR) for elasto-plastic porous materials is used for the host material that is based on the nonlinear homogenization approach. Scanning electron microscopy (SEM) images are used for characterization of porosity, alumina volume fraction, and void clusters as model inputs. Nanoindentation tests are used to provided inputs for stiffness for the matrix $(\gamma + \alpha_2)$-TiAl, and the reinforcement Al_2O_3 materials. Following this, quasi-static uniaxial compression tests are performed and coupled with digital image correlation (DIC) techniques to determine the stress-strain responses of the material, as well as the corresponding ratio of axial to lateral strain during loading. These experimental inputs are then used to validate the unit cell model. Following implementation and validation, the influences of the variability of the stiffness and volume fraction of alumina nano-particles, along with void volume fraction (porosity) on the stress-strain behavior of cermet are discussed in detail. The totality of the results allow us to further improve the material strength and performance through material optimization.

2.2 Experimental Procedures and Results

2.2.1 Material Composition and Microstructure

The $(\gamma+\alpha_2)$-TiAl/Al_2O_3 cermet being investigated in this study is fabricated through self-propagation high-temperature sintering, and is provided by Lumiant Corporation, British Columbia. Cermet tiles are cut into specimens with size of 2.3 mm (length) $\times$ 2.5 mm (width) $\times$ 2.7 mm (height) for mechanical testings. Shown in Figure 2.1 is a backscattered electron (BSE) SEM image (Figure 2.1a) with energy dispersive X-ray spectroscopy (EDS) density maps of the elements: Al (Figure 2.1b), Ti (Figure 2.1c), and O (Figure 2.1d). Altogether, Figure 2.1 is used to reveal the spatial

distribution of the phases within the material, with brighter colors in Figure 2.1b to Figure 2.1d corresponding to higher concentrations and darker colors corresponding to lower concentrations. This information is used for modeling inputs.

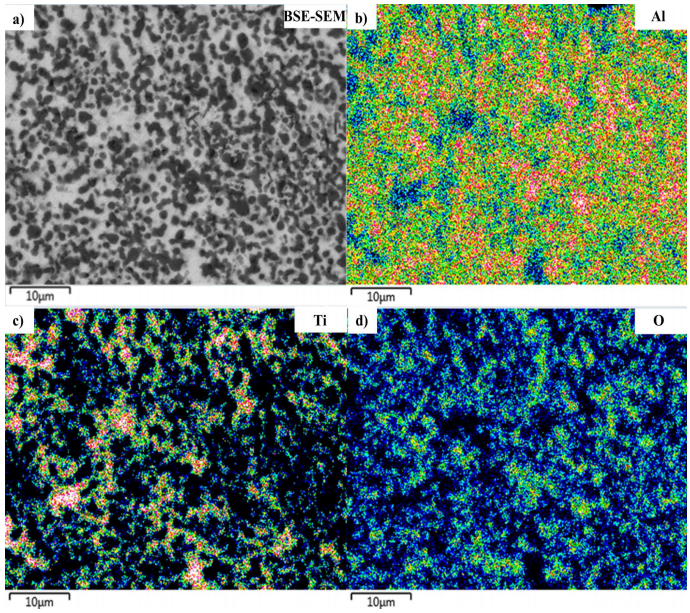

Figure 2.1: EDS concentration mapping on a 2000 times magnification SEM image showing distributions of selected element. Concentration of elements decrease based on the color sequence in the visible light spectrum. Brighter colors correspond to higher concentrations: a) FESEM image showing the phase distribution, where black regions correspond to the alumina phase and white regions correspond to the TiAl phase; b) Distribution and concentration of Al element in the FESEM image; c) Distribution and concentration of Ti element in the FESEM image; (d) Distribution and concentration of O element in the FESEM image.

In the Figure 2.1a, the lighter regions correspond to the TiAl phase because of the higher Z (atomic number) value; consequently, the darker regions are the Al_2O_3 phase. The darkest spots in the BSE figure correspond to the micro-pores present in the material, which have been confirmed with the field emission SEM (FESEM) images. It is observed that the pores tend to cluster around the boundary or within the alumina phase. To further analyze the features in the images, a MATLAB-based program was developed to quantify the areal fractions of the alumina and titanium aluminide phases, as well as the sizes of the alumina nanoparticles and pores. These methods are consistent with those developed in Hogan et al. [100]. As

an outcome of this analysis, the porosity level is determined as 1.2% to 3% at 2000 times magnification depending on a threshold setting. These values are within the range that is reported by the manufacture of 2%. Using similar image processing techniques, the average pore size was $0.07 \pm 0.02\,\mu$m, as measured by the major axis. The individual alumina particles appear spherical in shape and in clusters in the material with sizes of $0.5\,\mu$m to $1.5\,\mu$m with an average of $1 \pm 0.3\,\mu$m, and clusters sizes of $3\,\mu$m to $9\,\mu$m. The area fraction of the alumina phase is estimated as $65 \pm 1\%$ using the same image processing techniques.

Next, the concentration of constitutive elements are investigated using energy dispersive X-ray microanalysis. From Figure 2.1b, it is observed that Al is present everywhere in the material, with higher concentration in the alumina phase (darker phase in the SEM image). Comparing the Al (Figure 2.1b) with the Ti (Figure 2.1c) concentrations, it is observed that regions of higher concentrations of Al correspond to regions of lower concentrations of Ti. Similarly, regions of higher concentrations of Al correspond to regions of higher concentrations of O, which are believed to be the Al_2O_3 phases with trace amounts of O with the Ti and Al. This is the α_2-TiAl phases (confirmed with X-ray diffraction (XRD) but not shown for brevity).

2.2.2 Experimental Setup

The quasi-static uniaxial compression test was conducted on a standard MTS series 810 servo-hydraulic machine. Loading platens were made from hardened steel (M2 high-speed steel) and were held in alignment by the machine grip. Ti-6Al-4V titanium alloy jacketed tungsten carbide (WC) platens were used between the specimen and the loading platens to provide stress redistribution from the specimen to the loading platens, as well as to protect the machine load platens from indentation of the hard specimens. This is required by the ASTM C1424-15 [101]. As required, extreme pressure grease was applied on the WC platen surfaces to eliminate the frictional effect. The platens were then pre-loaded without specimen to create a thin, uniform

layer of lubricant. Good alignment was ensured by carefully bringing the platens and specimen in touch. The experiment was performed under displacement control with a nominal strain rate of $1 \times 10^{-4}\,\mathrm{s}^{-1}$. The cross-head displacement was measured by a linear variable differential transformer displacement sensor with an accuracy of 0.001 mm. A 100 kN load cell with background noise corresponding to approximately ± 1 N was used to record the force history during loading process. The acquisition rate of the MTS machine was set at 30 Hz. An AOS PROMON U750 high-speed camera was used to provide visualization on macroscopic deformation features on the specimen surface. The specimen was positioned normally to the optical axis of the camera to eliminate out-of-plane displacement. This camera has a full resolution of 1280×1024 pixels and recorded at a frame rate of 100 frames per second. In total, five experiments are presented in this study at the same loading condition to study variability and validate the model.

2.2.3 Digital Image Correlation Technique

2.2.3.1 Methodology

Digital image correlation was used to obtain the global strain field from the specimen surface during compression testing. The Correlated Solutions VIC2D 6 software [102] was used to produce the full-field strain measurements. In DIC analysis, a small subset of an image is tracked as the specimen translates and deforms. In each image, the subset in the deformed images are shifted to match the pattern in the reference image; the "match" is performed as the total difference in gray level at each point. In order to obtain the displacement information by tracking the deformation or displacement of subsets, a correlation peak is determined as the gray level for each subset [103]. The position of the peaks provides the local displacement and the height of the peaks gives the degree of correlation. During the analysis, the zero-normalized squared sum of difference (ZNSSD) method was chosen to perform the correlation. This method is known to be highly robust, which will not be affected by the offset and scale in

lighting [104]. Gaussian low-pass filter was selected to eliminate the high frequency signals and pre-smooth both reference and deformed images. The "Optimized 8-tap" interpolation scheme in the software was selected, which incorporated the highest order of spline scheme. In post processing, the rigid body motion was removed to compensate any possible vibration on the camera or the machine, which was deemed minimal in this experiment.

2.2.3.2 Setup

In the experiment, an ultra-fine point airbrush with 0.12 mm needle and nozzle was used to spray specialize airbrush paint with particle size down to 0.1 μm onto the specimen surface. A thin, white base coating was applied on the as-received shiny specimen surface to have a uniform background. Black speckles were then sprayed on the base coat with a continuously sweeping motion.

In these experiments, an ultra-bright LED light equipped with fiber optical light guide with a 7.6 mm diameter liquid light guide was used to provide high intensity uniform lighting environment over the specimen surface. A highly contrasted and overexposed surface condition was obtained. According to Jerabek et al. [105], a fine speckle pattern and appropriate light intensity gives a better result when it is under the condition of overexposure. With good specimen preparation and lighting environment, the PROMON U750 camera was used to capture the deformation process of the specimen. With the first image as the reference (undeformed) image and appropriate area of interest (AOI), the "suggested subset" function in the VIC2D package is used to obtain the proposed subset size with minimum estimated error. This could be used as an alternative way to examine the goodness of speckle pattern. It was observed that a consistent subset size was obtained on all specimens used in this study, where all subset sizes were in the range of 23×23 pixels to 30×30 pixels. To perform the analysis, the correlation step size was altered in each selected AOI from 2 to 7 based on the noise level to determine the optimal results. Several AOIs were tested in each

experiment to examine the repeatability of the results, including failure strain, strain rate, and slope change between axial and lateral strains. Finally, the smoothest strain field with least aliasing was picked and imported into MATLAB for further analysis with the stress data. Details on sensitivity analysis and filtering are beyond the scope of this study.

2.2.4 Experimental Results

2.2.4.1 The Stress-Strain Response of $(\gamma + \alpha_2)$-TiAl/Al_2O_3

Shown in Figure 2.2 is the engineering stress-strain plot of the material from the quasi-static uniaxial compression tests. The naming of the specimens follows the DIC speckle pattern sequences (i.e., sp1, sp2, etc.). Specimens sp1, sp4, and sp5 are tests that successfully showing the repeatability of the experiments. Some outliers, such as sp2 and sp3 in the figure, correspond to potential microstructural variabilities and surface deformation features during loading (sp3 had a visible fracture form on its surface at the corresponding dip in the stress). These are included to demonstrate the variability in the results.

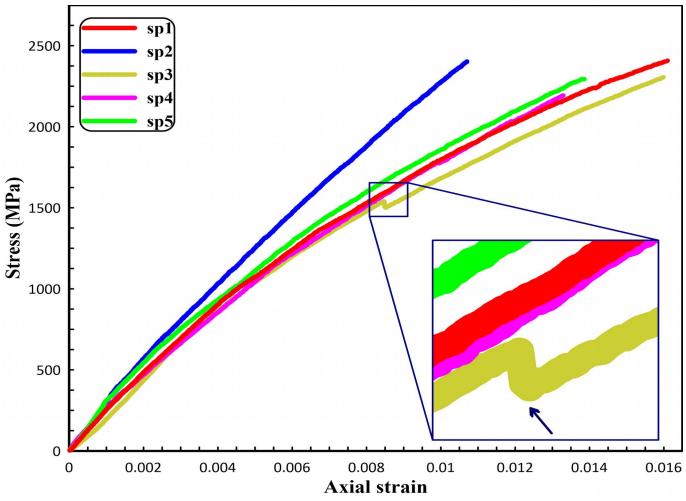

Figure 2.2: Variations of the experimental engineering stress with the DIC engineering strain.

From the figure, the failure strain of the materials is between 1.1% and 1.7%, with an

average of $1.4 \pm 0.2\%$. The compressive strength is between 2200 MPa and 2600 MPa, with an average of 2400 $\pm$ 120 MPa. Strain hardening effects are observed on all curves, which indicates ductility in the material when compared to, for example, alumina. Similar shaped curves for cermets have been reported by others in the literature [106, 107]. The slope of the initial part of the stress-strain curve, taken as the Young's modulus of the material, is between 240 GPa and 310 GPa, with an average of 274 $\pm$ 26 GPa.

2.2.4.2 The Transverse and Axial Strain Ratio During Loading

Next, the ratio of transverse (ε_{yy}) to longitudinal (ε_{xx}) strain is examined in Figure 2.3. Color schemes follow those from Figure 2.2. Again, three curves are presented for repeatability and two outliers are shown for potential microstructural variability. In Figure 2.3, the initial lateral to longitudinal strain ratio across all five samples is 0.227 with a standard deviation of 0.001. The ratio at the initial constant portion is identified as the Poisson's ratio of the intact material, which corresponds to the first order approximation for small values of length change. The value reported here is reasonable as the Poisson's ratio for alumina is 0.220 reported by Coorstek [CoorsTek Inc.], and for γ-phase titanium aluminide is 0.230-0.240 [108].

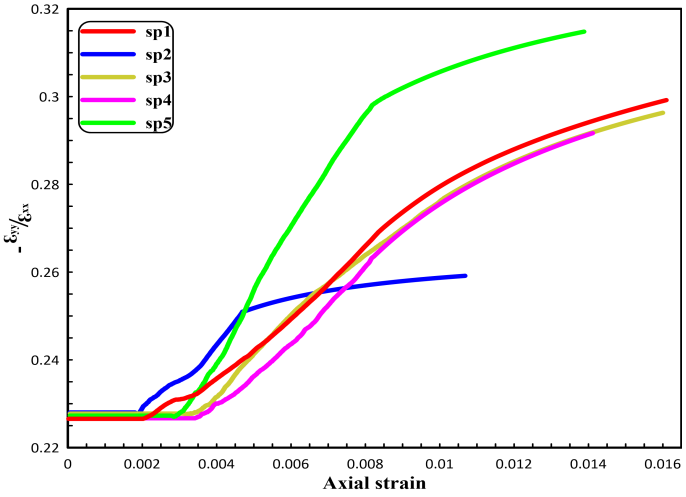

Figure 2.3: Variation of the lateral and longitudinal strain ratio with the DIC strain.

After the initial part of the curve, the ratio of lateral to longitudinal strain could be a representation of the deformation mechanisms that manifest in the material during loading. In Figure 2.3, all curves start near a constant value of 0.227 and remains flat until 0.2% to 0.4% strain, after which time the curves increase at variable rates until maximum values of 0.250 to 0.320 (average of 0.290 ± 0.020). The rise in the curves is a consequence of damage accumulation, and this appears to be increasing at a greater rate in the lateral direction (perpendicular to compression) than the axial direction (parallel to compression). Here, material failure is likely through a combination of plastic deformation and fracture. In tests sp1, sp3, and sp4, the ratio rises to approximately 0.300 before failure. Specimen sp2 shows a significantly lower final ratio than other tests at much lower failure strain. In addition, specimen sp5 has a much greater failure strain and higher final strain ratio. The reason for this is unknown, but is also likely due to the microstructural variability. Interestingly, no discernible features other than a minor transition in slopes is observed for sp3, where cracking occurred during compression testing. Altogether, these results provide insights into material deformation and will serve as data sets for validation our modeling efforts described next.

2.3 Numerical Modeling of $(\gamma + \alpha_2)$-TiAl/Al_2O_3 Cermets

2.3.1 Microstructure Representation

In this study, the microstructure is modeled as a two phase material: (i) the elastic-plastic and isotropic matrix $(\gamma + \alpha_2)$-TiAl phase, and (ii) the inclusion Al_2O_3 phase. Porosity is also generated by means of a Mathematica code. The microstructure representation is considered by ellipsoidal voids with both equal or unequal semi-axes a_1, a_2 and a_3, and this is shown schematically in Figure 2.4. Here, a three-dimensional unit cell with spherical isotropic elastic particles of alumina in a voided elasto-plastic

matrix is modeled. In our modeling approaches, the FCC crystal structure arrangement is considered in order to allow us to achieve representative volumetric densities of the secondary alumina phase ($\sim 65\%$).

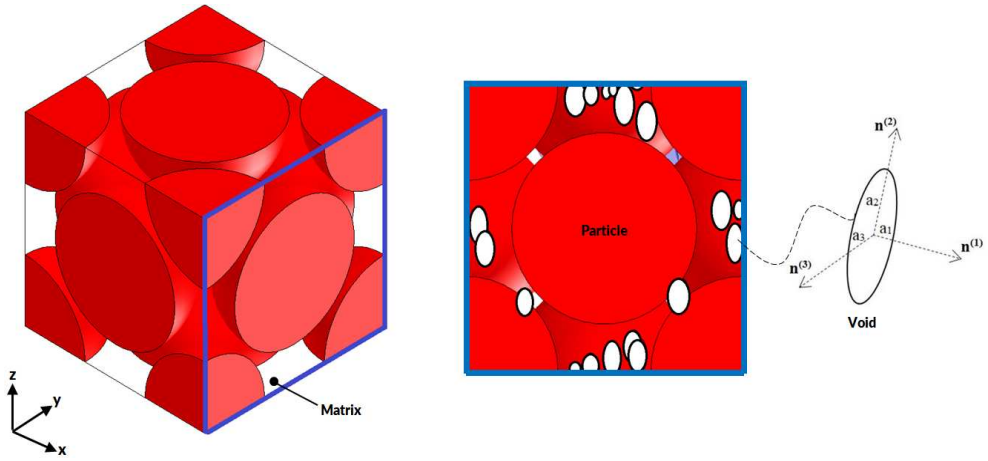

Figure 2.4: Schematic representation of microstructures presenting the local orientation axes of an ellipsoidal void with semi-axes a_1, a_2, and a_3.

In these simulations, the set of internal variables for describing the general state of microstructure are: accumulated plastic strain in the undamaged matrix ε_p^M, the volume fraction of the voids f, the local fraction of volume occupied by voids, two aspect ratios characterizing the ellipsoidal shape of the voids (w_1 and w_2) and their distribution functions, and the orientation of the principal axes of the voids (n_i with $i = 1, 2, 3$).

2.3.2 Constitutive Equations

The deformation behavior of (γ+α_2)-TiAl/Al_2O_3 material is distinguished by separating it into recoverable and nonrecoverable parts based on the additive decomposition of strain rates. The rate of deformation tensor D, at every material point of the homogenized porous material is written as

$$D = D^{el} + D^{pl}, \tag{2.1}$$

where D^{el} and D^{pl} are the elastic and plastic parts, respectively. As a consequence of the compressibility of the material behavior due to presence of voids, the plastic

strain rate tensor is only hydrostatic. In this case, linear elasticity is assumed for simplicity as

$$\sigma = E^{el} : \varepsilon^{el}, \tag{2.2}$$

which is the relation between the Cauchy stress σ, and elastic strain tensors ε^{el} through the fourth-order elasticity tensor E^{el}. A hypoelastic form is assumed for the elastic deformation tensor as

$$D^{el} = M^e : \mathring{\sigma}, \tag{2.3}$$

where M^e is the effective elastic compliance tensor and $\mathring{\sigma}$ is the corotational rate of the Cauchy stress given by

$$\mathring{\sigma} = \dot{\sigma} - \omega \cdot \sigma + \sigma \cdot \omega, \tag{2.4}$$

where ω is the spin of voids relative to a fixed frame, i.e., $\dot{n}^i = \omega \cdot n^i, i = 1, 2, 3$. The effective compliance tensor is written as [109]

$$M^e = M + \frac{f}{1-f} Q^{-1}, \tag{2.5}$$

In Eq 2.5, M is the elastic compliance tensor of the matrix material which is the inverse of the elastic modulus tensor E

$$\begin{aligned} E &= 2\mu K + 3\kappa \mathbb{J}, & (2.6)\\ \mathbb{J} &= \frac{1}{3}\delta_{ij}\delta_{kl}, & (2.7)\\ K &= \mathbb{I} - \mathbb{J}, & (2.8)\\ Q &= E : (\mathbb{I} - \mathbb{S}), & (2.9)\\ \mathbb{I}_{ijkl} &= \frac{\delta_{ik}\delta_{jl} + \delta_{il}\delta_{jk}}{2}, & (2.10) \end{aligned}$$

where μ and κ denote the elastic shear and bulk moduli of the matrix, δ and $\mathbb{I}$ are the symmetric second- and fourth-order identity tensors, f is the porosity, $\mathbb{S}$ is the fourth-order Eshelby tensor, and Q is the microstructural fourth-order tensor which

is proportional to the shear modulus, Poisson's ratio, aspect ratio of the voids, and also the orientation of the ellipsoidal voids [110].

The derivation of the constitutive relations is the variational procedure that is used to estimate the effective properties of the nonlinear porous material in terms of an appropriate linear comparison composite. The effective yield function can be written in the form [111]

$$\Phi(\sigma, s) = \frac{1}{1-f}\sigma\colon m\colon \sigma - \sigma_y^2(\bar{\varepsilon}^p), \tag{2.11}$$

where s is the set of internal variables; σ_y is the yield strength in tension of matrix material, and is taken to be a function of the equivalent plastic strain $\bar{\varepsilon}^p$ in the matrix material. Here, m is normalized effective viscous compliance tensor and is defined as

$$m = \frac{3}{2}K + \frac{3}{1-f}\mu Q^{-1}|_{\nu=0.5}, \tag{2.12}$$

where the limit for Poisson's ratio is due to assumption of plastic incompressibility. It is emphasized that the plastic behavior described by the macroscopic potential is fully compressible. If we limit our model to spherical voids, whose shape remain unchanged during deformation, the MVAR model reduces to the Gurson isotropic model

$$\Phi(\sigma, \bar{\varepsilon}^p, f) = \left(1 + \frac{2}{3}f\right)\left(\frac{\sigma_e}{1-f}\right)^2 + \frac{9}{4}f\left(\frac{p}{1-f}\right)^2 - \sigma_y^2(\bar{\varepsilon}^p) = 0, \tag{2.13}$$

where $\sigma_e = (\frac{3}{2}\sigma^d\colon \sigma^d)^{0.5}$ is the equivalent von Mises stress, $\sigma^d = \sigma - p\delta$ is the deviatoric part of the stress, and $p = \frac{1}{3}\sigma\colon I$ is the hydrostatic stress. It is assumed that only the plastic deformation of the matrix leads to change in microstructure because the voids do not carry load and the elastic strains are smaller than the plastic counterpart.

An effect of the mean normal stress on the plastic flow always exists when there is a non-vanishing void volume fraction. By implementing the normality hypothesis of plasticity, the plastic rate of deformation tensor is obtained by

$$D^{pl} = \dot{\lambda}\boldsymbol{N}, \tag{2.14}$$

$$\boldsymbol{N} = \frac{\partial\Phi}{\partial\sigma} = \frac{2}{1-f}m\colon \sigma, \tag{2.15}$$

where $\dot{\lambda} \geq 0$ is the plastic multiplier which can be obtained by consistency condition, and $\boldsymbol{N}$ is the direction of the plastic strain increment. With consideration of the equal relation between the macroscopic plastic work and microscopic work

$$\sigma \colon D^{pl} \equiv \dot{\lambda}\sigma \boldsymbol{N} = (1-f)\sigma_y \dot{\bar{\varepsilon}}^p, \tag{2.16}$$

the evolution of equivalent plastic strain is then obtained by

$$\dot{\bar{\varepsilon}}^p = \frac{\dot{\lambda}\sigma \colon \boldsymbol{N}}{(1-f)\sigma_y}, \tag{2.17}$$

For the damage evolution, the matrix material is assumed to be plastically incompressible (von Mises type) and the elastic volumetric strains are negligible. The evolution equation for porosity from the continuity equation is given by

$$\dot{f} = (1-f)D^p_{kk}, \tag{2.18}$$

where D^p_{kk} is the volumetric part of the plastic rate of deformation tensor and can be integrated to calculate the current f. The strain hardening response of the material matrix, following the J_2 flow rule, is described by the yield stress σ_y as a function of the accumulated equivalent plastic strain $\overline{\varepsilon}^p$ [109]

$$\sigma_y(\varepsilon^p_M) = \sigma_0 \left(1 + \frac{\varepsilon^p_M}{\varepsilon_0}\right)^n, \varepsilon_0 = \frac{\sigma_0}{E}. \tag{2.19}$$

In this expression, σ_0 and ε_0 are the initial yield stress and strain, respectively, and n is the strain hardening exponent.

In the MVAR model, a critical void volume fraction is used as a fracture criteria such that the damage evolution accelerates as the damage parameter reaches to a critical value. This characterizes the rapidly growing void volume fraction in the void coalescence phase. In Eq 2.18, one can use a damage rate coefficient K_D, which is defined as

$$K_D = \begin{cases} 1 & D \leq D_c, \\ \frac{f_m - f_c}{f_f - f_c} & D_c < D \leq 1, \end{cases} \tag{2.20}$$

where D_c is the damage critical value, f_f is the volume fraction at failure ($f = f_f$), f_c is the critical value of void volume fraction at coalescence under uniaxial tension, and $f_m = {}^1/_{q_1}$, with q_1 as a constant parameter introduced by Tvergaard [112]. This function was introduced by Tvergaard and Needleman [113] in order to account for the loss of load-carrying capacity after void coalescence.

In order to implement the local integration scheme, two methods have been commonly used: Runge–Kutta and the fully implicit method. In both schemes, the integrated variables are the elastic strain tensor ε_e, the accumulated plastic strain $\bar{\varepsilon}^p$, and the void volume fraction (porosity) f. In this study, we have used the fully implicit method with Newton–Raphson (N-R) scheme, which is the optimal choice for solving the constitutive equation because of the quadratic rates of convergence. This integration algorithm is first-order accurate, unconditionally stable, and easy for using the consistent tangent operators in the general N-R procedure. For implementing the fully implicit method, the generalized midpoint rule was used because of its efficiency. The integration algorithm of the constitutive equations for MVAR model is listed in Box-I.

Box-I. Local incremental integration algorithm for modified variational formulation model

1. The elastoplastic constitutive initial value problem

$$\dot{\varepsilon^e}(t) = \dot{\varepsilon}(t) - (1-f)\dot{\varepsilon^p}(t)\boldsymbol{N}, \tag{2.21}$$

$$\dot{f}(t) = (1-f)^2 tr(\boldsymbol{N})\ \dot{\varepsilon^p}(t). \tag{2.22}$$

2. The incremental form of constitutive equation

$$\varepsilon^e_{n+1} = \varepsilon^e_n + \Delta\varepsilon - (1-f)\Delta\varepsilon^p\boldsymbol{N}, \tag{2.23}$$

$$f_{n+1} = f_n + (1-f)^2 tr\boldsymbol{N}\ \Delta\varepsilon^p, \tag{2.24}$$

$$\Phi(\sigma_{n+1}, A_{n+1}) = 0; \quad \sigma_{n+1} = \bar{\rho}\left.\frac{\partial\psi}{\partial\varepsilon^e}\right|_{n+1}; \quad A_{n+1} = \bar{\rho}\left.\frac{\partial\psi}{\partial f}\right|_{n+1}. \tag{2.25}$$

3. The general viscoplastic constitutive equations

$$\varepsilon^e_{n+1} - \Delta\varepsilon + \Delta t g(\sigma_{n+1}, A_{n+1}) = 0, \tag{2.26}$$

$$f_{n+1} - f_n - \Delta t J(\sigma_{n+1}, A_{n+1}) = 0. \tag{2.27}$$

with consideration of

$$g\left(\sigma(t),A(t)\right)=\dot{\lambda}(\sigma(t),A(t))\ N(\sigma(t),A(t)), \tag{2.28}$$
$$J(\sigma(t),A(t))=\dot{\lambda}(\sigma(t),A(t))\ H(\sigma(t),A(t)). \tag{2.29}$$

where in our case we have

$$g(\sigma(t),A(t))=(1-f)\Delta\varepsilon^p\boldsymbol{N},\ J(\sigma(t),A(t))=(1-f)^2 tr(\boldsymbol{N})\Delta\varepsilon^p. \tag{2.30}$$

4. The linearized system of time-discrete equations

$$d\varepsilon^e+\Delta t\frac{\partial g}{\partial\sigma}\colon d\sigma+\Delta t\frac{\partial g}{\partial A}*dA \;=\; d\Delta\varepsilon \tag{2.31}$$
$$df-\Delta t\frac{\partial J}{\partial\sigma}*d\sigma+\Delta t\frac{\partial J}{\partial A}*dA \;=\; 0, \tag{2.32}$$

where * is the appropriate product and

$$g_{n+\theta}=g((1-\theta)\sigma_{n+1}+\theta\sigma_n,(1-\theta)A_n+\theta A_{n+1}), \tag{2.33}$$
$$J_{n+\theta}=g((1-\theta)\sigma_{n+1}+\theta\sigma_n,(1-\theta)H_n+\theta H_{n+1}). \tag{2.34}$$

5. The complete set of constitutive relations

$$\begin{pmatrix}\frac{\partial R^e}{\partial\Delta\varepsilon^e} & \frac{\partial R^e}{\partial\Delta\varepsilon^p} & \frac{\partial R^e}{\partial f}\\ \frac{\partial R^p}{\partial\Delta\varepsilon^e} & \frac{\partial R^p}{\partial\Delta\varepsilon^p} & \frac{\partial R^p}{\partial f}\\ \frac{\partial R^f}{\partial\Delta\varepsilon^e} & \frac{\partial R^f}{\partial\Delta\varepsilon^p} & \frac{\partial R^f}{\partial f}\end{pmatrix}\begin{pmatrix}\Delta\varepsilon^e+\Delta\varepsilon^p\\ \Delta f-\Delta t\dot{f}\\ \Phi(\sigma_{n+1},A_{n+1})\end{pmatrix}=\begin{pmatrix}\Delta\varepsilon\\ 0\\ 0\end{pmatrix}, \tag{2.35}$$

where

$$R^e \;=\; \Delta\varepsilon^e-\Delta\varepsilon+(1-f)\Delta\varepsilon^p\ \boldsymbol{N}, \tag{2.36}$$
$$R^p \;=\; \Delta\varepsilon^p-\Phi(\sigma,s)\Delta t \tag{2.37}$$
$$R^f \;=\; \Delta f-(1-f)^2\Delta\varepsilon^p\ tr(\boldsymbol{N}), \tag{2.38}$$

6. The Jacobian matrix components

$$\frac{\partial R^e}{\partial\Delta\varepsilon^e}=\mathbb{I}+(1-f)\Delta\varepsilon^p\frac{\partial\boldsymbol{N}}{\partial\sigma}\colon D^e\theta;\ \frac{\partial R^e}{\partial\Delta\varepsilon^p}=(1-f)\boldsymbol{N}; \tag{2.39}$$
$$\frac{\partial R^e}{\partial\Delta f}=-\Delta\varepsilon^p\boldsymbol{N}+(1-f)\Delta\varepsilon^p\frac{\partial\boldsymbol{N}}{\partial f};\quad \frac{\partial R^p}{\partial\Delta\varepsilon^p}=(1-f)\boldsymbol{N};\quad \frac{\partial R^p}{\partial\Delta\varepsilon^e}=\boldsymbol{N}\colon D^e\theta;$$
$$\frac{\partial R^p}{\partial\Delta\varepsilon^p}=-\frac{\partial\sigma_y}{\partial\varepsilon^p};\quad \frac{\partial R^p}{\partial\Delta f}=\frac{\partial\sigma_e}{\partial f};\quad \frac{\partial R^f}{\partial\Delta\varepsilon^e}=-(1-f)^2\Delta\varepsilon^p\theta\mathbb{I};$$
$$\frac{\partial R^f}{\partial\Delta\varepsilon^p}=-(1-f)^2\mathbb{I}\colon\boldsymbol{N};\quad \frac{\partial R^f}{\partial\Delta f}=1+\Delta\varepsilon^p\theta(1-f)\mathbb{I}\colon\left(2\boldsymbol{N}-(1-f)\frac{\partial\boldsymbol{N}}{\partial f}\right).$$

2.4 Model Validation and Application

2.4.1 Model Validation

Until now, a three-dimensional FCC unit cell model of the $(\gamma + \alpha_2)$-$TiAl/Al_2O_3$ commercial cermet has been presented based on a modified variational formulation of the Gurson model. In this section, some experiments and microscopy analysis are used as inputs into the model, and then the model is validated against quasi-static compression experiments. The mechanical properties of the matrix, reinforcements, and the damage parameter values are given in Table 2.1. The elastic modulus of the two phases in the material, E_M and E_P, are determined by using an ultra-nanoindentation tester from Anton Paar equipped with a diamond Berkovich indenter. A matrix of 30×30 indents are performed on an area of $290 \times 290\,\mu$m. The value of $E_P = 278\,$GPa obtained from nanoindentation tests is lower than those often reported for bulk scale high purity alumina, which ranges between 300 GPa and 410 GPa [114]. From the literature, a decrease in stiffness of nanocrystalline particles is a result of increased volume fraction of the grain boundary atoms [115, 116], and the effects of interactions across grain boundaries with increasing the number of grains or decreasing the grain size [117–119]. The values for ν_M, ν_P, σ_y^M, and f_0 are obtained from the literature. The baseline for the alumina volume fraction is 65%. The ratio of the size length of the unit cell to diameter of the reinforcements is 1.477, and the ratio of the average pore size to the average nanoparticle size is 0.03.

In these simulations, the uniaxial compression stress is applied in the x direction with displacement control type loading. In the absent of voids, the matrix is assumed to have an initial yield strain of $\varepsilon_0 = 0.001$ [99]. The commercial ABAQUS is used for performing the calculations and a ten-node quadratic tetrahedron element (C3D10 in the ABAQUS FEA notation) is employed for meshing the unit cell. The Dirichlet boundary condition is implemented for this simulation in order to compare with uniaxial compression experiments. Shown in Figure 2.5 is the engineering stress-

Table 2.1: Material properties and the related damage parameters for each component.

Parameters	Notation	Value	Reference
Young's modulus (Matrix)	E_M	$178 \pm 31\ GPa$	Nanoindentation test
Young's modulus (Particle)	E_P	$278 \pm 41\ GPa$	Nanoindentation test
Poisson's ratio (Matrix)	ν_M	0.23	[120]
Poisson's ratio (Particle)	ν_P	0.22	[CoorsTek Inc.]
Yield stress (Matrix)	σ_y^M	$0.45\ GPa$	[120]
Initial porosity (Matrix)	f_0	0.01	[99]

strain curve obtained numerically, and compared with experimental data previously shown in Figure 2.2. In the curve, we vary the strain hardening modulus in the matrix material between 1 GPa (b) to 2 GPa (a), because the strain hardening components are material parameters which are the most unknown in the model. From the figure, we observe that strain hardening components of $k = 1.5$ GPa and $n = 0.05$ (c) fit the data reasonably well, and are in acceptable ranges [121, 122]. We use these parameters in all subsequent modeling.

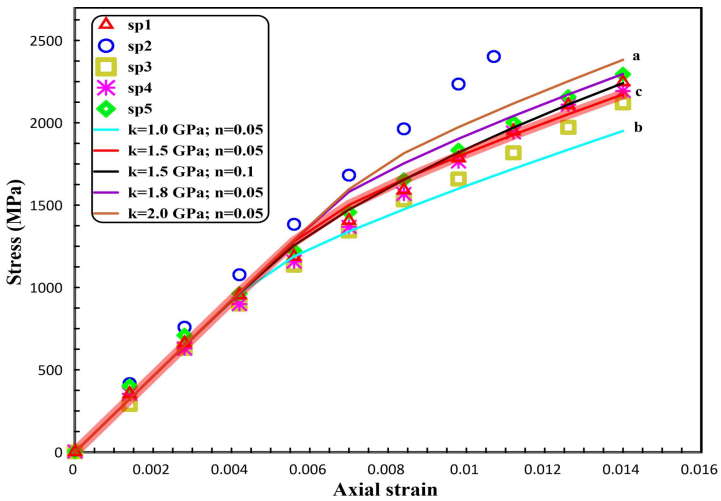

Figure 2.5: The engineering stress-strain behavior of ceramic-metal composite for various strain hardening parameters.

Next, we examine the ability of the model to capture the experimental results

in terms of stress-strain response. In order to study the experimental variability, 15 different realizations of the model were simulated based on varying matrix and particle stiffness. In these simulations, each alumina particle was assigned a different stiffness, and the matrix stiffness was left to vary, both assume a normal distribution about an average (from Table 2.1) with a 20% standard deviation. The summary of these simulations is shown in Figure 2.6 as the shaded regions, with realizations for the upper and lower bounds indicated in the legend. The realization that best fit the experimental data ($E_M = 178\,\text{GPa}$ and $E_P = 278\,\text{GPa}$) is indicated as a dashed-dot red line. By considering an elastic modulus for bulk scale alumina, $E_P = 380\,\text{GPa}$, the yield strength of the composite increases by 73 MPa (5% of the upper limit yield strength), and the peak stress decreases by 26.5 MPa (1% of the upper limit peak stress). Overall, the model reasonably captures the experimental stress-strain response considering how few parameters were fit to the experimental data.

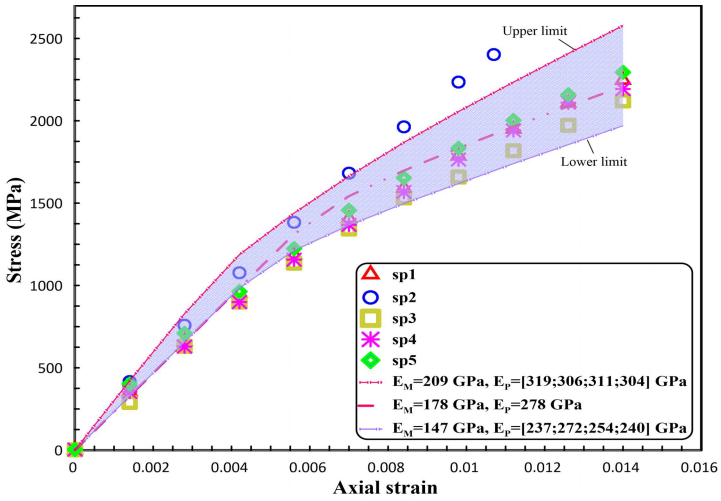

Figure 2.6: Variation of engineering stress versus engineering strain for both modeling results and experimental data.

Next, the ability of the model to predict deformation observed in the experiment is investigated by plotting outputs of the lateral (ε_{yy}) over the axial (ε_{xx}) strain in Figure 2.7. As before, matrix and alumina particles stiffness were varied to probe variability in the model and experimental outputs. From Figure 2.7, we observe

that the initial ratio of the lateral to axial strain computed numerically is 0.220 ± 0.002. This is slightly smaller than the experimental values (0.227 ± 0.001), but within reasonable agreement. The model seems to predict the onset of the transition to higher ratios at around 0.2% to 0.4% strain. The predicted peak value of the lateral to axial strain ratio is between 0.299 and 0.329, which is slightly greater than the experimental values, but still within reasonable magnitudes. The reasons for this are explained in the "Discussion" section. Altogether, these results indicate that the model framework with real-world inputs provide reasonable agreement with the experimentally-determined values of stress-strain responses and strain ratios.

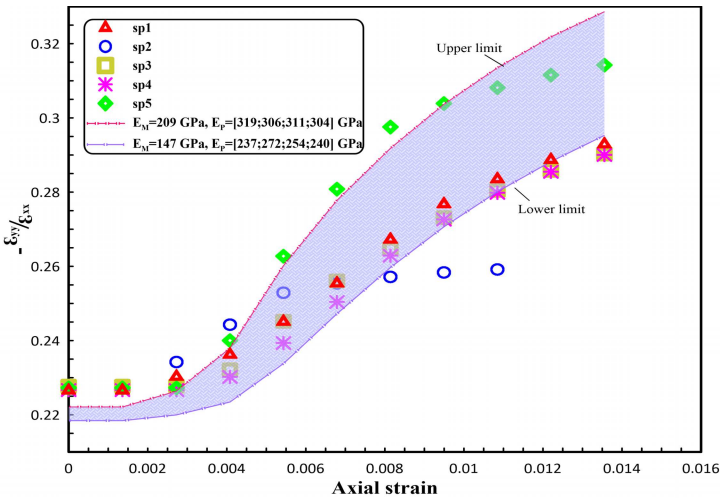

Figure 2.7: Variation of strain ratio during loading with axial strain.

2.4.2 The Effect of Alumina Volume Fraction, Porosity, and Unit Cell Size

After showing a good correlation between the proposed model and experimental trends, we now explore the effects of varying the concentrations of the alumina phase and porosity in order to study the implications for future materials design. In these simulations, we take the baseline parameters included in Table 2.1, and we change the volume fraction of the alumina and pores. This is meant to simulate realistic changes that can be made to the microstructure through processing. First, we begin by investigating the effect of varying the volume fraction of the alumina particles on

the engineering stress-strain behavior and ratio of lateral to axial strain (Figure 2.8). In this case, the particle sizes remained constant and different reinforcement volume fraction was obtained by changing the size of the unit cell. The baseline was considered for concentration of particles with an average of 65 ± 7%, which is believed to be an appropriate range to vary the alumina concentrations.

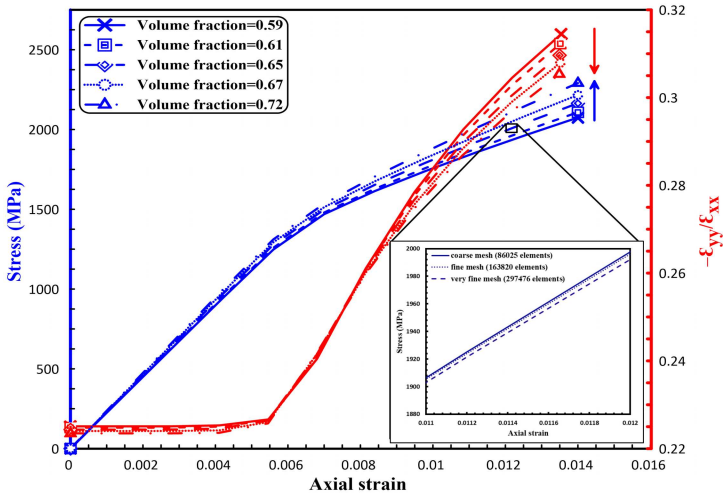

Figure 2.8: The effect of particle volume fraction on engineering stress-strain response and deformation profile of cermet during loading with consideration of various FE meshes (Arrows indicate increasing alumina volume fraction).

From Figure 2.8, the results show that increasing the alumina volume fraction from 65% to 72% (direction of marked arrow) can increase the peak stress by around 126 MPa (∼ 6% of the current strength). Conversely, the peak strength decreases by 90 MPa when the volume fraction is decreased from 65% to 59%, which represents 4% of the current strength. In addition, increasing the alumina particles volume fraction from 65% to 72% can lead to decreasing the maximum strain ratio by 0.004. Moreover, the onset of the transition to plastic region and higher strain ratios is predicted at around 0.4% to 0.6% strain. Lastly, the effect of different meshes on the results (very fine, fine, and coarse mesh) are plotted. The number of elements in each mesh is shown in the insert in Figure 2.8. The inset shows quite small differences in the material response for different number of elements, which shows mesh-insensitivity. Next, the effect of varying the void volume fraction and unit cell size ratio (S_{UC}), the

ratio of the size length of the unit cell to diameter of the alumina particles, on the engineering stress-strain behavior and ratio of lateral to axial strain is investigated in Figure 2.9. The results were obtained assuming equiaxed pore morphology (voids with equal semi-axis), and uniformly random distribution at a constant alumina particle volume fraction (65%). In addition, the baseline was considered for porosity values with an average of $1.5 \pm 0.7\%$, which is believed to be a reasonable amount one could vary the porosity in this material. As can be observed in Figure 2.9, the peak stress value decreases with increasing void volume fraction (direction of marked arrow) from lowest ($f = 0.001$) to highest ($f = 0.03$) porosity values by 105 MPa ($\sim 5\%$ of the current strength). Conversely, the strain ratio increases by 0.002 with increasing the void volume fraction from $f = 0.001$ to $f = 0.03$. With an increase in the unit cell size ratio, lower stress values were also observed. Similar behavior was predicted for mechanical properties of carbon nanotube polymer composites [123]. Considering the highest value of porosity ($f = 0.03$), the strength is decreased by 152 MPa, by varying the unit cell size ratio from $S_{UC} = 1.447$ to $S_{UC} = 1.526$, which shows a 7% reduction in the current strength. For lower porosity values ($f = 0.001$), the strength difference between values would be 168 MPa, 3% change across the range of unit cell size ratios. Conversely, the strain ratio increases with increasing unit cell size ratio for $f = 0.03$ by 3%. For all cases, mesh insensitivity is observed (not shown for brevity). Implications of these results are discussed in the following section.

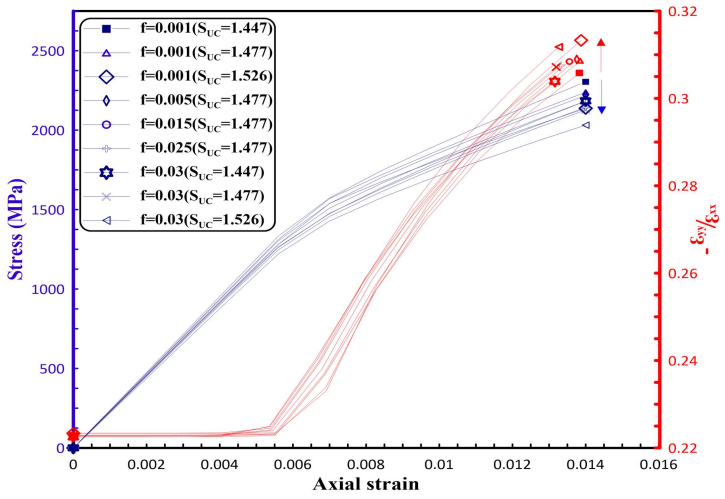

Figure 2.9: Predicted compressive engineering stress-strain curves and lateral to longitudinal ratio for the ceramic-metal composite with varying porosity and size of the unit cell (Arrows indicate increasing void volume fraction).

2.5 Discussions

In this study, a general modification of the Gurson-based models was proposed in order to investigate the micromechanical behavior of nano-grained $(\gamma + \alpha_2)$-TiAl/Al_2O_3 commercial cermets. Here, the previous works [124–126] on ductile nanoporous MMCs have been expanded to investigate the mechanical characteristics and the deformation profile of commercial cermets [127, 128] by incorporating a nonlinear homogenization variational structure for composites [129]. For the first time, a commercial cermet, rather than an idealised one [98], with high particles volume fraction ($\sim 65\%$) has been studied both numerically and experimentally. Material characterization was done to generate microstructural inputs into the model, including measurements of alumina size (average of $1 \pm 0.3\,\mu$m), alumina volume fraction ($65 \pm 1\%$), porosity size ($0.05\,\mu$m to $0.09\,\mu$m), and void volume fraction (1.2% to 3%). An FCC unit cell structure was considered as the microstructure of this novel oxide cermet to provide the highest possible reinforcement volume fraction. Once inputs were made, the model was validated against experiments through comparison of the compressive stress-strain response and the ratio of lateral to axial strain. Experimental data was obtained

from quasi-static uniaxial compression tests, coupled to novel DIC techniques. In the literature, limited measurements exist for the stress-strain response of cermets [107, 130, 131], likely due to the only recent advancements in the DIC technology. The stress-strain measurements on our cermet revealed that strength of the material was between 2200 MPa and 2600 MPa, with an average of 2400 $\pm$ 120 MPa, the stiffness was between 240 GPa and 310 GPa, with an average of 274 $\pm$ 26 GPa, and the failure strains were between 1.1% and 1.7%, with an average of 1.4 $\pm$ 0.2%. These values were much higher than the counterparts in MMCs [132] and idealised cermets [98], indicating the unique properties of this novel $(\gamma + \alpha_2)$-TiAl/Al_2O_3 cermet.

A comparison of the experimental and numerical results showed that the experimental values were in reasonable agreement with the numerical predictions of the stress-strain and ratio of strains responses (Figures 2.5 and 2.6). The numerical values for strength of the material was between 1970 MPa and 2580 MPa, and the stiffness was between 220 GPa and 260 GPa. Experimentally, minor differences may be attributed to residual stress in the material set as a consequence of different thermal coefficient between the constituent phases [133], reinforcements fracture during manufacturing process or mechanical loading [134], and particle shape and clustering that contributes to damage accumulation, cracks nucleation sites, and degradation of the mechanical properties of the cermet [135]. Numerically, the uniform and homogeneous distribution of alumina assumed in the model likely results in higher stress-strain values and ratio of strains, when compared to experimental results. There may also be some degree of porosity in the actual material that is not captured in the model, which can occur either by the fracture of the inclusions or by decohesion of the particle-matrix interfaces [136], that accumulates during loading and acts to reduce the strain ratio. Moreover, the model simulates mostly uniform void growth and coalescence throughout the body, whereas the failure in the experiment is likely due to the growth and coalescence of a few voids/cracks [133]. Furthermore, there was a gradual transition from low to high strain ratio, both numerically and experimentally,

which may attribute to different behavior of particle clustering as a single hard large particle or independent reinforcement [137] (Figure 2.7). Altogether, insights gained here for comparing the experiments and models can provide guidance for future work in directions motivated by discrepancies between the simulations and the test data.

Once the model was validated, the effect of changing the alumina volume fraction, porosity and unit cell size was explored. This exercise can provide valuable information for optimization the material mcirostructure for the mechanical response (e.g., strength, stiffness, and Poisson's ratio evolution). It was found that increasing the alumina particles volume fraction from 65% to 72% result in increasing the material strength by 6%. Physically, this increase in alumina volume fraction would lead to larger interfacial area between matrix and particles, which can result in more effective load-bearing capacity and increase the strength [133]. For porosity, it was observed that reducing the porosity from its current level of 1.5% to 0.1% results in an increase in strength of 2.5%. While possibly challenging to increase the alumina volume fraction and reduce the porosity to these levels, this information provides guidance to material manufactures with response to where efforts should be concentrated to improve the mechanical responses of this novel cermet material. For instance, reducing the presence of porosity sites such as fine oxide particles arising from manufacturing process can remove the barriers for dislocation motion in the matrix and increase the stiffness of the overall material [138].

2.6 Concluding Remarks

In the present study, a modified variational formulation of the Gurson model was employed for predicting the quasi-static behavior of a $(\gamma + \alpha_2)$-TiAl/Al_2O_3 cermet. This is the first time this material has been studied extensively, both numerically and experimentally. BSE-SEM and EDS analysis were used for determining the microstructure parameters as model inputs. Quasi-static uniaxial compression tests, coupled with DIC technique, were performed to investigate the mechanical response

and corresponding evolution of the deformation profile during loading. Following implementation, the experimental inputs were used to validate the unit cell model and reasonable agreement was found. The strain hardening components, which were the most unknown material parameters, were obtained by matching the modeling results with experimental trends. The strength of 2209 ± 239 MPa, stiffness of 240 ± 20 GPa, and strain hardening modulus of 1.5 ± 0.5 GPa were predicted from the presented model, which were in good agreement with experimental data. Once validated, the effects and implications of different parameters such as particle volume fraction, porosity, unit cell size ratio, and the variability of the inclusion stiffness were presented and discussed. Altogether, it is speculated that the proposed model together with appropriate measurements can be accounted for representing the unique mechanical responses of other commercial cermets as well.

2.7 Acknowledgments

This research was sponsored by the Natural Sciences and Engineering Research Council of Canada with support from PRE Labs Inc. and Lumiant Corporation. We thank Calvin Lo and Bernie Faulker for aiding in the completing the experiments.

Chapter 3

The Mechanical Response of a $\alpha_2(Ti_3Al) + \gamma(TiAl)$-Submicron Grained Al_2O_3 Cermet Under Dynamic Compression: Modeling and Experiment

Published in Acta Materialia

B. Amirian[a], H.Y. Li[a], James D. Hogan[a]

[a]*Department of Mechanical Engineering, University of Alberta, Edmonton AB T6G 2R3, Canada*

Abstract Novel experimental data, obtained using an advanced digital image correlation technique coupled to ultra-high-speed photography, have been used to develop and validate a microstructure-dependent constitutive model for a $\alpha_2(Ti_3Al) + \gamma(TiAl)$-submicron grained Al_2O_3 cermet. Utilizing experimental characterization for important simulation inputs (e.g., microstructural features size and constituent stiffness), the numerical model makes use of a variational form of the Gurson model, based on the nonlinear homogenization approach, to account for the experimentally observed deformation features in this composite (e.g., void deformation and growth and particle fracture). By considering the variability in

microstructural features (e.g., particle shape, size, and aspect ratio), as well as densely packed ceramic particles, the proposed model is evaluated by comparing the numerical responses to experimental results for quasi-static and dynamic stress-strain behavior of the material. The results show that the proposed approach is able to accurately predict the mechanical response and deformation of the microstructure. Once validated, the model is expanded for studying the predominant damage mechanisms in this material, as well as determining important mechanical response features such as transitional strain rates, flow stress hardening, extensive flow softening, and energy absorbing efficiency of the material as a function of void and particle volume fraction under high strain-rate loading. The totality of this work opens promising avenues for qualitative (damage micromechanisms) and quantitative (stress-strain curve) understanding of ceramic-metal composites under various loading conditions, and offer insights for designing and optimizing cermet microstructures.

Keywords: Microstructure-dependent constitutive model; Nonlinear homogenization approach; Dynamic uniaxial compression test; Digital image correlation; Materials design

---

3.1 Introduction

Due to its excellent corrosion resistance, high specific strength, sufficient creep resistance at elevated temperatures, and relatively low density, the two-phase titanium aluminide alloys are a potential candidate for aerospace and automotive structural applications [2–4, 139]. In comparison to their monolithic constituents, γ(TiAl) and α_2(Ti_3Al), these alloys can exhibit preferable mechanical performance as a result of containing multilayer phases with small inter-layer thickness [5, 6, 140, 81]. However, drawbacks such as poor fracture toughness and low ductility at room temperature [141, 142], and insufficient strength at high temperatures put a strict limit on their use in certain applications [7]. To remedy, introducing second phase particle reinforcements, termed intermetallic matrix composites (IMCs) can improve the toughness, creep resistance, and heat-resistance stability of the titantium aluminide material systems [8, 9, 143]. This class of ceramic-metal materials can be categorized as either metal matrix composites (MMCs) ($\geq$ 50 vol.% metal) [10, 78], or cermets ($\geq$ 50 vol.% ceramic) [11, 79]. With higher ceramic contents and associated greater strengths of cermets in comparison with MMCs, the former are expected to be far more effective as strike-face materials in aerospace and defense applications [12, 13]. In addition, ceramic-metal composites have higher fracture toughness and higher flexural strength in comparison to structural ceramics [80]. Among compatible and thermochemically stable strengthening phases for intermetallic TiAl such as SiC [14], TiB_2 [15], Ti_2AlC [16], Ti_5Si_3 [17], Al_2O_3 [18], and their combination [20, 19], this study is focused on a α_2(Ti_3Al) + γ(TiAl)-submicron grained alumina cermet due to its high temperature strength [21], excellent oxidation resistance [22], inclusive wear resistance [23], relatively low cost [24], and similarities between the coefficients of thermal expansion of the constituents [25, 33]. In addition, the submicrometer alumina grain size of the material under study here can lead to improved hardness, strength, and optical performance in comparison to the bulk alumina [26, 27, 144], which makes submicron

grained advanced cermets more favorable for a wide range of applications, from light-weight ballistic armor [28] to electronic packaging substrates and medical applications [29, 74].

Researchers have developed various methods such as reactive hot processing [30], mechanical alloying [31], and sintering process [32] for fabricating intermetallic TiAl-Al_2O_3 to compensate for the lower ductility and fracture toughness of ceramics, as well as poor strength and stiffness of metals, when combining these two materials [75, 76]. As a result of the $\alpha \rightarrow \gamma$ phase transformation and eutectoid reactions [81], the two-phase titanium aluminide contains a high volume fraction of lamellar grains. To date, there has been a number of published papers detailing the microstructure and mechanical properties of two-phase TiAl/Al_2O_3 (see e.g., [18, 25, 33, 86, 145]); however, limited studies have been devoted to the mechanical response of these unique materials under high strain rates. A limited number of research have attempted to explore the deformation mechanism of a γ(TiAl)-based alloys [146, 34, 147, 35], and dynamic fracture of nanograined transparent alumina [36, 37]. For example, Bertels et al. [146] confirmed the effects of superdislocations and mechanical twinning under dynamic compression loading in a γTiAl-based alloy. In addition, Belenky et al. [36] showed that the dynamic initiation toughness increased significantly when compared with the quasi-static regime. Studies of Ti-based cermets under dynamic loading include dynamic mechanical damage mechanisms in TiC-1080 steel cermets [148, 149], dynamic tensile failure of 6061-T_6/Al_2O_3 [150], and the effect of confinement on impact response of TiC/Ni cermet [151]. To date, no coupled numerical and experimental studies have been investigated the dynamic mechanical behaviors (e.g., stress-strain response), microstructure parameters (e.g., inclusion shape, size, and aspect ratio), and damage mechanisms (e.g., void deformation and growth) of an intermetallic TiAl-Al_2O_3 cermet, which are addressed in the present study.

The mechanical properties of cermets can be predicted numerically by implementing various types of modeling approaches [87–89]. For example, Pelletier et al. [90]

employed the limiting state of plastic collapse to relate the hardness of a nickel-based alloy cermet to its microstructure. Later, Engqvist et al. [91] proposed an empirical model for hardness of cemented carbides by studying the interactions between the binder and the carbide. Microstructural models, such as unit cell models [92] and dislocation-based models [93] have also generated interest in predicting the strengths of cermets. For example, Legarth [94] used a unit cell approach for investigating the non-monotonical effect of a material length scale parameter on the failure strain of MMCs. In addition, the combination of continuum plasticity theory with unit cell model to study the rigid particles in ductile matrix materials was carried out by Bao et al. [95]. There are other microstructure-independent approaches, such as self-consistent models, but their usefulness are restricted to composites with a low particle volume fraction [96]. However, in some commercial cermets, the particle volume fraction can reach up to 80% [97], such that the microstructure-independent approaches are no longer valid. As a result of existing significant variability for the commercial cermets with high particle volume fraction, modeling efforts to date have focused on idealised microstructure configurations, where a limited number of studies have been made to bridge these models with experimental inputs under high strain-rate loading [152, 98, 99]. For example, Ramesh and Ravichandran [153] investigated the evolution of damage and failure modes of boron carbide-aluminum cermet under dynamic loading conditions, by using the plate impact recovery technique. They found that most of the strain is accommodated by soft intermetallic phases during the initial compression pulses. Deobald and Kobayashi [154] experimentally characterized the dynamic fracture of Si/Al_2O_3 composites. Their study revealed an increased percentage of transgranular fracture in the dynamic fracture zone. Compton and Zok [79] described the operative damage and deformation mechanisms of TiC/Ni cermets under impact loading. Their results showed that cermets with higher toughness exhibits greater amounts of local particle cracking. The lack of understanding of the dynamic behavior and damage mechanisms of commercial cermets along with high

submicron particle volume fraction motivates this jointed numerical and experimental investigation.

In the present work, an experimental setup that enables digital image correlation measurements of the deformation field during uniaxial compression tests is outlined, and these experimental results are considered for numerical simulation comparisons. Scanning electron microscopy (SEM) is performed at room temperature on the fragments recovered from the uniaxial compression tests to investigate the fracture mechanisms of $\alpha_2(\mathrm{Ti_3Al}) + \gamma(\mathrm{TiAl})$-submicron grained alumina cermet under quasi-static and dynamic loading, and on the material microstructure before experiments to quantify the secondary phase alumina size and shape, and porosity in the material. To incorporate the void deformation and growth in a constitutive framework of the porous host material, a modified variational formulation of the Gurson model (MVAR) is proposed for a microstructure-based three-dimensional face centered cubic (FCC) unit cell model with a monodisperse distribution of voids along with a polynomial cohesive zone models for decohesion of particle-matrix interface. The compression behaviors of the cermet, such as flow and compression strengths, as well as possible damage mechanisms under low and high strain rates are discussed and compared with experimental results. The influence of material microstructural variabilities (e.g., particle shapes, size, and aspect ratio), as well as particles with variability in stiffness and volume fraction are included for better simulation of true specimens under uniaxial compressive loading. The proposed model is shown to provide a good correspondence to the experimental data, and can serve as a fundamental approach for further material design and optimization such as increasing the confidence limits of these materials.

3.2 Material and Experiments

The material investigated in this study is an $\alpha_2(\mathrm{Ti_3Al}) + \gamma(\mathrm{TiAl})$-submicron grained alumina cermet. The material is supplied by Lumiant Corporation, British Columbia,

and fabricated using solid flame combustion self-propagation high-temperature sintering (SHS) process. The initial powders are aluminum (Al) and titanium dioxide (TiO_2) phases to form the chemical reaction required for obtaining the final composite. The reaction is done in the presence of metallic binder phase additives (Fe, Co, Cr, Ni, Mo, and Ni−Mo) to facilitate the densification process of the cermet [155].

3.2.1 Material Characterization

Backscattered electron (BSE)-SEM are taken on a Zeiss Sigma field emission scanning electron microscope with the acceleration voltage (EHT) set at 20 kV and a working distance of approximately 3.8 mm (Figure 3.1). The lighter regions correspond to the two-phase TiAl phase because of the higher atomic number, while the darker regions are the alumina phase. By using image processing with thresholding in grayscale, the porosity level is determined as 1.2% to 3% at 2000 to 6000 times magnification, which tends to cluster around the boundary or within the alumina particle phase. The average pore size is $0.07 \pm 0.02\,\mu$m, as measured by the major axis. The individual alumina particles appear spherical in shape and in clusters in the material with size between $0.5\,\mu$m to $1.5\,\mu$m with an average of $1 \pm 0.3\,\mu$m, and cluster sizes of $3\,\mu$m to $9\,\mu$m. The area fraction of the alumina phase is estimated as $65 \pm 1\%$. The area fraction of 65% is assumed to be equal to the particle volume fraction as an input for the simulation in the absence of volumetric data. These results from the micrographs are averaged from nine different locations randomly taken across three samples. In addition, the elastic modulus of the matrix ($E_M = 178 \pm 31$ GPa) and alumina particles ($E_P = 278 \pm 41$ GPa) are determined by nanoindentation using an ultra-nanoindentation tester equipped with a diamond Berkovic indenter performed on an area of $290 \times 290\,\mu$m with 900 indents in total. All the mechanical properties for the matrix and the particle are listed and discussed in Table 3.1 in the "Results" section.

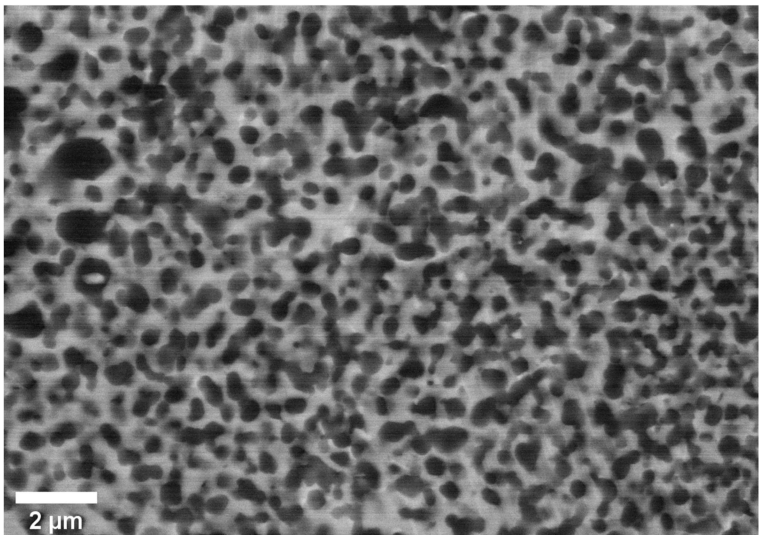

Figure 3.1: The experimental characterization of two-phase titanium aluminide-submicron grained alumina cermet using BSE-SEM. The black regions correspond to the alumina phase and white regions correspond to the two-phase TiAl phase.

3.2.2 Material Testing

3.2.2.1 Uniaxial Compression Testing

Cermet tiles are cut into specimens with size of 2.3 mm (length) $\times$ 2.7 mm (width) $\times$ 3.5 mm (height) for mechanical testing. The quasi-static uniaxial compression test is detailed in Amirian et al. [72] and is briefly recounted here for completeness. The test is conducted on a standard MTS series 810 servo-hydraulic machine, and is performed under displacement control with a nominal strain rate of $1 \times 10^{-4}\,\mathrm{s}^{-1}$. A 100 kN load cell with background noise corresponding to approximately ± 1 N is used to record the force history during loading process. An AOS PROMON U750 high speed camera with a full resolution of 1280 $\times$ 1024 pixels is used to provide visualization on macroscopic deformation features on the specimen surface. This is coupled with the digital image correlation strain measurements using the VIC2D 6 software [102]. For these measurements, the highest quality of the brightness and contrast on the material surface is obtained by using a combination of high intensity LED with optical light guide and metallic paint. The system is adjusted so that images with good sharpness and overexposure are obtained, where an optimal subset

size in the VIC2D software is achieved.

The dynamic uniaxial compression tests are conducted on a modified version of a split-Hopkinson pressure bar (SHPB), where similar setups have been well documented in the literature [156–158], and the technique has been widely used on ceramics and cermets testing [156, 159]. In the current study, the SHPB equipment comprised a striker bar, an incident bar, and a transmitted bar (made from maraging steel C-350) with the length of 1016 mm and 914 mm and a common diameter of 12.7 mm for incident and transmitted bars, respectively. The signals for the stress are measured by a strain gauge mounted on the transmitted bar. The specimens are placed between two impedance matched Ti-6Al-4V titanium alloy jacketed tungsten carbide (WC) platens, where the interfaces are lubricated with extreme pressure grease to reduce friction and allow the specimen to expand freely in the lateral dimension. A mild steel pulse shaper with a thickness of 0.0635 mm is placed in front of the incident bar (against the striker) to create a ramped signal profile. This specific pulse shaper provides a proper rise time ($8 - 10\,\mu$s) and ramp time for which the material can reach equilibrium under a single pass of a loading compressive wave, and the natural response of the material can be captured. In this case, the total time of the whole event is within $20\,\mu$s.

For data acquisition, an HBM Gen3i high-speed recorder from Durham instruments is used to capture the voltage signals with the sampling rate at 25 MHz, and only the transmitted signal is used to compute the stress-time profile. An ultra-high-speed Shimadzu HPV-X2 camera is used to capture the failure process of the specimen during SHPB testing at 2 million frames per second with an exposure time of 200 ns. The camera has a full resolution of 400×250 pixels, where 128 frames can be captured at the specific frame rate. In this setup [160], a light ring equipped with 32 high-power LED emitters with a focal point of approximately 330.2 mm (from REL. Inc.) is placed concentric to the camera lens for providing further lighting to the specimen, which can further enhance the brightness and contrast conditions for the post-DIC

analysis. Similar to quasi-static tests, DIC is used to obtain the global strain field in the dynamic tests. In these dynamic experiments, a K2 DistaMax lens from Infinity Photo-Optical Inc. is used to achieve a field of view where the full spatial resolution of the DIC analysis can be utilized. Altogether, these setups enable us to obtain stress-strain measurements and visualization of the surface deformation, and these are used to validate the model developed in this study.

3.3 Constitutive Modeling

In this section, a numerical model is presented for the mechanical response of the $\alpha_2(Ti_3Al) + \gamma(TiAl)$-submicron grained Al_2O_3 cermet under high strain-rate loading. First, a porous three-dimensional FCC unit cell model with four inclusions is considered for the geometry of the specimen, and the modified variational formulation of the Gurson model is presented for the constitutive response of the unit cell. The model has been implemented with a user-material (UMAT) fortran user-subroutine provided by ABAQUS/Standard. Next, the damage of matrix-particle interface is modeled by introducing a cohesive zone model, which was informed by deformation mechanisms observed in the experiments.

3.3.1 Geometry and Model Properties

Following different modeling strategies such as empirical [161] or microstructurally-motivated model [88, 162], which are valid for low particle volume fraction and are described through statistical information, a three-dimensional model comprising a FCC arrangement of periodic rigid particles is considered in this study. This model is computationally less expensive than the geometrically realistic unit cell models [163], and is able to reach higher particle volume fraction (up to 73%) and local strains in the matrix. Moreover, the face-centered cubic structure of TiAl single crystal makes this assumption a more reasonable for geometry model of the material.

The schematic view of the arrangement of the inclusions used in the finite ele-

ment models is marked in Figure 3.2. The unit cell is comprised of isotropic elastic particles with a Young's modulus of $E_P = 278\,\text{GPa}$, which was obtained from an ultra-nanoindentation tester from Anton Paar, and Poisson's ratio of $\nu_P = 0.22$. The rigid spherical particles is filled with a porous isotropic elastic-plastic matrix, with a Young's modulus and Poisson's ratio of $E_M = 178\,\text{GPa}$ and $\nu_M = 0.23$, respectively. All of the related mechanical properties along with the damage parameters are given later in Table 3.1, with corresponding sources of the information. For spherical voids with a uniform monodisperse distribution that are constructed by means of a random sequential adsorption algorithm [164] and are generated by a Mathematica code, the radius of each void is

$$R_v = L\left(\frac{3f}{4\pi N}\right)^{\frac{1}{3}}, \tag{3.1}$$

where L is the length of the unit cell, N is the number of pores in the unit cell, and f is the void volume fraction. The microstructure representation of cermet is also considered by ellipsoidal voids with unequal semi-axes. The ratios of L and pore size to the diameter of alumina phase are 1.477 and 0.03, respectively.

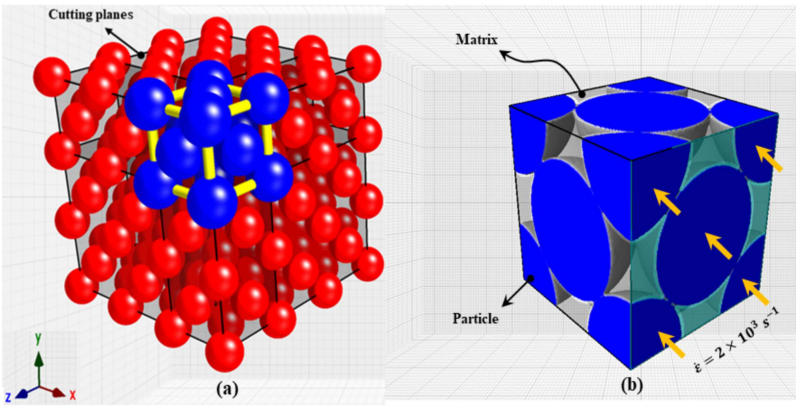

Figure 3.2: Sketches of the arrangement of the ceramic particles used in the finite element models: (a) Three-dimensional periodic arrangements of particles; (b) Three-dimensional FCC arrangement of inclusions with the unit cell subjected to high strain-rate loading.

3.3.2 The Theoretical Framework of $\alpha_2(\mathbf{Ti_3Al}) + \gamma(\mathbf{TiAl})$-$\mathbf{Al_2O_3}$ Cermet

In order to derive the constitutive equations, small strain formulation is used which is common for studying these materials [99, 165]. By separating the deformation behavior of the homogenized porous material into elastic and plastic parts, the rate of deformation tensor, D, at every material point of the $\alpha_2(\mathrm{Ti_3Al}) + \gamma(\mathrm{TiAl})$-submicron grained $\mathrm{Al_2O_3}$ cermet is decomposed as

$$D = D^{el} + D^{pl}, \tag{3.2}$$

where D^{el} and D^{pl} are the elastic and plastic parts, respectively. As a consequence of the compressibility of the material behavior due to presence of voids, the plastic strain-rate tensor is only hydrostatic.

3.3.2.1 Elastic Constitutive Equations

The elastic deformation tensor of the cermet material follows the hypoelastic form as

$$D^{el} = M^e : \mathring{\sigma}, \tag{3.3}$$

where M^e and $\mathring{\sigma}$ are the effective compliance tensor and Jaumann rate of the Cauchy stress, respectively. These are defined as [109]

$$M^e = M + \frac{f}{1-f} Q^{-1}; \quad \mathring{\sigma} = \dot{\sigma} - \omega \cdot \sigma + \sigma \cdot \omega, \tag{3.4}$$

where ω is the spin of voids relative to a fixed frame, i.e., $\dot{n}^i = \omega \cdot n^i, i = 1, 2, 3$, and M is the elastic compliance tensor of the matrix phase which is assumed to be isotropic such that

$$M_{ijkl} = \frac{1}{2\mu} K_{ijkl} + \frac{1}{3\kappa} \mathbb{J}_{ijkl}, \tag{3.5}$$

$$\mathbb{J}_{ijkl} = \frac{1}{3} \delta_{ij} \delta_{kl}, \tag{3.6}$$

$$K_{ijkl} = \mathbb{I}_{ijkl} - \mathbb{J}_{ijkl}, \tag{3.7}$$

$$\mathbb{I}_{ijkl} = \frac{\delta_{ik}\delta_{jl} + \delta_{il}\delta_{jk}}{2}, \tag{3.8}$$

$$Q_{ijkl} = E_{ijkl} : (\mathbb{I}_{ijkl} - \mathbb{S}_{ijkl}), \tag{3.9}$$

where μ and κ denote the elastic shear and bulk moduli of the matrix, δ and $\mathbb{I}$ are the symmetric second- and fourth-order identity tensors, f is the porosity, $\mathbb{S}$ is the fourth-order Eshelby tensor [166], and Q is the microstructural fourth-order tensor which is proportional to the shear modulus, Poisson's ratio, aspect ratio of the voids, and the orientation of the ellipsoidal voids [110]. It is worth noting that the components of the effective compliance tensor depend on the void volume fraction, shape, and orientation of the voids, and these evolve in time.

3.3.2.2 Plasticity Behavior

For obtaining the rate-dependent constitutive relations of nonlinear cermet material, the local behavior of the matrix phase is described by an isotropic, viscoplastic dissipation potential $W(\sigma)$ as [129]

$$W(\sigma) = (1-f)\frac{\dot{\varepsilon_0}\sigma_{flow}}{n+1}\left(\frac{\hat{\sigma_e}}{\sigma_{flow}(\varepsilon_M^p)}\right)^{n+1}, \tag{3.10}$$

where σ_{flow} is the flow stress of the matrix in tension which is the function of the accumulated plastic strain ε_M^p, $\dot{\varepsilon_0}$ is the reference strain rate, and n is the inverse of strain rate sensitivity parameter ($n = 1$ for linearly viscous material and $n \to \infty$ for rate-independent material response). The variational procedure, detailed in Castaneda [129], is used to derive the constitutive relations of the composite. The effective yield function can be written as [111]

$$\Phi(\sigma, s) = \frac{1}{1-f}\sigma\colon m^{MVAR}\colon \sigma - \sigma_y^2(\bar{\varepsilon}^p), \tag{3.11}$$

where s is the set of internal variables and is the function of local equivalent plastic strain, porosity, the aspect ratio of local ellipsoids, and the unit vectors in the directions of the principal axes of the voids. The overestimation of the original variational formulation and the Gurson model for the effective response of the porous material at high stress triaxialities and low porosity [167] is corrected by using the MVAR model.

Here, m is the normalized effective viscous compliance tensor defined as [109]

$$m_{ijkl}^{MVAR} = m_{ijkl}^{VAR} + (q^2-1)J_{ijpq}m_{pqrs}^{VAR}J_{rskl}, \tag{3.12}$$

$$m_{ijkl}^{VAR} = \frac{3}{2}K_{ijkl} + \frac{3}{1-f}\mu Q_{ijkl}^{-1}|_{\nu=0.5}, \tag{3.13}$$

$$q = \frac{1-f}{\sqrt{f}ln(\frac{1}{f})}, \tag{3.14}$$

$$Q_{ijkl}^{-1}(\mu,\nu) = \frac{1}{2\mu}\left(15\frac{1-\nu}{7-5\nu}K_{ijkl} + \frac{3}{2}\frac{1-\nu}{1+\nu}J_{ijkl}\right), \tag{3.15}$$

The scalar factor q preserves the convexity and smoothness of the yield surface for all the microstructural configurations. By substituting Eqs 3.12-3.15 into Eq 3.11, the yield surface is obtained as

$$\Phi(\sigma,f) = \left(1+\frac{2}{3}f\right)\sigma_e^2 + \frac{9}{4}\left(\frac{1-f}{lnf}\right)^2 p^2 - (1-f)^2\sigma_y^2 = 0, \tag{3.16}$$

where $\sigma_e = (\frac{3}{2}\sigma^d\colon\sigma^d)^{0.5}$ is the equivalent von Mises stress, $\sigma^d = \sigma - p\delta$ is the deviatoric part of the stress, $p = \frac{1}{3}\sigma\colon I$ is the hydrostatic Cauchy stress, and σ_y is the yield strength of the parent phase with zero porosity. The strain hardening response of the material matrix, following the J_2 flow rule, is described by the yield stress as a function of the accumulated equivalent plastic strain $\overline{\varepsilon}^p$ [109]

$$\sigma_y(\varepsilon_M^p) = \sigma_0\left(1+\frac{\varepsilon_M^p}{\varepsilon_0}\right)^N;\ \varepsilon_0 = \frac{\sigma_0}{E}. \tag{3.17}$$

In this expression, σ_0 and ε_0 are the initial yield stress and strain, respectively, and N is the strain hardening exponent. It is observed that in the special case of spherical voids and equaling f to zero, Eq 3.16 reduces to the classic Huber–Mises model. For the strain rate sensitivity of the matrix phase, it is assumed that only the plastic deformation of the matrix leads to changes in microstructure because the voids do not carry load and the elastic strains are smaller than the plastic counterpart [168]. By implementing the normality hypothesis of plasticity, consideration of the equal relation between the macroscopic plastic work and consistency condition, the plastic rate of deformation tensor is obtained as

$$\sigma\colon D^{pl} \equiv \dot{\lambda}\sigma\colon\mathbb{N} = (1-f)\sigma_y\dot{\bar{\varepsilon}}^p; \quad \dot{\bar{\varepsilon}}^p = \frac{\dot{\lambda}\sigma\colon\mathbb{N}}{(1-f)\sigma_y}, \tag{3.18}$$

where $\dot{\lambda} \geq 0$ is the plastic multiplier, which can be obtained by consistency condition, and $\mathbb{N}$ is the direction of the plastic strain increment.

3.3.2.3 Evolution of Damage

For the damage evolution, the porosity is viewed as the main damage parameter in the material. The evolution equation for porosity from the continuity equation is given by [169]

$$\dot{f} = (1 - f) D^p_{kk} + \frac{f_N}{s_N \sqrt{2\pi}} exp \left[\frac{-1}{2} \left(\frac{\dot{\bar{\varepsilon}}^p - \epsilon_N}{s_N} \right)^2 \right], \tag{3.19}$$

where the first and second term on the right hand side account for void growth and plastic strain controlled nucleation process, respectively. D^p_{kk} is the volumetric part of the plastic rate of deformation tensor, f_N is the particle volume fraction of nucleating voids, s_N is the standard deviation of the nucleation strain, and ϵ_N is the void nucleation strain. A critical void volume fraction is used as a fracture criteria such that the damage evolution accelerates as the damage parameter reaches to a critical value [170]. This characterizes the rapidly growing void volume fraction in the void coalescence phase. In Eq 3.19, one can use a damage rate coefficient K_f, which is defined as

$$K_f = \begin{cases} 1 & f \leq f_c, \\ \frac{f_m - f_c}{f_f - f_c} & f_c < f \leq 1, \end{cases} \tag{3.20}$$

where f_f is the void volume fraction at failure ($f = f_f$) [171], f_c is the critical value of void volume fraction at coalescence under uniaxial tension, and $f_m = {}^1/_{q_1}$ with q_1 as a constant parameter introduced by Tvergaard [112]. This function was introduced in order to account for the loss of load-carrying capacity after void coalescence.

For implementing the local integration scheme, the integrated variables are the elastic strain tensor ε_e, the accumulated plastic strain $\bar{\varepsilon}^p$, and the void volume fraction (porosity). In this study, the fully implicit method with a Newton–Raphson (N-R) scheme are used for the local integration scheme, which is detailed in Amirian et al. [72]

3.3.2.4 Interface Decohesion Model

Interfaces have effects on the material design of ceramic-metal composites because of their highest responsibility for stiffness, strength, fracture behavior, and stress-bearing capacity [172, 173]. As a result of existing ceramic particles in the microstructure, debonding along the reinforcement/matrix interface is one of the main fracture micromechanisms, which is highly localized in front of the crack tip [174].

There are different models for characterizing interfaces, such as a narrow region of continuum with graded properties and cohesive zones with specific traction-separation laws [175, 176]. The facilitation of numerical implementations are the major reasons for using a continuum mechanics framework rather than ad hoc methods [177], and these frameworks are commonly called *cohesive zone laws*. In this model, the traction is taken to be a function of the displacement jump across the interface, where in order to simulate the interfacial behavior of cermet, a polynomial cohesive zone model is used [178]. The normal traction (T_n) separation (δ_n) relation with the assumption of $\delta_t = 0$ is demonstrated in Figure 3.3.

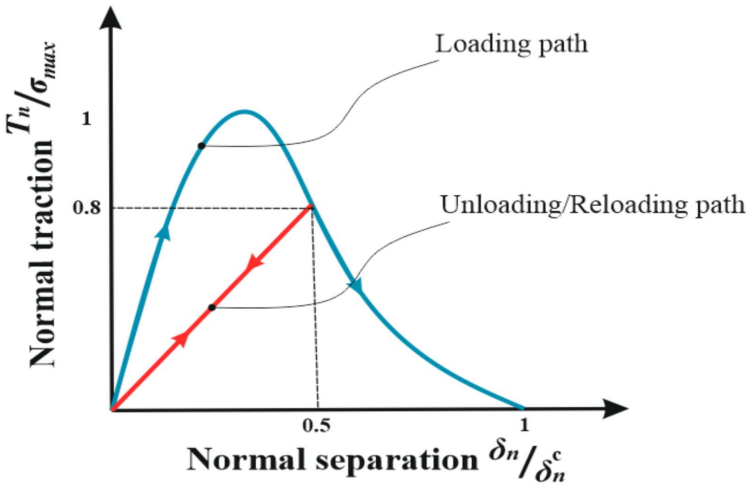

Figure 3.3: A traction-separation law for the polynomial cohesive zone model applied at the particle-matrix interface.

By increasing interfacial separation, the traction increases to the maximum value, which is defined as the interfacial bonding strength. After this maximum value, the

traction decreases to zero where complete failure occurs. For the unloading/reloading path, the interface behavior can be evaluated by the sign of λ and $\dot{\lambda}$ which is followed the same linear relationship. For the interface under compression, the normal and tangential traction for loading and unloading path are defined as

$$T_n = \mathbb{K}\frac{\delta_n}{\delta_n^c}, \quad \mathbb{K} > 10E_P, \tag{3.21}$$

$$T_t = \xi\frac{27}{4}\sigma_{max}\frac{\delta_t}{\delta_t^c}(1-\lambda)^2, \lambda = \lambda_{max} < 1 \text{ and } \dot{\lambda} \geq 0; \text{Loading Path}, \tag{3.22}$$

$$T_t = \xi\frac{27}{4}\sigma_{max}\frac{\delta_t}{\delta_t^c}(1-\lambda_{max})^2, \lambda < \lambda_{max} \text{ or } \dot{\lambda} < 0; \text{Unloading Path}, \tag{3.23}$$

where δ_n^c and δ_t^c are critical normal and tangential separation values, respectively, σ_{max} is the maximum normal stress of the interface, ξ is the ratio of maximum tangential strength to normal strength $\left(\frac{\tau_{max}}{\sigma_{max}}\right)$, E_P is the particle's stiffness, and λ is the non-dimensional damage parameter which is induced from interface decohesion

$$\lambda = \left\{\left(\frac{|\delta_n|}{\delta_n^c}\right) + \left(\frac{|\delta_t|}{\delta_t^c}\right)\right\}^{\frac{1}{\zeta}}, \tag{3.24}$$

where ζ defines the interaction of the normal and tangential separations. In the present study, the same cohesive behavior is assumed along the normal and tangential directions ($\xi = 1$ and $\delta_n^c = \delta_t^c$) and no strain rate effects are assumed to simplify the model in order to capture the basic physics. In order to describe the interfacial debonding behavior, the interface fracture energy G, which is equal to the area under curve shown in Figure 3.3, is used [178]

$$G = \frac{9}{16}\sigma_{max}\delta_n^c. \tag{3.25}$$

This indicates that in purely normal separation, σ_{max} is the maximum traction and the total separation occurs at $u_n = \delta_n$. It is worth stating that only the cracking of the $\alpha_2(\mathrm{Ti_3Al}) + \gamma(\mathrm{TiAl})$-submicron grained alumina cermet is considered as the principal contributions to the interface fracture energy, and the residual strain energy released by the cracking of the reaction products along with the energy dissipated by periodic cracking of the reaction products are ignored. Next, the model is validated against the mechanical responses and failure behaviors of the experimental results.

3.4 Results

The mechanical behavior of the $\alpha_2(Ti_3Al) + \gamma(TiAl)$-submicron grained alumina cermet under high strain rate uniaxial compression is explored using a three-dimensional FCC unit cell model in combination with a modified variational formulation of the Gurson model. The numerical results are validated against the experimental data, and then are used to provide insights into various aspects of the material response during dynamic loading. The mechanical properties of each unit cell constituents along with the damage parameter values are given in Table 3.1, and will serve as reference values in the remainder of this article. The baseline for the submicron grained alumina volume fraction is 65%, and the ratio of the average pore size to the average particle size is 0.02. The quasi-static and dynamic response of the unit cell are simulated using commercial finite element software ABAQUS by implementing UMAT. For meshing the unit cell, approximately 350,000 ten-node quadratic tetrahedron elements (C3D10 in the ABAQUS FEA notation) are employed. In these simulations, the inclusions are assumed to be perfectly bonded to an elastic-plastic matrix. In order to compare with the uniaxial quasi-static and dynamic compression tests, a fixed-displacement boundary condition is implemented to one end of the unit cell and the simulations are performed by imposing a controlled displacement (uniform constant-velocity boundary condition), with low ($10^{-4}\,s^{-1}$) and high ($2000\,s^{-1}$) strain rates in the axial direction, which are approximately the nominal loading rates in the experiments (shown schematically in Figure 3.2(b)) [179].

3.4.1 Quasi-Static and Dynamic Compression Behaviors

The simulated stress-strain relationships of the ceramic-metal composite compressed at low and high strain rates together with the experimental results are summarized in Figure 3.4. The numerical data range are obtained by changing the stiffness, shape, volume fraction, and aspect ratio of the inclusions in the unit cell structure in order

Table 3.1: Material properties and the related damage parameters for the unit cell constitutents (M for matrix and P for particles).

Parameters	Notation	Value	Reference
Young's modulus (M)	E_M	$178 \pm 31\ GPa$	Nanoindentation
Young's modulus (P)	E_P	$278 \pm 41\ GPa$	Nanoindentation
Density (M)	ρ_M	$4.1\ \left(\frac{g}{cm^3}\right)$	[120]
Poisson's ratio (M)	ν_M	0.23	[120]
Poisson's ratio (P)	ν_P	0.22	[CoorsTek Inc.]
Yield stress (M)	σ_y^M	$0.45\ GPa$	[120]
Initial yield stress (M)	σ_0	0.3 GPa	[109]
Strain hardening exponent (M)	N	0.05	[72]
Initial porosity (M)	f_0	0.01	[99]
Initial yield strain (M)	ε_0	0.001	[99]
Specific heat (M)	C_{p_M}	$559.77\ \left(\frac{J}{Kg\ K}\right)$	[180]
Surface energy (P)	γ_P	$0.97 \pm 0.04\ (Jm^{-2})$	[181]
Interface fracture energy	G	$4\ (Jm^{-2})$	[182]

to account for the variabilities of the material, and to compensate for the discrepancy between experimental and numerical results. For each of these parameters, random realizations of the properties are generated by assuming a normal distribution of the mean (values in Table 3.1) and a 20% uncertainty. The stress-strain data for all cases are presented as shaded regions (except for dynamic numerical loading) that represent lower and upper bounds on the stress and strain values. The different regions of the curve that correspond to the various particle shapes are noted in the caption, and this is done for ease of comparison and clarity. Figure 3.4(a) is discussed in the subsequent paragraph. First, the representative curves from the quasi-static and dynamic experiments are presented in Figure 3.4(b) in order to demonstrate the common softening and hardening behavior in the cermet, especially for the dynamic case. As observed, the quasi-static curves (blue) tend to follow a convex behavior (values

presented later when describing Figure 3.4(a)). For the dynamic case (red curves), the behavior is more complicated as it exhibits cycling hardening and softening behavior, which was observed in other types of cermets [149, 183, 184]. This is believed to be a consequence of a texturing phenomenon (e.g., plastic deformation) observed during dynamic loading [160]. In addition, the sensitivities of numerical stress-strain curves to inclusion shapes (prism, platelet, icosahedron, and ellipsoid) compared to experimental results are illustrated in Figure 3.4(c). It can be seen that the prism shape exhibits the greatest softening post peak, while the cylinder shows a softening then hardening behavior. Overall, and as will be discussed next with respect to Figure 3.4(a), the numerical results reasonably capture the experimental data. The raw data is provided as supplementary to this article.

Referring back to the Figure 3.4(a), for the experimental data under low strain rates (red shaded region), the failure strain which is the peak strain in this case is between 1.1% and 1.4% with an average of $1.3 \pm 0.2\%$. The quasi-static compressive strength, which is defined as the magnitude of the peak axial stress that is sustained by the specimen, is between 2121 MPa and 2402 MPa, with an average of 2262 ± 141 MPa. Strain hardening effects are observed which indicates ductility in the material when compared to, for example alumina, which behaves in a linear elastic manner until failure [106, 107]. The stress-strain curve also exhibits a yielding behavior which commences at a strength of $\sim$ 1173 MPa. For the quasi-static case, the Young's modulus of the material is between 240 GPa and 310 GPa, with an average of 274 ± 26 GPa. The tangent modulus (strain hardening rate) at 0.7% strain (the cross point of numerical and experimental data) varies in the range of 109 GPa and 197 GPa, with an average of 153 ± 44 GPa.

For the numerical data under quasi-static loading (gray shaded region in Figure 3.4(a)), 15 different realizations of the model are simulated across variable void and particle concentration, and mechanical properties. Results show that the high work hardening rate is maintained until about 1.4% strain. The quasi-static compressive

strength is between 1970 MPa and 2578 MPa, with an average of 2274 $\pm$ 304 MPa. The Young's modulus changes from 234 GPa and 282 GPa, with an average of 258 $\pm$ 24 GPa. The strain hardening rate at 0.7% strain is between 87 GPa and 130 GPa, with an average of 108.5 $\pm$ 21.5 GPa. For an upper limit in the elastic stiffness, the yield strength of the composite increases by 73 MPa (5% of the upper limit yield strength), and the peak stress decreases by 26.5 MPa (1% of the upper limit peak stress).

Next, the dynamic stress-strain behavior of the ceramic-metal composites are explored experimentally (brown shaded region in Figure 3.4(a)). The stress-strain response initially behaves as a typical brittle material with a linear stress-strain curve at which time the material rapidly damages and there is an appreciable drop in stress, and thus, dynamic compressive strength. The dynamic Young's modulus (taking the slope of the stress-strain curve at 0.1% strain) is between 240 GPa and 270 GPa, with an average of 255 $\pm$ 11 GPa. The high work hardening rate is maintained until about 0.6% strain, after which it begins to soften or reduce near the peak stress ranged from 2696 MPa to 3447 MPa, with an average of 3133 $\pm$ 237 MPa. Following this initial peak stress, there is then a decrease (softening) in the stress in the material until 1.1% to 1.4% strain. This initial decrease is then followed by an increase in stress until approximately 2% strain, after which the curve collapses and the material fails catastrophically.

Numerically for the high strain-rate loading (hatched blue in Figure 3.4(a)), more than 30 different realizations in terms of particle volume fraction (60%, 65%, and 70%), Young's modulus, and different void volume fraction (0.5%, 1.5%, and 3%) are simulated as a result of experimentally observed microstructure variabilities, as many of the alumina appears clustered in the microstructure, and so attempts are made for these considerations on the stress-strain response for these strain rates. Specifically, the numerical results for the dynamic case show that by increasing the axial strain, the stress linearly increases with slopes change from 277 GPa (region VI for platelet

inclusions with 3% void volume fraction) to 329 GPa (region I for ellipsoid particles with 0.5% void volume fraction), with an average of 303 $\pm$ 37 GPa (measured at 0.1% strain) until $\sim$0.9% strain. The stress-strain response then starts to yield until a dynamic compressive strength between 2757 MPa (at 1.1% strain in region VI) and 3484 MPa (at 1.6% strain in region III), with an average of 3074 $\pm$ 250 MPa . The $\alpha_2(Ti_3Al)+\gamma(TiAl)$-submicron grained alumina ceramic-metal composites tend to lose their load-bearing capacity at strains ranging from 1.1% to 1.6%, with an average of 1.3 $\pm$ 0.2%. The softening rate in this region decreases from 1.8 GPa to 1.7 GPa. As can be seen in the figure, most of the dynamic properties are much higher than the quasi-static compressive properties. For example, the failure strain of the composite at high strain rates is larger than that of quasi-static loading (increasing from 1.4% to 2.3%). For both numerical and experimental results under dynamic loading, the peak stress is followed by extensive flow softening, whose softening rate is less at lower strains and considerably higher at higher strains. This softening behavior may be related to the temperature increase subjected to adiabatic process in dynamic loading [185]. Numerically, the growth and coalescence of microvoids plays the role of softening parameter and thus enables modeling reduction in material load-bearing capacity before failure, which are detailed in the "Discussion" section.

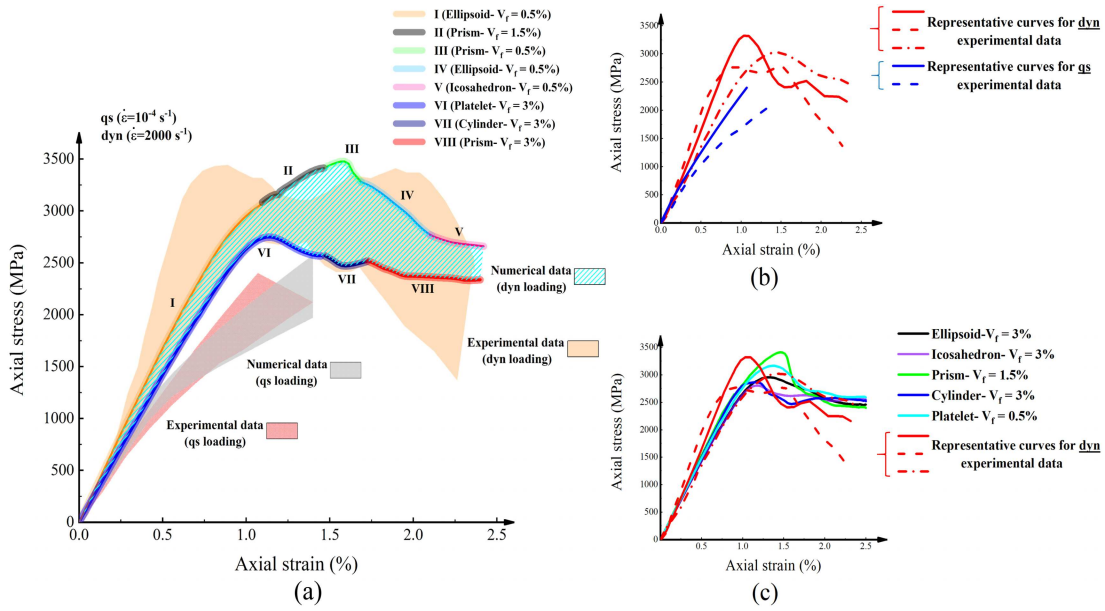

Figure 3.4: The mechanical response of ceramic-metal composite under uniaxial compression test: (a) The numerical and experimental axial stress vs. strain under quasi-static (qs; red- and gray-shaded region at $1 \times 10^{-4}\,\mathrm{s}^{-1}$ strain rate) and dynamic (dyn; brown shaded region and hatched blue at $\sim 2000\,\mathrm{s}^{-1}$ strain rate) loading for both numerical (Num) and experimental (Exp) cases; (b) Representative curves for qs and dyn experimental data; and (c) Sensitivities of numerical stress-strain curves to particle shapes compared to selected experimental data.

Shown in Figure 3.5 is the variation of the compressive strength as a function of the strain rate. Two groups of experimental data, including some results from a previous study [72], are plotted and compared with the numerical data. The experimentally observed quasi-static compressive strengths are between 2121 MPa and 2402 MPa with an average of 2262 $\pm$141 MPa, and the dynamic compressive strengths are between 2696 MPa and 3447 MPa with an average of 3133 $\pm$ 237 MPa. It is observed that a rate dependency of compressive strength occurs. The experimental compressive strength is about 1.3 times the quasi-static strength with seven order increase in strain rate. In comparison with the experimental results, the numerical compressive strength increases from 2250 MPa to 2480 MPa, with the strain rates from $1 \times 10^{-4}\,\mathrm{s}^{-1}$ to $800\,\mathrm{s}^{-1}$. Above the strain rate of $800\,\mathrm{s}^{-1}$, there occurs a transition into a regime of rapid strain rate strengthening where the compressive strength

increases from 2480 MPa to 5101 MPa across an increase in strain rates of $800\,\mathrm{s}^{-1}$ to $3500\,\mathrm{s}^{-1}$. The strain rate at $800\,\mathrm{s}^{-1}$ is considered as the transitional strain rate ($\dot{\varepsilon}_{tr}$) for this material, which has been shown to be dependent on the particle volume fraction, the hardening exponent, and the strain rate sensitivity of the matrix [186]. For $800\,\mathrm{s}^{-1} \leq \dot{\varepsilon} \leq 3500\,\mathrm{s}^{-1}$, the rate-dependency of the compressive strength σ_c, is represented by a power law fit with the equation $\sigma_c \propto \dot{\varepsilon}^{0.89}$, which the exponent is the slope of the blue dash-dot line in this semi-log plot. The increase in rate-dependency exponent will be discussed in the context of advanced ceramics in the "Discussion" section. According to the numerical simulations, for strain rates higher than $3500\,\mathrm{s}^{-1}$, the strain rate strengthening tends to increase at a lower rate, and this can be a consequence of thermal softening or damage accumulation. The numerical results are also compared with different experimental data from the literature for single phase alumina [187–190]. It shows that for high strain-rate regimes, the compressive strength of the $\alpha_2(\mathrm{Ti_3Al}) + \gamma(\mathrm{TiAl})$-submicron grained alumina cermet reasonably follows the behavior of alumina inclusions.

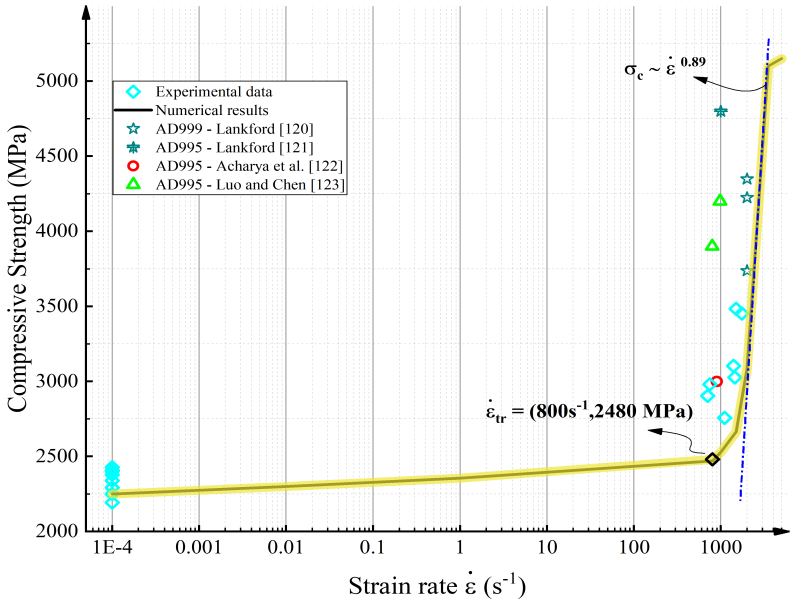

Figure 3.5: The change of compressive strength with strain rate, compared with experimental data. Note the logarithmic scale of the strain rate axis.

3.4.2 Rate- and Particle Volume Fraction-Dependent Flow Stress

Another consideration of the mechanical response of ceramic-metal composites is the variation of the flow stress for three different reinforcement volume fraction by changing the strain rates from $10^{-4}\,s^{-1}$ to $5000\,s^{-1}$ (Figure 3.6). Here, the flow stress at 1.25% strain replaces the 0.2% offset flow stress commonly used in other studies, as a consequence of mitigating stress equilibrium issues at small strains during SHPB tests [146]. The experimental flow stresses at quasi-static case change from 1962 MPa to 2149 MPa. For the dynamic case ($2000\,s^{-1}$), the experimentally measured flow stresses range from 2680 MPa to 3137 MPa. Numerically, it is observed that increasing the submicron grained alumina volume fraction increases the flow stress. For quasi-static case, increasing the particle volume fraction from 60% to 70% results in an increase in the flow stress by 174 MPa. While for the dynamic loading ($2000\,s^{-1}$), the flow stress increases from 2956 MPa to 3088 MPa. Over the rates presented here, the flow stress at 1.25% strain for 65% particle volume fraction increases from 1900 MPa to 3200 MPa by changing the strain rates from $10^{-4}\,s^{-1}$ to $5000\,s^{-1}$. The strain hardening rate for strain rates between $100\,s^{-1}$ to $2000\,s^{-1}$ is higher than its counterpart for lower strain value. While, for strain rates lower than $1\,s^{-1}$, the strain hardening rate is negligible for three different particle volume fraction and the curves are nearly parallel to each other. Notable for 70% alumina concentration composite is that it begins to soften for strain rates higher than $5000\,s^{-1}$, likely as a consequence of experiencing high concentration of damage accumulation (nucleation, growth, and coalescence of the voids) which is detailed later in the study.

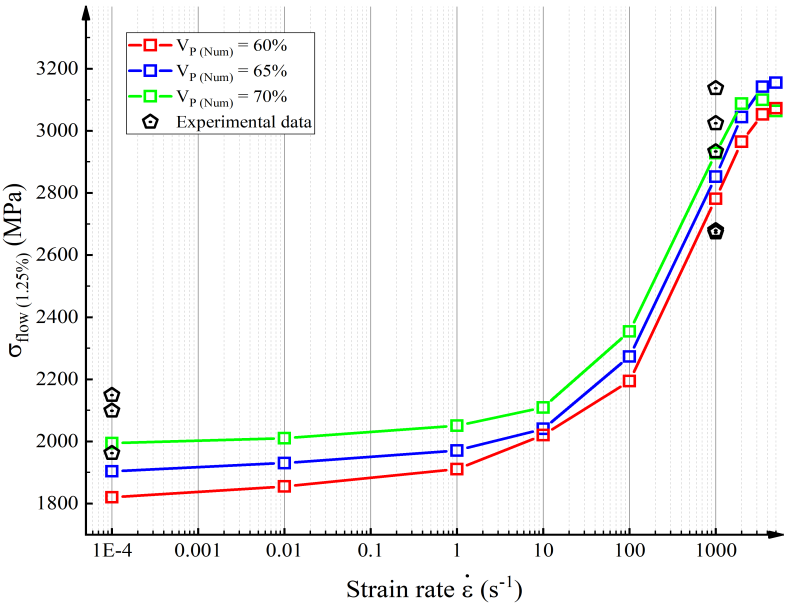

Figure 3.6: The variation of flow stress with strain rate at 1.25% strain along for three different particle volume fractions V_P, compared with the experimental data. Note the logarithmic scale of the strain rate axis.

3.4.3 Toughening Behavior Under Quasi-Static and Dynamic Loading

In order to use the ceramic-metal composites in high-rate applications such as aircraft and space vehicles, understanding the toughening and energy absorption during dynamic loading is crucial towards fully realizing their potential. Experimentally, the determination of dynamic fracture toughness of cermets is complicated due to the presence of stress waves and inertial effects [191]. The effect of increasing the toughness of monolithic alloys by adding ceramic particles is investigated in this subsection by probing the effect of void volume fraction and shape on toughness. To do this, values from the dynamic stress-strain curves are utilized, which are comprised of the compressive strength (peak stress), strain to compressive strength, strain in the stress-drop zone (for strains greater than 1%), total strain, and the stress-bearing capacity, defined as the slope of the stress-strain curve in the stress-drop zone (Figure 3.7). The areas underneath the curve before compressive strength and beneath the stress-drop zone are called the *initiation* (K_{IC}^{I}) and *propagation* (K_{IC}^{P}) toughness,

respectively [192].

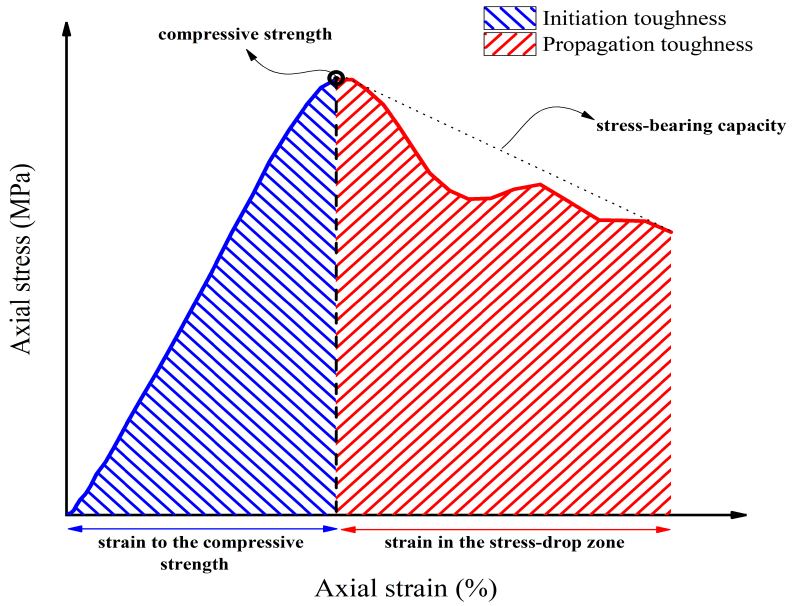

Figure 3.7: Schematic showing toughening behavior and its associated terms: compressive strength, strain to compressive strength, strain to stress-drop zone, stress-bearing capacity, initiation toughness, and propagation toughness.

The change of the initiation and propagation toughness with void volume fraction for different particle shapes (icosahedron, sphere, platelet, and prism) are shown in Figure 3.8. Higher and lower void volume fractions than are currently assessed in the material via SEM are probed to look at the sensitivity of void concentration on toughness. This is motivated by the fact that the void concentrations throughout a larger plate of the material are believed to be variable as a consequence of the SHS manufacturing process. For all of the shapes, increasing the void volume fraction decreases the initiation toughness and increases the propagation toughness. The icosahedron particle shape has the broadest range for initiation toughness (decreasing from 31 MPa $m^{\frac{1}{2}}$ to 18 MPa $m^{\frac{1}{2}}$ by increasing the void volume fraction from 0.5% to 3%). The lowest range is related to prismatic particles (decreasing from 34 MPa $m^{\frac{1}{2}}$ to 28 MPa $m^{\frac{1}{2}}$ over the strain range of 0% to 1%). For the prism inclusion shapes with 0.5% void volume fraction, the energy absorbed by the specimen in the region defined for initiation toughness is the highest (34 MPa $m^{\frac{1}{2}}$). The minimum initiation tough-

ness is for platelet inclusions with 3% void volume fraction (17.5 MPa $m^{\frac{1}{2}}$). In the case of the propagation toughness, the highest increase is related to icosahedron particles (increasing from 24 MPa $m^{\frac{1}{2}}$ to 31 MPa $m^{\frac{1}{2}}$ by increasing the void volume fraction from 0.5% to 3%). The prism inclusions have the lowest increase of propagation toughness (increasing from 22 MPa $m^{\frac{1}{2}}$ to 24 MPa $m^{\frac{1}{2}}$ by increasing the void volume fraction). The highest and lowest values for propagation toughness are related to the platelet particles with 3% void volume fraction (32 MPa $m^{\frac{1}{2}}$) and prism shapes with 0.5% void volume fraction (22 MPa $m^{\frac{1}{2}}$), respectively. The maximum total dynamic fracture toughness (defined as the summation of initiation and propagation toughness) is for prism inclusions with 0.5% void volume fraction (56 MPa $m^{\frac{1}{2}}$). The main reason would be the alignment of compression loading with prism (angular) inclusions axes, which can serve to strengthen the microstructure under dynamic loading. The minimum total toughness (49 MPa $m^{\frac{1}{2}}$) is for platelet (polygonal) particles with 3% void volume fraction. Previous studies showed that angular alumina particles rarely damage by the nucleation and growth of matrix voids, whereas polygonal alumina matrix voiding occurs about as frequently as particle fracture [188]. Together, this leads to increasing the energy absorbed by the microstructure. The higher fracture toughness of experimental results under dynamic loading (65 MPam$^{\frac{1}{2}}$) than numerical results can be related to existing metallic or glassy secondary phases [193, 194], which has been shown to decrease the brittleness and increase the fracture toughness of ceramic-metal materials. In addition, the transition of transgranular fracture of the ceramic particles to intergranular fracture of the composite through the matrix phase is another explanation for the enhanced toughness [191]. Overall, these results demonstrate the importance of particle shape and void volume fraction on energy-absorption capabilities of ceramic-metal materials in damage tolerant design.

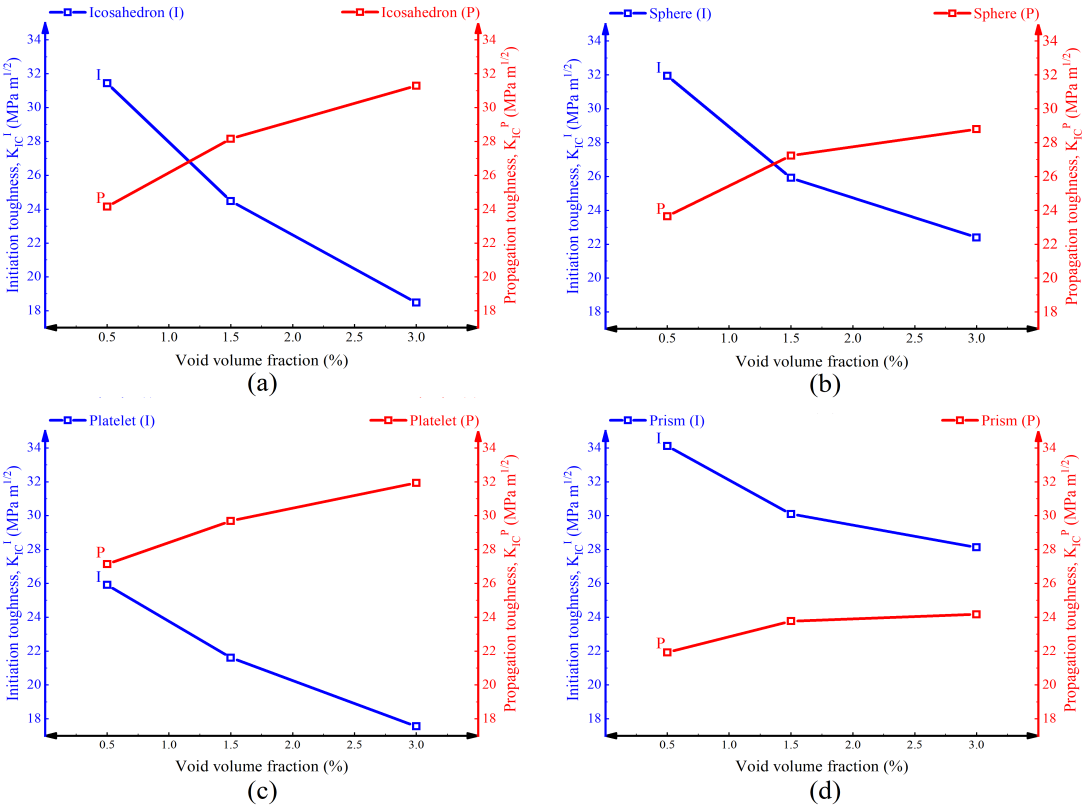

Figure 3.8: The change of initiation (K_{IC}^{I}) and propagation (K_{IC}^{P}) toughness with void volume fraction for: (a) icosahedron; (b) sphere; (c) platelet; and (d) prism inclusion shapes.

3.4.4 Deformation and Fracture Mechanisms of Dynamically Compressed Composites

In order to examine the fracture and deformation mechanisms of the dynamically compressed $\alpha_2(\mathrm{Ti_3Al}) + \gamma(\mathrm{TiAl})$-submicron grained alumina cermet, fracture surface of the recovered fragments are investigated using SEM, and these are compared with the contour of equivalent von Mises stress from the numerical simulation (Figure 3.9). Shown in Figure 3.9(a) is the FESEM micrograph taken on the fracture surface obtained from one of the recovered fragment in a dynamic experiment for postmortem analysis and characterization of microscopic failure. The overall failure is a combination of intergranular fracture through the matrix and transgranular fracture inside the submicron grained alumina phase. The crack is observed to start from the top

left corner (sufficiently high local stress concentration at the particle-particle contact points), and this appears to propagate along the alumina particles and through the titanium aluminide matrix. There is also evidence of particle pull-out followed by particle cracking along the crack path. Shown in Figure 3.9(b) is a magnified view on one of the fracture sites of alumina particles. It is observed that a transgranular fracture through the alumina particle occurs, where its neighbor particles remained intact. To compare these particle cracking mechanisms, a plot of the equivalent von Mises stress in the FCC unit cell is shown in Figure 3.9(c). For the numerical simulations, the icosahedron (20 face polyhedron with aspect ratio of 1, sphericity of $\approx$0.94, and volume fraction of 65%) shape is considered for the reinforcements to capture the real shape of particles observed in the composite at this scale. It is observed that the crack spans from one corner of polygonal alumina particle, which is limited by the matrix and other particles, and it passes to the upper particle (on planes parallel to the compressive loading axis) until it is arrested by the ductile matrix. It is observed that the stress state is spatially very heterogeneous, and there exist regions wherein the von Mises stress is positive (tensile stresses) within the matrix. These tensile stresses result in the dilation of the matrix. Generally, the fracture behaviors of the material captured by using the three-dimensional unit cell model under dynamic compression loading is in good agreement with the experimental observations. The stress analysis on cracked particle as a result of internal effects induced by rapid loading is studied in "Discussion" section.

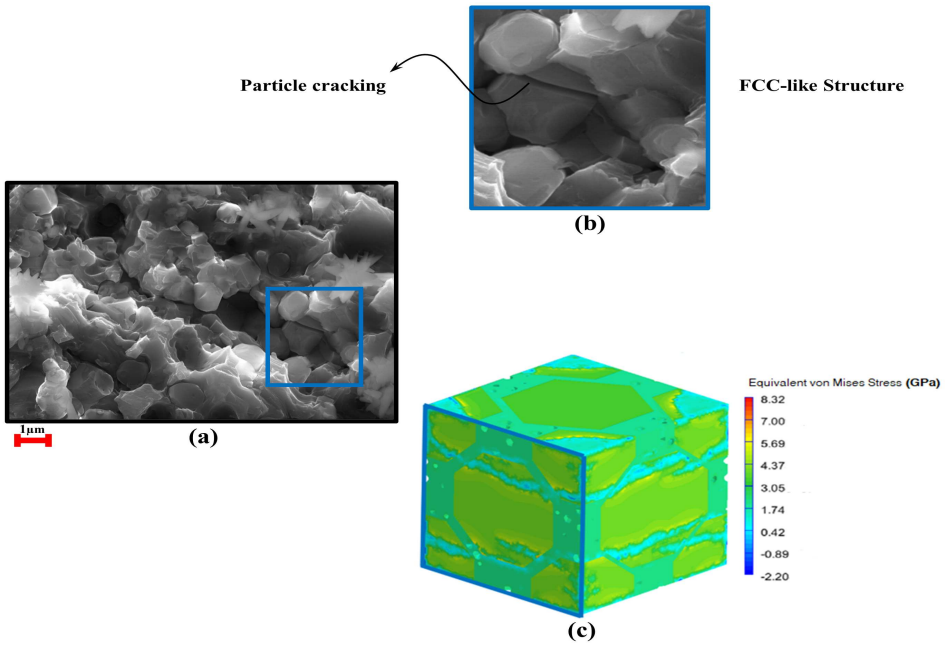

Figure 3.9: The fracture mechanism (particle cracking) of dynamically compressed composites: (a) SEM image of the fracture surface; (b) The magnified region with FCC-like structure comprised of particle cracking; and (c) Contours of equivalent von Mises stress demonstrating fracture pattern through the alumina particle.

As a result of having a porous matrix (void volume fraction of 1.5 ± 1%), the other fracture phenomenon in this type of cermet is the deformation of two-phase TiAl matrix via the growth and coalescence of voids, which is explored in Figure 3.10. Shown in Figure 3.10(a) is an SEM image demonstrating internal ductile void growth and coalescence in a dynamically compressed fragment. In the image, it is observed that the crack has a high tendency to initiate from the existing voids and propagate through the neighboring voids, leading to softening behavior (loss of load-bearing capacity) of the cermet. In the magnified image in Figure 3.10(b), a void can be seen on the crack path, where its orientation coincides with the likely stress concentration point leading to fracture initiation and growth. The experimental observations are compared with simulation results of void growth around particles (Figure 3.10(c)) for various strain evolution (Figure 3.10(d)). The failure criterion in the simulation is modeled by the modified variational formulation of the Gurson model, which incorporates the void deformation and growth after large deformation,

as the damage parameter reaches to a critical value. For the simulation results, the void with an ellipsoid geometry and aspect ratio of 1 with the ratio of void to particle size changing from 0.02 to 0.04 is used, and a mesh sensitivity analysis is performed to ensure no mesh size dependence of the results. In these simulations, the initial void volume fraction is considered to be 0.1%, and this is determined from SEM images on as-received (undeformed) materials. The contours of axial strain in the loading direction at different total engineering strains of 0.5%, 1%, 1.25%, 1.5%, 2%, and 2.25% are given in Figure 3.10(d). It is observed that strains begin to accumulate for selected voids for strains lower than the yield (0.5% strain) in the loading direction, and these evolve and connect adjacent voids, which are close to the particle by 1% strain. After coalescence (1.25% strain), additional voids begin to accumulate strain (1.5% strain), and the strain fields from these voids eventually coalesce with neighboring voids (2% strain). The complete coalescence (2.25% strain) coincides with an increase in global strain. It is worth noting that voids tend to grow toward the particle-matrix interface until it is arrested at the free edges. In addition, the positive heterogeneous total strain (tensile strain) shows dilation in the matrix. As can be seen, void growth behavior qualitatively match with that observed experimentally.

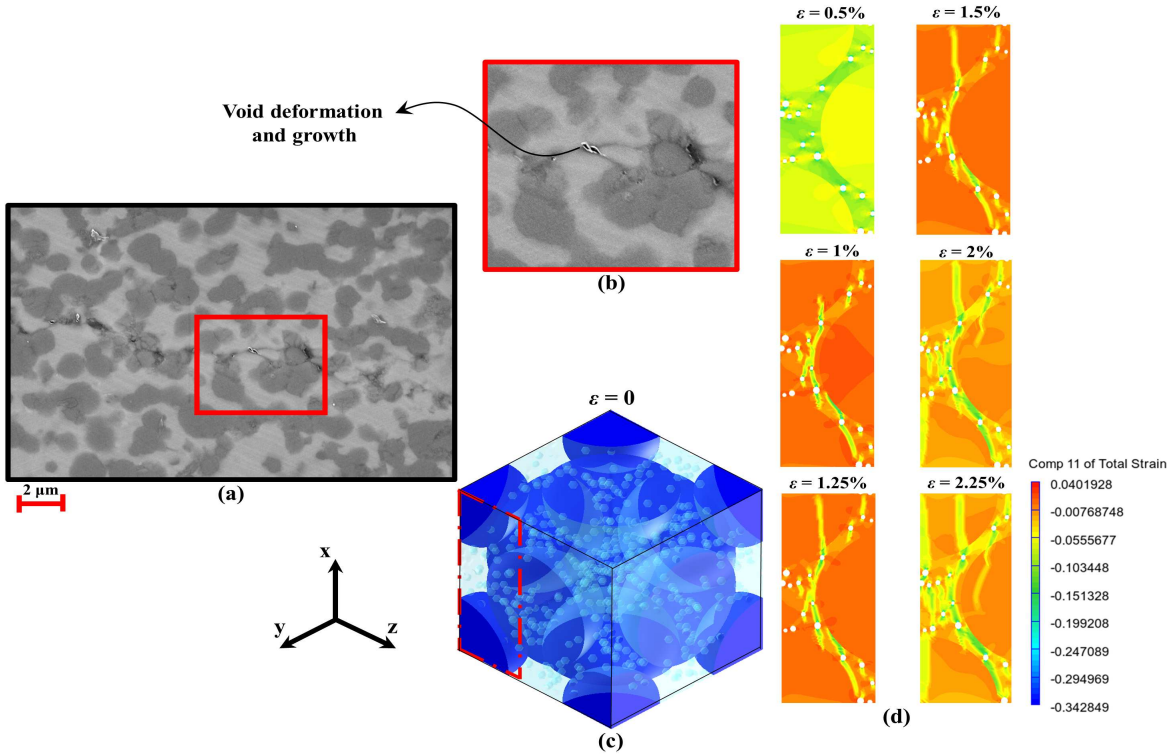

Figure 3.10: The fracture mechanism (void growth) of dynamically compressed $\alpha_2(Ti_3Al) + \gamma(TiAl)$-submicron grained alumina cermet: (a) SEM image of the polished fracture surface; (b) Close-up observation of the framed area in (a) including void deformation and growth; (c) Three-dimensional unit cell with porous matrix; and (d) Contours of compressive total strains at $\varepsilon = 0.5\%$, $\varepsilon = 1\%$, $\varepsilon = 1.25\%$, $\varepsilon = 1.5\%$, $\varepsilon = 2\%$, and $\varepsilon = 2.25\%$.

Finally, interfacial debonding damage is numerically investigated by using the polynomial cohesive zone model and compared with the experimental results. The SEM images along with contour mapping of equivalent plastic strain in the unit cell are illustrated in Figure 3.11. Figures 3.11(a) and 3.11(b) are micrographs taken on the fracture surfaces showing the interfacial debonding mechanisms. As can be seen, the debonding can happen in both the matrix-particle and particle-particle interfaces. The propensity of these two debonding mechanisms is hard to quantify, but it is postulated that the density of the matrix-particle debonding will be higher due to less amount of energy needed to break apart the titanium aluminide-alumina interface. It is observed that the top and bottom boundaries of the particle are separated from the matrix during loading (Figure 3.11(b)). The numerical comparisons are shown in

Figures 3.11(c) and 3.11(d), in which the former shows the arrangement of the particles and voids in the FCC unit cell, and the latter demonstrates equivalent plastic strain contours and associated particle debonding (indicated with arrows). For the numerical model, the interface fracture energy and the plane strain Young's modulus of $\alpha_2(Ti_3Al) + \gamma(TiAl) - Al_2O_3$ are assumed to be about $4\,Jm^{-2}$ and 180 GPa, respectively [182]. According to Figure 3.11(d), at small strain ($\varepsilon = 0.5\%$), a small debond is found along the lower interface of the middle particle. By increasing the strain ($\varepsilon = 0.7\%$), the upper interface of the particle starts to debonding. A further increase in applied strain ($\varepsilon = 0.9\%$) leads to additional particle decohesion, and the strain distribution becomes heterogeneous. At the final stage ($\varepsilon = 1.3\%$), debonding begins to propagate from left to right along the interface, and the debond arrest occurs at the location of around 45° from the compression axis. Similar behavior has been shown for rate-dependent interfacial debonding of MMCs by Zhang et al. [195]. Also, the maximum equivalent plastic strain seems to happen at two adjacent voids between the particle and the boundary edge in the loading direction. The comparisons between experimental observation and numerical result are found to be reasonable.

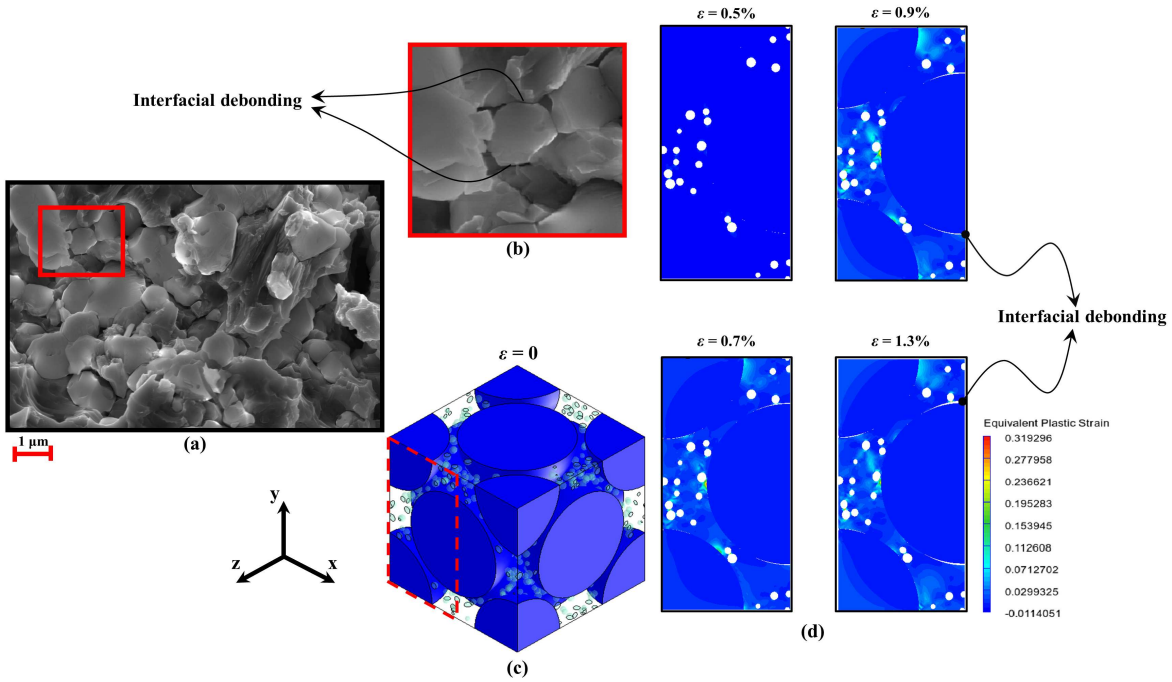

Figure 3.11: The fracture mechanism (interface debonding) of dynamically compressed $\alpha_2(Ti_3Al) + \gamma(TiAl)$-submicron grained alumina cermet: (a) SEM image of the fracture surface; (b) The magnified region with FCC-like structure comprised of interfacial debonding; and (c) Three-dimensional unit cell with porous matrix along with (d) contours of the equivalent plastic strain at $\varepsilon = 0.5\%$, $\varepsilon = 0.7\%$, $\varepsilon = 0.9\%$, and $\varepsilon = 1.3\%$.

3.5 Discussion

In this study, a modeling framework was developed to predict the mechanical behavior of a $\alpha_2(Ti_3Al) + \gamma(TiAl)$-submicron grained alumina cermet under low ($1 \times 10^{-4} s^{-1}$) and high (up to $5000\,s^{-1}$) strain-rate uniaxial compressive loading. A modified variational formulation of the Gurson model was employed to a three-dimensional FCC unit cell for an elastic-plastic porous matrix, and three main damage mechanisms were studied and then validated with experimental results obtained from quasi-static and dynamic uniaxial compression tests: 1. particle cracking, 2. void deformation and growth, and 3. interface decohesion. The previous works on quasi-static and dynamic behavior of MMCs and idealised cermets with low reinforcement volume fraction and pore-free matrix [152, 99, 196] have been expanded both numerically and experimen-

tally. Material characterization was carried out using SEM scans in order to generate microstructural inputs into the proposed model, and the experimental stress-strain responses were obtained from a novel DIC technique coupled to high-speed imaging and uniaxial compression experiments. Altogether, this study can give insights for designing and implementing of ceramic-metal composites in reliable structures. In the following sections, the results are summarized and implications are presented.

3.5.1 The Investigation of Material Response Under Quasi-Static and Dynamic Loading Conditions

The experimental and numerical stress-strain behavior of the $\alpha_2(Ti_3Al) + \gamma(TiAl)$-submicron grained alumina cermet under uniaxial compression in quasi-static and dynamic loading were first compared in Figure 3.4. The high strain rates obtained from the SHPB experiments were in the range of $1100\,s^{-1}$ to $2000\,s^{-1}$. By taking the slope of the experimental and numerical stress-strain curve at 0.1% strain, the average quasi-static and dynamic stiffnesses were $274 \pm 26\,GPa$ and $255 \pm 11\,GPa$ ($258 \pm 24\,GPa$ and $303 \pm 37\,GPa$), respectively. The increasing trend in stress-strain behavior was maintained until about 0.7% and 1.4% strain for high and low strain rates, respectively. In both the experimental and numerical cases, the initial behavior of the material was the same as typical brittle material with a linear stress-strain behavior. The difference between the stress in the material for the experimental and numerical results (from 0.1% to 0.9% strain) can be attributed to particle clustering in the specimen that was observed in SEM images (Figure 3.1), and was not accounted for explicitly in the unit cell model (schematic in Figure 3.2). This experimentally observed particle agglomeration leads to increasing the plastic strains accumulated in the matrix, higher strain hardening, and thus a higher flow stress. For the quasi-static case, there is also likely some degree of porosity in the actual material along with assuming uniform and homogeneous distribution of alumina submicron particles in the model, resulting in higher numerical stress-strain values as compared with the

experimental data [136]. Additionally, the generation, pinning down, and accumulating dislocations within the grain, and existing precipitates in the grain interior is another reason for higher strengths value of experimental than numerical results in that region [197].

After the linear region, the stress in the material starts to yield until the peak stress. The higher stress-strain values of experimental data under dynamic loading in comparison with numerical results in the stress-drop zone can be related to the limited number of reinforcements used in the unit cell model. The compressive strength and failure strain were around 1.3 times the values obtained from quasi-static tests with a seven order increase in strain rate from $1 \times 10^{-4}\,\mathrm{s}^{-1}$ to $2000\,\mathrm{s}^{-1}$. After the peak stress, the strain hardening effect of plastic deformation was quickly accompanied by the flow softening behavior of the material. One reason is increased damage formation and accumulation processes, which was experimentally and numerically initiated at 0.9% and 1.3% strain, respectively. The other potential reason is related to prolific banding and associate surface rumpling within the matrix, as observed experimentally by Longy and Cagnoux [198].

3.5.2 The Effect of Adiabatic Thermal Softening

Under high strain-rate loading, thermal softening due to the work exerted on the matrix can be one of the reasons for the flow softening behavior after the peak stress in stress-strain curve, which can be evaluated under an adiabatic assumption as [185]

$$\Delta T = \frac{0.95\eta}{\rho_M C_{pM}} \int_0^{\varepsilon} \sigma d\varepsilon, \tag{3.26}$$

where ρ_M is the density of the material, C_{pM} is the specific heat, and η is the thermal efficiency that is given by [199]

$$\eta = \begin{cases} 0 & \dot{\varepsilon} \leq 10^{-3} s^{-1}, \\ 0.316 \log \dot{\varepsilon} + 0.95 & 10^{-3} s^{-1} < \dot{\varepsilon} < 1.0 s^{-1}, \\ 0.95 & \dot{\varepsilon} \geq 1.0 s^{-1} \end{cases} \tag{3.27}$$

In this study, the potential temperature increase is explored as a consequence of existing flow softening in the numerical and experimental results. By substituting the related parameters from Table 3.1 into Eq 3.26, the average temperature increase under dynamic loading is around $25°K$, which is lower than the melting point of the matrix. An adiabatic temperature rise about $20°K$ for 60% TiB_2/Al composite and less than $5°K$ for 55% Al_2O_3/Al have been previously reported [200, 184]. From this analysis, these low global temperature increases are not believed to play roles in the experimentally and numerically flow softening behavior of the cermet. However, there still may be localize temperature rises in the narrow region of ceramic-metal interfaces, which were not captured in the simulations or observed in the SEM analysis. This highly localized temperature increase occurs as a result of lower thermal conductivity for alumina nanoparticles ($22\,\mathbb{W}m^{-1}K^{-1}$) than that of two-phase TiAl ($35\,\mathbb{W}m^{-1}K^{-1}$). In addition, the highly non-uniform local strain rate distribution in the matrix due to constraining effects from particles, along with rapid sliding of particles under high strain rates, may result in softening or even melting of the low melting point matrix [201, 202].

3.5.3 Strain Rate Effects on Compressive Strength

The compressive strength of the cermet for quasi-static and dynamic strain rates was studied both numerically and experimentally, and then compared with different alumina materials from the literature (Figure 3.5). Unlike experimental data which were carried out for only two strain rate regimes, the numerical method was able to investigate the material response under intermediate strain rates and rates slightly greater than those achievable in the SHPB tests. Experimentally, the quasi-static compressive strength were between 2121 MPa and 2402 MPa with an average of 2262 ± 141 MPa. While for the dynamic case, the dynamic compressive strength was between 2696 MPa and 3447 MPa with an average of 3133 ± 237 MPa. The experimental compression strength increases from 2402 MPa to 2696 MPa with a seven order increase in strain

rates in the minimum case. In the maximum case, increasing the strain rate lead to varying the compressive strength from 2121 MPa to 3447 MPa. In addition, the experimental failure strain increases from 1.1% to 2.3% with increasing strain rates from quasi-static to dynamic loading ranges. Numerically, increasing the strain rate from $1 \times 10^{-4}\,\mathrm{s}^{-1}$ to $800\,\mathrm{s}^{-1}$ leads to increasing the compressive strength of the material by 10% (from 2250 MPa to 2480 MPa). For high strain-rate regimes ranging from $800\,\mathrm{s}^{-1}$ to $3500\,\mathrm{s}^{-1}$, a 106% increase in compressive strength was observed over these rates (from 2480 MPa to 5101 MPa). For this $\alpha_2(\mathrm{Ti_3Al}) + \gamma(\mathrm{TiAl})$-submicron grained alumina cermet, the critical strain rates was about $\dot{\varepsilon} \simeq 800\,\mathrm{s}^{-1}$, above which a rapid transition occurred into a high strain-rate strengthening regime. Differences in the rate effects between the experiments and numerical model may be attributed to additional porosity [203] that likely exists in the material due to the particle clustering that is not captured in the model. For strain rates lower than the transitional value, the matrix material dictates the strain rate sensitivity (0.02 for two-phase titanium aluminide [120]) of the compressive strength, which is controlled by the thermally-activated growth of microcracks. For higher strain rates value, the constraining effect of the particles can result in increasing the local strain rate near the particulate-matrix interface, and pushes the composite into the high strain rate regime [186]. For $\alpha_2(\mathrm{Ti_3Al}) + \gamma(\mathrm{TiAl})$-submicron grained alumina cermet under dynamic loading, the strain rate exponent was found to be 0.89 in excess of the cube-root theoretical maximum for brittle materials. By using the model of Paliwal and Ramesh [204], the strain rate sensitivity exponent was found to be closer to $^2/_3$ for advanced ceramics, and was considered as a scaling model for the compressive strength of brittle materials [205]. For experimental studies on hot-pressed silicon nitride and pyroceramic matrix reinforced with SiC, the strain rate exponents were 0.87 and 0.77, respectively [206]. A reason for this high strain rate exponent has been related to the possibility of kink nucleation and propagation by cermet with high particle volume fraction which involves very high local strain rates [206]. Additionally, a strain rate exponent higher

than 0.33 implies that the consequence of increasing strain rate must be to involve crack initiation as well as crack propagation, which may manifest itself through rate-dependent localized plasticity [207]. This local plastic flow can be suppressed by high loading rates, thereby inhibiting dislocation-nucleated microfracture and increasing the strength rapidly [208].

3.5.4 The Study of Flow Stress of the $\alpha_2(\mathbf{Ti_3Al}) + \gamma(\mathbf{TiAl})$-Submicron Grained Alumina Cermet

In this study, the effect of different particle volume fractions (60%, 65%, and 70%) on the rate-dependent flow stress in the material taken at 1.25% strain was also investigated (Figure 3.6). The experimental quasi-static flow stress was between 1962 MPa and 2149 MPa. Under dynamic loading ($2000\,s^{-1}$), the experimentally measured flow stress ranged from 2680 MPa to 3137 MPa. The proposed numerical model was used to evaluate the flow stress for strain rates up to $5000\,s^{-1}$. The numerical flow stress varied from 1820 MPa to 1994 MPa for low strain-rates loading. While for high strain-rates loading ($1000\,s^{-1}$), the numerical flow stress ranged from 2781 MPa to 2928 MPa. For this part of the study, the numerical results were reasonably captured the experimental data. At higher strain rates for highest particle volume fraction, the stress softening rate was more significant than the other cases due to relatively shorter deformation times. By increasing the strain rates, it has been shown that the presence of high volume fraction of ceramic nanoparticles in ceramic-metal composites increases the flow stress as a consequence of stronger constraining effect of the particles [209]. In addition, Zhu et al. [201] investigated that high particle content composites form a network structure whereby the external load can be transferred directly via particles, results in higher flow stress. For cermets with particle volume fractions higher than 70%, where the inter-particle spacing is much smaller than average, the structure becomes unstable and collapse by particle sliding as a result of existing tangential stress between adjacent particles [210]. Moreover, the adiabatic heating generated from the

work hardening process promotes the occurrence of dynamic recrystallization, which leads to rapidly decrease of flow stress with the continuous increase of strain rate [211]. On the other hand, the small size alumina inclusions can increase the resistance to crack propagation by reducing the size of the nucleating flaws. This refined microstructure plays an important role as barriers to the enablement and transmission of dislocations [197], matrix hardening by geometrically necessary dislocations, and channeled plastic flow in the matrix between particles [212]. In other words, the Orowan strengthening, which results from the interaction between dislocations and the highly-dispersed reinforcement, becomes favorable in the materials [213].

To study the flow stress of the material in terms of strain rate sensitivity (SRS), the corresponding relation is often used [214]

$$SRS = \frac{\sigma_{fd} - \sigma_{fq}}{\sigma_{fq}} \frac{1}{ln(\frac{\dot{\varepsilon_d}}{\dot{\varepsilon_q}})}, \tag{3.28}$$

where σ_{fq} and σ_{fd} are the quasi-static ($1 \times 10^{-4}\,\mathrm{s}^{-1}$) and dynamic ($2000\,\mathrm{s}^{-1}$) flow stress at a constant plastic strain. By taking the flow stress at 1.25% strain, the results showed an increase of the SRS from 0.005 ($1\times10^{-4}\,\mathrm{s}^{-1}$) to 0.04 ($2000\,\mathrm{s}^{-1}$). The reported strain rate sensitivities for Al_2O_3/Al, B_4C/Al, and TiB_2/2024Al composites were in the range of 0.02 to 0.05 [215, 216]. A strain rate sensitivity ranging from 0.02 to 0.04 (at 1.25%) was obtained from experimental data in this study, which has been shown to be controlled by the sensitivity of the matrix and the interaction of particles and matrix [186]. The variation of experimental SRS can be related to a material microstructural variabilities related to the coupling of the strain rate sensitivity of the matrix and the constraining effect of the particles, which is stronger when the applied strain rate is higher or the particle volume fraction is larger. In addition, the stress distributed on the particles increases as the strain rate increases under dynamic loading, which enhances the SRS of the composite [217].

3.5.5 The Micromechanisms of Internal Damages

The theoretical models for analyzing particle cracking, matrix void-induced damage, and interface debonding have been developed for MMCs material under low and high applied strain rates [218–220]; however, the experimental data are lacking between the low and high strain rate regimes for ceramic-metal composites with high particle volume fractions. Limited studies involving the modeling of ceramic-metal composites have considered rate effects, different damage mechanisms, and real microstructural variables which are addressed in the present work. Among the different damage modes present in particle-reinforced ceramic-metal composites, particle fracture is commonly encountered for composites containing brittle reinforcements that are strongly bonded to a tough matrix (Figure 3.9). To further analyze particle fracture results in this study, this subsection investigates the fracture stress on the submicrometer alumina inclusions.

Particle cracking by propagation of an internal defect is given by the Griffith equation [221]:

$$\sigma_p = \left(\frac{2E_P \gamma_P}{\pi C} \right)^{0.5}, \tag{3.29}$$

where σ_p is the stress on the particle, γ_P is the particle fracture surface energy, E_P is the Young's modulus of particle, and C is the internal crack length. By substituting the related values from Table 3.1 into Eq 3.29, considering the crack length equal to $1\,\mu$m, it can be calculated that the stress on the particle is about 440 MPa under dynamic loading. This is deemed to be comparable with the scale provided in Figure 3.9(c). One of the main reasons for particle cracking in this cermet is likely related to the clustering of the alumina inclusions within the microstructure (see Figure 3.1), which has been shown to influence cracking propensity [222]. In addition, for higher inclusion volume fractions, there are more inter-particle contact points per particle which can increase the stress in a local region of contact point, and, thus, desire for cracking [223]. Moreover, local positive tensile stress generated by inhomogeneous

local deformation in the neighborhood of the voids and observed in the simulations likely contributes to local tensile microcracks that were found to nucleate at pre-existing defects (porosity of the matrix).

Another experimentally observed damage micromechanism in the $\alpha_2(Ti_3Al)$ + γ(TiAl)-submicron grained alumina cermet was the matrix failure due to void deformation and growth. For the failure of the porous matrix, the modified variational formulation of the Gurson model was implemented. The results (see Figure 3.10) showed that voids tend to grow towards the particle-matrix interface, and this is accompanied by a bulk volume increase (positive strain) because of the fracture porosity in the cavitation matrix. The interfacial debonding is another damage mechanism which was observed experimentally and modeled numerically by implementing polynomial cohesive zone models [178]. A three-dimensional cubic unit cell with interfacial layer between particulates and matrix was pictured in Figure 3.11. It was shown that there is a debond initiating along the upper half interface of one particle, propagating from left to right along the interface, and then arrest at the location of around 45° from the compression axis. The similar behavior for rate-dependent interfacial decohesion of MMCs has been demonstrated by Zhang et al. [195]. In the current study, the simulations showed that further increasing the applied strain results in further increases in the maximum equivalent strain and does not influence the microscopic distribution of deformation. According to the study of fracture in particulate reinforced MMCs [224], it is recognized that these damage mechanisms are responsible for softening and failure of the composites under dynamic loading.

3.6 Conclusions

This work is aimed at understanding the stress-strain behavior of a $\alpha_2(Ti_3Al)$ + γ(TiAl)-submicron grained alumina cermet, considering high particle volume fraction, under high strain-rates loading, and accounting for deformation mechanisms (i.e., particle cracking, void deformation and growth, and interfacial debonding). Ex-

periments along with a novel DIC technique was used to measure the global strain fields through the specimen, and the experimentally obtained stress-strain curves were used for the purpose of validating the numerical model. For numerical simulations, the FCC unit cell model was used for reaching to the high particle volume fraction up to 70% in this cermet. A modified variational formulation of the Gurson model was performed to investigate the effect of damage in the form of porous elastic-plastic matrix void nucleation. By considering different realizations accounting for the experimental variabilities in mechanical properties and microstructure, the model was able to reasonably predict the stiffness, compressive strength, and failure strains from the experiments. Exploring the material response outside of the experimentally-accessible conditions was allowed by the numerical validated model for the two experimental conditions, thus enabling a more comprehensive understanding on the rate-dependent response of the composite.

The experimentally observed damage micromechanisms such as particle cracking and interface decohesion (acting as strain-deteriorating parameters), and failure in the matrix by micro-void growth and coalescence (beneficial for the microstructure in terms of having higher fracture resistance) was also modeled numerically. It was shown that the predicted numerical model was in good agreement with experimental observations in terms of quantitative (e.g., stress-strain curve and compressive behavior) and qualitative (e.g., internal damage behavior) properties of the cermet.

3.7 Acknowledgments

This research was sponsored by the Natural Sciences and Engineering Research Council of Canada with support from PRE Labs Inc. and Lumiant Corporation. We thank Calvin Lo and Bernie Faulker for aiding in the completing the experiments.

Chapter 4

An Advanced Phase-Field Approach to Evolution and Interaction of Twins in Single Crystal Magnesium

Under Peer Review in Acta Materialia

B. Amirian[a], H. Jafarzadeh[b], B.E. Abali[c], A. Reali[b], J.D. Hogan[a]

[a]*Department of Mechanical Engineering, University of Alberta, Edmonton AB T6G 2R3, Canada*

[b]*Department of Civil Engineering and Architecture, University of Pavia, I-27100 Pavia, Italy*

[c]*Department of Materials Science and Engineering, Uppsala University, Uppsala 751 21, Sweden*

Abstract This study utilizes a novel time-resolved phase-field model to explore the time-dependent growth and interactions of twinning in magnesium single crystal at the nanoscale, a topic that is yet to be fully understood. The model is efficiently solved within a monolithic scheme for the first time in the literature using a highly parallelized open source finite element solver. We validate the model using published molecular dynamics simulations and non-time-resolved phase-field results for magnesium where twinning has been shown to be important in its dynamic

behavior. Once the numerical implementation is validated, we exercise the model in order to gain new insights into kinetic energy coefficients, growth of twin morphology, temporally-evolving spatial distribution of the shear stress field in the vicinity of the nanotwin, and multi-twin and twin-defect interactions. Overall, this research addresses gaps in our fundamental understanding of twin growth, while providing motivation for future discoveries in twin evolution and their effect on next-generation material performance.

4.1 Introduction

Developing next-generation materials with controlled twinning behaviors offers promising opportunities for improved mechanical properties [59, 60] and performance in engineering applications (e.g., gas turbine engines [61] and light-weight automotive structures [225]). Among materials that exhibit twinning [226–229], magnesium (Mg) [41, 230–232] is an example of a light-weight metal where twinning plays an important role in its mechanical response. In magnesium, single twinning occurs through contraction [233] and extension strains [234] along the c axis [235]. Recent studies have focused on observations of asymmetric twin growth due to heterogeneous grain deformation in the vicinity of the twin [236]. The results showed that interaction of twin boundaries with other defects (i.e., voids and self-interstitials) would increase the likelihood for void nucleation, cracking, and premature failure, leading to a degradation of material performance and reduction of material lifetime [237, 238]. Recent efforts have also been made to better understand the twin local stress and the role of neighboring grains to accommodate the transformation [239]. In engineering applications, there is a broad interest in incorporating magnesium in high strain-rate applications (e.g., aerospace [44]), where twin growth and evolution are important in mechanical performance [240]. However, knowledge gaps in understanding twin growth [241], thickening [242], and interactions [243] need to be addressed before the adoption of magnesium-based alloys into these applications; these will be studied in this research for a single crystal Mg material system.

To date, few experimental measurements exist on time-resolved twin evolution in magnesium [244]. Limited in-situ data is likely a result of the limitations in available diagnostics to capture growth and evolution behaviors at sufficient length and time scales [67]. To this end, atomistic simulations have been widely adopted to probe effects such as atomic shuffling mechanisms for propagation of twins in magnesium [245], disconnections and other defects associated with the twin interface [246], and reac-

tion of lattice dislocation with twin boundaries [247]. While new understandings have been gained to accurately model plastic deformation and fracture in magnesium [248, 249], atomistic simulations are limited in their ability to simulate twinning behaviors at relevant length and time scales needed for practical implementation in engineering applications. Challenges also exist in molecular dynamics in applying characterization algorithms (e.g., centrosymmetry parameter [250] and bond angle analysis [251]) to interpret post-deformation crystal structure defect types (e.g., twinning) [252]. In another approach, continuum mechanics modeling utilizing crystal plasticity theory is also an important tool for predicting the twinning and de-twinning response in materials with hexagonal close-packed crystal structures [253, 49, 254, 255]; however, crystal plasticity modeling cannot spatially capture the twinning process due to treating the twinning deformation as an unidirectional shear deformation mode [256]. More importantly, the conventional crystal plasticity model is unable to investigate the effect of twin microstructure on the mechanical behavior of magnesium at the nanometer scale [257]. Altogether, these limitations motivate the development of cutting-edge computational models in this study to unravel time-evolved twinning behavior in small-scale magnesium.

Building on these past works, this current article utilizes an advanced physics-based phase-field approach to study the nanoscale growth of existing twins in anisotropic single crystal magnesium. A fully nonlinear phase-field theory is employed allowing for anisotropic surface energy, nonlinear elasticity in the null temperature, and large elastic strains in nanoscale defect-free volumes and high pressures. To the author's knowledge, this is the first continuum-based model in the literature that accounts for time-dependencies of the interfacial motion of twinning, motivated by previous literature [258, 259]. The coupled equilibrium and phase-field equations are solved using a monolithic scheme to increase the computational accuracy. This approach enables efficient solutions and flexibility to extend the physics-based model to additional length scales. In the present study, we initially focus on validating our time-resolved

continuum-based model for magnesium using previous static phase-field models [50] and molecular dynamics simulations [260] (Figure 4.1). Twin propagation speeds are then explored (Figure 4.2) and compared with molecular dynamics results [260] and analytical solutions [261]. Insights in growth rates are important given the limited available data [244] and studying these behaviors is vital in high-rate applications of magnesium [262]. The results are then validated in terms of twin area fraction and the average global shear stress (Figure 4.3), and the role of twin-twin and twin-defect interactions is explored (Figure 4.4). Through these approaches, the research offers broad potential in materials design and motivates promising directions in experimental and computational materials science.

4.2 Results

4.2.1 Theory

In this study, we use standard continuum mechanics notation, where Latin indices refer to spatial coordinates. We adopt Einstein's summation convention over repeated indices. All tensors are expressed in Cartesian coordinates. We designate the contraction of tensors $\boldsymbol{A} = \{A_{ij}\}$ and $\boldsymbol{B} = \{B_{ij}\}$ over one and two indices as $\boldsymbol{A}\cdot\boldsymbol{B} = \{A_{ij}B_{jk}\}$ and $\boldsymbol{A} : \boldsymbol{B} = \{A_{ij}B_{ij}\}$; the dyadic product is represented by $\otimes$; δ_{ij} denotes the Kronecker delta; the transposition, inversion, determinant, trace, symmetric part, and skew-symmetric part of $\boldsymbol{A}$ are indicated by $\boldsymbol{A}^T$, $\boldsymbol{A}^{-1}$, $\det(\boldsymbol{A})$, $\mathrm{tr}(\boldsymbol{A})$, $\mathrm{sym}(\boldsymbol{A})$, and $\mathrm{skew}(\boldsymbol{A})$, respectively. The symbols ∇_0 and ∇ represent the gradient operators in the initial and current configurations, respectively. The superscripts E and IE stand for elastic (recoverable) and inelastic (irreversible) deformations, respectively. For the description of the twin, the order parameter η, is introduced where $\eta = 0$ denotes the parent crystal and $\eta = 1$ is the twin. The total deformation gradient $\boldsymbol{F}$, in a large-displacement formulation, is multiplicatively decomposed as

$$F_{ij} = F^{\mathrm{E}}_{ik} F^{\mathrm{IE}}_{kj}. \tag{4.1}$$

The kinematics for twinning in simple shear is given by [263]

$$F_{ij}^{\mathrm{IE}} = \delta_{ij} + \phi(\eta)\gamma_0 s_i m_j, \tag{4.2}$$

where $\phi(\eta) = \eta^2(3-2\eta)$ is the interpolation function [264], γ_0 is the magnitude of maximum twinning shear, and $\boldsymbol{s}$ and $\boldsymbol{m}$ are the unit vectors along the twinning direction and normal to the twinning plane, respectively. Considering the mechanical load, the constitutive equation for the Helmholtz free energy density is $\psi = \psi(\boldsymbol{F}^E, \eta, \nabla_0\eta)$. Using a thermodynamically compatible modeling approach [265] and assuming a linear approximation between the time rate of change of the twin order parameter and the driving forces, the expressions for the first Piola–Kirchhoff stress tensor $\boldsymbol{P}$, and the Ginzburg–Landau equation are obtained as

$$\begin{aligned}
P_{ij} &= F_{ik}^{\mathrm{E}} \frac{\partial \psi^{\mathrm{E}}}{\partial E_{km}^{\mathrm{E}}} \left(F_{jm}^{\mathrm{IE}}\right)^{-1}; \psi^{\mathrm{E}} = \frac{1}{2} E_{ij}^{\mathrm{E}} \mathcal{C}_{\mathfrak{e}_{ijkl}} E_{kl}^{\mathrm{E}}; E_{ij}^{\mathrm{E}} = \frac{1}{2}\left(F_{ki}^{\mathrm{E}} F_{kj}^{\mathrm{E}} - \delta_{ij}\right), && (4.3)\\
\mathcal{C}_{\mathfrak{e}_{ijkl}} &= \frac{\partial^2 \psi^{\mathrm{E}}}{\partial E_{ij}^{\mathrm{E}} \partial E_{kl}^{\mathrm{E}}}, && (4.4)\\
\dot{\eta} &= -\mathcal{L}\left(\frac{\partial \psi^{\mathrm{E}}}{\partial \eta} + \frac{\partial \psi^{\nabla}}{\partial \eta} - \left(\frac{\partial \psi^{\nabla}}{\partial \eta_{,0}}\right)_{,0}\right), && (4.5)
\end{aligned}$$

where $\mathcal{C}_{\mathfrak{e}}(\eta) = \mathcal{C}_{\mathfrak{e}}(0) + \left(\mathcal{C}_{\mathfrak{e}}(1) - \mathcal{C}_{\mathfrak{e}}(0)\right)\phi(\eta)$ is the total tangent elastic modulus, being $\mathcal{C}_{\mathfrak{e}}(0)$ at the parent phase and $\mathcal{C}_{\mathfrak{e}}(1)$ at the twin phase, and $\mathcal{L}$ is the kinetic coefficient. The elasticity tensor at the twin phase is related to the parent phase by considering the reorientation matrix associated with twinning $\mathcal{Q}$ within a centrosymmetric structure [266]

$$\mathcal{C}_{ijkl}(1) = \mathcal{Q}_{im}\mathcal{Q}_{jn}\mathcal{Q}_{ko}\mathcal{Q}_{lp}\mathcal{C}_{mnop}(0). \tag{4.6}$$

The elastic strain energy density, ψ^{E}, (compressible neo–Hookean elasticity [267]) and the interfacial energy, ψ^{∇}, (a standard double-well potential [268, 269]) per unit reference volume are

$$\psi^{\mathrm{E}} = \frac{\mu}{2}\left(I_{C_{ij}^{\mathrm{E}}} - 3\right) - \mu \ln J + \frac{\lambda}{2}(\ln J)^2, \quad \psi_1^{\nabla}(\eta) = A\eta^2(1-\eta)^2 + \kappa_{ij}\eta_{,i}\eta_{,j}, \tag{4.7}$$

where $A = 12\frac{\Gamma}{l}$ characterizes the energy barrier between two stable phases (minima), related to the twin boundary surface energy, Γ, and the twin boundary thickness, l; $\kappa_{ij} = \kappa_0 \delta_{ij}$ with κ_0 being the gradient energy parameter, $I_{\boldsymbol{C}^{\mathrm{E}}} = C^{\mathrm{E}}_{ii}$ and $J^2 = \epsilon_{ijk} C^{\mathrm{E}}_{i1} C^{\mathrm{E}}_{j2} C^{\mathrm{E}}_{k3}$, with ϵ_{ijk} defined as the Levi–Civita (permutation) symbol, are invariants of C^{E}, and μ and λ are the Lame coefficients. Transient, rate effects, and path dependence of solutions could be included by substituting the expressions for the free energy in Eq 4.5 dictating twin evolution in the material configuration

$$\begin{aligned} \dot{\eta} &= -\mathcal{L}^{\eta}\Bigg(2A\eta\left(1-3\eta+2\eta^2\right) - \phi'(\eta)\gamma_0\left(\mu\delta_{ij} + \left(\lambda \ln J - \mu\right)\left(C^{\mathrm{E}}_{ij}\right)^{-1}\right) \times \\ & \qquad C^{\mathrm{E}}_{ij} s_i m_j - 2\kappa_0 \eta_{,ij}\Bigg). \end{aligned} \tag{4.8}$$

The boundary conditions for the evolution of the twin order parameter are obtained from the same thermodynamic procedure that leads to Eqs 4.3 and 4.5

$$\rho_0 n_{0i} \frac{\partial \psi}{\partial \eta_{,0i}} = 0 \quad \text{or} \quad \eta(t) = 0 \quad \text{or} \quad \eta(t) = 1, \tag{4.9}$$

where ρ_0 and n_0 are the density and unit external normal in the undeformed (initial) configuration, respectively.

4.2.2 Validation of the Phase-Field Model and Twin Order Parameter for Single Crystal Magnesium

At first, we validate our time-resolved phase-field model for single crystal magnesium using previous static phase-field results [50] and molecular dynamics simulations [260] (Figure 4.1). The presence of pronounced mechanical anisotropy, local stress concentrations, and high pressure in nanoscale defect-free magnesium implies employing ansiotropic mechanical properties, anisotropic surface energy, and a large displacement formulation in our simulations. The material parameters for all simulations are given in Table S1 from the Supplementary Information section. The nucleation and evolution of deformation twinning in a magnesium single crystal are simulated using the same initial twin geometry as in [50]. A circular twin embryo of initial radius

$r = 3\,\text{nm}$ (corresponding to the analytical sharp interface solution [270]) is embedded into a rectangular domain of dimensions $40 \times 40\,\text{nm}$ in plane strain conditions. The $\langle 1\,0\,\bar{1}\,1\rangle$ plane and $\{1\,0\,\bar{1}\,2\}$ directions are considered as the primary twinning system [271]. This twin system can easily nucleate and grow due to the lower shear and shuffle displacements needed for atoms in order to twin [272]. The validation simulations in Figure 4.1 are performed to investigate the twin parameter distribution subjected to simple shear with Dirichlet boundary conditions on the order parameter for different cases, including an isotropic (Figure 4.1(a, c, d, g, h)) and an anisotropic surface energies (Figure 4.1(b, e, f, i, j)) at three different time instants (see Supplementary Information for more information about the definitions of isotropic and anisotropic surface energies). Within the simulation time of 500 ps, the twin embryo grows until it is repelled by the rigid outer boundaries. For the anisotropic case, the equilibrium shape of the twin embryo is wider in the horizontal direction (parallel to the habit plane) and flatter normal to the habit plane when compared with the isotropic case, which is in good qualitative agreement with the reference phase-field results shown in Figure 4.1(m) [50]. In addition, the twin interface thickness has a lower value normal to the habit plane for the anisotropic surface energy when compared with the ideal isotropic one. This may be related to the contribution of the core and elastic energies to the total surface energy of the interface [273]. For large deformation simulations (Figure 4.1(b, d, f, h, j)), an orientation of the twin evolution is realized due to the difference in the driving force for twinning, which is a factor of $(\boldsymbol{F}^{\eta})^{-1}$. Overall, the twin shape predicted by the current time-dependent phase-field approach shows features in good agreement with the molecular dynamics simulation (Figure 4.1(k)) [260] and steady-state continuum-based model (Figure 4.1(l, m)) [50]. Finally, it is worth mentioning that the twin tended to shrink and eventually disappear when the magnitude of the shear loading was lower than $\gamma_0 = 0.07$ or the size of the initial nucleus were lower than 3 nm. This detwinning mechanism has been observed previously in copper [274] and gold nanowires [275], but this is not the focus of the present

contribution.

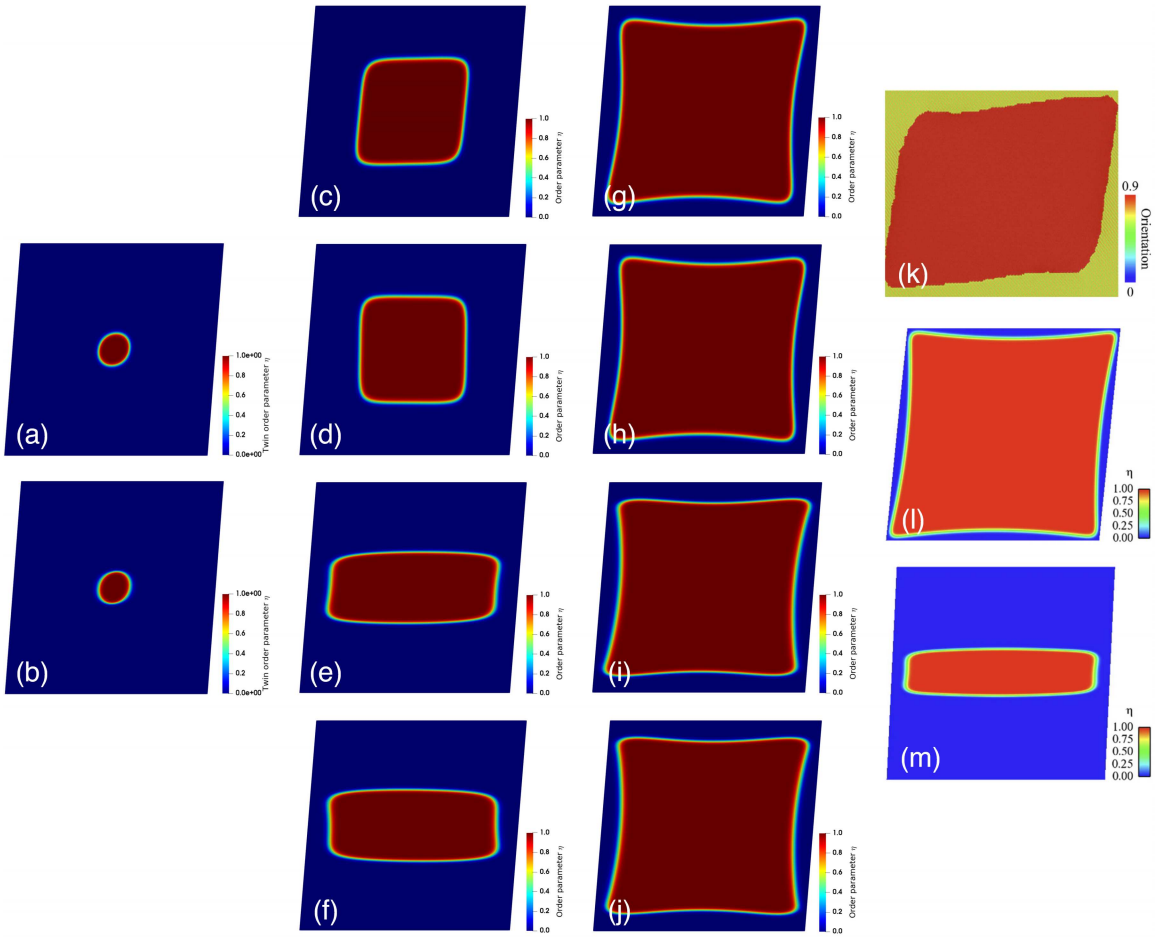

Figure 4.1: Distribution of the twin order parameter, η, for an initially circular single twin with radius of 3 nm in a simple-sheared rectangular domain in both small and large deformations considering both isotropic and anisotropic surface energies and elasticity with zero orientation of the habit plane. The initial conditions are chosen to match results published in the literature using a static phase-field approach [50] and molecular dynamics model [260], while the choice of times are selected to show the evolution of the twin growth under noted conditions: (a,b) Twin order parameter for small and large strains with an isotropic surface energy at $t = 1$ ps; (c,d) Twin order parameter for small and large strains and isotropic surface energy at $t = 50$ ps; (e,f) Twin order parameter for small and large strains and anisotropic surface energy at $t = 50$ ps; (g,h) Twin order parameter for small and large strains and isotropic surface energy at $t = 500$ ps; (i,j) Twin order parameter for small and large strains and anisotropic surface energy at $t = 500$ ps; (k) Local orientation of the twinned region obtained from molecular dynamics simulations [260] and used to contrast with (g) and (h); and (l,m) Order parameter for both isotropic and anisotropic surface energy under simple shear loading using a phase-field model from the literature [50], to be compared with (e) and (g). (k) and (l,m) are reproduced with permission from [260] and [50], respectively. (For interpretation of the references to color in this figure, the reader is referred to the web version of this article.)

4.2.3 The Determination of the Kinetic Coefficient for Magnesium Using Twin Tip and Twin Boundary Velocities

Next, the kinetic coefficient for single crystal magnesium is obtained using interface velocity profiles in both twin tip and twin boundary directions (Figure 4.2) by comparing the present time-resolved phase-field results with molecular dynamics simulations [260]. The kinetic parameter plays an important role in describing the twin boundary propagation as a key plasticity mechanism [276], and there is a lack of experimental studies that quantify the twin boundary mobility in magnesium given the difficulty of the measurements. For the simulations in Figure 4.2, we used the same simulation setup as [260] by considering one rectangular twin embryo with an initial length of 7 nm and width of 4.3 nm inserted at the center of a 77×55 nm rectangular plate undergoing a constant shear strain of 7% (see Figure 4.2(a)). In Figure 4.2(a), the $\left(\bar{1}012\right)$ twinning planes (i.e., the upper and lower planes) are referred to as twin boundaries (TB) because of the twin thickening through twin boundary migration, and the $\left(10\bar{1}2\right)$ twinning planes (i.e., the vertical planes) are referred to as twin tips (TT) as a result of the lateral motion of the twin tip. Applying the shear deformation in the $[10\bar{1}1]$ direction results in the twin interface profiles illustrated in Figures 4.2(b) and 4.2(c) for the twin boundary and twin tip for times noted in the subfigures, respectively. In the case of twin boundaries, the interface profiles along the width of the sample at different time instants are illustrated in Figure 4.2(b). The boundary velocity is calculated by tracking the bottom and top boundaries of the twin at $\eta = 0.5$ over time (green line in Figure 4.2(b)). The inset in Figure 4.2(b) shows the interface displacement in the vertical direction Δy, indicating that the twin boundary velocity is decreasing as it approaches the outer boundaries. In calculating the twin tip velocity in Figure 4.2(c), the horizontal displacement of the interface Δx at $\eta = 0.5$ is tracked through time (see insets). The results indicate that Δx and the twin tip velocity is constant, with values of velocity summarized later in Figure 4.2(d). The constant trend of twin tip mobility may be ascribed to the large back

stress arising at the twin tip [277]. Mapped in red onto Figure 4.2(c) is the explicit analytical solution for the stationary Ginzburg–Landau equation given by [261]

$$\eta_{\text{analytical}} = \left(1 + \exp\left(\frac{-x}{w}\right)\right)^{-1}; \quad w = \sqrt{\frac{\kappa_0}{2A}}. \tag{4.10}$$

The comparison of numerical results with this analytical solution enables the twin interface width (i.e., difference between twin interface position at $\eta = 0.01$ and $\eta = 0.99$) to be calculated. The determination of the twin interface width is important because its size can guide the selection of the element size and spatial mesh refinement in finite element simulations of twinning [269]. Finally, Figure 4.2(d) shows the time-evolved twin boundary (black) and tip (blue) velocities obtained using the proposed phase-field model, compared with molecular dynamics simulations [260]. The proposed continuum and molecular dynamics results are in excellent agreement. Altogether, Figure 4.2 provides a good validation for the present time-dependent phase-field approach, and, more importantly, enables the determination of the kinetic energy coefficient ($4200\,(\text{Pa}\cdot\text{s})^{-1}$) for single crystal magnesium. This is the first ever reported value in the literature for twinning, and its determination is of great importance in understanding the kinetics of twin growth and its dependence on other parameters (e.g., shear stress) during the early stages of twin evolution [277].

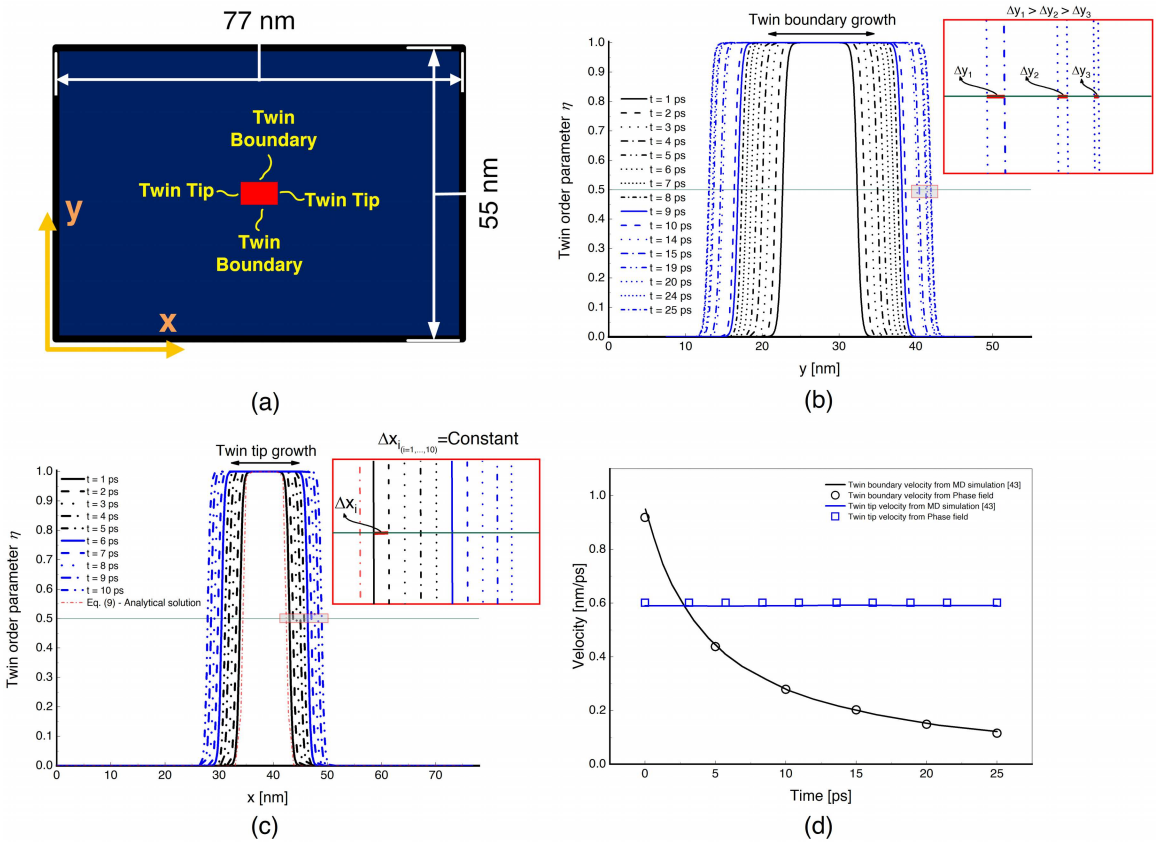

Figure 4.2: Evolution of twin growth in a single crystal pure magnesium: (a) Numerical setup of the rectangular single crystal with an initial rectangular twin with boundaries and tips in material configuration; (b) Time evolution of the twin order parameter as a function of the position y normal to the habit plane. A horizontal line starting from point $\eta = 0.5$ is chosen for measuring the twin boundary interface velocity to show the vertical interface displacement Δy. The inset demonstrates the interface profile at six different time instants to show the time-dependent growth of the twin; (c) Time evolution of the twin order parameter as a function of the position x in the direction of the habit plane. Fewer time instants than shown in (b) are used to demonstrate the constant twin tip interface velocity. Similarly, the point $\eta = 0.5$ is chosen for measuring the tip interface velocity and to show the constant horizontal interface displacement Δx. The analytical solution of the explicit Ginzburg–Landau equation, which corresponds to $t = 0\,\text{ps}$, is shown as the dotted red color; (d) Twin tip and twin boundary velocities as a function of time obtained from (b) and (c), and compared with those from the molecular dynamics simulations [260]. (For interpretation of the references to color in this figure, the reader is referred to the web version of this article.)

4.2.4 The Time-Evolved Shear Stress in the Combined Matrix-Twin Embryo

Here, the evolution of the twin area fraction and the shear stress σ_{12}, in the parent and twin phase are studied (Figure 4.3). This part of the investigation is motivated by the necessity of better understanding the intense local stress within a small region in the microstructure as this is the driving force for the propagation and growth of a twin. These insights may inform about the sequence of events leading to the formation of the visible twins at an early stage in magnesium. In Figure 4.3, the same boundary conditions and a constant 7% shear strain are used in the same rectangular twin embryo system depicted in Figure 4.3(a). Initially, the length and width of a single rectangular twin embryo at different times are calculated in Figure 4.3(a); this will be used to obtain the twin area fraction in Figure 4.3(b). In the figure, values are calculated for $\eta = 0.5$ on the interface profile as shown in the insets at $t = 5\,\text{ps}$. Results indicate that the twin growth is larger in the twin tip direction rather than in the twin boundary direction, and this difference decreases at later time instants as the twin approaches the outer boundaries. Next, the change of the twin area fraction, defined as the ratio of the twinned to the whole simulated area, is shown in Figure 4.3(b) under shear loading, and this is compared with molecular dynamics simulations [260]. The insets in Figure 4.3(b) show the morphology of the twin at two different times for visualizing how the twins grow. Knowing the twin area fraction evolution is important towards enhancing our understanding of the crystal grain reorientation associated with deformation twinning, where limited data exists because of the special experimental tools required to access the length and time scales needed to capture such measurements [244]. As seen in Figure 4.3(b), the present phase-field model reasonably predicts the evolution of the twin area fraction. Next, the shear stress profile acting parallel to the x direction is plotted for various times in Figure 4.3(c), which is used to demonstrate the redistribution of internal stresses resulting from twinning [278]. The plateau and decreasing regions indicate the shear

stress variation in the matrix and twin phases, respectively. By progressing in time, the shear stress decreases as the x position approaches the center of the simulation geometry, until it reaches its minimum. The magnitude of the shear stress within the twin decreases as a function of time, and, eventually, becomes negative for the last time instants of the simulation. This phenomenon is consistent with experimental results [236]. At the same time, the profile evolves spatially and temporally. Finally, the average global shear stress field is shown in Figure 4.3(d), where the field is taken as the average across the red line spanning both the twin and the matrix depicted in the inset. The measurements are important because they can provide insights into the complex load sharing mechanisms that are generated by the parent and the twin phase [279]. The results are also compared with molecular dynamics simulations [260], both qualitatively (the insets at $t = 10\,\text{ps}$ and $t = 25\,\text{ps}$) and quantitatively. The phase-field results match the molecular dynamics simulations well. The results show that the global shear stress is decreasing as the twin size evolves. Altogether, results from Figure 4.3 are important for determining the activation force required for twin embryo growth that may serve as an input into higher scale models [280].

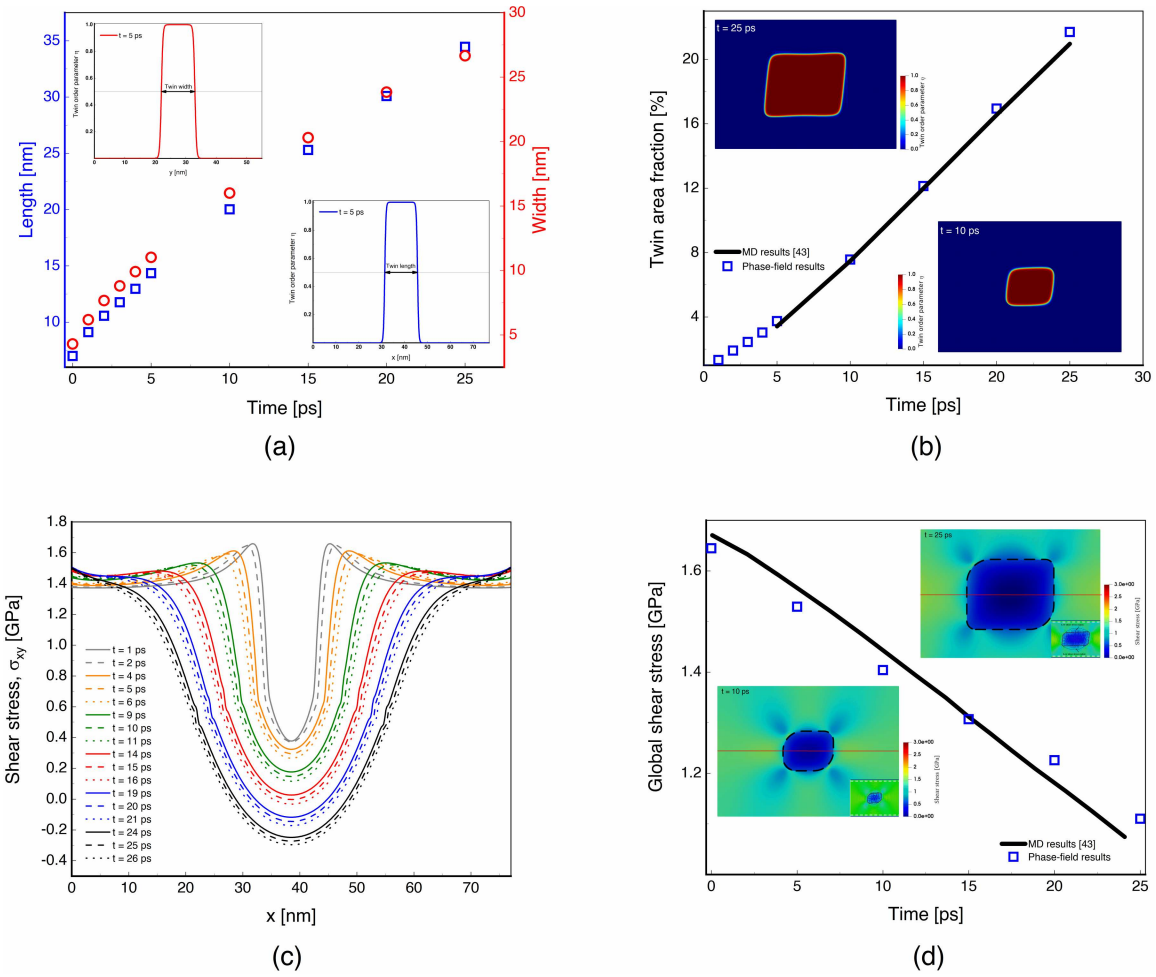

Figure 4.3: The time-evolved shear stress acquired from the phase-field model on deformation twinning of pure single crystal magnesium: (a) Time evolution of the length (blue squares) and width (red circles) of a single rectangular twin embryo that grows at 7% shear strain. The insets show the twin interface profiles at $t = 5\,\text{ps}$, parallel and orthogonal to the habit plane, by which the twin size is obtained; (b) Growth of the twin area fraction (i.e., the ratio of twinned area to the total area of the numerical geometry) predicted by the proposed phase-field approach (blue squares) and compared with molecular dynamics simulations (black line) [260]. The same numerical geometry setup as [260] was used. The insets show the distribution of the twin order parameter at $t = 10\,\text{ps}$ and $t = 25\,\text{ps}$ to illustrate areal growth; (c) Spatial variation of initial shear stress along the x-axis in single-twinned magnesium at various time instants; (d) Variation of the average global shear stress as a function of time. The numerical results (blue squares) are compared with molecular dynamics data (black line) [260]. The insets show the spatial distribution of local shear stress at $t = 10\,\text{ps}$ and $t = 25\,\text{ps}$ along the red mid-line. The boundaries of the twin embryo are denoted by the black dashed line. In the bottom of each insets, the atomic shear stress from snapshots taken at similar times as [260] are given for comparison. (For interpretation of the references to color in this figure, the reader is referred to the web version of this article.)

4.2.5 Studying Twin Interactions Toward Microstructure Tailoring and Materials Design

Finally, simulations have been performed to study the effect of twin-twin and twin-defect interactions (Figure 4.4). Understanding these interactions is an important step toward developing better predictive models for designing materials with tailored properties and microstructures [281–284]. In real materials, twin interactions may result in the formation of twin-twin junctions that may cause strain hardening [285] and crack initiation [286], leading to a strong influence on the overall material performance. First, the change of area fraction of the middle twin as a function of time for a different number of embryos is illustrated in Figure 4.4(a). Only the middle embryo is considered in the analysis in order to better isolate the interactions and reduce boundary effects. The location of the twins for the three embryo cases is illustrated in the inset. In Figure 4.4(a), it is shown that increasing the number of twins leads to a decrease in the twin area fraction of the middle embryo as a result of its interaction with the other twins. The difference of the twin area fraction for multi-embryo cases becomes larger at later time instants. This finding is important as it highlights the effects of twin interactions on twin evolution, where experimental measurements are currently very limited [287]. Next, the spatial variation of the order parameter and the corresponding shear stress at $t = 10\,\text{ps}$ and $t = 20\,\text{ps}$ are depicted in Figure 4.4(b). This result reveals insights into the expansion of the twin domain through the accumulation of large plastic shear strain at the nanoscale [288]. The homogeneous growth in the twin area is exemplified in the top left inset in Figure 4.4(b), where the twins have not changed in shape until $t = 10\,\text{ps}$. The corresponding shear stress distribution at $t = 10\,\text{ps}$ is shown in the bottom left inset, where the shear stress inside the twins is negative while it is positive in the matrix. The heterogeneous stress distribution around the twins is due to a sudden change in the stresses within the twin-matrix interfaces, associated with the need to accommodate deformation in this region [256]. From the spatial shear stress distribution, it is observed that the local

shear stress reaches a minimum in the center of each twin. Outside the twins, the shear stress is lower at the bottom left and top right twins because of the constraining effect of the adjacent twins to the middle one. In the right insets, the deviatoric deformation in twin morphology at $t = 20\,\text{ps}$ is identified due to the interaction of the twins with each other and the disturbing of the stress field by them. The stress distribution in the vicinity of the twin-matrix interfaces at $t = 20\,\text{ps}$ is heterogeneous as a result of high stress concentrations in the matrix near the twin boundaries. It is also shown that the middle twin experiences a maximum shear stress resulting from the compressive forces generated by the other twins. The local stress concentration is one main interaction of crack and twins where some nucleation site appears in the interfaces inside and around the interface [289].

Next, the change of shear stress along a horizontal line through a middle section of the simulation area as a function of a 1, 2, or 3 twin embryo system is shown in Figure 4.4(c). It is observed that increasing the number of twins leads to decreasing the shear stress values in the matrix phase, while the difference in shear stress values for the later time instants are larger as a result of twin-twin interactions. In the twinned regions at later times, the junctions of different embryos result in a negative shear stress with steeper slopes as compared with earlier times. In addition, it can be observed that the stress concentration in the matrix, predominantly in the vicinity of the twin boundaries, increases only marginally with increasing twin thickness (black lines in Figure 4.4(c)). Finally, the interaction of a twin and a defect is investigated in Figure 4.4(d) by comparing the change in the twin tip velocity towards the boundary and the void along the blue dashed horizontal line. The numerical setup is also given in the inset, where symmetric boundary conditions are used. The radius of 2 nm is chosen for the void. For all times, the results indicate that the tip velocity is linearly decreasing in time in a direction approaching the left boundary. For the void, the velocity at the tip is constant until some point after which a sudden decrease in the velocity occurs, resulting from the twin-defect interaction. In addition, the twin tip

velocity is larger toward the void because of the higher stress concentration influence by the void.

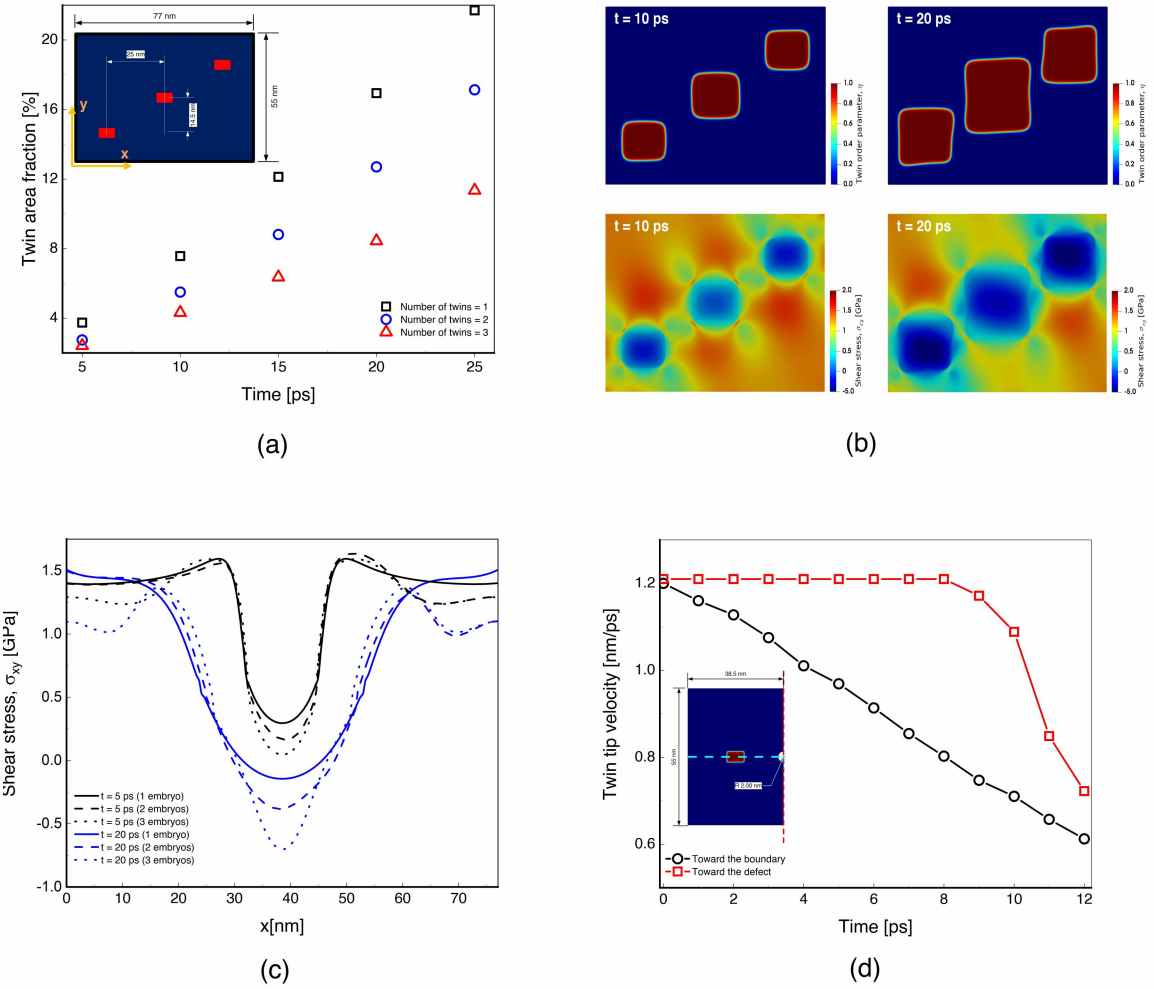

Figure 4.4: Exploration of twin-twin and twin-defect interactions to inform fundamental growth mechanisms in single crystal magnesium: (a) Evolution of twin area fraction for 1, 2, and 3 twin embryos. The inset shows the location of each twin for the three-embryo simulation. The area of the middle twin is measured using its length and width obtained from the interface profile at $\eta = 0.5$, as was done for Figure 4.2; (b) Spatial distribution of the twin order parameter and shear stress in the parent and twin phases for the numerical setup shown in the inset of (a) at $t = 10\,\text{ps}$ and $t = 20\,\text{ps}$; (c) Evolution of the shear stress along a horizontal line through the middle of the single crystal microstructure for different numbers of embryos. The numerical setup is subjected to 7% shear strain as was done in the other cases; (d) Study of twin-defect interactions by considering the time-evolved twin tip interface towards the boundary and the void. The related simulation dimensions are given in the inset, which also shows that symmetric boundary conditions were used (the symmetry line is shown by the dash red line). (For interpretation of the references to color in this figure, the reader is referred to the web version of this article.)

4.3 Discussion

In this study, the evolution of twinning in magnesium has been studied using a validated and calibrated phase-field model to gain better insights into the time-evolved twin morphology, the spatial distribution of the internal shear stress, and the twin interactions. A highly-accurate monolithic iterative procedure has been implemented for solving the coupled balance and Ginzburg–Landau equations, and the governing equations have been solved in an open-source high-level computing platform FEniCS. For engineering examples with FEniCS, please refer to [290]. The results presented in this work confirmed the impact of the current model by capturing the behavior of the leading deformation mechanism in single crystal magnesium, twinning. By means of the proposed implementation, the state variables (i.e., the displacement and the twin order parameter) have been computed monolithically for various scenarios in discrete time steps, including small and large deformations with both isotropic and anisotropic surface energies and elasticity. The data have been compared with a continuum mechanics model [50] and molecular dynamics simulations [260]. The findings are qualitatively consistent with both literature approaches. A notable result emerging from the proposed model is the prediction of the critical strain and initial twin embryo size required for growth and propagation under the chosen numerical settings. This computational implementation is particularly useful because identifying such features experimentally is challenging given the length and time scales needed to reproduce these events [291]. Next, the interface velocities for the twin tips and twin boundaries have been explored in order to determine the kinetic coefficient using the phase-field model and compared with recent molecular dynamics simulation [260]. Studying velocity growths is important because they affect hardening, texture evolution, and ductility in the material [292]. To the authors' best knowledge, the present work pioneers the analysis of the interface mobility, showing different trends of twin evolution in the direction parallel and orthogonal to the twin habit plane. The

interface velocity is considered to be an important factor to determine the thermodynamic driving force for interface propagation, because knowing the interface velocity for any value of the driving force potentially leads to the determination of the kinetic coefficient for any range of materials [293]. The interface profile was also compared with the analytical solution of the stationary Ginzburg–Landau equation, and the obtained numerical interface width of 1.58 nm was close to the analytical value of 1.62 nm [261]. This information guides mesh selection and refinement when modeling twinning in this system [294]. In addition, the current phase-field modeling approach overcomes the challenges existing in molecular dynamic simulations for calculating the twin size, such as identifying the orientation of each atom in the twinned region [252], and is able to capture new behavior of twin growth for $t \leq 5$ ps, comparing well with previous molecular dynamics data [260]. The strong point of the current approach is to track multiple interfaces in order to measure twins' size with no additional efforts for samples larger or smaller than in atomistic simulations.

A further considerable implication of the proposed model is the possibility of investigating the local and global shear stress field inside the parent and twinned phases. Analysis of twin shear stress fields induced in these cases provides further evidence for the effect of twins' thickness and their mutual position on further twin growth and/or further twin nucleation [295–297]. Moreover, the importance of an appropriate strategy for partitioning the stress fields between the twinned and untwinned domains have been demonstrated in this study. A final upshot of the current phase-field model has been to explore new understandings in twin-twin and twin-defect interactions. For the case where multiple twins grow in one grain, a common occurrence observed in experiments [298], it is highlighted that the stress concentration around the void could significantly increase the twin interface velocity, affecting subsequent expansion of the twins. Taken together, our study provides a framework for a new way to understand local deformation mechanisms in materials by analyzing the evolution and interaction of twins at the nanoscale.

4.4 Methods

The problem-specific parts of the computer code used to perform the simulations have been generated automatically from a high-level description that resembles closely the notation used in this work by using a number of tools from the FEniCS Project [299, 300]. The time stepping parameters are chosen such that the momentum balance scheme is second-order accurate and stable. Quadratic and linear Lagrange functions are used for the finite element approximation of the displacement and the twin order parameter, respectively. A mesh of 423,500 triangular elements is adopted. Initial conditions are also prescribed as part of the solution procedure. More importantly, a fully-coupled solution strategy is used, and a Newton–Krylov method is employed to solve the nonlinear equilibrium and Ginzburg–Landau equations in each time step, with a minimum of 5000 time steps for studying the twinning behavior in magnesium. It is noted that 10 elements are considered at the interface to resolve the sharp variation along the interface width. The conjugate gradient method with a Jacobi preconditioner from PETSc packages [301] has been employed for solving the nonlinear equations. The simulation has been performed by a computing node using Intel Xeon E7-4850, in total 64 cores each with 40 MB cache, equipped with 256 GB Memory in total, running Linux Kernel 5 Ubuntu 20.04.

4.5 Data Availability

The authors declare that the main data supporting the findings of this study are available within this article. Extra data are available from the corresponding authors upon reasonable request.

4.6 Code Availability

The Python code, generated during the current study, is part of the FEniCS project available at http://www.fenicsproject.org/download, and an example for the compu-

tational implementation is available in [302] to be used under the GNU Public license [303].

4.7 Acknowledgments

The authors acknowledge support from Natural Sciences and Engineering Research Council of Canada (NSERC) Discovery Grant 2016-04685 and NSERC DNDPJ 531130-18, and partial support of the MIUR-PRIN project XFAST-SIMS (no. 20173C478N).

4.8 Author Contributions Statement

B.A developed the model, wrote the code, designed and performed all simulations, analyzed results, and wrote the original draft. H.J developed the model, analyzed results, reviewed, and edited the submitted journal article. B.E.A helped with the code, allocated the computational resources, reviewed and edited the submitted journal article. A.R helped in computational aspects, reviewed and edited the submitted journal article. J.D.H supervised the research, acquired funding, reviewed, and edited the submitted journal article. All authors discussed the results.

4.9 Competing Interests

The authors declare no competing interests.

4.10 Supplementary Information

4.10.1 Summary of Content

Here, we provide the equations for calculating the effective bulk modulus, shear modulus, and Poisson's ratio. The relations for the phase-field parameters, including the double-well barrier, gradient energy, and the reorientation matrix are then given. The mechanical properties for the single crystal magnesium is provided in Table 4.1.

4.10.2 The Effective Bulk Modulus, Shear Modulus, and Poisson's Ratio

The Bulk modulus, shear modulus, and the Voigt average Poisson's ratio for crystals with trigonal or hexagonal symmetry are obtained as [304]

$$K = \frac{(C_{11}+C_{12})\,C_{33}-2C_{13}^2}{C_{11}+C_{12}+2C_{33}-4C_{13}}; \tag{4.11}$$

$$\mu = \frac{1}{15}\Big(2C_{11}+C_{33}-C_{12}-2C_{13}+\frac{3}{2}\,(C_{11}-C_{12})+6C_{44}\Big); \tag{4.12}$$

$$\nu = \frac{3K-2\mu}{6K+2\mu}, \tag{4.13}$$

where C are the second order elastic constants extrapolated from 4.2 °K to 0 °K.

4.10.3 The Transformation Barrier and Gradient Energy Parameter

The energy barrier between two stable phases (minima) A, and the gradient energy κ_0, are given as [50]

$$A = 12\frac{\Gamma}{l}; \quad \kappa_0 = \frac{3}{4}\Gamma l, \tag{4.14}$$

where Γ is the twin boundary surface energy and l is the twin boundary thickness.

4.10.4 The Reorientation Matrix

The reorientation matrix $\mathcal{Q}$, associated with the twinning within a centrosymmetric structure is obtained by [266]

$$\mathcal{Q} = \begin{cases} 2m_i m_j - \delta_{ij} & \text{type I twins,} \\ 2s_i s_j - \delta_{ij} & \text{type II twins,} \end{cases} \tag{4.15}$$

where $\boldsymbol{s} = (\cos\theta, \sin\theta)^T$ and $\boldsymbol{m} = (-\sin\theta, \cos\theta)^T$ are the lattice orientation vectors in the vector form, δ is the Kronecker delta, and θ denotes the orientation of the habit plane. Type I and type II twins differ in reflections or rotations of the lattice vectors in the twin and parent phase.

4.10.5 The Matrix Form of the Gradient Coefficient

The gradient energy parameter in the matrix form can be written as

$$\boldsymbol{\kappa} = \begin{pmatrix} \kappa_{11} & 0 \\ 0 & \kappa_{22} \end{pmatrix}, \tag{4.16}$$

for both isotropic ($\kappa_{11} = \kappa_{22} = \kappa_0$) and anisotropic ($\frac{\kappa_{11}}{2} = 2\kappa_{22} = \kappa_0$) twin boundary surface energies.

Table 4.1: Material properties and model constants for single crystal magnesium

Parameters	Notation	Value	Reference
Elastic constants	C_{11}	63.5 GPa	[305]
”	C_{12}	25.9 GPa	[305]
”	C_{13}	21.7 GPa	[305]
”	C_{33}	66.5 GPa	[305]
”	C_{44}	18.4 GPa	[305]
Bulk modulus	K	36.9 GPa	Eq 4.11
Shear modulus	μ	19.4 GPa	Eq 4.12
Poisson’s ratio	ν	0.276	Eq 4.13
Twin boundary energy	Γ	0.117 $^{\mathrm{J}}/_{\mathrm{m}^2}$	[242]
Twinning shear	γ_0	0.1295	[235]
Regularization length	l	1.0 nm	[268]
Transformation barrier	A	1.404 GPa	Eq 4.14
Gradient energy parameter	κ_0	0.0878 $^{\mathrm{nJ}}/_{\mathrm{m}}$	Eq 4.14
Kinetic factor	$\mathcal{L}$	4200 $(\mathrm{Pa} \cdot \mathrm{s})^{-1}$	Calibrated with MD [260]

Chapter 5

Time-Evolved Phase-Field Model for Capturing Twinning, Fracture-Induced Twinning, and Fracture at Large Strains in Anisotropic Brittle Materials

Under Peer Review in Journal of the Mechanics and Physics of Solids

B. Amirian[a], H. Jafarzadeh[b], B.E. Abali[c], A. Reali[b], J.D. Hogan[a]

[a]*Department of Mechanical Engineering, University of Alberta, Edmonton AB T6G 2R3, Canada*

[b]*Department of Civil Engineering and Architecture, University of Pavia, I-27100 Pavia, Italy*

[c]*Department of Materials Science and Engineering, Uppsala University, Uppsala 751 21, Sweden*

Abstract A time-dependent phase-field approach is developed for modeling twinning, fracture, and fracture-induced twinning in anisotropic brittle nano single crystals. Considering anisotropic elastic properties and phase boundary energy, a detailed finite element procedure is developed for studying the behavior of brittle solids subjected to large stresses and finite deformations. Two separate order

parameters related to the fracture and twinning are used, and the evolution of the order parameters is governed by coupled elasticity and Ginzburg–Landau equations. To the authors' best knowledge, for the first time, a monolithic strategy is employed for solving the governing equations in order to improve the computational accuracy of the model. To discretize the time derivative equations, a second-order backward difference scheme is used. A finite element code was then developed within the Python-based open-source platform FEniCS for a system with twinning and fracture and employed to solve three problems: (i) twin evolution in two-dimensional single crystal magnesium and boron carbide under simple shear deformation; (ii) crack-induced twinning for single crystal magnesium under pure mode I and mode II loading; and (iii) study of fracture in homogeneous single crystal boron carbide under biaxial compressive loading. The results for these problems are compared with the available experimental data, previous stationary phase-field results, and analytical solutions from the literature. The algorithm can also be extended for the study of phase transformations under dynamic loading or thermally-activated mechanisms, where the competition between various deformation mechanisms is accounted for within the current comprehensive model approach. Altogether, the proposed model opens a number of interesting possibilities for simulating and controlling failure pattern development in anisotropic brittle solids experiencing extreme mechanical loading.

Keywords: Phase-field model; Anisotropic brittle solids; Single crystals; Finite element method; Fracture and twinning; Monolithic scheme

---

5.1 Introduction

Understanding and predicting anisotropic fracture and damage evolution in brittle materials have been long-standing problems in engineering designs. Owing to the advent of novel modeling techniques and the advances in computational capabilities, the usage of accurate and robust numerical methods plays a key role in situations where purely experimental approaches are of high cost and not always readily accessible (e.g., high-energy in-situ X-ray computed microtomography [306], in-situ electron backscattered diffraction (EBSD) [307], and micro/nano-mechanical testing [308]). In the literature, the simulation of fracture in solids at the atomic scale is commonly treated by molecular dynamics (MD) [309], density functional theory (DFT) [310], or lattice static models that are based on spring networks [311]. Despite addressing nonlinearities at the crack tip, avoiding singularity-related issues, and considering bond breaking between atoms [312–314], there exist challenges in using atomistic models to cover the time and length scales necessary to analyze the structural response at the macroscale needed for engineering applications.

Conventionally, there are two main categories of numerical approaches that can be employed to provide realistic simulations of material failure: (i) discrete crack models (e.g., the discrete element method [315, 316], the extended finite element (XFEM) method [317], the cohesive zone method [318], and the cohesive segment method [319]) in which the displacement field is allowed to be discontinuous across the fracture surfaces, and (ii) smeared (continuum) crack models (e.g., damage models [320], and diffuse interface models [321]) that consider a continuous displacement everywhere, assuming gradually decreasing stresses to model the degradation process. Regardless of showing much success in modeling crack propagation [322], the discrete crack models need additional criteria based on stress, strain energy density, energy release rate, or virtual crack closure techniques [323] to predict the crack initiation (nucleation), growth, and branching in dynamic fracture problems [324]. Further, the

sharp representation of cracks requires remeshing algorithms or using the partition of unity method [325], both having their own difficulties in tracking the multiple crack fronts in complex three-dimensional morphologies [326, 327].

In the smeared crack approach, regularizing strong discontinuities caused by strain localizations within a finite and thin band leads to a precise approximation of the crack topology [328]. The gradient damage model [329], physical/mechanical community-based phase-field fracture model [330–332] that traces back to the reformulation of Griffith's principle [333], and peridynamics [334], which can be regarded as generalized non-local continuum mechanics, fall within this category. Replacing partial differential equations in the phase-field model by integrals in peridynamics allows for topologically complex fractures such as intersecting and branching to be handled in both two and three dimensions [335]. Coupling the smeared and discrete crack approaches, for example, the element deletion method [336], the combined non-local damage and cohesive zone method [337], and thick level-set method [338] have also shown promising results in modeling fracture. In the thick level-set method, a discontinuous crack description is surrounded by continuous strain-softening regions, which is defined by a level-set function to separate the undamaged from the damaged zone [339]. However, the dependence of the results on the finite element meshes and the convergence of the solutions, for a mesh size tending to zero, results in numerical errors [340].

As an alternative approach, the phase-field model has been widely used recently in the context of phase transition processes, ranging from solidification [341] and phase transformation in a solid [342] to the modeling of ferroelectric materials [343]. Having the capability to model the microstructural evolution, it has been successfully adopted in the simulation of martensitic phase transformations [264], reconstructive phase transformations [344], phase transformations in liquids [345], dislocations [346], twinning [50], damage [347], and their interactions [348–350]. Initiated with the celebrated work by Francfort and Marigo on the variational approach to brittle fracture

[351], where the total energy is minimized simultaneously with respect to the crack geometry and the displacement field, the concept of applying the phase-field method in fracture mechanics has gained significant interest in the literature [261, 352–354, 289, 355–359]. Due to the thermodynamic driving forces, the evolution of interfaces (e.g., merging and branching of multiple cracks) is predicted with no additional effort [360]. Also, being quantitative and material-specific as well as simple to couple to other calculations (e.g., stress or temperature [361]) makes phase-field modeling a powerful and flexible method for studying the fracture of single-crystalline [362] and polycrystalline materials [363]. The high computational cost in the phase field due to resolving the gradient term by using sufficiently refined mesh in the damaged zone can be straightforwardly tackled by parallel implementations [364] and adaptive remeshing [365].

Using the phase-field model to study the failure mechanisms in brittle materials has recently received increasing attention [366–370]. Unlike ductile failure behavior, brittle solids often fail catastrophically along grain boundaries [371], or cracks propagate along the interstitials in the case of geomaterials [372]. In the mechanics community, Wu applied a unified phase-field model to simulate the mechanics of damage and failure of concrete [373]. In his work, a fourth-order model for the phase-field approximation of brittle materials was developed using the explicit Hilber–Hughes–Taylor–α [374] method and the phase-field models were represented by a phase transformation-independent single-well energy potential to describe the fracture behavior. In the physics community, on the other hand, the phase-field models are commonly derived by adapting the phase transition formalism of Landau and Ginzburg [375]. For example, Aranson et al. [376] combined elastic equilibrium with the Ginzburg–Landau (GL) equation, which accounted for the dynamics of defects, to study the crack propagation in brittle amorphous solids. Another GL-based phase-field approach restricted to mode III fracture (antiplane shear) was proposed by Karma et al. [330] and Hakim and Karma [321] in the two- and three-dimensional settings, respectively. Consider-

ing fracture as a solid-gas transformation, the double-well energy potential appeared in phase-field modeling of damage in the study by Levitas et al. [354]. Some of the disadvantages of the double-well potential, such as crack widening and lateral growth during crack propagation, can be eliminated by using a single-well term; however, the realistic shape of the stress-strain curves obtained from the experiments or atomistic simulations cannot always be captured by the single-well free energy density [261].

In numerical implementations, nonlinear problems with a strong coupling between the equilibrium equation and the phase-field parameter can be solved through two approaches: (1) the most-commonly used one is the staggered solution scheme, which is based on decoupling the momentum equation and phase-field problem into the system of two equations that can be solved in a staggered manner [377, 378]. Regardless of its robustness due to giving rise to two convex minimization problems, a significant amount of staggered iterations is required at a fixed loading step, thus resulting in a high computational cost [379]; (2) the alternative option would be implying the solution of the phase-field formalism for both variables' increments (e.g., displacement and phase-field variables) simultaneously [380]. As compared with the staggered scheme, the monolithic solution is more efficient as a result of needing less Newton–Raphson iterations [381]. To the best of our knowledge, no studies have focused on solving the GL-based phase-field problem for predicting the twinning and fracture behavior of brittle materials by using a monolithic scheme; this is addressed in the current study.

The applications of fracture mechanics have traditionally focused on crack growth problems under mode I mechanisms [382, 383]. Earlier phase-field models have not extensively considered the effect of loading conditions (e.g., tensile and compressive states) on fracture behavior of the brittle materials [330, 355, 376]. Most of the previous studies are focused on the mechanism of crack initiation and growth of opening (mode I) cracks since experimental observations indicate that pure mode I crack growth is usually preferred to mixed-mode or pure mode II crack growth [384, 385]. In some models, it is assumed that the crack grows under opening mode con-

ditions, even in the case of pure shear loading, as a result of local tensile stresses at the tip [386]. To achieve this behavior in conventional phase-field approach, a common technique is to distinguish between tensile and compressive states by decomposing the strain energy density, either using a spectral decomposition [377] or a hydrostatic-deviatoric approach [387]; however, as reported in [388, 389], presenting a sufficiently high confining pressure to obtain mode II cracks and a low ratio between the critical stress intensity factors K_{IIc} and K_{Ic} may lead to fracture under a sliding mode. In addition, numerical techniques such as the Miehe and Amor decompositions present disadvantages that have yet to be addressed in order to solve the crack propagation under compressive loading in anisotropic materials [390]. For example, the Miehe decomposition shows unphysical stiffening at the final part of the force-displacement curve instead of a complete stiffness loss for the fully cracked specimen [391]. As another example, the Amor decomposition appears to have some limitations for compression-dominated loading [392]. Accordingly, presenting a more comprehensive model to predict the crack path under compression for anisotropic materials is needed, as will be addressed in this research.

Goals and outlook: In the present study, we seek to extend the GL phase-field approach to predict fracture and twinning in single crystal anisotropic brittle materials (e.g., magnesium Mg, and boron carbide B_4C). For the first time in the literature to our best knowledge, this study focuses on increasing the computational accuracy of the method by means of implementing the monolithic scheme for solving the coupled differential equations in the open-source parallel computing platform FEniCS [393]. As a result of large elastic strains by local stress concentrations in nanoscale defect-free volumes or by high pressures [265], as well as large shears arising from twinning [394], a fully geometrically and physically nonlinear phase-field theory along with an anisotropic surface energy and nonlinear elasticity is employed. In the current study, a new decomposition for the strain energy density based on [391] is used to reproduce the experimentally-observed crack propagation under compressive loading, and the

simulated results are compared with analytical solutions. In these comparisons, a double-well energy potential is considered for studying the fracture behavior (e.g., crack initiation, growth, and propagation) and twinning in brittle solids.

The remainder of this study is outlined as follows. In Section 5.2, a brief description about the materials' choice is presented. The theoretical aspects of the phase-field theory, including finite deformation kinematics, balance laws, a thermodynamically sound derivation of equations, and the weak forms of the governing PDEs are presented in Section 5.3. Finite element discretization details and the numerical implementation are given in Section 5.4. Results and representative material properties for brittle materials along with the discussion of phase-field simulations are reported in Section 5.5. The conclusions of the study are finally drawn in Section 5.6.

Throughout this study, the following notations will be used. Contractions of second-order tensors $\boldsymbol{A} = \{A_{ij}\}$ and $\boldsymbol{B} = \{B_{ij}\}$ over one and two indices are defined as $\boldsymbol{A}\cdot\boldsymbol{B} = \{A_{ij}B_{jk}\}$ and $\boldsymbol{A} : \boldsymbol{B} = \{A_{ij}B_{ij}\}$, where the repeated indices denote Einstein's summation, and A_{ij} and B_{ij} are the components of the tensors in a right-handed orthonormal Cartesian basis $\{\boldsymbol{e}_1, \boldsymbol{e}_2, \boldsymbol{e}_3\}$; the dyadic product of vectors $\boldsymbol{a} = \{a_i\}$ and $\boldsymbol{b} = \{b_j\}$ is represented by $[\boldsymbol{a} \otimes \boldsymbol{b}]_{ij} = \{a_i b_j\}$; Cross product $\times$ for any tensor $\boldsymbol{D} = D^{ijkl}\boldsymbol{e_i}\otimes\boldsymbol{e_j}\otimes\boldsymbol{e_k}\otimes\boldsymbol{e_l}$ is defined as $\boldsymbol{Q}\times\boldsymbol{D} = D^{ijkl}(\boldsymbol{Q}\cdot\boldsymbol{e_i})\otimes(\boldsymbol{Q}\cdot\boldsymbol{e_j})\otimes(\boldsymbol{Q}\cdot\boldsymbol{e_k})\otimes(\boldsymbol{Q}\cdot\boldsymbol{e_l})$ with $\boldsymbol{Q}$ being an orthogonal tensor. $\boldsymbol{I}$ denotes the second order identity tensor; δ_{ij} denotes the Kronecker delta; the transposition, inversion, determinant, trace, symmetric part, and skew-symmetric part of $\boldsymbol{A}$ are indicated as $\boldsymbol{A}^T$, $\boldsymbol{A}^{-1}$, $\det(\boldsymbol{A})$, $\mathrm{tr}(\boldsymbol{A})$, $\mathrm{sym}(\boldsymbol{A})$, and $\mathrm{skew}(\boldsymbol{A})$, respectively. The symbols ∇_0 and ∇ represent the gradient operators in the initial $\mathfrak{B}_0$ and current $\mathfrak{B}$ configurations, respectively. Subscripted commas denote partial coordinate differentiation. The symbol := denotes equality by definition.

5.2 Materials

The focus of the present study is to model the deformation behavior of magnesium and boron carbide single crystals, assuming these to be elastically stiff and brittle. The low ductility of these materials can lead to large driving forces for dislocation glide, leading to other mechanisms such as phase transformations [395], deformation twinning [396], and fracture [397].

5.2.1 Magnesium

Having low density ($\sim$23% of steel and $\sim$66% of aluminum), high strength, and durability for a wide range of temperatures in high performance automotive and aerospace applications, magnesium and its alloys have attracted considerable attention in recent years [398, 399]. Mg alloys tend to be brittle due to the limited number of dislocation systems [400]. As a result of possessing low-symmetry crystallographic structure, twinning is the dominant deformation mode [401, 402] that results in transitions in the material behavior at high strain rates [403]. A previous study indicated that the formation of intersecting twins can improve the ductility of Mg alloys [404]. Therefore, understanding and predicting the twinning behavior during plastic deformation of magnesium is critical towards the realization of next-generation light-weight metallic materials for application in automotive and defense industries. To investigate twinning in magnesium, various techniques such as high-resolution transmission electron microscopy [286], visco-plastic self-consistent polycrystal models [405], elasto-plastic self-consistent polycrystal models [406], molecular dynamics simulations [241], crystal plasticity models [407], and quasi-static phase-field models [50] have been employed. In this study, the fracture and twinning behaviors of single crystal magnesium are studied using an advanced time-dependent phase-field theory by numerically solving engineering problems.

5.2.2 Boron Carbide

As a result of possessing hardness above 30 GPa, low density ($2.52\,{}^{g}/_{cm^3}$), and high Hugoniot elastic limit (17-20 GPa), boron carbide (B_4C) has received considerable attention in ballistic applications [408]. Due to its high melting point and thermal stability [409], extreme abrasion resistance [410], and high temperature semiconductivity [53], boron carbide excels in refractory, nuclear, and novel electronic applications, respectively; however, its performance is hindered by one or more of a number of inelastic deformation mechanisms, including deformation twinning [411], stress-induced phase transformations [412], and various fracture behaviors [68] when subjected to mechanical stresses exceeding their elastic limit. The key failure mechanisms in boron carbide (e.g., cleavage fracture and twinning) are commonly studied experimentally using numerous characterization techniques (e.g., transmission electron microscopy [413] and Raman spectroscopy [414]). Fracture in the form of shear failure, cavitation, and cleavage has been confirmed from atomic simulation results, either via first principles or molecular dynamics simulations [415, 416]. Finite deformation continuum models, such as cohesive zone models for fracture [417] and crystal plasticity [418] have also been used to investigate inelastic deformation in single and polycrystalline boron carbide. The present time-evolved phase-field model seeks to engineer the next generation of anisotropic boron carbide-based armor ceramics by understanding the important plastic deformation and brittle fracture mechanisms that govern its high rate performance.

5.3 Formulation

In this section, a time-dependent phase-field theory is developed for a solid body in the context of large and small strain theories based on thermodynamic laws with single twinning and fracture systems. The present approach extends that of Clayton and Knap [50, 362, 419, 420] to account for the time-evolution of order parameters towards

an equilibrium state and predicting the twinning and crack paths in anisotropic single crystal materials.

5.3.1 Order Parameters

The main desired feature of the proposed model is to introduce a separate order parameter η assigned to each material point $\mathbf{X}$ for the description of the twinning, which is equal to 0 in the parent elastic crystal and 1 in the twin. The twin boundary zone is determined by $\eta \in (0,1)$. The second order parameter, denoted by ξ, is used to represent fracture. $\xi = 0$ indicates undamaged material, $\xi = 1$ fully damaged material, and $\xi \in (0,1)$ partially degraded material. Both of these state variables are commonly assumed to be at least $\mathcal{C}^2$-continuous with respect to $\mathbf{X}$ according to the diffuse interface theory [421, 422].

5.3.2 Kinematics

An arbitrary multigrain body is considered in the reference ($\mathfrak{B}_0 \subset \mathbb{R}^d$, with $d \in \{1,2,3\}$), stress-relaxed intermediate, and current configuration ($\mathfrak{B} \subset \mathbb{R}^d$). The external boundaries of $\mathfrak{B}_0$ and $\mathfrak{B}$ are $\partial\mathfrak{B}_0$ and $\partial\mathfrak{B}$, respectively. We denote the traction (Neumann) boundary of $\mathfrak{B}_0$ by $\partial\mathfrak{B}_{0_{\mathcal{N}i}}$ and the displacement (Dirichlet) boundary by $\partial\mathfrak{B}_{0_{\mathcal{D}i}}$. The same boundaries in the current configurations are $\partial\mathfrak{B}_{\mathcal{N}i}$ for the traction and $\partial\mathfrak{B}_{\mathcal{D}i}$ for the displacement (see Figure 5.1).

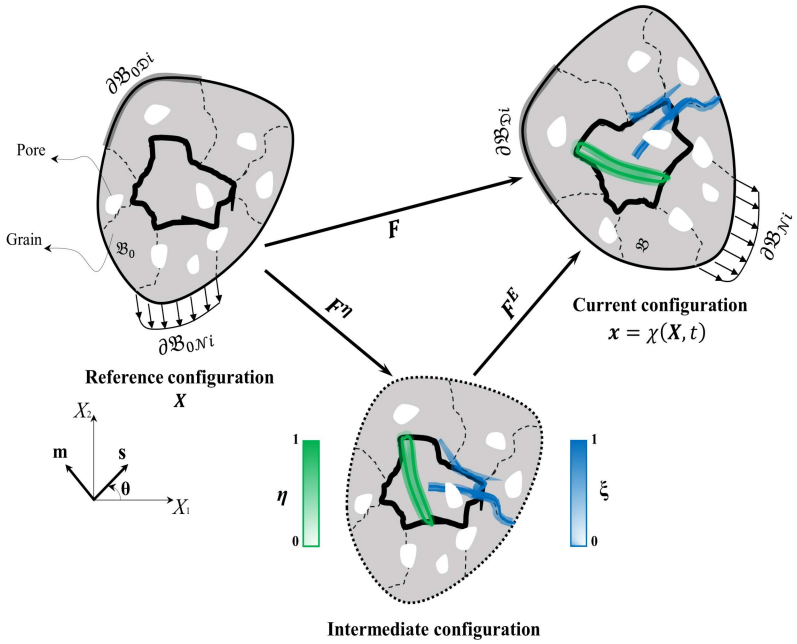

Figure 5.1: Multiplicative decomposition of the deformation gradient into elastic $\boldsymbol{F}^{\mathrm{E}}$ and irreversible plastic $\boldsymbol{F}^{\eta}$ parts with corresponding configurations. The reference stress-free configuration $\mathfrak{B}_0$, the deformed configuration $\mathfrak{B}$, and an arbitrary intermediate configuration $\mathfrak{B}_*$ of a polycrystal material are shown. The Neumann and Dirichlet boundary conditions corresponding to each configuration are also illustrated. Two separate order parameters for fracture ξ (blue color) and twinning η (green color) are also considered. (For interpretation of the references to color in this figure, the reader is referred to the web version of this article.)

The motion of solid material with twinning and fracture will be described by a vector function $\mathbf{x} = \boldsymbol{\mathcal{X}}(\mathbf{X}, t)$, where $\mathbf{x}$ and $\mathbf{X}$ are the positions of points at time t in material $\mathfrak{B}_0$, and spatial $\mathfrak{B}$, configurations, respectively. Let $\mathbf{u}(\mathbf{X}, t) = \mathbf{x}(\mathbf{X}, t) - \mathbf{X}$ denote the displacement of a point $\mathbf{X}$ at time t. The displacement field satisfies time-dependent Dirichlet boundary conditions $u_i(\mathbf{X}, t) = g_i(\mathbf{X}, t)$, on $\partial\mathfrak{B}_{\mathcal{D}i}$, and time-dependent Neumann boundary conditions on $\partial\mathfrak{B}_{\mathcal{N}i}$. The deformation gradient is defined as $\boldsymbol{F} = \nabla_0 \mathbf{x} = \frac{\partial x_i}{\partial X_j} \boldsymbol{e_i} \otimes \boldsymbol{e_j}$. The total deformation gradient in the fully large-strain formulation is a second order tensor multiplicatively decomposed as

$$F_{ij} = F^{\mathrm{E}}_{ik} F^{\eta}_{kj}, \tag{5.1}$$

where $\boldsymbol{F}^{\mathrm{E}}$ is the recoverable elastic deformation conjugated to the applied stress, and $\boldsymbol{F}^{\eta}$ is the irreversible deformation associated with structural defects, such as twinning,

evolving within the material. In contrast to $\boldsymbol{F}$ which always satisfies compatibility conditions $\nabla \times \boldsymbol{F} = \boldsymbol{0}$, the deformation maps $\boldsymbol{F}^{\mathrm{E}}$ and $\boldsymbol{F}^{\eta}$ are generally not integrable as a result of existing crystal defects [423, 424]. Additional structural changes can be included in this theory for representation of other defects, such as point defects [425] or dislocation slips [257]. In small deformations, the multiplicative decomposition Eq 5.1, is replaced by

$$\boldsymbol{\varepsilon}_{ij} = \boldsymbol{\varepsilon}^{\mathrm{E}}_{ij} + \boldsymbol{\varepsilon}^{\eta}_{ij}, \tag{5.2}$$

where $\boldsymbol{\varepsilon}^{\mathrm{E}}$ is the elastic distortion and $\boldsymbol{\varepsilon}^{\eta}$ is the twinning shear-related deformation. The kinematics for twinning in simple shear [263] is given as

$$\begin{aligned} \boldsymbol{\varepsilon}^{\eta} &= \phi(\eta)\gamma_0 \boldsymbol{s} \otimes \boldsymbol{m}; \quad \varepsilon^{\eta}_{ij} = \phi(\eta)\gamma_0 s_i m_j; \\ \boldsymbol{F}^{\eta}(\eta) &= \boldsymbol{I} + \phi(\eta)\gamma_0 \boldsymbol{s} \otimes \boldsymbol{m}; \quad F^{\eta}_{ij} = \delta_{ij} + \phi(\eta)\gamma_0 s_i m_j, \end{aligned} \tag{5.3}$$

where $\boldsymbol{s}$ and $\boldsymbol{m}$ are the orthogonal unit vectors (in initial configuration) in the directions of twinning and normal to the twinning plane, respectively; and γ_0 is the magnitude of the maximum twinning shear. The interpolation function $\phi(\eta)$ is obtained from a general representative function $\varphi(a, \eta)$ within a fourth-degree potential defined as [264]

$$\varphi(a, \eta) = a\eta^2(1-\eta)^2 + \eta^3(4 - 3\eta), \tag{5.4}$$

where a is a constant parameter, and to ensure that $\varphi(a, \eta)$ is a monotonous function, a should be chosen between 0 and 6. The interpolation function $\varphi(a, \eta)$ satisfies the conditions $\varphi(a, 0) = 0$, $\varphi(a, 1) = 1$, $\frac{\partial \varphi(a,0)}{\partial \eta} = \frac{\partial \varphi(a,1)}{\partial \eta} = 0$. $\phi(\eta) = \varphi(3, \eta) = \eta^2(3 - 2\eta)$. For $a = 0$, $\phi(\eta) = \varphi(3, \eta) = \eta^2(3 - 2\eta)$ which obeys the antisymmetry condition, i.e., $\phi(1 - \eta) = 1 - \phi(\eta)$. We define the Jacobian determinant, $J = \det \boldsymbol{F} = \det \boldsymbol{F}^{\mathrm{E}} := \frac{dV}{dV_0}$, where dV_0 and dV are the volumes of an infinitesimal element in material and spatial configurations, respectively. This indicates that $\det \boldsymbol{F}^{\eta} = 1$, which means that twinning preserves the volume and mass density of the material elements. The Green–

Lagrange total and elastic strains in large and small deformations are introduced as

$$\boldsymbol{E} = \frac{1}{2}(\boldsymbol{C} - \boldsymbol{I}); \quad E_{ij} = \frac{1}{2}(C_{ij} - \delta_{ij}), \tag{5.5}$$

$$\boldsymbol{E}^{\mathrm{E}} = \frac{1}{2}(\boldsymbol{C}^{E} - \boldsymbol{I}); \quad E^{\mathrm{E}}_{ij} = \frac{1}{2}(C^{E}_{ij} - \delta_{ij}), \tag{5.6}$$

$$\boldsymbol{\varepsilon}^{\mathrm{E}} = \frac{1}{2}\left[\nabla \boldsymbol{u} + (\nabla \boldsymbol{u})^{T} - \phi(\eta)\gamma_0 \left(\boldsymbol{s} \otimes \boldsymbol{m} + \boldsymbol{m} \otimes \boldsymbol{s}\right)\right]; \tag{5.7}$$

$$\varepsilon^{\mathrm{E}}_{ij} = \frac{1}{2}\left[u_{i,j} + u_{j,i} - \phi(\eta)\gamma_0 \left(s_i m_j + m_i s_j\right)\right],$$

respectively, where $\boldsymbol{C} = \boldsymbol{F}^{T} \cdot \boldsymbol{F}$ $(C_{ij} = F_{ki}F_{kj})$ and $\boldsymbol{C}^{\mathrm{E}} = (\boldsymbol{F}^{\mathrm{E}})^{T} \cdot \boldsymbol{F}^{\mathrm{E}}$ $\left(C^{\mathrm{E}}_{ij} = F^{\mathrm{E}}_{ki}F^{\mathrm{E}}_{kj}\right)$ are the right Cauchy–Green total strain and elastic strain tensors, respectively. Considering twinning as an isochoric process results in $\boldsymbol{C} = \boldsymbol{C}^{\mathrm{E}}$ and $J = \sqrt{\det \boldsymbol{C}^{\mathrm{E}}}$.

5.3.3 Laws of Thermodynamics and Constitutive Equations

For an arbitrary volume V_0 (or V) with an external surface $\boldsymbol{S_0}$ (or $\boldsymbol{S}$) and unit external normal $\boldsymbol{n}_0$ (or $\boldsymbol{n}$) in the undeformed (or deformed) configuration $\mathfrak{B}_0$ (or $\mathfrak{B}$), the first law of thermodynamics leads to the global energy balance equation reads (in indicial notation)

$$\int_{S_0} (p_{0_i} v_i - h_{0_i} n_{0_i}) dS_0 - \frac{d}{dt}\int_{V_0} \rho_0 (U + \frac{1}{2} v_i v_i) dV_0 + \int_{V_0} \rho_0 (f_i v_i + r) dV_0 = 0, \tag{5.8}$$

$$\int_{S} (p_i v_i - h_i n_i) dS - \frac{d}{dt}\int_{V} \rho (U + \frac{1}{2} v_i v_i) dV + \int_{V} \rho (f_i v_i + r) dV = 0, \tag{5.9}$$

where $p_{0_i} = n_{0_j} P_{ji}$ $(p_i = n_j \sigma_{ji})$ is the traction vector on the external surface $\boldsymbol{S_0}$ (or $\boldsymbol{S}$), $\boldsymbol{P}$ (or $\boldsymbol{\sigma}$) is the first nonsymmetric Piola–Kirchhoff stress tensor (or the symmetric Cauchy stress tensor), $\boldsymbol{v}$ is the particle velocity, $\boldsymbol{h}_0$ (or $\boldsymbol{h}$) is the heat flux , U is the specific internal energy (per unit mass), ρ_0 (or ρ) is the mass density in the material (or spatial) configuration, $\boldsymbol{f}$ is the body force per unit mass, and r is the heat source per unit mass per unit time. The second law of thermodynamics is the combination of the global entropy balance equation with the Clausius–Duhem inequality for the

whole volume V_0 (or V)

$$\frac{d}{dt}\int_{V_0}\rho_0 s dV_0 - \int_{V_0}\rho_0\frac{r}{\theta}dV_0 + \int_{S_0}\frac{1}{\theta}h_{0_i}n_{0_i}dS_0 := S_{\rm i} \geq 0, \tag{5.10}$$

$$\frac{d}{dt}\int_{V}\rho s dV - \int_{V}\rho\frac{r}{\theta}dV + \int_{S}\frac{1}{\theta}h_i n_i dS := S_{\rm si} \geq 0, \tag{5.11}$$

where $S_{\rm i}$ (or $S_{\rm si}$) is the total entropy production rate in the initial (or current) configuration, s is the specific entropy, and θ is the temperature. The first and second law of thermodynamics can be transformed to the following volume integrals by using the balance of linear momentum and the Gauss theorem

$$\int_{V_0}\left(P_{ij}\dot{F}_{ji} - \rho_0\dot{U} - \left(h_{0_i}\right)_{,0i} + \rho_0 r\right)dV_0 = 0, \tag{5.12}$$

$$S_{\rm i} := \int_{V_0}\bar{S}_{\rm i}dV_0 \geq 0, \quad \bar{S}_{\rm i} = \rho_0\dot{s} - \rho_0\frac{r}{\theta} + \left(\frac{h_{0_i}}{\theta}\right)_{,0i}, \tag{5.13}$$

$$\int_{V}\left(\sigma_{ij}\dot{\varepsilon}_{ij} - \rho\dot{U} - \left(h_i\right)_{,i} + \rho r\right)dV = 0, \tag{5.14}$$

$$S_{\rm si} := \int_{V}\bar{S}_{\rm si}dV \geq 0, \quad \bar{S}_{\rm si} = \rho\dot{s} - \rho\frac{r}{\theta} + \left(\frac{h_i}{\theta}\right)_{,i}, \tag{5.15}$$

where $\left(\frac{h_{0_i}}{\theta}\right)_{,0i} = \frac{1}{\theta}\left(h_{0_i}\right)_{,0i} - \frac{1}{\theta^2}h_{0_i}\theta_{,0i}$ $\left(\left(\frac{h_i}{\theta}\right)_{,i} = \frac{1}{\theta}\left(h_i\right)_{,i} - \frac{1}{\theta^2}h_i\theta_{,i}\right)$. Multiplying Eqs 5.13 and 5.15 by θ, the global dissipation rate in the undeformed (or deformed) state is introduced as

$$\bar{\mathfrak{D}} := \int_{V_0}\left(\rho_0\theta\dot{s} - \rho_0 r + \theta\left(\frac{h_{0_i}}{\theta}\right)_{,0i}\right)dV_0 \geq 0, \tag{5.16}$$

$$\bar{\mathfrak{D}}_{\rm s} := \int_{V}\left(\rho\theta\dot{s} - \rho r + \theta\left(\frac{h_i}{\theta}\right)_{,i}\right)dV \geq 0. \tag{5.17}$$

Combining Eqs 5.12 and 5.14 with Eqs 5.16 and 5.17, the following dissipation inequalities in the reference (or current) configuration are derived as

$$\mathfrak{D} = \int_{V_0}\left(P_{ij}\dot{F}_{ji} - \rho_0\dot{U} + \rho_0\theta\dot{s} - \frac{1}{\theta}h_{0_i}\theta_{,0i}\right)dV_0 \geq 0, \tag{5.18}$$

$$\mathfrak{D}_{\rm s} = \int_{V}\left(\sigma_{ij}\dot{\varepsilon}_{ij} - \rho\dot{U} + \rho\theta\dot{s} - \frac{1}{\theta}h_i\theta_{,i}\right)dV \geq 0. \tag{5.19}$$

The inequalities 5.18 and 5.19 can be split into the Planck's inequalities ($\mathfrak{D}_{\mathrm{m}}, \mathfrak{D}_{\mathrm{sm}}$) and the Fourier's inequalities ($\mathfrak{D}_{\mathrm{t}}, \mathfrak{D}_{\mathrm{st}}$) as

$$\mathfrak{D}_{\mathrm{m}} = \int_{V_0} \left(P_{ij}\dot{F}_{ji} - \rho_0 \dot{U} + \rho_0 \theta \dot{s} \right) dV_0 \geq 0; \quad \mathfrak{D}_{\mathrm{t}} = \int_{V_0} - \left(\frac{1}{\theta} h_{0_i} \theta_{,0i} \right) dV_0 \geq 0, \tag{5.20}$$

$$\mathfrak{D}_{\mathrm{sm}} = \int_{V} \left(\sigma_{ij}\dot{\varepsilon}_{ij} - \rho \dot{U} + \rho \theta \dot{s} \right) dV \geq 0; \quad \mathfrak{D}_{\mathrm{st}} = \int_{V} - \left(\frac{1}{\theta} h_i \theta_{,i} \right) dV \geq 0. \tag{5.21}$$

By introducing the specific Helmholtz free energy $\psi = U - \theta s$ and substituting it into Eqs 5.20(1) and 5.21(1), and using temperature as an independent thermodynamic parameter instead of entropy, the final dissipation inequalities are obtained as

$$\mathfrak{D}_{\mathrm{m}} = \int_{V_0} \left(P_{ij}\dot{F}_{ji} - \rho_0 \dot{\psi} - \rho_0 s \dot{\theta} \right) dV_0 \geq 0, \tag{5.22}$$

$$\mathfrak{D}_{\mathrm{sm}} = \int_{V} \left(\sigma_{ij}\dot{\varepsilon}_{ij} - \rho \dot{\psi} - \rho s \dot{\theta} \right) dV \geq 0. \tag{5.23}$$

Here, we assume that the Helmholtz free energy exhibits the following functional dependency

$$\psi = \psi(\boldsymbol{F}^{\mathrm{E}}, \eta, \nabla_0 \eta, \theta, \xi, \nabla_0 \xi), \tag{5.24}$$

$$\psi_{\mathrm{s}} = \psi_s(\boldsymbol{\varepsilon}^{\mathrm{E}}, \eta, \nabla \eta, \theta, \xi, \nabla \xi), \tag{5.25}$$

in the initial and the current configurations, respectively. The dependencies on position and temperature gradient have been neglected because of objectivity. After the substitution of the rate of free energy

$$\dot{\psi} = \frac{\partial \psi}{\partial F^{\mathrm{E}}_{ij}} \dot{F}^{\mathrm{E}}_{ij} + \frac{\partial \psi}{\partial \eta} \dot{\eta} + \frac{\partial \psi}{\partial \eta_{,0i}} \dot{\overline{\eta_{,0i}}} + \frac{\partial \psi}{\partial \theta} \dot{\theta} + \frac{\partial \psi}{\partial \xi} \dot{\xi} + \frac{\partial \psi}{\partial \xi_{,0i}} \dot{\overline{\xi_{,0i}}}, \tag{5.26}$$

$$\dot{\psi}_{\mathrm{s}} = \frac{\partial \psi_{\mathrm{s}}}{\partial \varepsilon^{\mathrm{E}}_{ij}} \dot{\epsilon}^{\mathrm{E}}_{ij} + \frac{\partial \psi_s}{\partial \eta} \dot{\eta} + \frac{\partial \psi_s}{\partial \eta_{,i}} \dot{\overline{\eta_{,i}}} + \frac{\partial \psi_s}{\partial \theta} \dot{\theta} + \frac{\partial \psi_s}{\partial \xi} \dot{\xi} + \frac{\partial \psi_s}{\partial \xi_{,i}} \dot{\overline{\xi_{,i}}}, \tag{5.27}$$

into Eqs 5.22 and 5.23, one obtains

$$\begin{aligned}
\mathfrak{D}_{\mathrm{m}} &= \int_{V_0}\left[\left(P_{ik}F^{\eta}_{jk}-\rho_0\frac{\partial\psi}{\partial F^{\mathrm{E}}_{ij}}\right)\dot{F}^{\mathrm{E}}_{ji}+\left(P_{ij}\frac{\partial F^{\eta}_{ki}}{\partial\eta}F^{\mathrm{E}}_{jk}-\rho_0\frac{\partial\psi}{\partial\eta}\right)\dot{\eta}\right. \\
&\quad -\rho_0\left(s+\frac{\partial\psi}{\partial\theta}\right)\dot{\theta}-\rho_0\frac{\partial\psi}{\partial\eta_{,0i}}\dot{\overline{\eta_{,0i}}}+\left(P_{ij}\frac{\partial F^{\xi}_{ki}}{\partial\eta}F^{\mathrm{E}}_{jk}-\rho_0\frac{\partial\psi}{\partial\xi}\right)\dot{\xi} \\
&\quad \left.-\rho_0\frac{\partial\psi}{\partial\xi_{,0i}}\dot{\overline{\xi_{,0i}}}\right]dV_0\geq 0, \qquad (5.28)\\
\mathfrak{D}_{\mathrm{sm}} &= \int_{V}\left[\left(\sigma_{ij}-\rho\frac{\partial\psi_s}{\partial\varepsilon^{\mathrm{E}}_{ij}}\right)\dot{\varepsilon}^{\mathrm{E}}_{ij}+\left(\sigma_{ij}\frac{\partial\varepsilon^{\eta}_{ij}}{\partial\eta}-\rho\frac{\partial\psi_s}{\partial\eta}\right)\dot{\eta}\right. \\
&\quad -\rho\left(s+\frac{\partial\psi}{\partial\theta}\right)\dot{\theta}-\rho\frac{\partial\psi}{\partial\eta_{,i}}\dot{\overline{\eta_{,i}}}+\left(\sigma_{ij}\frac{\partial\varepsilon^{\xi}_{ij}}{\partial\eta}-\rho\frac{\partial\psi_s}{\partial\xi}\right)\dot{\xi} \\
&\quad \left.-\rho\frac{\partial\psi}{\partial\xi_{,i}}\dot{\overline{\xi_{,i}}}\right]dV\geq 0. \qquad (5.29)
\end{aligned}$$

Assuming independency of the dissipation rate on $\dot{F}^{\mathrm{E}}_{ji}$, $\dot{\varepsilon}^{\mathrm{E}}_{ij}$, and $\dot{\theta}$ leads to the expressions for the elasticity law and entropy in the material and spatial configurations

$$\sigma_{ij}=\rho\frac{\partial\psi_s}{\partial\varepsilon^{\mathrm{E}}_{ij}};\quad P_{ik}F^{\eta}_{jk}=\rho_0\frac{\partial\psi}{\partial F^{\mathrm{E}}_{ij}}=\rho_0F^{\mathrm{E}}_{in}\frac{\partial\psi}{\partial E^{\mathrm{E}}_{nj}};\quad s=-\frac{\partial\psi}{\partial\theta}. \qquad (5.30)$$

For homogeneous materials, by considering the terms proportional to $\dot{\eta}$, $\dot{\eta}_{,0i}$ (or $\dot{\eta}_{,i}$), $\dot{\xi}$, and $\dot{\xi}_{,0i}$ (or $\dot{\xi}_{,i}$) in Eqs 5.28 and 5.29, and using the permutability of time and space differentiation in the reference (or current) configuration along with the differentiation product rule and the Gauss theorem, the dissipation rate becomes

$$\begin{aligned}
\mathfrak{D}_{\mathrm{m}} &= \int_{V_0}\left[\left(F^{\mathrm{E}}_{ki}P_{kj}\frac{\partial F^{\eta}_{ji}}{\partial\eta}-\rho_0\frac{\partial\psi}{\partial\eta}+\rho_0\left(\frac{\partial\psi}{\partial\eta_{,0i}}\right)_{,0i}\right)\dot{\eta}\right. \\
&\quad \left.+\left(F^{\mathrm{E}}_{ki}P_{kj}\frac{\partial F^{\xi}_{ji}}{\partial\xi}-\rho_0\frac{\partial\psi}{\partial\xi}+\rho_0\left(\frac{\partial\psi}{\partial\xi_{,0i}}\right)_{,0i}\right)\dot{\xi}\right]dV_0 \\
&\quad -\int_{S_0}\left[\left(\rho_0n_{0i}\frac{\partial\psi}{\partial\eta_{,0i}}\right)\dot{\eta}+\left(\rho_0n_{0i}\frac{\partial\psi}{\partial\xi_{,0i}}\right)\dot{\xi}\right]dS_0\geq 0, \qquad (5.31)\\
\mathfrak{D}_{\mathrm{sm}} &= \int_{V}\left[\left(\sigma_{ij}\frac{\partial\varepsilon^{\eta}_{ij}}{\partial\eta}-\rho\frac{\partial\psi_s}{\partial\eta}+\rho\left(\frac{\partial\psi_s}{\partial\eta_{,i}}\right)_{,i}\right)\dot{\eta}\right. \\
&\quad \left.+\left(\sigma_{ij}\frac{\partial\varepsilon^{\xi}_{ij}}{\partial\xi}-\rho\frac{\partial\psi_s}{\partial\xi}+\rho\left(\frac{\partial\psi_s}{\partial\xi_{,i}}\right)_{,i}\right)\dot{\xi}\right]dV \\
&\quad -\int_{S}\left[\left(\rho n_i\frac{\partial\psi_s}{\partial\eta_{,i}}\right)\dot{\eta}+\left(\rho n_i\frac{\partial\psi_s}{\partial\xi_{,i}}\right)\dot{\xi}\right]dS\geq 0, \qquad (5.32)
\end{aligned}$$

$$\rho_0 n_{0i} \frac{\partial \psi}{\partial \eta_{,0i}} = \rho n_i \frac{\partial \psi_s}{\partial \eta_{,i}} = 0, \tag{5.33}$$

$$\rho_0 n_{0i} \frac{\partial \psi}{\partial \xi_{,0i}} = \rho n_i \frac{\partial \psi_s}{\partial \xi_{,i}} = 0. \tag{5.34}$$

Then, the assumed mutually independent dissipation inequalities for the fracture and twin order parameters can be expressed in the following decoupled form

$$\mathfrak{D}_{\mathrm{m}_\eta} = \int_{V_0} \mathfrak{X}_\eta \dot{\eta} dV_0 \geq 0; \quad \mathfrak{D}_{\mathrm{m}_\xi} = \int_{V_0} \mathfrak{X}_\xi \dot{\xi} dV_0 \geq 0, \tag{5.35}$$

$$\mathfrak{D}_{\mathrm{sm}_\eta} = \int_{V} \mathfrak{X}_{s\eta} \dot{\eta} dV \geq 0; \quad \mathfrak{D}_{\mathrm{sm}_\xi} = \int_{V} \mathfrak{X}_{s\xi} \dot{\xi} dV \geq 0, \tag{5.36}$$

where

$$\begin{aligned}
\mathfrak{X}_\eta : &= P_{ki} F^{\mathrm{E}}_{kj} \frac{\partial F^\eta_{ij}}{\partial \eta} - \rho_0 \frac{\partial \psi}{\partial \eta} + \rho_0 \left(\frac{\partial \psi}{\partial \eta_{,0i}} \right)_{,0i}; \qquad (5.37)\\
\mathfrak{X}_\xi : &= P_{ki} F^{\mathrm{E}}_{kj} \frac{\partial F^\eta_{ij}}{\partial \xi} - \rho_0 \frac{\partial \psi}{\partial \xi} + \rho_0 \left(\frac{\partial \psi}{\partial \xi_{,0i}} \right)_{,0i},\\
\mathfrak{X}_{\mathrm{s}\eta} : &= \sigma_{ij} \frac{\partial \varepsilon^\eta_{ij}}{\partial \eta} - \rho \frac{\partial \psi_s}{\partial \eta} + \rho \left(\frac{\partial \psi_s}{\partial \eta_{,i}} \right)_{,i}; \qquad (5.38)\\
\mathfrak{X}_{\mathrm{s}\xi} : &= \sigma_{ij} \frac{\partial \varepsilon^\xi_{ij}}{\partial \xi} - \rho \frac{\partial \psi_s}{\partial \xi} + \rho \left(\frac{\partial \psi_s}{\partial \xi_{,i}} \right)_{,i},
\end{aligned}$$

are the thermodynamic forces conjugate to $\dot{\eta}$ and $\dot{\xi}$ in the material and spatial configurations, respectively. In the case of local relationships between the driving forces and time evolution corresponding to each order parameter, Eqs 5.35 and 5.36 give rise to

$$\rho_0 \mathcal{D}_\eta = \mathfrak{X}_\eta \dot{\eta} dV_0 \geq 0; \quad \rho_0 \mathcal{D}_\xi = \mathfrak{X}_\xi \dot{\xi} dV_0 \geq 0, \tag{5.39}$$

$$\rho \mathcal{D}_{\mathrm{s}\eta} = \mathfrak{X}_{\mathrm{s}\eta} \dot{\eta} dV \geq 0; \quad \rho \mathcal{D}_{\mathrm{s}\xi} = \mathfrak{X}_{\mathrm{s}\xi} \dot{\xi} dV \geq 0. \tag{5.40}$$

In order to satisfy the above inequalities, one can assume a linear approximation between the time rate of change of order parameters and the driving forces, and, thus, Eqs 5.39 and 5.40 transform to the Ginzburg–Landau equations for both state variables as

$$\dot{\eta}_j = \mathcal{L}^\eta_{ji} \mathfrak{X}^\eta_i, \tag{5.41}$$

$$\dot{\xi}_j = \mathcal{L}^\xi_{ji} \mathfrak{X}^\xi_i, \tag{5.42}$$

where $\mathcal{L}^{\eta}_{ji} = \mathcal{L}^{\eta}_{ij}$ and $\mathcal{L}^{\xi}_{ji} = \mathcal{L}^{\xi}_{ij}$ are the positive definite kinetic coefficients related to the twinning and fracture mechanisms.

5.3.4 Free Energy and Kinetic Equations

Considering the mechanical loads, the Helmholtz free energy per unit undeformed (or deformed) volume is defined in the following form

$$\psi(\boldsymbol{F}^{\mathrm{E}}, \eta, \nabla_0\eta, \xi, \nabla_0\xi) = \psi^{e}\left(\boldsymbol{C}^{\mathrm{E}}(\boldsymbol{F}, \eta), \eta, \xi\right) + \psi^{\nabla}(\eta, \xi, \nabla_0\eta, \nabla_0\xi), \quad (5.43)$$

$$\psi_s(\boldsymbol{\varepsilon}, \eta, \nabla\eta, \xi, \nabla\xi) = \psi^{e}_{s}\left(\boldsymbol{\varepsilon}^{\mathrm{E}}(\nabla\boldsymbol{u}, \eta), \eta, \xi\right) + \psi^{\nabla}_{s}(\eta, \xi, \nabla\eta, \nabla\xi), \quad (5.44)$$

where ψ^{e}(or ψ^{e}_s) and ψ^{∇}(or ψ^{∇}_s) are the elastic strain energy and the interfacial energy per unit reference (or current) volume, respectively. In geometrically nonlinear theory, the strain energy density for fracture and twinning is expressed within the framework of compressible neo-Hookean elasticity as a result of describing the usual increase in tangent bulk modulus with increasing compressive pressure when large volume changes are involved [50, 267]

$$\psi^{\mathrm{e}} = \frac{\mu}{2}(I_{C^{\mathrm{E}}_{ij}} - 3) - \mu \ln J + \frac{\lambda}{2}(\ln J)^2, \quad (5.45)$$

where $I_{\boldsymbol{C}^{\mathrm{E}}} = C^{\mathrm{E}}_{ii}$, and $J^2 = \epsilon_{ijk} C^{\mathrm{E}}_{i1} C^{\mathrm{E}}_{j2} C^{\mathrm{E}}_{k3}$, with ϵ_{ijk} being the permutation symbol. For small strains, the following isotropic linear elasticity strain energy density is used for simplicity and computational efficiency

$$\psi^{\mathrm{e}}_s = \frac{1}{2}\lambda(\nabla\cdot\boldsymbol{u})^2 + \frac{1}{4}\mu \,\mathrm{tr}\left\{\left[\left(\nabla\boldsymbol{u} + (\nabla\boldsymbol{u})^T\right)\right]^2\right\}. \quad (5.46)$$

The constants λ and μ are material coefficients with equal dependency on ξ as

$$k = \lambda + \frac{2}{3}\mu; \;\; \mu = \mu_0\hat{\phi}(\xi); \;\; \lambda = \lambda_0\hat{\phi}(\xi). \quad (5.47)$$

In Eq 5.47, $\hat{\phi}(\xi) = \zeta + (1-\zeta)(1-\xi)^2$ is a degradation function, and k is the bulk modulus. The constant ζ ensures a minimal residual stiffness for fully fractured materials. The quadratic degradation of elastic stiffness has likewise been used in a number

of other phase-field and gradient damage models [426–428]; however, the reflection or rotation of the reference frame of the crystal lattice commensurate with twinning should be taken into account for anisotropic elastic constants [266]. Considering this, the elastic strain energy density in the reference frame is written as

$$\psi^e = \frac{1}{2} E^{\mathrm{E}}_{ij} \mathcal{C}_{\mathfrak{e}_{ijkl}} E^{\mathrm{E}}_{kl}; \;\; \mathcal{C}_{\mathfrak{e}_{ijkl}} = \frac{\partial^2 \psi^e}{\partial E^{\mathrm{E}}_{ij} \partial E^{\mathrm{E}}_{kl}}. \tag{5.48}$$

The tangent elastic modulus at each material point is then determined using

$$\mathcal{C}_{\mathfrak{e}} = \mathcal{C}_{\mathfrak{e}}(0) + (\mathcal{C}_{\mathfrak{e}}(1) - \mathcal{C}_{\mathfrak{e}}(0))\, \phi(\eta), \tag{5.49}$$

where $\mathcal{C}_{\mathfrak{e}}(0)$ denotes the elasticity tensor of the parent phase. For the twin phase, $\mathcal{C}_{\mathfrak{e}}(1)$ is expressed in index form as

$$\mathcal{C}_{ijkl}(1) = \mathcal{Q}_{im} \mathcal{Q}_{jn} \mathcal{Q}_{ko} \mathcal{Q}_{lp} \mathcal{C}_{mnop}(0), \tag{5.50}$$

where $\boldsymbol{\mathcal{Q}}$ is the reorientation matrix associated with twinning within a centrosymmetric structure [266]

$$\mathcal{Q}_{ij} = \begin{cases} 2m_i m_j - \delta_{ij} & \text{type I twins,} \\ 2s_i s_j - \delta_{ij} & \text{type II twins.} \end{cases} \tag{5.51}$$

Type I and type II twins differ in reflections or rotations of the lattice vectors in the twin and parent phase. For the interfacial energy per unit reference (or current) volume, one can write the following specific form

$$\begin{aligned} \psi^{\nabla}(\eta, \xi, \nabla_0 \eta, \nabla_0 \xi) = \psi^{\nabla}_{\mathrm{s}}(\eta, \xi, \nabla \eta, \nabla \xi) \;\; &= \;\; \psi^{\nabla}_1(\eta, \xi) + \psi^{\nabla}_2(\eta, \xi, \nabla \eta) + \\ &\quad \psi^{\nabla}_3(\xi) + \psi^{\nabla}_4(\eta, \xi, \nabla \xi). \end{aligned} \tag{5.52}$$

The first term consists of a standard double-well potential [268, 269, 293]

$$\psi^{\nabla}_1(\eta, \xi) = A \eta^2 (1 - \eta)^2 \, \iota(\xi), \tag{5.53}$$

where $A = 12 \frac{\Gamma}{l}$ characterizes the energy barrier between two stable phases (minima) and this is related to the twin boundary surface energy Γ and the twin boundary

thickness l; $\iota(\xi)$ is a coupling degradation function which degrades with the fracture parameter ξ. It is assumed that $\iota(\xi) = \hat{\phi}(\xi)$, meaning that the twin boundary energy and the elastic shear modulus degrade with damage according to the same quadratic function. The regularization length is taken as the cohesive process zone for shear failure [429]

$$l = \frac{16\pi\Upsilon}{\mu_0\left(1-\nu_0\right)}, \tag{5.54}$$

where Υ is the fracture surface energy, $\mu_0/2\pi$ is the theoretical shear failure strength, and $\nu_0 = (3k_0 - 2\mu_0)/(6k_0 + 2\mu_0)$ [430]. The second term on the right-hand side of Eq 5.52 follows from the Cahn–Hilliard formalism [421]

$$\psi_2^{\nabla}(\xi, \nabla\eta) = \kappa_{ij}\eta_{,i}\eta_{,j}; \quad \kappa_{ij} = \kappa_0\iota(\xi)\delta_{ij}; \quad \kappa_0 = \frac{3\Gamma l}{4}, \tag{5.55}$$

where κ_{ij} and κ_0 are a diagonal tensor of rank two and gradient energy parameter, respectively.

For cleavage fracture, which is the primary failure mode in boron carbide,

$$\psi_3^{\nabla}(\xi) = \mathcal{B}\xi^2, \tag{5.56}$$

$$\psi_4^{\nabla}(\nabla\xi) = \omega_{ij}\xi_{,i}\xi_{,j}; \quad \omega_{ij} = \omega_0\left[\delta_{ij} + \beta\left(\delta_{ij} - M_iM_j\right)\right], \tag{5.57}$$

where $\mathcal{B} = \Upsilon/h$ is the ratio of fracture surface energy and crack thickness, $\omega_0 = \Upsilon h$ is a material constant, β is the cleavage anisotropy factor, and $\boldsymbol{M}$ is the orientation of the cleavage plane which is known a priori [377, 378]. The cleavage plane can be a plane of low surface energy or low intrinsic strength in the crystal [431]. The parameter β penalizes fracture on planes not normal to $\boldsymbol{M}$ so that $\beta = 0$ results in isotropic damage. Eq 5.56 has been used in a number of recent continuum models of fracture as a result of its ability to converge to the correct surface energy of a singular surface when the twin boundary thickness tends to zero [387, 432]. Transient, rate effects, and path dependence of solutions could be included by substituting the expressions

for the free energy in Eqs 5.41 and 5.42 dictating their evolution in the material

$$\begin{aligned}
\dot{\eta}_j &= -\mathcal{L}^{\eta}_{ji}\left\{\frac{\partial\psi^{\mathrm{e}}}{\partial\eta_i}+\frac{\partial\psi^{\nabla}}{\partial\eta_i}-\left(\frac{\partial\psi^{\nabla}}{\partial\eta_{,0i}}\right)_{,0i}\right\} = -\mathcal{L}^{\eta}_{ji}\left\{2A\eta_i\left(1-3\eta_i+2\eta_i^2\right)\times\right. \qquad (5.58)\\
&\quad \hat{\imath}(\xi_i)-\phi'(\eta_i)\gamma_0\left[\mu\delta_{ij}+\left(\lambda\ln J-\mu\right)\left(C^{\mathrm{E}}_{ij}\right)^{-1}\right]\left[C^{\mathrm{E}}_{ij}s_im_j\right]\\
&\quad \left.-2\kappa_0\left[\hat{\imath}(\xi)\eta_{,ij}+\hat{\imath}'(\xi_i)\xi_{,i}\eta_{,j}\right]\right\},\\
\dot{\xi}_j &= -\mathcal{L}^{\xi}_{ji}\left\{\frac{\partial\psi^{\mathrm{e}}}{\partial\xi_i}+\frac{\partial\psi^{\nabla}}{\partial\xi_i}-\left(\frac{\partial\psi^{\nabla}}{\partial\xi_{,0i}}\right)_{,0i}\right\} = -\mathcal{L}^{\xi}_{ji}\left\{2\mathcal{B}\xi_i\left[\kappa_0|\eta_{,0i}|^2+A\eta_i^2\left(1-\eta_i\right)^2\right]\times\right.\\
&\quad \hat{\imath}'(\xi_i)-2\omega_0\left[\xi_{,ij}+\beta\left(\xi_{,ij}-M_iM_je_i\frac{\partial}{\partial x_i}\left(\xi_{,j}\right)\right)\right] \qquad (5.59)\\
&\quad \left.+\frac{1}{2}\frac{\partial\lambda}{\partial\xi_i}\left(\ln J\right)^2-\frac{1}{2}\frac{\partial\mu}{\partial\xi_i}\left(2\ln J-C^{\mathrm{E}}_{ii}+3\right)\right\},
\end{aligned}$$

or spatial configurations

$$\begin{aligned}
\dot{\eta}_j &= -\mathcal{L}^{\eta}_{ji}\left\{\frac{\partial\psi^{\mathrm{e}}_s}{\partial\eta_i}+\frac{\partial\psi^{\nabla}}{\partial\eta_i}-\left(\frac{\partial\psi^{\nabla}}{\partial\eta_{,i}}\right)_{,i}\right\} = -\mathcal{L}^{\eta}_{ji}\left\{2A\eta_i\left(1-3\eta_i+2\eta_i^2\right)\hat{\imath}(\xi_i)\right. \qquad (5.60)\\
&\quad \left.-\tau-2\kappa_0\left[\hat{\imath}(\xi)\eta_{,ij}+\hat{\imath}'(\xi_i)\xi_{,i}\eta_{,j}\right]\right\},\\
\dot{\xi}_j &= -\mathcal{L}^{\xi}_{ji}\left\{\frac{\partial\psi^{\mathrm{e}}_s}{\partial\xi_i}+\frac{\partial\psi^{\nabla}}{\partial\xi_i}-\left(\frac{\partial\psi^{\nabla}}{\partial\xi_{,i}}\right)_{,i}\right\} = -\mathcal{L}^{\xi}_{ji}\left\{2\mathcal{B}\xi_i\left[\kappa_0|\eta_{,0i}|^2+A\eta_i^2\left(1-\eta_i\right)^2\right]\times\right.\\
&\quad \hat{\imath}'(\xi_i)-2\omega_0\left[\xi_{,ij}+\beta\left(\xi_{,ij}-M_iM_je_i\frac{\partial}{\partial x_i}\left(\xi_{,j}\right)\right)\right] \qquad (5.61)\\
&\quad \left.+\frac{1}{2}\left(\frac{\partial k}{\partial\xi}-\frac{2}{3}\frac{\partial\mu}{\partial\xi}\right)\left(u_{i,j}\right)^2+\frac{\partial\mu}{\partial\xi}\varepsilon_{ik}\varepsilon_{kj}\right\},
\end{aligned}$$

where $\tau=\mu\phi'(\eta)\gamma_0\left[\phi(\eta)\gamma_0-u_{,i}\left(s_im_j+m_is_j\right)\right]$.

5.3.5 Mechanical Equilibrium Equations

The mechanical governing equations and the associated boundary conditions over the reference and current configuration are, neglecting the body and inertia forces,

$$P_{ij,j}=0 \quad \text{in} \quad V_0; \quad \sigma_{ij,j}=0 \quad \text{in} \quad V, \qquad (5.62)$$

$$P_{ij}n_{0j}=p_{0i} \quad \text{on} \quad S_0; \quad \sigma_{ij}n_j=p_i \quad \text{on} \quad S, \qquad (5.63)$$

$$P_{ik}F_{jk}=F_{ik}P_{jk} \quad \text{in} \quad V_0; \quad S_{ij}=S_{ji} \quad \text{in} \quad V, \qquad (5.64)$$

with

$$P_{ij}=\frac{\partial W}{\partial F_{ij}}\Big|_{\eta,\xi}=F^{\mathrm{E}}_{ik}\frac{\partial\psi^e}{\partial E^{\mathrm{E}}_{km}}\left(F^{\eta}_{jm}\right)^{-1}; \quad \sigma_{ij}=\frac{\partial W}{\partial u_{,i}}\Big|_{\eta,\xi}. \qquad (5.65)$$

Eqs 5.63 and 5.64 are the Neumann boundary conditions on the external surface $\boldsymbol{S_0}$ (or $\boldsymbol{S}$) and the Cauchy's second law of motion in the reference (or current) configuration, respectively.

5.3.6 Weak Forms of the Governing Equations

Considering the variational formulations of initial boundary value problems associated with the material configuration, the weak forms of the equilibrium equations given by Eq 5.62 and Ginzburg–Landau equations for both state variables obtained in Eqs 5.58-5.61 are derived and will be used in computing numerical examples later in the manuscript. The presented numerical simulations employ a novel monolithic strategy by which the equilibrium equations and all of the phase-field equations are solved in a coupled manner. For each time step, both displacements and order parameters are solved simultaneously. We denote the test function for the displacement by $\boldsymbol{\delta u}$, which are vanished on the displacement boundary S_{0u}. The test functions for the order parameters are denoted by $\delta\xi$ and $\delta\eta$, respectively, such that $\delta\xi = \delta\eta = 0$ on the corresponding order parameter boundary. To formulate a finite element problem, we let $\mathscr{T}$ be a triangulation of Ω into finite element cells such that $\mathscr{T} = \{\mathscr{K}\}$. Working with the usual Lagrange finite element basis

$$\mathscr{V}_K \;=\; \left\{\mathfrak{v} \in \mathscr{H}^1(\Omega), \mathfrak{v} \in \mathscr{P}_K(\mathscr{K}) \;\; \forall \mathscr{K} \in \mathscr{T}\right\}, \tag{5.66}$$

where $\mathscr{H}^1(\Omega)$ is a conforming finite element space and $\mathscr{P}_K(\mathscr{K})$ denotes the space of Lagrangian polynomials of order K on a finite element cell. Given the data at time t_n, we will solve $\boldsymbol{u_h}$, η_h, $\xi_h \in (\mathscr{V}_{K_2})^d \times \mathscr{V}_{K_1} \times \mathscr{V}_{K_1}$ at time t_{n+1} such that

$$\mathscr{L}(\boldsymbol{\delta u}, \delta\eta, \delta\xi; \boldsymbol{u_h}, \eta_h, \xi_h) \;=\; 0 \quad \forall(\boldsymbol{\delta u}, \delta\eta, \delta\xi) \in (\mathscr{V}_{K_2})^d \times \mathscr{V}_{K_1} \times \mathscr{V}_{K_1}, \tag{5.67}$$

where $K_2 > 1$ and $K_1 > 0$, and the subscript h will be used to denote an approximate quantity. As a result of the linearity, functional $\mathscr{L}$ can be additively decomposed into

$$\begin{aligned}\mathscr{L}(\boldsymbol{\delta u}, \delta\eta, \delta\xi; \boldsymbol{u_h}, \eta_h, \xi_h) \;=\; & \mathscr{L}_u(\boldsymbol{\delta u}; \boldsymbol{u_h}, \eta_h, \xi_h) + \mathscr{L}_\eta(\delta\eta; \boldsymbol{u_h}, \eta_h, \xi_h) + \\ & \mathscr{L}_\xi(\delta\xi; \boldsymbol{u_h}, \eta_h, \xi_h),\end{aligned} \tag{5.68}$$

where $\mathscr{L}_u$, $\mathscr{L}_\eta$, and $\mathscr{L}_\xi$ represent the contributions of linear momentum, evolution of the twinning, and fracture order parameters, respectively. The corresponding functional will be the input to the code. In addition, high-level tools are exploited to generate computer code automatically by performing automatic differentiation and linearization, yielding the Jacobian for use in a Newton solver. For all time-dependent equations, implicit time integrator will be used.

5.3.6.1 Residual for Balance of Linear Momentum

Multiplying Eq 5.62 by $\boldsymbol{\delta u}$ and applying integration by parts, the weak form (residual) of the mechanical equilibrium equation is derived as

$$\mathscr{R}(\boldsymbol{u_h}, \boldsymbol{\delta u_h}) = -\int_{V_0} P_{ij,j}\delta u_{h_i} dV_0 = 0; \quad -\int_V \sigma_{ij,j}\delta u_{h_i} dV = 0. \tag{5.69}$$

Considering the relation $(P_{ji}\delta u_i)_{,j} = P_{ji,j}\delta u_i + P_{ji}\delta u_{i,j}$ and applying the Gauss divergence theorem yields

$$\begin{aligned} \mathscr{R}(\boldsymbol{u_h}, \boldsymbol{\delta u_h}) \quad = \quad & \int_{V_0} P_{ji}\delta u_{h_{i,j}} dV_0 - \int_{S_0} p_{0i}\delta u_{h_i} = 0; \\ & \int_V \sigma_{ij}\delta u_{h_{i,j}} dV - \int_S p_i \delta u_{h_i} = 0, \end{aligned} \tag{5.70}$$

where

$$\mathscr{L}_u = \int_{V_0} P_{ji}\delta u_{h_{i,j}} dV_0 - \int_{S_0} p_{0i}\delta u_{h_i}; \quad P_{ij} = F^{\mathrm{E}}_{ik}\mathcal{C}_{klmn}E^{\mathrm{E}}_{mn}F^{\eta-1}_{jl}. \tag{5.71}$$

Here, $\boldsymbol{P}$ is the first Piola–Kirchhoff stress tensor in terms of elastic and irreversible deformation tensors.

5.3.6.2 Ginzburg–Landau Equations: Time Discretization and Weak Form

In this section, the weak forms of two independent time-dependent Ginzburg–Landau equations are acquired. The time derivative of order parameters are discretized using the θ-scheme over a time period of $t \in \left[t^i, t^f\right]$, where t^i and t^f denote the initial and final time instants, respectively. This scheme requires the solution from the

current time step, which is provided by the initial conditions. With Eqs 5.58-5.61, the following time-discretization is introduced, where a superscript n indicates the number of a time step and $\Delta t_n = t_n - t_{n-1}$ is the length of the current time step

$$\begin{aligned}
\frac{\eta_{h_j}^n - \eta_{h_j}^{n-1}}{\Delta t_n} &+ \mathcal{L}_{ji}^{\eta} \Big\{ 2A\eta_{h_i}^{n-\alpha} \left(1 - 3\eta_{h_i}^{n-\alpha} + 2\left(\eta_{h_i}^{n-\alpha}\right)^2\right) \hat{\iota}\left(\xi_{h_i}^{n-\alpha}\right) \qquad (5.72)\\
&+6\eta_{h_i}^{n-\alpha}\left(1-\eta_{h_i}^{n-\alpha}\right)\gamma_0 \left[\mu\left(\xi_{h_i}^{n-\alpha}\right)\delta_{ij} + \left(\lambda\left(\xi_{h_i}^{n-\alpha}\right)\ln J - \mu\left(\xi_{h_i}^{n-\alpha}\right)\right) C_{ij}^{\mathrm{E}-1}\right]\\
&\left[C_{ij}^{\mathrm{E}} s_i m_j\right] - 2\kappa_0 \left[\hat{\iota}\left(\xi_{h_i}^{n-\alpha}\right)\eta_{h,ij}^{n-\alpha} + \hat{\iota'}\left(\xi_{h_i}^{n-\alpha}\right)\xi_{h,i}^{n-\alpha}\eta_{h,i}^{n-\alpha}\right] \Big\} = 0,\\
\frac{\xi_{h_j}^n - \xi_{h_j}^{n-1}}{\Delta t_n} &+ \mathcal{L}_{ji}^{\xi} \Big\{ 2\mathcal{B}\xi_{h_i}^{n-\alpha} \left[\kappa_0 |\eta_{h,i}^{n-\alpha}|^2 + A\left(\eta_{h_i}^{n-\alpha}\right)^2\left(1-\eta_{h_i}^{n-\alpha}\right)^2\right] \hat{\iota'}\left(\xi_{h_i}^{n-\alpha}\right) \qquad (5.73)\\
&-2\omega_0 \left[\xi_{h,ij}^{n-\alpha} + \beta\left(\xi_{h,ij}^{n-\alpha} - M_i M_j e_i \frac{\partial}{\partial X_i}\xi_{h,j}^{n-\alpha}\right)\right] + \frac{1}{2}\left(\frac{\partial \lambda}{\partial \xi_{h_i}}\right)^{n-\alpha} (\ln J)^2\\
&-\frac{1}{2}\left(\frac{\partial \mu}{\partial \xi_{h_i}}\right)^{n-\alpha} \left(2\ln J - C_{ii}^{\mathrm{E}} + 3\right)^2 \Big\} = 0,\\
\frac{\eta_{h_j}^n - \eta_{h_j}^{n-1}}{\Delta t_n} &+ \mathcal{L}_{ji}^{\eta} \Big\{ 2A\eta_{h_i}^{n-\alpha} \left(1 - 3\eta_{h_i}^{n-\alpha} + 2\left(\eta_{h_i}^{n-\alpha}\right)^2\right) \hat{\iota}\left(\xi_{h_i}^{n-\alpha}\right) \qquad (5.74)\\
&+6\eta_{h_i}^{n-\alpha}\left(1-\eta_{h_i}^{n-\alpha}\right)\gamma_0 \tau\left(\eta_{h_i}^{n-\alpha}, \xi_{h_i}^{n-\alpha}\right) - 2\kappa_0\\
&\left[\hat{\iota}\left(\xi_{h_i}^{n-\alpha}\right)\eta_{h,ij}^{n-\alpha} + \hat{\iota'}\left(\xi_{h_i}^{n-\alpha}\right)\xi_{h,i}^{n-\alpha}\eta_{h,i}^{n-\alpha}\right] \Big\} = 0,\\
\frac{\xi_{h_j}^n - \xi_{h_j}^{n-1}}{\Delta t_n} &+ \mathcal{L}_{ji}^{\xi} \Big\{ 2\mathcal{B}\xi_{h_i}^{n-\alpha} \left[\kappa_0 |\eta_{h,i}^{n-\alpha}|^2 + A\left(\eta_{h_i}^{n-\alpha}\right)^2\left(1-\eta_{h_i}^{n-\alpha}\right)^2\right] \hat{\iota'}\left(\xi_{h_i}^{n-\alpha}\right) \qquad (5.75)\\
&-2\omega_0 \left[\xi_{h,ij}^{n-\alpha} + \beta\left(\xi_{h,ij}^{n-\alpha} - M_i M_j e_i \frac{\partial}{\partial X_i}\xi_{h,j}^{n-\alpha}\right)\right] + \frac{1}{2}\left(\frac{\partial k}{\partial \xi_{h_i}}\right)^{n-\alpha}\\
&-\frac{2}{3}\left(\frac{\partial \mu}{\partial \xi_{h_i}}\right)^{n-\alpha} (u_{i,j})^2 + \left(\frac{\partial \mu}{\partial \xi_{h_i}}\right)^{n-\alpha} \varepsilon_{ik}\left(\eta_{h_i}\right)^{n-\alpha} \varepsilon_{kj}\left(\eta_{h_i}\right)^{n-\alpha} \Big\} = 0,
\end{aligned}$$

where $y_h^{n-\alpha} = (1-\alpha)y_h^{n-1} + \alpha y_h^n$. This discretization yields for $\alpha = 0$, $\alpha = 1$, and $\alpha = 0.5$ the first-order accurate explicit Euler method, first-order accurate implicit Euler method, and second-order accurate Crank–Nicolson method, respectively [433]. The next step is to discretize the spatial variables using the finite element methodology. To this end, we multiply each equation with a test function, integrate over the entire

domain, and integrate by parts where necessary. This leads to

$$\int_{V_0} \frac{\eta_{h_j}^n - \eta_{h_j}^{n-1}}{\Delta t_n} \delta\eta_{h_j}^n dV_0 + \int_{V_0} \mathcal{L}_{ji}^{\eta} \Big\{ 2A\eta_{h_i}^{n-\alpha} \left(1 - 3\eta_{h_i}^{n-\alpha} + 2\left(\eta_{h_i}^{n-\alpha}\right)^2\right) \hat{\iota}\left(\xi_{h_i}^{n-\alpha}\right) \tag{5.76}$$
$$+6\eta_{h_i}^{n-\alpha}\left(1-\eta_{h_i}^{n-\alpha}\right)\gamma_0 \left[\mu\left(\xi_{h_i}^{n-\alpha}\right)\delta_{ij} + \left(\lambda\left(\xi_{h_i}^{n-\alpha}\right)\ln J - \mu\left(\xi_{h_i}^{n-\alpha}\right)\right) C_{ij}^{E-1}\right]$$
$$\left[C_{ij}^E s_i m_j\right]\Big\} \delta\eta_{h_i}^n dV_0 + \int_{V_0} 2\kappa_0 \mathcal{L}_{ji}^{\eta} \hat{\iota}\left(\xi_{h_i}^{n-\alpha}\right) \eta_{h,i}^{n-\alpha} \delta\eta_{h,i}^n dV_0 +$$
$$\int_{V_0} 2\kappa_0 \mathcal{L}_{ji}^{\eta} \hat{\iota'}\left(\xi_{h_i}^{n-\alpha}\right) \eta_{h,i}^{n-\alpha} \xi_{h,i}^{n-\alpha} \delta\eta_{h_i}^n dV_0 - \int_{S_0} 2\kappa_0 \mathcal{L}_{ji}^{\eta} \hat{\iota}\left(\xi_{h_i}^{n-\alpha}\right) \eta_{h,i}^{n-\alpha} n_{0j} dS_0 = 0,$$
$$\int_{V_0} \frac{\xi_{h_j}^n - \xi_{h_j}^{n-1}}{\Delta t_n} \delta\xi_j^n dV_0 + \int_{V_0} \mathcal{L}_{ji}^{\xi} \Big\{ 2\mathcal{B}\xi_{h_i}^{n-\alpha} \left[\kappa_0 |\eta_{h,i}^{n-\alpha}|^2 + A\left(\eta_{h_i}^{n-\alpha}\right)^2 \left(1-\eta_{h_i}^{n-\alpha}\right)^2\right]$$
$$\times \hat{\iota}\left(\xi_{h_i}^{n-\alpha}\right) + \frac{1}{2}\left(\frac{\partial\lambda}{\partial\xi_{h_i}}\right)^{n-\alpha} + (\ln J)^2 - \frac{1}{2}\left(\frac{\partial\mu}{\partial\xi_{h_i}}\right)^{n-\alpha} \left(2\ln J - C_{ii}^E + 3\right)^2 \Big\} \delta\xi_i^n dV_0$$
$$+ \int_{V_0} 2\omega_0(1+\beta)\mathcal{L}_{ji}^{\xi} \xi_{h,i}^{n-\alpha} \delta\xi_{,i}^n dV_0 + \int_{V_0} 2\omega_0 \mathcal{L}_{ji}^{\xi} M_i M_j \xi_{h,i}^{n-\alpha} \delta\xi_{,j}^n dV_0 \tag{5.77}$$
$$- \int_{S_0} 2\omega_0(1+\beta)\mathcal{L}_{ji}^{\xi} \xi_{h,i}^{n-\alpha} n_{0j} dS_0 = 0,$$

in large deformations, and

$$\int_{V} \frac{\eta_{h_j}^n - \eta_{h_j}^{n-1}}{\Delta t_n} \delta\eta_{h_j}^n dV + \int_{V} \mathcal{L}_{ji}^{\eta} \Big\{ 2A\eta_{h_i}^{n-\alpha} \left(1 - 3\eta_{h_i}^{n-\alpha} + 2\left(\eta_{h_i}^{n-\alpha}\right)^2\right) \hat{\iota}\left(\xi_{h_i}^{n-\alpha}\right) \tag{5.78}$$
$$+6\eta_{h_i}^{n-\alpha}\left(1-\eta_{h_i}^{n-\alpha}\right)\gamma_0\tau\left(\eta_{h_i}^{n-\alpha}, \xi_{h_i}^{n-\alpha}\right)\Big\} \delta\eta_{h_i}^n dV_0 + \int_{V} 2\kappa_0 \mathcal{L}_{ji}^{\eta} \hat{\iota}\left(\xi_{h_i}^{n-\alpha}\right) \eta_{h,i}^{n-\alpha} \delta\eta_{h,i}^n dV$$
$$+ \int_{V} 2\kappa_0 \mathcal{L}_{ji}^{\eta} \hat{\iota'}\left(\xi_{h_i}^{n-\alpha}\right) \eta_{h,i}^{n-\alpha} \xi_{h,i}^{n-\alpha} \delta\eta_{h_i}^n dV - \int_{S} 2\kappa_0 \mathcal{L}_{ji}^{\eta} \hat{\iota}\left(\xi_{h_i}^{n-\alpha}\right) \eta_{h,i}^{n-\alpha} n_j dS = 0,$$
$$\int_{V} \frac{\xi_{h_j}^n - \xi_{h_j}^{n-1}}{\Delta t_n} \delta\xi_j^n dV + \int_{V} \mathcal{L}_{ji}^{\xi} \Big\{ 2\mathcal{B}\xi_{h_i}^{n-\alpha} \left[\kappa_0 |\eta_{h,i}^{n-\alpha}|^2 + A\left(\eta_{h_i}^{n-\alpha}\right)^2 \left(1-\eta_{h_i}^{n-\alpha}\right)^2\right] \tag{5.79}$$
$$\times \hat{\iota}\left(\xi_{h_i}^{n-\alpha}\right) + \frac{1}{2}\left(\frac{\partial k}{\partial\xi_{h_i}}\right)^{n-\alpha} - \frac{2}{3}\left(\frac{\partial\mu}{\partial\xi_{h_i}}\right)^{n-\alpha} (u_{i,j})^2 + \left(\frac{\partial\mu}{\partial\xi_{h_i}}\right)^{n-\alpha} \varepsilon_{ik}\left(\eta_{h_i}\right)^{n-\alpha}$$
$$\times \varepsilon_{kj}\left(\eta_{h_i}\right)^{n-\alpha}\Big\} \delta\xi_i^n dV + \int_{V} 2\omega_0(1+\beta)\mathcal{L}_{ji}^{\xi} \xi_{h,i}^{n-\alpha} \delta\xi_{,i}^n dV + \int_{V} 2\omega_0 \mathcal{L}_{ji}^{\xi} M_i M_j \xi_{h,i}^{n-\alpha} \delta\xi_{,j}^n dV$$
$$- \int_{S} 2\omega_0(1+\beta)\mathcal{L}_{ji}^{\xi} \xi_{h,i}^{n-\alpha} n_j dS = 0,$$

in small deformations.

5.4 Finite Element Implementation

The finite element method is applied to discretize the weak forms of the nonlinear problems discussed in the previous sections approximating the primary variables (i.e.,

displacement, and twinning and fracture order parameters). For this purpose, the geometry of a continuous body $\mathfrak{B}_0$ in the initial configuration is approximated as

$$\mathfrak{B}_0 \approx \mathfrak{B}_0^h = \bigcup_1^{n_e} \mathfrak{B}_{0_e}, \tag{5.80}$$

where n_e is the number of finite elements. All kinematic variables and the geometry are interpolated using the isoparametric concept within one finite element $\mathfrak{B}_{0_e}$ as

$$X_e = \sum_{I=1}^{n_g} N_I(\vartheta) X_I, \tag{5.81}$$

where $N_I(\vartheta)$ is the shape function defined within the reference element, ϑ denotes the coordinates of the isoparametric reference element, and n_g is the number of nodes in each element. The mapping from the reference element $\mathfrak{B}_{\text{fe}}$ to the initial configuration $\mathfrak{B}_{0_e}$ and to the current configuration $\mathfrak{B}_e$ are defined as

$$\begin{aligned}
&\boldsymbol{F}_{\text{fe}} = \boldsymbol{j}_{\text{fe}} \boldsymbol{J}_{\text{fe}}^{-1}; \quad \boldsymbol{J}_{\text{fe}} = \sum_{I=1}^{n_g} \boldsymbol{X}_I \otimes \nabla_\vartheta N_I; \quad \boldsymbol{j}_{\text{fe}} = \sum_{I=1}^{n_g} \boldsymbol{x}_I \otimes \nabla_\vartheta N_I; \\
&\nabla \boldsymbol{u}_{\text{fe}} = \sum_{I=1}^{n_g} \boldsymbol{u}_I \otimes \boldsymbol{J}_{\text{fe}}^{-T} \nabla_\vartheta N_I; \quad \nabla \delta \boldsymbol{u}_{\text{fe}} = \sum_{I=1}^{n_g} \delta \boldsymbol{u}_I \otimes \boldsymbol{J}_{\text{fe}}^{-T} \nabla_\vartheta N_I; \\
&\nabla \Delta \boldsymbol{u}_{\text{fe}} = \sum_{I=1}^{n_g} \Delta \boldsymbol{u}_I \otimes \boldsymbol{J}_{\text{fe}}^{-T} \nabla_\vartheta N_I.
\end{aligned} \tag{5.82}$$

In these equations, $\nabla_\vartheta N_I$ is the gradient of the scalar function N_I with respect to the coordinates $\boldsymbol{\vartheta}$; $\nabla \boldsymbol{u}_{\text{fe}}$, $\nabla \delta \boldsymbol{u}_{\text{fe}}$, and $\nabla \Delta \boldsymbol{u}_{\text{fe}}$ are the material gradients of the displacement, the gradients of their weighting functions, and their increments, respectively [434].

5.4.1 Finite Element Formulation of the Weak Form of the Equilibrium Equation

The first Piola–Kirchhoff stress tensor in Eq 5.70 is replaced by the second Piola–Kirchhoff stress tensor, leading to

$$P_{ij} \delta u_{i,j} = S_{ik} F_{jk} \delta u_{i,j} = \frac{1}{2} S_{ik} \left(F_{kj} \delta u_{i,j} + \delta u_{j,i} F_{kj} \right) = S_{ij} \delta E_{ij}, \tag{5.83}$$

where δE_{ij} denotes the variation of the Green–Lagrange strain tensor. Discretizing and using the gradient of the displacement vector within an element $\mathfrak{B}_{fe}$

$$\delta E_{\mathrm{fe}_{ij}} = \frac{1}{2}\sum_{I=1}^{n_g}\left[F_{\mathrm{fe}_{ik}}N_{I,j} + N_{I,i}F_{\mathrm{fe}_{kj}}\right]\delta u_{kI} = \sum_{I=1}^{n_g} B_{kI}\delta u_{kI}, \tag{5.84}$$

where

$$B = \begin{pmatrix} N_{I,1} & 0 & 0 \\ 0 & N_{I,2} & 0 \\ 0 & 0 & N_{I,3} \\ N_{I,2} & N_{I,1} & 0 \\ 0 & N_{I,3} & N_{I,2} \\ N_{I,3} & 0 & N_{I,1} \end{pmatrix}. \tag{5.85}$$

Thus, the virtual work of the equilibrium equation can be approximated with finite elements by

$$\int_{\mathfrak{B}_0} \delta E_{ij} S_{ij} = \bigcup_{e=1}^{n_e}\sum_{I=1}^{n_g} \delta u_{Ik} \int_{\mathfrak{B}_{\mathrm{fe}}} B_{Ik} S_{\mathrm{fe}_{kj}} \tag{5.86}$$

5.4.2 Discretization of the Ginzburg–Landau Equations

Considering the following discretizations for the variables in the reference element

$$\begin{aligned} \eta^{\mathrm{fe}} &= \sum_{I=1}^{n_g} N_I(\vartheta)\,\hat{\eta}_I; \quad \delta\eta^{\mathrm{fe}} = \sum_{I=1}^{n_g} N_I(\vartheta)\,\delta\hat{\eta}_I; \quad \Delta\eta^{\mathrm{fe}} = \sum_{I=1}^{n_g} N_I(\vartheta)\,\Delta\hat{\eta}_I; \\ \xi^{\mathrm{fe}} &= \sum_{I=1}^{n_g} N_I(\vartheta)\,\hat{\xi}_I; \quad \delta\xi^{\mathrm{fe}} = \sum_{I=1}^{n_g} N_I(\vartheta)\,\delta\hat{\xi}_I; \quad \Delta\xi^{\mathrm{fe}} = \sum_{I=1}^{n_g} N_I(\vartheta)\,\Delta\hat{\xi}_I, \end{aligned} \tag{5.87}$$

and performing the standard assembly operation, the systems of algebraic equations for obtaining the nodal twinning and fracture order parameters are derived as

$$(\boldsymbol{M}_i^{\eta} + \Delta t_n \boldsymbol{L}_i^{\eta} + \Delta t_n \boldsymbol{R}_i^{\eta}) \cdot \Delta\eta_i^{\mathrm{fe}} = -\boldsymbol{r}_i^{\eta}, \tag{5.88}$$

$$\left(\boldsymbol{M}_i^{\xi} + \Delta t_n \boldsymbol{L}_i^{\xi} + \Delta t_n \boldsymbol{R}_i^{\xi}\right) \cdot \Delta\xi_i^{\mathrm{fe}} = -\boldsymbol{r}_i^{\xi}, \tag{5.89}$$

where

$$\mathcal{L}^{\eta}\boldsymbol{M}_i^{\eta} = \mathcal{L}^{\xi}\boldsymbol{M}_i^{\xi} = \bigcup_{e=1}^{n_e}\sum_{I=1}^{n_g}\sum_{K=1}^{n_g}\int_{\mathfrak{B}_{\mathfrak{fe}}} N_I N_K dV_0; \tag{5.90}$$

$$\boldsymbol{L}_i^{\eta} = \bigcup_{e=1}^{n_e}\sum_{I=1}^{n_g}\sum_{K=1}^{n_g}\int_{\mathfrak{B}_{\mathfrak{fe}}} 2\kappa_0\mathcal{L}^{\eta}\hat{\imath}\left(\xi^{\mathrm{fe}}\right)\nabla N_I^T\nabla N_K dV_0;$$

$$\boldsymbol{R}_i^{\eta}\left(\eta_n,\xi_n\right) = \bigcup_{e=1}^{n_e}\sum_{I=1}^{n_g}\sum_{K=1}^{n_g}\int_{\mathfrak{B}_{\mathfrak{fe}}} \frac{\partial f_i^{\eta}\left(\eta_n,\xi_n\right)}{\partial\eta_n} N_I N_K dV_0;$$

$$\frac{\partial f_i^{\eta}\left(\eta_n,\xi_n\right)}{\partial\eta_n} = 2A\eta_n\left(1-3\eta_n+2\eta_n^2\right)\hat{\imath}\left(\xi_n\right);$$

$$\boldsymbol{r}_i^{\eta}\left(\eta_n,\xi_n\right) = \left(\mathcal{L}^{\eta}\boldsymbol{M}_i^{\eta}+\Delta t_n\boldsymbol{L}_i^{\eta}\right)\eta_n^{\mathrm{fe}} - \mathcal{L}^{\eta}\boldsymbol{M}_i^{\eta}\eta_{n-1}^{\mathrm{fe}} + \Delta t_n\boldsymbol{f}_i^{\eta}\left(\eta_n,\xi_n\right);$$

$$\boldsymbol{f}_i^{\eta}\left(\eta_n,\xi_n\right) = \bigcup_{e=1}^{n_e}\sum_{I=1}^{n}\int_{\mathfrak{B}_{\mathfrak{fe}}} f_i^{\eta}\left(\eta_n,\xi_n\right)N_I dV_0;$$

$$\boldsymbol{L}_i^{\xi} = \bigcup_{e=1}^{n_e}\sum_{I=1}^{n_g}\sum_{K=1}^{n_g}\int_{\mathfrak{B}_{\mathfrak{fe}}} 2\omega\mathcal{L}^{\xi}\nabla N_I^T\nabla N_K dV_0;$$

$$\boldsymbol{R}_i^{\xi}\left(\eta_n,\xi_n\right) = \bigcup_{e=1}^{n_e}\sum_{I=1}^{n_g}\sum_{K=1}^{n_g}\int_{\mathfrak{B}_{\mathfrak{fe}}} \frac{\partial f_i^{\xi}\left(\eta_n,\xi_n\right)}{\partial\xi_n} N_I N_K dV_0;$$

$$\frac{\partial f_i^{\xi}\left(\eta_n,\xi_n\right)}{\partial\xi_n} = 2\mathcal{B}\xi_n\left[\kappa_0|\nabla\eta_n|^2 + A\eta_n^2\left(1-\eta_n\right)^2\right]\hat{\imath}'\left(\xi_n\right);$$

$$\boldsymbol{r}_i^{\xi}\left(\eta_n,\xi_n\right) = \left(\mathcal{L}^{\xi}\boldsymbol{M}_i^{\xi}+\Delta t_n\boldsymbol{L}_i^{\xi}\right)\xi_n^{\mathrm{fe}} - \mathcal{L}^{\xi}\boldsymbol{M}_i^{\xi}\xi_{n-1}^{\mathrm{fe}} + \Delta t_n\boldsymbol{f}_i^{\xi}\left(\eta_n,\xi_n\right);$$

$$\boldsymbol{f}_i^{\xi}\left(\eta_n,\xi_n\right) = \bigcup_{e=1}^{n_e}\sum_{I=1}^{n}\int_{\mathfrak{B}_{\mathfrak{fe}}} f_i^{\xi}\left(\eta_n,\xi_n\right)N_I dV_0.$$

In Eqs 5.87 and 5.88, $\boldsymbol{M}_i$ is the phase field kinetic matrix, $\boldsymbol{L}_i$ is the phase-field stiffness matrix, $\Delta\eta_i^{\mathrm{fe}}$ and $\Delta\xi_i^{\mathrm{fe}}$ corresponds to the increment of the order parameters, $\boldsymbol{G}_i$ is a $n_i \times n_i$ symmetric global matrix, n_i is the total number of degrees of freedom for the order parameters, and $\boldsymbol{f}_i^{\xi,\eta}\left(\eta_n,\xi_n\right)$ and $\boldsymbol{r}_i^{\xi,\eta}\left(\eta_n,\xi_n\right)$ are $n_i \times 1$ global column matrices corresponds to driving forces and residuals for each state variables, respectively.

5.5 Numerical Examples

A number of numerical examples under various loading conditions in two-dimensional samples are now presented to demonstrate that the model captures the deformation mechanisms observed in metallic magnesium and ceramic boron carbide, both quali-

tatively and quantitatively. The material properties used in the simulations are shown in Table 5.1 for Mg and B_4C. The time stepping parameters are chosen such that the momentum balance scheme is second-order accurate and stable. Quadratic and linear Lagrange functions are used for the displacement and all other fields, respectively. Size, time, and stress are normalized by 1 nm, 1 ps, and 1 GPa, respectively. Initial conditions are also prescribed as part of the solution procedure.

Table 5.1: Material properties and model constants for magnesium and boron carbide

Parameters	Value-Mg	Value-B_4C	Reference
Elastic constants (C_{11})	63.5 GPa	487 GPa	[305, 435]
" (C_{12})	25.9 GPa	117 GPa	[305, 435]
" (C_{13})	21.7 GPa	66 GPa	[305, 435]
" (C_{33})	66.5 GPa	525 GPa	[305, 435]
" (C_{44})	18.4 GPa	133 GPa	[305, 435]
Shear modulus (μ)	19.4 GPa	193 GPa	[436, 437]
Bulk modulus (k)	36.9 GPa	237 GPa	[436, 437]
Twin surface energy (Γ)	0.12 $^{\mathrm{J}}/_{\mathrm{m}^2}$	0.54 $^{\mathrm{J}}/_{\mathrm{m}^2}$	Eq 5.53
Twinning shear (γ_0)	0.13	0.31	[411, 235]
Gradient energy parameter (κ_0)	0.0878 $^{\mathrm{nJ}}/_{\mathrm{m}}$	0.4212 $^{\mathrm{nJ}}/_{\mathrm{m}}$	Eq 5.55
Transformation barrier (A)	1.404 GPa	3.01 GPa	[415, 235]
Regularization length ($l,\ h$)	1.00 nm	1.04 nm	Eq 5.54

A fully coupled solution strategy along with a Newton–Krylov method is employed to solve the non-linear equations in each time step. The problem-specific parts of the computer code used to perform the simulations have been generated automatically from a high-level description that resembles closely the notation used in this work by

using a number of tools from the FEniCS Project ([299], [438], [300]). The preconditioned Jacobi for nonlinear equations is employed as the method of solution. Three different problems have been solved:

(i) Twin propagation in two-dimensional magnesium and boron carbide single crystals (Section 5.5.1);

(ii) Analysis of twinning induced by a crack under pure mode I or mode II loading (Section 5.5.2);

(iii) Fracture in homogeneous boron carbide single crystals under biaxial compressive loading (Section 5.5.3).

Parameters such as time instance after the $(n-1)^{th}$ iteration t^n, final time t^f, and the maximum number of iterations for the elasticity and the phase field equations are chosen differently in each case and are reported while discussing the respective problems.

5.5.1 Phase-Field Approach to Model Twin Growth and Propagation

In this example, the nucleation and evolution of deformation twinning in a single crystal of magnesium (Section 5.5.1.1) and boron carbide (Section 5.5.1.2) are simulated in a two-dimensional domain in plain strain conditions (Figure 5.2).

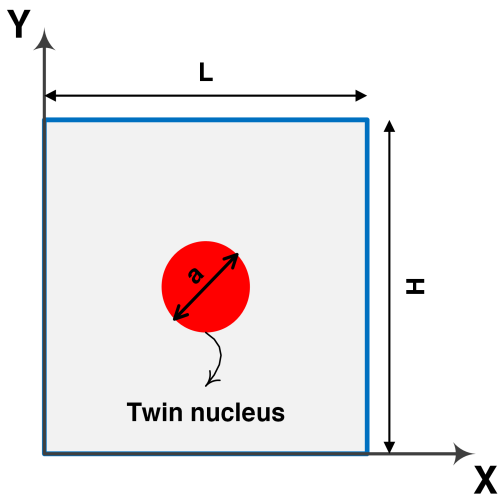

Figure 5.2: The numerical setup of the rectangular single crystal including a single twin embryo in the material configuration.

For validation, the model is initially solved for elastically isotropic pure magnesium single crystals with the properties listed in Table 1. A circular twin nucleus ($\eta = 1$) of initial radius $a = 3\,\text{nm}$ is embedded in a rectangular domain ($\eta = 0$) of dimensions $40 \times 40\,\text{nm}$ for the magnesium simulations. The initial radius of the twin embryo is set to 3 nm as a result of the fact that a bifurcation from circular to elliptical shape occurs for a radius of 3.2 nm, corresponding to the analytical sharp interface solution [270]. The lattice orientation vectors are in the form

$$\boldsymbol{s} = (\cos\theta, \sin\theta)^T\,; \quad \boldsymbol{m} = (-\sin\theta, \cos\theta)^T\,, \tag{5.91}$$

where θ denotes the orientation of the habit plane. Also, according to the following matrix-form gradient coefficient

$$\boldsymbol{\kappa} = \begin{pmatrix} \kappa_{11} & 0 \\ 0 & \kappa_{22} \end{pmatrix}, \tag{5.92}$$

both isotropic ($\kappa_{11} = \kappa_{22} = \kappa_0$) and anisotropic ($\frac{\kappa_{11}}{2} = 2\kappa_{22} = \kappa_0$) twin boundary surface energies are employed in our simulations to explore their effects and for validation purposes. The following simple shear with Dirichlet boundary condition on

the order parameter is considered

$$\{u_1 = \Lambda Y,\ u_2 = 0,\ \eta = 0\} \quad \forall X,\ Y \in \partial\mathfrak{B}, \tag{5.93}$$

where $\Lambda = 0.08$ is the magnitude of applied shear for all simulations in the following section.

5.5.1.1 Twin Embryo Propagation and Growth in Single Crystal Magnesium

Figure 5.3 shows contour plots demonstrating the spatial distributions of numerical results for the growth of a circular twin embryo in single crystal magnesium with an orientation of the habit plane $\theta = 0$. The embryo is undergoing simple shear at 8%. Parameters of interest include the twin order parameter (i, ii), y displacement (iii, iv), and shear stress (v, vi). Each image pair considers both small (left side) and large strains (right side), as well as isotropic (a, b) and anisotropic surface energies (c, d). The results are illustrated at time instants of $t = 50\,\text{ps}$ and $t = 500\,\text{ps}$ to show the evolution of twin's morphology. The mesh of the rectangular domain includes 160,000 linear triangular elements. By using a standard h-convergence, we obtained that the chosen mesh is fine enough to deliver mesh insensitive results. The $\langle 1\,0\,\bar{1}\,1\rangle$ plane and $\{1\,0\,\bar{1}\,2\}$ direction are considered as the primary twinning system in magnesium [271]. The phase field results in this chapter can be improved through additional consideration of mechanisms across more loading conditions. The current results are meant to highlight the application of phase field modeling approaches to computational material science.

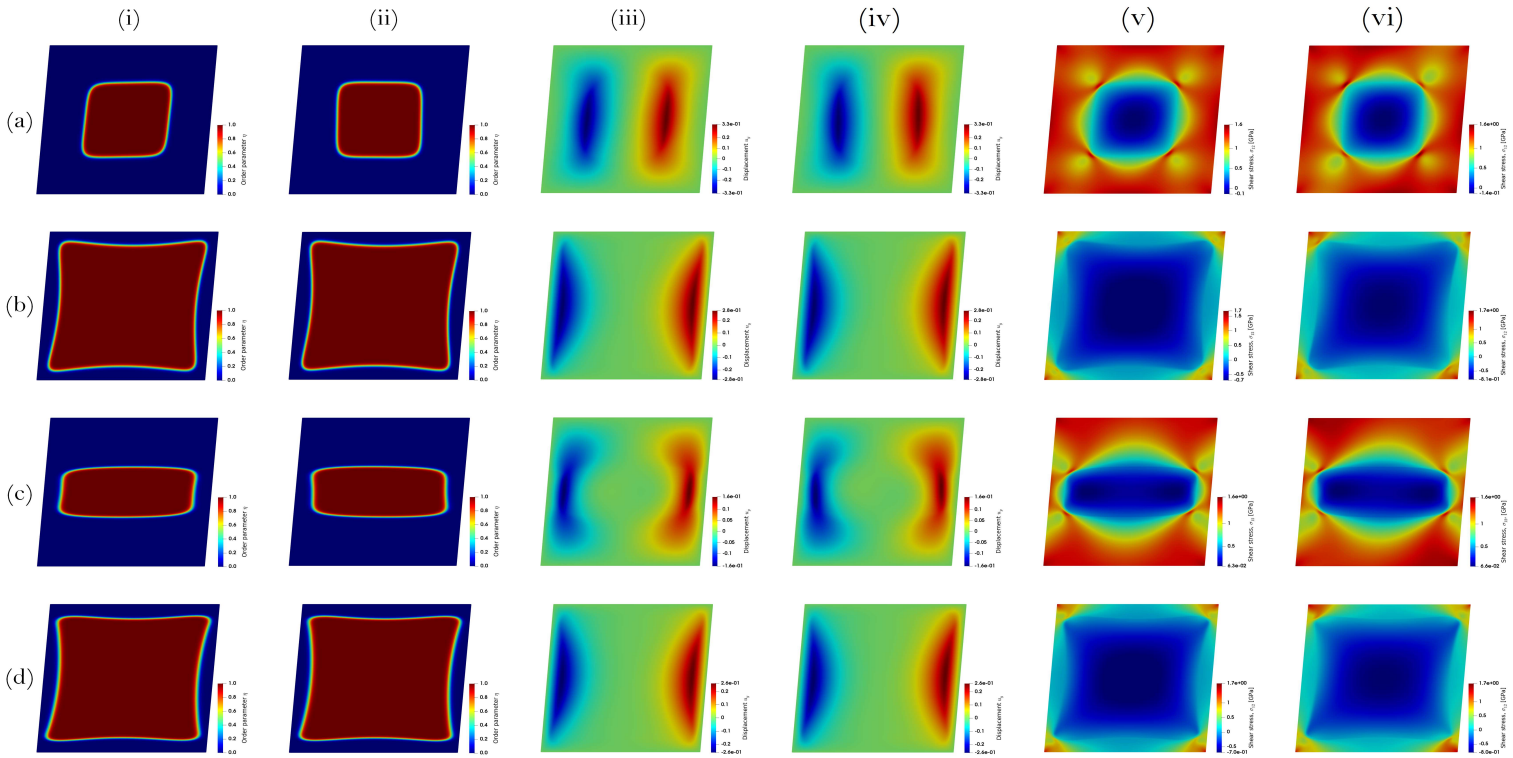

Figure 5.3: The numerical results showing of a circular twin embryo in a rectangular domain in single crystal magnesium in both small (left side in image pair) and large (right side in image pair) deformations considering isotropic and anisotropic surface energies and elasticity with orientation of the habit plane $\theta = 0$: (a) Twin order parameter (i, ii), displacement in the y direction (iii, iv), and distribution of the shear stress (v, vi) for small (left side in image pair) and large strains (right side in image pair) and isotropic surface energy at $t = 50\,\text{ps}$; (b) Twin order parameter (i, ii), displacement in the y direction (iii, iv), and distribution of the shear stress (v, vi) for small and large strains and isotropic surface energy at $t = 500\,\text{ps}$; (c) Twin order parameter (i, ii), displacement in the y direction (iii, iv), and distribution of the shear stress (v, vi) for small and large strains and anisotropic surface energy at $t = 50\,\text{ps}$; and (d) Twin order parameter (i, ii), displacement in the y direction (iii, iv), and distribution of the shear stress (v, vi) for small and large strains and anisotropic surface energy at $t = 500\,\text{ps}$. (For interpretation of the references to color in this figure, the reader is referred to the web version of this article.)

First, the evolution of the twin order parameter subjected to simple shear with the boundary conditions defined in Eq 5.93 at $t = 50\,\text{ps}$ and $t = 500\,\text{ps}$ for small and large deformation with isotropic twin boundary energy are shown in the deformed state in Figure 5.3(a, b)(i, ii). As can be seen, the twin embryo grows until it is repelled by the rigid outer boundaries where the order parameter is set to zero. Under these numerical conditions, a small orientation of the twin evolution is realized due to the difference in the driving force for twinning, which is a factor of $(\boldsymbol{F}^{\eta})^{-1}$. Finally, it is worth noting that the twin morphology at the final stage is in qualitative agreement with the reference static phase-field results [50] and molecular dynamics simulations [241], thus serving to validate the set of results in Figure 5.3(a, b)(i, ii) for the proposed time-dependent phase-field model. Next, the distribution of the displacement in the y direction for the domain under simple shear loading for small and large strains at different times are depicted in Figure 5.3(a, b)(iii, iv). The positive and negative displacement values indicate that the left and right sides of the twinned boundary regions are under compressive and tensile loading, respectively. The range of displacement magnitudes at the very last time instant are lower than those at initial times as a result of inhibiting by the boundaries. The corresponding evolution of the shear stress for small and large strains with consideration of the isotropic surface energy at various times are illustrated in Figure 5.3(a, b)(v, vi). Investigating the shear stress distribution improves our knowledge of the redistribution of high local stress resulting from twinning [278], and this provides new insights into demonstrating the driving force for the propagation and growth of twin within a small region in the microstructure. Finally, in Figure 5.3(a, b)(v, vi), it is also shown that the shear stress within the twinning regions has negative values with different lower limits for small and large strains.

Next, the effect of anisotropic surface energy is studied in Figure 5.3(c, d)(i - vi). For the twin order parameter in Figure 5.3(c)(i, ii), the equilibrium shape of the twin embryo under small strains is wider in the horizontal direction (parallel to

the habit plane) and flatter in the vertical direction at $t = 50\,\text{ps}$ as compared to the isotropic energy results shown in Figure 5.3(a)(i, ii). This behavior has been observed previously in the time-independent phase-field approach [50], where the results are in agreement with those in this study, thus providing an additional confirmation of validation for our time-dependent phase-field model. After completing its growth in the horizontal direction, Figure 5.3(c)(i, ii), the twin begins to grow in width for later times, $t = 500\,\text{ps}$, Figure 5.3(d)(i, ii). This behavior is correlated to the surface energy anisotropy ratio κ_{11}/κ_2 [50]. Moreover, the twin interface thickness has a lower value in the direction normal to the habit plane for the anisotropic surface energy scenario depicted in Figure 5.3(c, d)(i, ii) as compared with the isotropic case from Figure 5.3(a, b)(i, ii). This phenomenon is consistent with that observed by Clayton [50] and is related to the contribution of the core and elastic energies to the total surface energy of the interface [273]. The displacement for the anisotropic case Figure 5.3(c, d)(iii, iv) is lower than in the isotropic one from Figure 5.3(a, b)(iii, iv). Finally, the variation of shear stresses for anisotropic surface energies at various time instants under small and large strains are depicted in Figure 5.3(c, d)(v, vi). Considering the results at $t = 500\,\text{ps}$, Figure 5.3(c, d)(vi), the maximum and minimum shear stress values for the current simulations are within a 7% difference of the results obtained in [50] for a time-*independent* phase-field model, again validating our current time-*dependent* phase-field model. For both isotropic and anisotropic surface energies, the magnitude of the shear stress within the twinning region decreases as a function of time and, eventually, becomes negative. This is consistent with experimental results for single crystal magnesium under simple shear loading [236].

For the next set of simulation examples in Figure 5.4, the same boundary conditions and numerical setup from Figure 5.3 are considered for $\theta = \pi/6$. The layout of the figure is similar to that of Figure 5.3 with $\theta = 0$ where (a, b)(i - vi) and (c, d)(i - vi) are the simulation results for the order parameter, displacement, and shear stress under small and large strains at $t = 50\,\text{ps}$ and $t = 500\,\text{ps}$ for isotropic and anisotropic

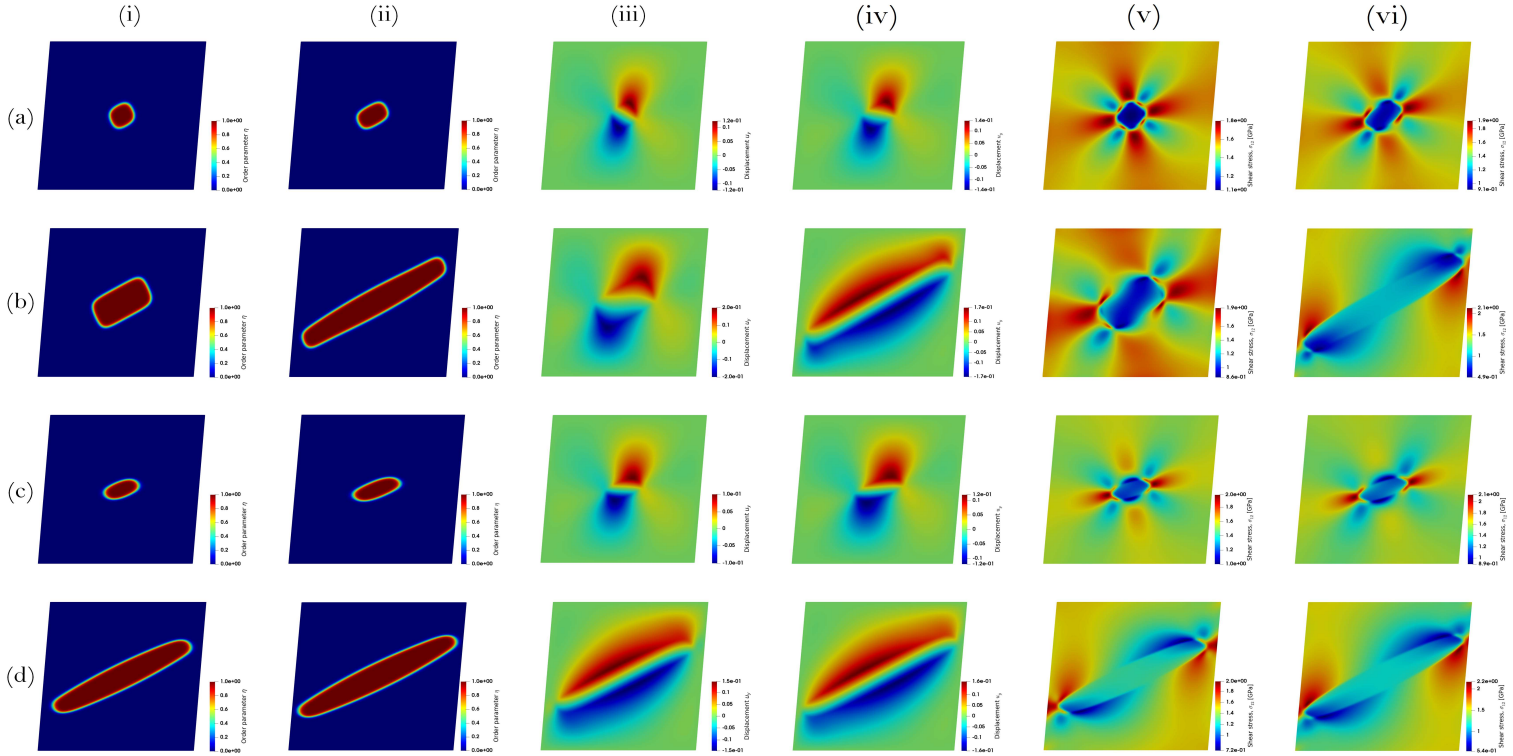

Figure 5.4: The numerical results showing of a circular twin embryo in a rectangular domain in single crystal magnesium in both small (left side in image pair) and large (right side in image pair) deformations considering isotropic and anisotropic surface energies and elasticity with orientation of the habit plane $\theta = \pi/6$: (a, b) Twin order parameter (i, ii), displacement in the y direction (iii, iv), and distribution of the shear stress (v, vi) for small and large strains and isotropic surface energy at $t = 50\,\text{ps}$ and $t = 500\,\text{ps}$, respectively; (c, d) Twin order parameter (i, ii), displacement in the y direction (iii, iv), and distribution of the shear stress (v, vi) for small and large strains and anisotropic surface energy at $t = 50\,\text{ps}$ and $t = 500\,\text{ps}$, respectively. (For interpretation of the references to color in this figure, the reader is referred to the web version of this article.)

surface energies, respectively. For the isotropic surface energy case in Figure 5.4(a)(i, ii) at $t = 50\,\text{ps}$, the twin is smaller as a consequence of less driving force under the same shear loading of 8% as compared with Figure 5.3(a)(i, ii). Further, the twin area fraction at $t = 500\,\text{ps}$ shown in Figure 5.4(b)(i, ii) is much smaller than the case when the orientation of the habit plane is aligned with the shear loading direction (Figure 5.3(a)(i, ii)). In the case of large strains, the twin tends to grow more prominently in the direction of the habit plane when $\theta = \pi/6$ than when $\theta = 0$ (Figure 5.4(a)(ii)). The displacement contours shown in Figure 5.4(a - d)(iii, iv) shows that the upper and lower sides of the twin's interface are under tensile and compressive loading, respectively, which is similar to Figure 5.3(a - d)(iii, iv). The displacement in the vertical direction (Figure 5.4(a)(iv)) is ∼17% greater than that for the small deformation case depicted in Figure 5.4(a)(iii), and the maximum shear stress under large strain conditions (Figure 5.4(a)(vi)) is 5% greater than that for the small deformation case (Figure 5.4(a)(v)). At $t = 500\,\text{ps}$, the twin embryo has a greater thickness for small deformations (Figure 5.4(b)(i)) as compared with its growth in length in the direction of the habit plane for the case of large deformations (Figure 5.4(b)(ii)), until it is prohibited by the boundaries. The displacement at the end of the simulation is around 17% larger for small strains (Figure 5.4(b)(iii)) as compared with the large deformation result (Figure 5.4(b)(iv)). Lastly, the spatial variations of shear stress at $t = 50\,\text{ps}$ and $t = 500\,\text{ps}$ are depicted in Figure 5.4(a, b)(v, vi). As can be seen, the minimum and maximum shear stress values happen in the twinned region and matrix, respectively. The heterogeneous stress distribution around the twins is due to a sudden change in the stresses within the twin interface [256].

Next, the phase-field results for the anisotropic surface energy and $\theta = \pi/6$ are shown in Figure 5.4(c, d)(i-vi). Considering the distribution of the twin order parameter for small strains, Figure 5.4(c, d)(i, ii), the twin boundaries tend to be expanded parallel to the habit plane when compared with the isotropic case because the elongation in the

direction of $\boldsymbol{s}$ is favored due to a decreasing contribution of the gradient energy term [50]. Pointing to Figure 5.4(c)(iii, iv), the maximum displacement values for large deformations are 20% higher than those in the small deformation case from Figure 5.4(a)(iii, iv). At the tip of the twin, the shear stress is maximum and ∼10% larger for large strain conditions (Figure 5.4(a)(vi)) as compared to the small deformation case (Figure 5.4(a)(v)). For the same boundary conditions, the results are depicted for $t = 500\,\text{ps}$ in Figure 5.4(b, d). Here, the twin embryo has a different equilibrium shape than what shown in Figure 5.3 for $\theta = 0$. Namely, the twin is rotated in such a way that one axis in the reference coordinate is aligned to the direction $\boldsymbol{s}$ of twinning shear, as shown in Figure 5.4(d)(i, ii). The twin interface also has a lower thickness in the direction normal to the habit plane due to the various contributions of the core and elastic energies to the interface energy [273]. For the displacement contour, the values are 30% larger for the anisotropic energy (Figure 5.4(d)(iii, iv)) as compared to the isotropic case, while the difference in shear stress for small and large strains is negligible.

5.5.1.2 Twin Embryo Propagation and Growth in Single Crystal Boron Carbide

Following the validation for Mg single crystals, the model is employed to predict the twin growth in single crystal boron carbide. In superhard materials, B_4C in this study, the failure is often correlated with twins and stacking faults at room temperature [439, 440]. The presence of twins in pressureless sintered and hot-pressed B_4C has been identified by a high-resolution TEM [441], and reported in previous literature [53, 442], ranging from $t = 1\,\text{nm}$ up to $t = 30\,\text{nm}$ in width for milled and unmilled samples [443]. It has been hypothesized that the formation of nanotwins and the presence of twin boundaries in boron carbide could lead to strengthening the materials by arresting twin boundary slip within the nanotwins [444]. The homogeneous and heterogeneous nucleation and growth of twin embryos will lead to formation of mature

twins with the length and thickness of several hundred nanometers or micrometers [445, 446]. Given the lack of true images of the twin interfaces in boron carbide [411, 447] as well as the difficulty in experimentally tracking the twin growth process, the present continuum mechanics model will provide insight into the deformation behavior of pre-existed twinned B_4C, which have been largely neglected in previous works [50, 71]. In addition, the morphology of mature twins will be affected by the early stages of the twin nucleus evolution, which necessitates a comprehensive model such as the one proposed herein. In this light, understanding how twins are formed and then developing effective strategies for incorporating twin boundaries into polycrystalline microstructures constitute an attractive approach for enhancing the mechanical response of ceramics. To address this, we conducted numerical simulations using the phase-field model in a boron carbide single crystal. The combination of growth of a single twin embryo in two critical directions, including the twin thickening through twin boundary (TB) migration and the twin tip (TT) propagation have been measured and compared with experiments (Figure 5.5). Shear strains are applied by displacing all the boundary regions, while the bottom side is fixed. A time step of $\Delta t = 1\,\text{fs}$ is chosen for solving the problem. The dimensions of the simulation domain are $40 \times 40\,\text{nm}$ in the X and Y directions, and contains 160,000 linear triangular elements. One circular twin embryo with a radius of $5\,\text{nm}$ is inserted at the center of a square containing the perfect B_4C crystal lattice, using the Eshelby method as in [448]. The magnitude of applied shear Λ is set to 0.3, which is maximum at the top and zero at the bottom. Additional simulations showed that choosing a shear magnitude lower than 0.3 leads to shrinking and disappearing of the twin.

Schematics of the simulation result for an initially circular twin embryo in boron carbide at $t = 1\,\text{ps}$ and $t = 2\,\text{ps}$ with the X-axis along the $[1\bar{1}0\bar{1}]$ direction are shown in Figures 5.5(a) and 5.5(b), respectively. Figure 5.5(a) depicts the "twin tip", which occurs in the primary direction of twin growth, and the "twin boundary", which occurs in a direction perpendicular to the twin growth. Under shear loading, the size and

shape of the initial circular twin changed until reaching a stable configuration. Similar to other ceramics such as calcite, the twin was contracted at the beginning of loading, and this has been shown to be related to the stress reversal [449]. Next, the twin embryo's shape and growth direction at $t = 2\,\text{ps}$ from Figure 5.5(b) is compared with the high resolution transmission electron microscope images (Figure 5.5(c)) and density functional theory results (Figure 5.5(d)) [444]. The shape and angle of twin embryo obtained from the numerical simulations are in good agreement with the previously published results, showing the symmetric twin with an inclination angle of 73.1° to 73.3°.

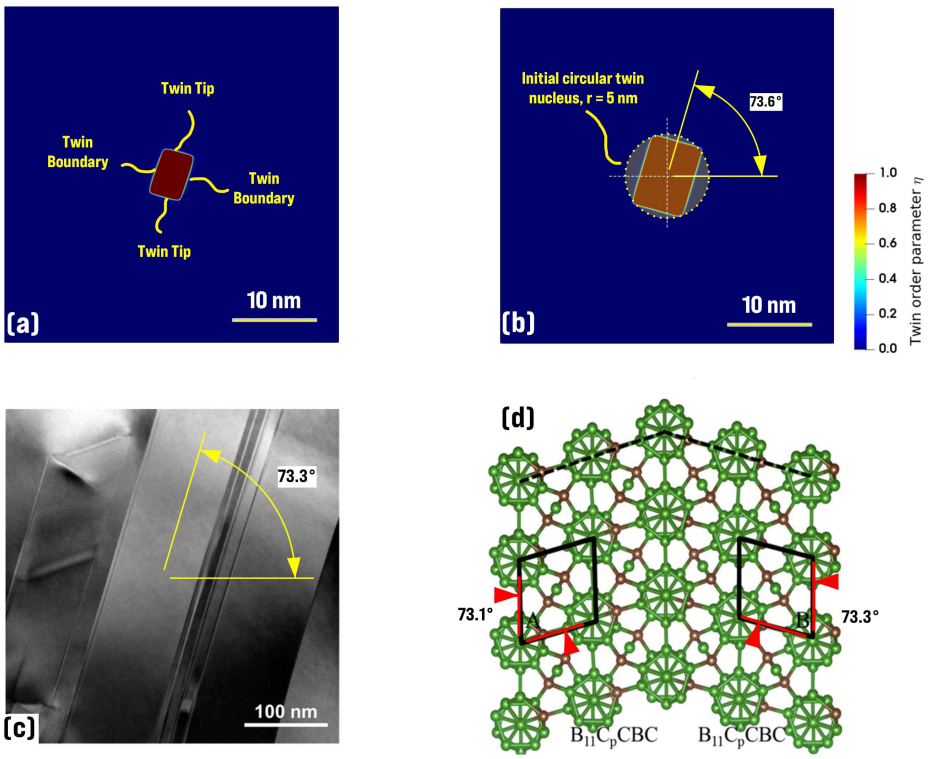

Figure 5.5: The distribution of twin order parameter in boron carbide from snapshots taken at (a) 1 ps and (b) 2 ps for samples deformed under shear strain: (a) Various interfaces associated with a single twin embryo; (b) Direction of twin propagation in a 40×40 nm plate with an initial circular twin nucleus of radius 5 nm denoted by yellow dotted line; (c) TEM image showing the larger twin spacing in boron carbide at the 100 nm scale with an angle of 73.3° [444]; and (d) Symmetric twin in boron carbide with inclination angles of 73.1° and 73.3° on the two sides predicted by density functional theory [444]. (c) and (d) reproduced with permission from [444]. (For interpretation of the references to color in this figure, the reader is referred to the web version of this article.)

Following this basic validation for boron carbide with results under restrictions of experimental limitations in the literature, the change of the twin size (e.g., length and thickness) and twin interactions in a single crystal boron carbide are explored in order to measure the velocity of twin tips and boundaries (Figure 5.6). Being an important parameter for indicating the twin boundary propagation as a key plasticity mechanism, the present findings have important implications for studying the morphology of twins. To accomplish this, the velocities are calculated by tracking the mid points ($\eta = 0.5$) on the twin tip and twin boundary interfaces with respect to

time. Currently, there is no such statistical data on twin boundary velocity for single crystalline boron carbide, and so we hope our results will provide some new insights for future research. Considering only one nucleus in the center of the domain, the twin boundary (red colored) and twin tip (blue colored) velocities are shown in Figure 5.6(a). The distribution of the twin order parameter at different steps along with the direction for twin tip and twin boundary are also shown in the inset, where the applied shear loading of 0.3 is in the $[1\bar{1}0\bar{1}]$ direction. By choosing $\Delta t = 1\,\text{fs}$ as the time step, the initial circular nucleus shrinks in size until reaching to a stable shape. After that time, the twin starts to grow in the direction of 73.6° with respect to the loading direction. In this case, the twin tip and twin boundary velocities are larger at the beginning of the loading in comparison with later time instants due to the detwinning process [449] and larger space for unconfined propagation. In addition, the average of twin tip velocities ($2.71 \pm 0.86\,^{\text{nm}}/_{\text{ps}}$) are larger than twin boundaries ($2.91 \pm 0.37\,^{\text{nm}}/_{\text{ps}}$) as a result of having a larger aspect ratio. For the two nuclei scenario shown in Figure 5.6(b), the average of twin boundary velocities of the middle embryo ($2.76 \pm 0.48\,^{\text{nm}}/_{\text{ps}}$) are larger than the single twin case because of the tendency of the middle twin to interact with the twin at the top of the inset (termed as Twin #2). The variation of the twin tip velocity is also smaller than the single twin case on the basis of the fast growth of the twin's aspect ratio. Moreover, Twin #2 has a lower aspect ratio, indicating that the two twins will have a wedge shape in the case of interaction between each other. The spreading of a wedge shaped twin has been seen for other ceramics as a result of rapid load drop associated with the twinning process [450].

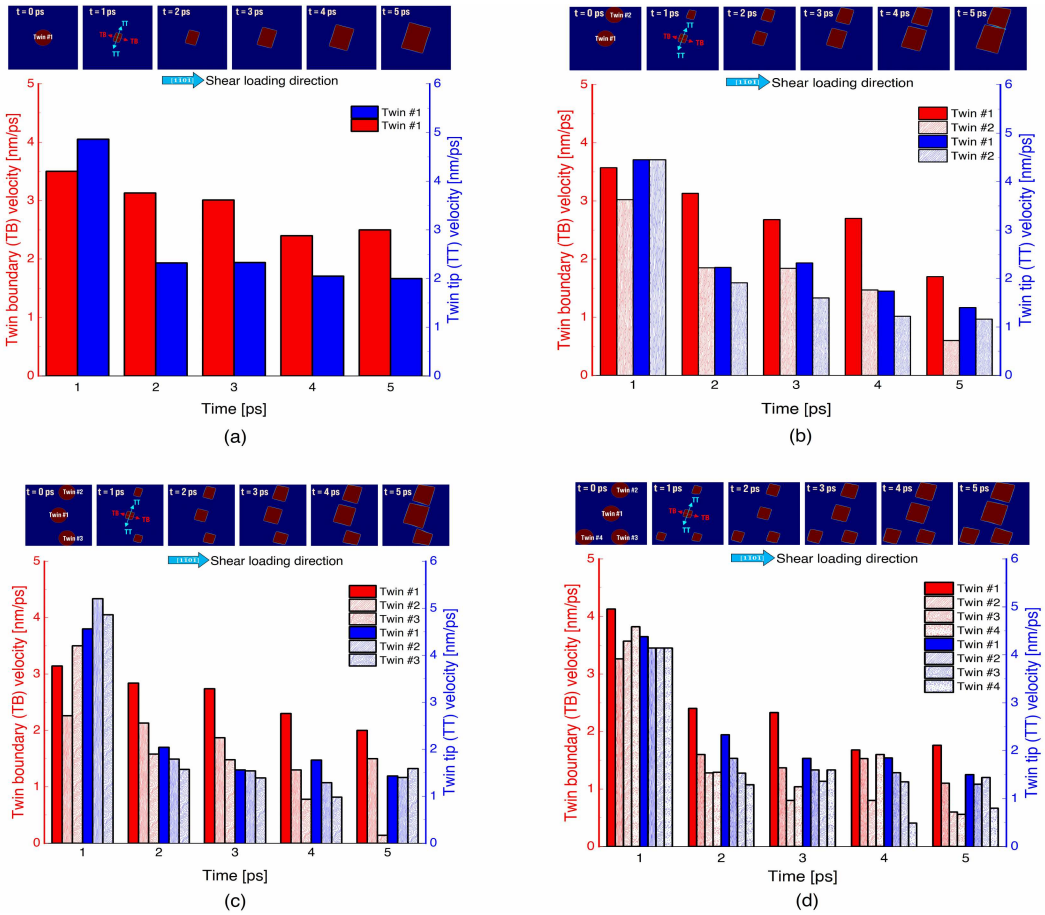

Figure 5.6: Bar charts showing the twin boundary (red arrow) and twin tip (blue arrow) velocities for a single crystal boron carbide by considering different numbers of twin embryos under a shear loading of 0.3: (a) Velocities of a single twin in the center of the numerical geometry at various noted time steps. The insets show the evolution of the twin, parallel and orthogonal to the habit plane; (b) Velocities of two nuclei with respect to time. In the inset, the second twin is inserted at $x = 25\,\text{nm}$ and $y = 35\,\text{nm}$; (c) Velocities are shown for three twin embryos. A different growth direction for the third twin is clear in the inset; (d) Change of twin boundary and twin tip velocities for four nucleus. The growth of each embryo is illustrated in the inset. (For interpretation of the references to color in this figure, the reader is referred to the web version of this article.)

When placing Twin #3 at the bottom right of the specimen near the fixed boundary conditions (Figure 5.6(c)), the average twin boundary velocities of Twins #1 and #2 are increased. This is likely a consequence of increasing the twins' aspect ratio, which can be related to the high tendency of twins to interact. Moreover, Twin #3 grows in the direction perpendicular to other embryos because of arresting at the boundary in

the scenario depicted for the three twin systems in Figure 5.6(c). By adding another embryo close to the fixed boundary condition in a four twin system (Figure 5.6(d)), all the twins' aspect ratio decreased, with Twin #2 decreased by ∼30% in both length and width. Furthermore, the embryo in the middle tended to connect to the nucleus at the top of the domain as a result of the proximity of Twin #2 with the shear loading. Altogether, adding more twin nuclei leads to decreasing the twin boundary velocity of Twin #1, which can be caused by the local stress created from other nuclei to restrict the movement of the boundary.

5.5.2 Fracture-Induced Twinning in Single Crystal Magnesium

The next example seeks to evaluate the current phase-field approach for studying twinning at a crack tip in magnesium. This is motivated by our need to better understand the sequence and competition of twinning and fracture, which is difficult to unravel experimentally [308] (e.g., via nanoindentation tests). In this subsection, a stationary pre-existing crack is considered by a thin notch in a two-dimensional geometry for studying twinning under mode I and mode II cracking. The numerical setup is shown in Figure 5.7. An initially square domain of size 100 nm by 100 nm with a pre-existing edge crack of length 50 nm and thickness 4 nm with a rounded tip of radius 2 nm is considered for simulations under a plain-strain condition. The crack is assigned a finite radius to alleviate extreme deformations due to singular stress fields at the tip [451]. For this problem, only Eqs 5.83 and 5.88 are solved iteratively. For boundary conditions, the crack surface is free of traction ($P_{ij}n_j = 0$) and the force conjugate to the order parameter ($2\kappa_{ij}\eta_{,i}n_j$) is set to zero along all of the boundary conditions. Along each external boundary condition except for the crack surface, the displacements for pure mode I or mode II loading are imposed as was done in [452]. The orientation of the twin system, $\boldsymbol{s}$ and $\boldsymbol{m}$, is chosen such that the resolved shear stress is maximum (i.e., $\theta = 1.2$ rad for mode I and $\theta = 0$ for mode II). In addition, a small twin nucleus with a radius of 0.8 nm at the crack tip is considered as the initial

condition for the twin order parameter.

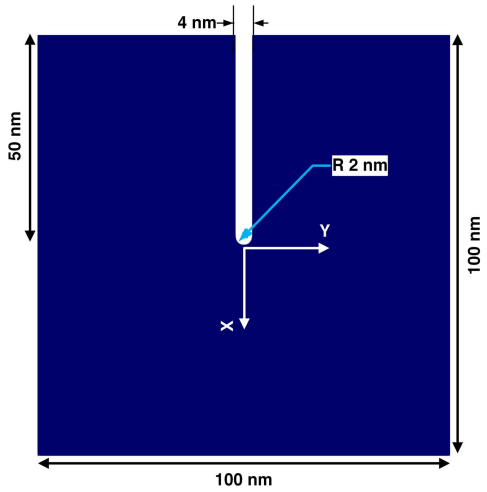

Figure 5.7: A square domain containing an edge crack for numerical simulations under plain strain condition. The origin of the (X, Y) coordinate system is at the crack tip, with positive X downward and positive Y to the right.

The phase-field results for mode I loading are illustrated in Figure 5.8 where a contour of the twin order parameter is plotted. It is clear that the twin growth to the external boundaries is prohibited by the imposed displacement boundary conditions. By progressing in time, the $\langle 1\,0\,\bar{1}\,1\rangle\{\bar{1}\,0\,1\,2\}$ twin band is nucleated at the crack tip and develops at an externally applied strain of 5% due to the stress concentration. The shape and angle of the twin of 69.4° at $t = 110\,\mathrm{ps}$ are in agreement with the atomic simulation results of tensile twinning in single crystal magnesium [453], where a value of 69° was reported.

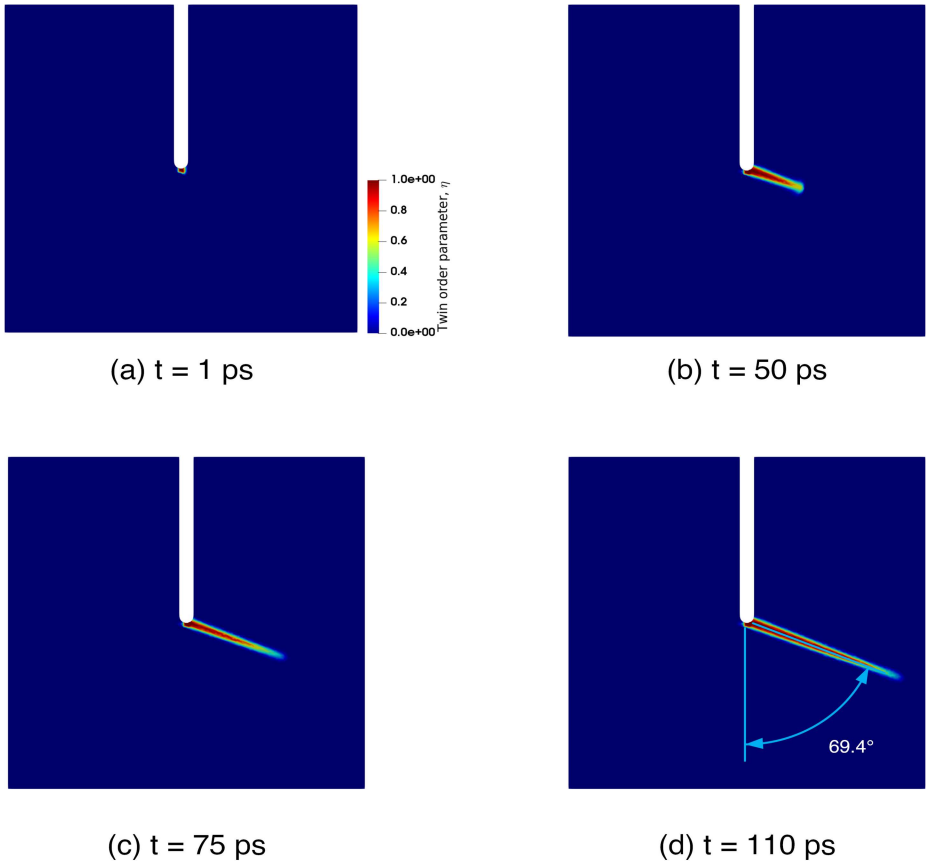

Figure 5.8: Time-evolved twin morphology for mode I loading of a single crystal magnesium at 4% tensile strain: (a) $t = 1\,\text{ps}$; (b) $t = 50\,\text{ps}$; (c) $t = 75\,\text{ps}$; and (d) $t = 110\,\text{ps}$. The resulting twin propagation angle is 69.4°, which is close to the molecular dynamics results of $\sim 69°$ [453]. (For interpretation of the references to color in this figure, the reader is referred to the web version of this article.)

The mode II case is shown in Figure 5.9 for the twin order parameter at various time instants. Similar to the mode I case, the twin nucleates at the crack tip and starts to grow until it is inhibited by the right boundary condition. As expected, the twin system is aligned in a direction that has the maximum resolved shear stress ($\theta = 0$). This results is in qualitative agreement with the stationary phase-field model under similar boundary conditions [419], thus providing additional validation for our time-resolved phase-field model. This needle-shaped lenticular twin, which has also been observed in [454], suggests that twin growth occurs by extension of a fast twin tip followed by a coordinated slower migration of the boundaries [244].

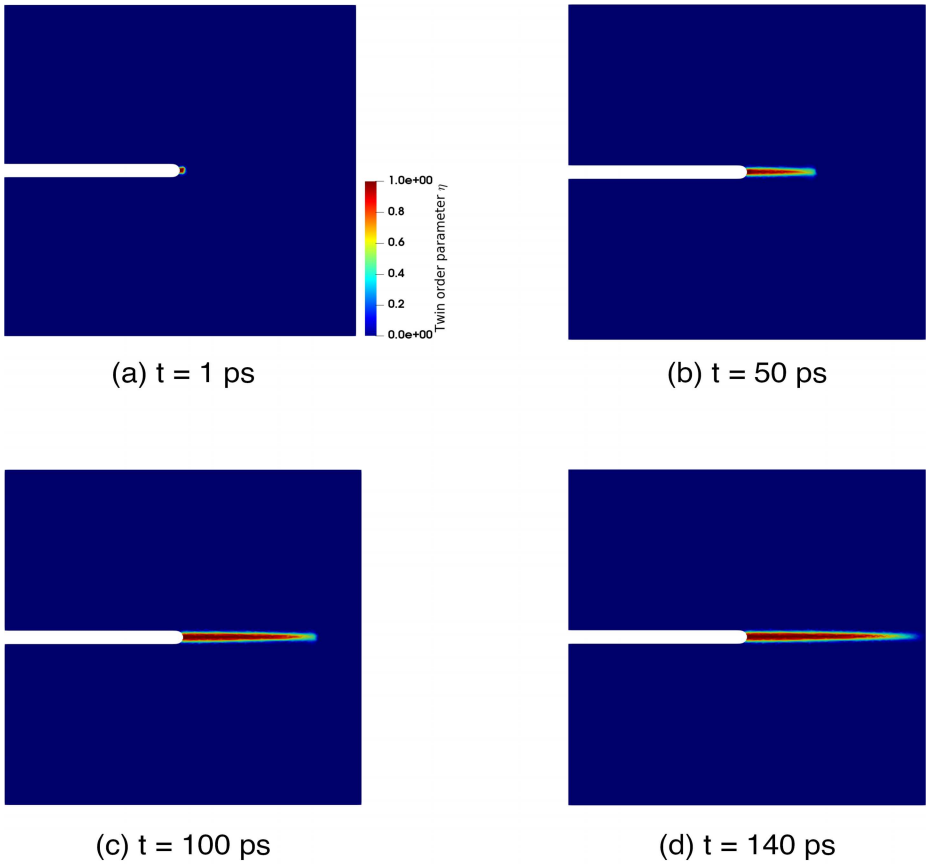

Figure 5.9: Time-evolved order parameter for mode II loading of a single crystal magnesium at 5% tensile strain: (a) $t = 1\,\text{ps}$; (b) $t = 50\,\text{ps}$; (c) $t = 100\,\text{ps}$; and (d) $t = 140\,\text{ps}$. (For interpretation of the references to color in this figure, the reader is referred to the web version of this article.)

5.5.3 Phase-Field Modeling of Fracture Subjected to Shear and Compressive Loading in Anisotropic Boron Carbide Single Crystals

The subject of crack growth in the literature has mainly focused on mode I fracture because opening mode crack growth is preferred before that under mixed mode or pure shear mode conditions [455]. It is recognized that, even under pure shear loading, local tensile stresses at the tip result in crack growth under mode I conditions [456]. However, cracks can grow in brittle materials under mode II loading when the ratio between the critical stress intensity factors, ${}^{K_{IIc}}/_{K_{Ic}}$, is low [389]. It is also believed that at a sufficiently high confining pressure, the crack is assumed to extend along

a smooth curved path that maximizes K_{II} [457]. In heterogeneous brittle solids, the different microstructural inhomogenities (e.g., voids and microcraks) result in a large process regions at the crack tip, and this may lead to macroscopic mode II failure under compressive loads in such materials [458]. The study of crack initiation and propagation of mode II fracture is, thus, important in order to better understand the behavior of cracks in brittle solids.

Classically in phase-field modeling in the literature [426], it is assumed that for compressive deformation states, crack growth does not take place. To deal with this, a common technique is to decompose the strain energy density into tensile and compressive parts using a spectral decomposition [377], or a hydrostatic-deviatoric approach [387]; however, both of the decomposition have disadvantages that have yet to be addressed. Specifically, regarding the spectral decomposition, the force-displacement curve shows unphysical stiffening in the fully-cracked specimen [390]. For the hydrostatic-deviatoric method, there are limitations for compression-dominated loading (e.g., the material is allowed to crack in volumetric expansion and shear, but not in volumetric compression) [356]. In addition, both of these popular decompositions can only be used for isotropic materials [391]. Nevertheless, boron carbide has strong anisotropic elasticity ($\frac{E_{\max}}{E_{\min}} = 8.11$, where $E_{\max}$ and $E_{\min}$ are the general maximum and minimum Young's modulus, respectively) [459]. To address these limitations in the current study, the elastic strain energy density, Eq 5.45, in small deformations can be rewritten as [391]

$$\Psi^e = \frac{1}{2}\,\mathrm{tr}\,(\boldsymbol{\Psi})^2\,; \quad \boldsymbol{\Psi} = \boldsymbol{\Psi}_\lambda + \boldsymbol{\Psi}_\mu, \tag{5.94}$$

where $\boldsymbol{\Psi}_\lambda = \sqrt{\lambda}\varepsilon^e$ and $\boldsymbol{\Psi}_\mu = \sqrt{\mu}\varepsilon^e$ are the tensorial square roots of the elastic strain energy density, which are dependent on the material directions. Finding the principle roots of the strain energy densities $\boldsymbol{\Psi}_1$, $\boldsymbol{\Psi}_2$ and $\boldsymbol{\Psi}_3$ with corresponding principle directions $\boldsymbol{n}_1$, $\boldsymbol{n}_2$, and $\boldsymbol{n}_3$, the total principle strain energy densities under

compressive (-) or tensile (+) types of deformation can be written respectively as

$$\Psi_{-}^{e} = \frac{1}{2}\langle \boldsymbol{\Psi}_1 \rangle_{-} + \frac{1}{2}\langle \boldsymbol{\Psi}_2 \rangle_{-} + \frac{1}{2}\langle \boldsymbol{\Psi}_3 \rangle_{-}\,, \tag{5.95}$$

$$\Psi_{+}^{e} = \frac{1}{2}\langle \boldsymbol{\Psi}_1 \rangle_{+} + \frac{1}{2}\langle \boldsymbol{\Psi}_2 \rangle_{+} + \frac{1}{2}\langle \boldsymbol{\Psi}_3 \rangle_{+}\,. \tag{5.96}$$

This new energy density decomposition will be employed to predict the crack propagation under mixed mode loading in boron carbide.

5.5.3.1 Crack Initiation and Propagation Under Biaxial Compressive Stress in Single Crystal Boron Carbide

Consider the biaxial compression test of a single crystal B_4C specimen with a single pre-existing notch under plane strain condition as shown in Figure 5.10. The dimensions of the square domain are those of Figure 5.7, and the material parameters are the same as those mentioned in Table 5.1. Additionally, the fracture surface energy (Υ) and cleavage anisotropy factor (β) are set to 3.27 and $100\,{}^{\mathrm{J}}/_{\mathrm{m}^2}$ (or 0 for isotropic damage), respectively [460]. In the simulations, a total of 323,460 triangular elements were used to discretize the domain with a finer mesh assigned to critical zones. A high confining stress is chosen such that the opening stress intensity factors at the tip of the crack in any direction is zero. The stress parallel to the crack plane is assumed to be larger than the stress values normal to the crack plane ($\sigma_{\mathrm{XX}} > \sigma_{\mathrm{YY}}$). The initial condition for the time-dependent fracture order parameter and time step are set to $\xi(t=0) = 0.01$ and $\Delta t = 0.5\,\mathrm{fs}$, respectively. In the simulations, all the frictional effects on the crack surfaces are disregarded.

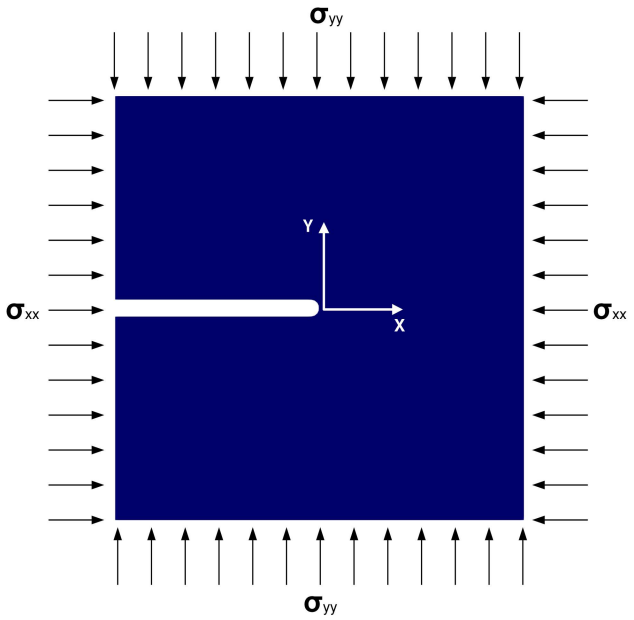

Figure 5.10: Geometry and boundary conditions in the numerical simulations of biaxial loading in a pre-notched domain. The Cartesian coordinate system is considered at the crack tip.

The crack evolution process under these numerical conditions is depicted in Figure 5.11. As shown, biaxial compression first leads to the initiation of the crack from the tip of the notch (Figure 5.11(a)). The range of the fracture order parameter indicates that the crack is not fully formed at $t = 0.5\,\text{ps}$. At $t = 0.75\,\text{ps}$ (Figure 5.11(b)), the crack kinks as two single straight branched cracks at a small angle. By progressing in time to $t = 0.9\,\text{ps}$, two anti-symmetric cracks begin to propagate toward the top and bottom boundaries due to the larger compressive normal stress parallel with the crack plane (Figure 5.11(c)). In addition, the crack grows in incrementally small steps that are consistent with experimental observations for other brittle materials [461, 462]. At the last time frame of $t = 1\,\text{ps}$, the propagation path of cracks in single crystal B_4C is shown (Figure 5.11(d)). As can be seen, the crack patterns follow a curvilinear path described by a function ax^b. The crack paths reported analytically in [463] and measured experimentally in [461] support this result. In the studied experiments, b was found in the interval 1.43 to 1.58 for pre-fractured specimens of gypsum under

uniaxial and biaxial compression [457]. From the analytical model, the exponent was required to be equal to 1.5 in order to be independent of the crack extension length [463]. For boron carbide in this study, the exponent b is obtained as 1.66 ± 0.06 and this is in reasonable agreement with the predicted theory for brittle materials [457]. The curvature parameter a is equal to $0.49 \pm 0.08\,(\mathrm{nm})^{-0.66}$ and the angle of the branched kink is 73.1°, which is in good agreement with the value (70°) reported in [388].

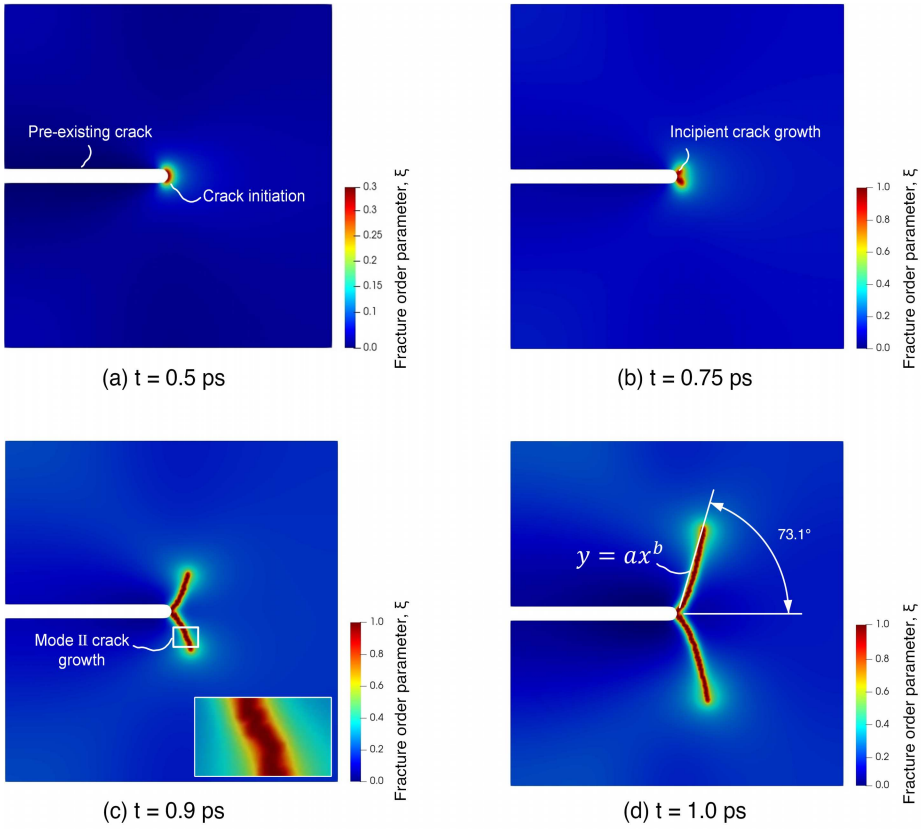

Figure 5.11: Crack evolution obtained with the phase-field approach under a biaxial stress loading condition in single crystal B_4C: (a) At $t = 0.5\,\mathrm{ps}$, the fracture order parameter starts to accumulate at the tip of the pre-existing notch. The maximum value of the order parameter is 0.3, showing that the crack region is not fully formed; (b) Two fully cracked regions start to grow via an incipient kink at $t = 0.5\,\mathrm{ps}$; (c) Two anti-symmetric cracks at $t = 0.9\,\mathrm{ps}$ which emerged first at the crack tip. The inset shows the mode II crack growth under a combined load of shear and high compression. (d) Stable propagation of cracks along a curvilinear path described by $y = ax^b$ at $t = 1.0\,\mathrm{ps}$. The angle from the previous crack plane to the new assumed direction of crack growth is 73.1°. (For interpretation of the references to color in this figure, the reader is referred to the web version of this article.)

The homogeneous damage distribution ($\xi \sim 0.5$) in Figure 5.11 is also due to the hydrostatic nature of the loading. As it is shown in [354], the damage initiation criteria in the current phase-field potential for fracture is fulfilled at infinitesimal load; however, at the crack free surface where the load is not applied, the color is dark blue, which indicates no damage, as expected.

5.6 Concluding Remarks

A robust finite element procedure for solving a coupled system of equilibrium and time-dependent Ginzburg–Landau equations has been derived based on thermodynamic laws. The model has been used for studying the evolution of twinning deformation and fracture in anisotropic single crystal magnesium and boron carbide at finite strains. The formulation considers distinct order parameters for fracture and twinning. For the first time, a monolithic strategy has been employed for solving the coupled mechanical equilibrium and order parameters evolution equations. The computational procedures and numerical algorithms are implemented using the Python-based open-source platform FEniCS. The present nonlinear finite element code has been developed and used to study: (i) the growth and propagation of deformation twinning in single crystal magnesium and boron carbide, (ii) fracture-induced twinning in single crystal magnesium under pure mode I and mode II loading, and (iii) the prediction of the crack path under biaxial compressive stress loading in single crystal boron carbide. The numerical results for all the problems are in agreement with the available experimental data and analytical solutions in the literature. It has been demonstrated through numerical simulations that the proposed model delivers adequate results matching qualitatively a variety of observed phenomena, including the growth of existing twin embryos, the effect of pre-existing cracks on the twin path under various loading, and the propagation of cracks under compression for highly anisotropic boron carbide. The current contribution opens up new possibilities for multi-scale fracture models. In the future, our finite element-based phase-field model

can be applied for studies of phase transformations (e.g., amorphization) and interaction between plasticity and fracture under high strain-rate loading. As a next step, the current model could be combined with the discrete localized plastic flow (e.g., shear band and dislocation pileups) and thermally-activated mechanisms (e.g., melting) to capture the behavior of the brittle materials in laser spall experiments.

5.7 Data Availability

The authors declare that the main data supporting the findings of this study are available within this article. Extra data are available from the corresponding authors upon reasonable request.

5.8 Code Availability

The Python code, generated during the current study, is part of the FEniCS project available at http://www.fenicsproject.org/download, and an example for the computational implementation is available in [302] to be used under the GNU Public license [303].

5.9 Declaration of Competing Interests

The authors declare no competing financial interests or personal relationships.

5.10 CRediT Authorship Contributions Statement

B.A developed the model, wrote the code, designed and performed all simulations, analyzed results, and wrote the original draft. H.J developed the model, analyzed results, reviewed, and edited the submitted journal article. B.E.A helped with the code, allocated the computational resources, reviewed and edited the submitted journal article. A.R helped in computational aspects, reviewed and edited the submitted

journal article. J.D.H supervised the research, acquired funding, reviewed, and edited the submitted journal article. All authors discussed the results.

5.11 Acknowledgements

The authors acknowledge support from Natural Sciences and Engineering Research Council of Canada (NSERC) Discovery Grant 2016-04685 and NSERC DNDPJ 531130-18, and partial support of the MIUR-PRIN project XFAST-SIMS (no. 20173C478N).

Chapter 6

Conclusions & Future Work

6.1 Conclusions

This thesis developed advanced physics-based computational models to study the mechanical response of novel light-weigh materials under various loading conditions, seeking to address the limitations that exists in experimental approaches (e.g., high Z contrast necessary for good imaging quality in X-ray microtomography [464]) or first principle methods (e.g., molecular dynamics simulations, density functional theory, and lattice static models). Various computational approaches were applied to explore the failure mechanisms of three different materials system: 1. novel self-propagating high-temperature synthesized $(\gamma + \alpha_2)$-TiAl/Ti_3Al-Al_2O_3 ceramic-metal composites, 2. nanoscale single crystal magnesium, and 3. nano-grained single crystal boron carbide. For the cermet material system, a three-dimensional microstructure-based finite element method, employing a modified variational formulation of the Gurson model, was used to capture the strain rate dependent behavior. Then, the numerical results were validated through multi-scale testing and imaging (e.g., quasi-static and dynamic uniaxial compression tests). For magnesium and boron carbide, a time-resolved phase field approach was developed to investigate the predominant deformation mechanisms, including fracture and twinning. The finite element method was utilized to deal with the coupled phase-field and elasticity equations, and a monolithic iterative procedure was applied in an open-source finite element computing platform to solve the gov-

erning equations. Due to the limited published data involving single crystal boron carbide, the model was initially solved for the growth and propagation of a single twin embryo in single crystal magnesium, and the phase-field results were validated with the most recent molecular dynamic simulations for twin interface velocities from this material. After using and validating the model for magnesium, the phase-field approach was extended to describe the fracture and twinning in single crystal boron carbide.

This thesis achieves its objective of providing a comprehensive study of the mechanical response and deformation mechanisms of novel light-weight materials used in impact applications in the form of two peer-reviewed published papers (Chapters 2 and 3) and two submitted papers (Chapters 4 and 5). The main results from this thesis are summarized for further emphasis:

- Considering a commercial cermet rather than an idealised one with high particle volume fraction, a three-dimensional FCC unit cell model could reasonably capture the experimentally observed stress-strain response under quasi-static uniaxial compression tests. The numerical results also showed that increasing the particles volume fraction from 65% to 72% resulted in increasing the material strength by 6%. In addition, there was a gradual transition from low to high strain ratio (the ratio of transverse to longitudinal strain), attributed to different behavior of particle clustering or independent reinforcements.

- Proposing a modified variation formulation of the Gurson model along with a polynomial cohesive zone model for the decohesion of the particle-matrix interface, the results indicated that most of the dynamic properties of the $(\gamma + \alpha_2)$-TiAl/Ti_3Al-Al_2O_3 cermet (e.g., failure strain) are much higher than the quasi-static loading. A transitional strain rate describing the increase in compressive strength was $800\,s^{-1}$ at 2480 MPa, which were in good agreement with experimental data. Furthermore, for different particle shapes, increasing the void

volume fraction resulted in decreasing the initiation toughness and increasing the propagation toughness.

- Implementing a time-resolved phase-field model for studying the evolution of twins in Mg, the interface velocity profiles in both twin tip and twin boundary directions were extracted to obtain the kinetic coefficient by validating the results with molecular dynamics simulations. The results indicated that the twin tip velocities were constant, while the twin boundary velocities were decreasing when approaching to the outer boundary conditions. In addition, the magnitude of the shear stress in the twinned region decreased as a function of time and became negative; this has been observed experimentally.

- Employing calibrated and validated continuum mechanical theory, the physical mechanisms of twinning and fracture in anisotropic brittle materials were studied. The sequence of deformation mechanisms were modeled in the ceramic boron carbide by solving the simultaneous geometric nonlinearity, nonlinear elasticity, and surface energy anisotropy with the finite element method. Results in this thesis provided new insights into activity or inactivity of different inelasticity mechanisms under compression and shear. For example, the crack propagation and growth in boron carbide was predicted for specimen under biaxial compressive loading by comparing with an analytical solution from the literature.

6.2 Future Work

The majority of future work will be centered around modeling and validation of the dynamic failure of boron carbide. Specific activities will include:

- Considering the thermal and plastic parts into the phase-field formulation for fracture, the current model from Chapter 5 can be expanded to study phase transformation in brittle ceramics under high impact loading. By considering

the complete terms for the inelastic part of the deformation gradient, including temperature [465], dislocation [466], and amorphization [71], the competition of these mechanisms can be quantified and serve as a foundation for future optimization of boron carbide under ballistic impact loading. Further challenges arise since many of these deformation features may be inherent in as-formed plates [467], in additional to being able to be activated during dynamic failure [468].

- Tracking complex crack trajectories induced by the spatial variation of microstructure features across a heterogeneous material that are difficult to capture with conventional numerical methods [469] can be achievable. In fact, the nano-grained boron carbide, with smaller grains and more grain boundaries than conventional 15 μm-sized B_4C [470], has been observed to have differences in crack propagation (i.e., conventional boron carbide is solely transgranular [100], while the nano-grained B_4C is a combination of trans- and inter-granular [471]). Therefore, predicting the crack path during loading can be of great help for future material design.

- Implementing the model for large scale problems using high performance computing clusters to simulate the crack behavior in engineering applications [472] ($\sim 10 \times 10 \times 1\,\text{cm}$). From a modeling perspective, current computing capacity limits the study of multi-length scale material response at a realistic physical dimension.

- Extension of the model to study the boundary value problems involving more complicated geometries and boundary conditions [473]. This includes improvements in meshing strategies for multi-scale fracture or different orientation of crystal structure [474].

- Generalizing the interpolation functions used in the phase field model to match

additional data for other stress-deformation states. These can be higher order functions with different coefficients, which can be obtained from MD simulations [475] to better predict the dynamic behavior of boron carbide.

- The integration of these activities into a comprehensive physics-based model for nano-grained boron carbide will allow us to provide guidance to our partners at USA Army Research Laboratory (ARL) for material refinement. This could include, for example, informing ARL of the effects of grain size or spatially-distributed twinning on properties and performance. ARL would lead activities to determine what processing conditions and additives are needed to produce the desired microstructure, and we would use these directions through computational materials science.

Bibliography

[1] E. Greenhalgh and M. Hiley, "The assessment of novel materials and processes for the impact tolerant design of stiffened composite aerospace structures," *Composites Part A: Applied Science and Manufacturing*, vol. 34, no. 2, pp. 151–161, 2003.

[2] K. Rao and Y. Prasad, "Processing map and hot working mechanisms in a p/m tial alloy composite with in situ carbide and silicide dispersions," *Materials science and engineering: A*, vol. 527, no. 24-25, pp. 6589–6595, 2010.

[3] M Yamaguchi *et al.*, "High-temperature structural intermetallics," *Acta Materialia*, vol. 48, no. 1, pp. 307–322, 2000.

[4] X. Wu, "Review of alloy and process development of tial alloys," *Intermetallics*, vol. 14, no. 10-11, pp. 1114–1122, 2006.

[5] C. Fu and M. Yoo, "Interfacial energies in two-phase tial-ti3al alloy," *Scripta materialia*, vol. 37, no. 10, pp. 1453–1459, 1997.

[6] G. Was and T Foecke, "Deformation and fracture in microlaminates," *Thin Solid Films*, vol. 286, no. 1-2, pp. 1–31, 1996.

[7] T. Wang and J. Zhang, "Thermoanalytical and metallographical investigations on the synthesis of tial3 from elementary powders," *Materials chemistry and physics*, vol. 99, no. 1, pp. 20–25, 2006.

[8] C. Koch, "Intermetallic matrix composites prepared by mechanical alloying—a review," *Materials Science and Engineering: A*, vol. 244, no. 1, pp. 39–48, 1998.

[9] K. Kumar and J. Whittenberger, "Discontinuously reinforced intermetallic matrix composites via xd synthesis," *Materials science and technology*, vol. 8, no. 4, pp. 317–330, 1992.

[10] C. G. Mangin *et al.*, "Mmcs for automotive engine applications," *JoM*, vol. 48, no. 2, pp. 49–51, 1996.

[11] D. Liu and W. Tuan, "Microstructure and thermal conduction properties of al2o3-ag composites," *Acta Materialia*, vol. 44, no. 2, pp. 813–818, 1996.

[12] M. Karamis *et al.*, "Analyses of metallurgical behavior of al–sicp composites after ballistic impacts," *Composite Structures*, vol. 64, no. 2, pp. 219–226, 2004.

[13] H. Chang *et al.*, "High strain rate characteristics of 3-3 metal–ceramic interpenetrating composites," *Materials Science and Engineering: A*, vol. 528, no. 6, pp. 2239–2245, 2011.

[14] W. Wrzesinski and J. Rawers, "Self-propagating high-temperature synthesis of tial-sic and tial-al2o3 intermetallic composites," *Journal of Materials Science Letters*, vol. 9, no. 4, pp. 432–435, 1990.

[15] C. Yeh and S. Su, "In situ formation of tial–tib2 composite by shs," *Journal of alloys and compounds*, vol. 407, no. 1-2, pp. 150–156, 2006.

[16] R Ramaseshan *et al.*, "Microstructure and some properties of tial-ti2alc composites produced by reactive processing," *Intermetallics*, vol. 7, no. 5, pp. 571–577, 1999.

[17] D. E. Alman, "Reactive sintering of tial–ti5si3 in situ composites," *Intermetallics*, vol. 13, no. 6, pp. 572–579, 2005.

[18] Z. Li *et al.*, "High temperature oxidation behaviour of a tial–al2o3 intermetallic matrix composite," *Corrosion Science*, vol. 46, no. 8, pp. 1997–2007, 2004.

[19] S. Shu *et al.*, "Effect of b4c size on the fabrication and compression properties of in situ tib2–ti2alc/tial composites," *Journal of Alloys and Compounds*, vol. 551, pp. 88–91, 2013.

[20] S. Shu *et al.*, "Comparative study of the compression properties of tial matrix composites reinforced with nano-tib2 and nano-ti5si3 particles," *Materials Science and Engineering: A*, vol. 560, pp. 596–600, 2013.

[21] S. M. Wiederhorn and L.-S. H. Lum, "Structural behavior of ceramics," Tech. Rep., 2016.

[22] M. Anglada, "Assessment of mechanical properties of ceramic materials," in *Advances in Ceramic Biomaterials*, Elsevier, 2017, pp. 83–109.

[23] M.-S. Suh *et al.*, "Friction and wear behavior of structural ceramics sliding against zirconia," *Wear*, vol. 264, no. 9-10, pp. 800–806, 2008.

[24] D. Zhang *et al.*, "Low cost ti (al/o)/al2o3 and tixaly/al2o3 composites," *Materials Technology*, vol. 18, no. 2, pp. 94–98, 2003.

[25] N Travitzky *et al.*, "Alumina–ti aluminide interpenetrating composites: Microstructure and mechanical properties," *Materials Letters*, vol. 57, no. 22-23, pp. 3422–3426, 2003.

[26] A. Krell and P. Blank, "Grain size dependence of hardness in dense submicrometer alumina," *Journal of the American Ceramic Society*, vol. 78, no. 4, pp. 1118–1120, 1995.

[27] A. Krell and P. Blank, "The influence of shaping method on the grain size dependence of strength in dense submicrometer alumina," *Journal of the European Ceramic Society*, vol. 16, no. 11, pp. 1189–1200, 1996.

[28] E. Medvedovski, "Ballistic performance of armour ceramics: Influence of design and structure: Part i," *Ceramics International*, vol. 36, no. 7, pp. 2103–2115, 2010.

[29] J. Chevalier and L. Gremillard, "Ceramics for medical applications: A picture for the next 20 years," *Journal of the European Ceramic Society*, vol. 29, no. 7, pp. 1245–1255, 2009.

[30] Y. Wang *et al.*, "Microstructural characteristics of ti–45al–8.5 nb/tib2 composites by powder metallurgy," *Journal of alloys and compounds*, vol. 468, no. 1-2, pp. 505–511, 2009.

[31] N Forouzanmehr *et al.*, "Study on solid-state reactions of nanocrystalline tial synthesized by mechanical alloying," *Journal of Alloys and Compounds*, vol. 471, no. 1-2, pp. 93–97, 2009.

[32] W. Zhang *et al.*, "Tial/b4c composite fabricated by high energy ball milling and hot press sintering processes and its mechanical properties," *Materials Science and Engineering: A*, vol. 527, no. 27-28, pp. 7436–7441, 2010.

[33] Z. Cai and D. Zhang, "Sintering behaviour and microstructures of ti (al, o)/al2o3, ti3al (o)/al2o3 and tial (o)/al2o3 in situ composites," *Materials Science and Engineering: A*, vol. 419, no. 1-2, pp. 310–317, 2006.

[34] S. Maloy and G. Gray III, "High strain rate deformation of ti48al2nb2cr," *Acta Materialia*, vol. 44, no. 5, pp. 1741–1756, 1996.

[35] S Osovski *et al.*, "The respective influence of microstructural and thermal softening on adiabatic shear localization," *Mechanics of Materials*, vol. 56, pp. 11–22, 2013.

[36] A. Belenky *et al.*, "Static and dynamic fracture of transparent nanograined alumina," *Journal of the Mechanics and Physics of Solids*, vol. 58, no. 4, pp. 484–501, 2010.

[37] A. Krell *et al.*, "Subcritical crack growth in al2o3 with submicron grain size," *Journal of the European Ceramic Society*, vol. 23, no. 1, pp. 81–89, 2003.

[38] W. J. Joost, "Targeting high impact r&d for automotive magnesium alloys," in *Magnesium Technology 2017*, Springer, 2017, pp. 5–6.

[39]A. A. Luo, "Magnesium casting technology for structural applications," *journal of Magnesium and Alloys*, vol. 1, no. 1, pp. 2–22, 2013.

[40]W. McG. Tegart, "Independent slip systems and ductility of hexagonal polycrystals," *Philosophical Magazine*, vol. 9, no. 98, pp. 339–341, 1964.

[41]W. J. Joost and P. E. Krajewski, "Towards magnesium alloys for high-volume automotive applications," *Scripta Materialia*, vol. 128, pp. 107–112, 2017, ISSN: 1359-6462. DOI: https://doi.org/10.1016/j.scriptamat.2016.07.035. [Online]. Available: https://www.sciencedirect.com/science/article/pii/S1359646216303621.

[42]Y Liu, P. Tang, M. Gong, R. McCabe, J Wang, and C. Tomé, "Three-dimensional character of the deformation twin in magnesium," *Nature communications*, vol. 10, no. 1, pp. 1–7, 2019.

[43]J Wang, R. Hoagland, J. Hirth, L Capolungo, I. Beyerlein, and C. Tomé, "Nucleation of a (1 012) twin in hexagonal close-packed crystals," *Scripta materialia*, vol. 61, no. 9, pp. 903–906, 2009.

[44]X. Zhao *et al.*, "Direct observation and impact of co-segregated atoms in magnesium having multiple alloying elements," *Nature Communications*, vol. 10, no. 1, p. 3243, 2019, ISSN: 2041-1723. DOI: 10.1038/s41467-019-10921-7. [Online]. Available: https://doi.org/10.1038/s41467-019-10921-7.

[45]C. L. Williams *et al.*, "Real-time observation of twinning-detwinning in shock-compressed magnesium via time-resolved in situ synchrotron xrd experiments," *Physical Review Materials*, vol. 4, no. 8, p. 083 603, 2020.

[46]Q Sun *et al.*, "Characterization of basal-prismatic interface of twin in deformed titanium by high-resolution transmission electron microscopy," *Philosophical Magazine Letters*, vol. 95, no. 3, pp. 145–151, 2015.

[47]J.-H. Shin *et al.*, "Nanoindentation study for deformation twinning of magnesium single crystal," *Scripta Materialia*, vol. 68, no. 7, pp. 483–486, 2013.

[48]C. D. Barrett and H. El Kadiri, "The roles of grain boundary dislocations and disclinations in the nucleation of {1 0 1 2} twinning," *Acta materialia*, vol. 63, pp. 1–15, 2014.

[49]J. Cheng and S. Ghosh, "A crystal plasticity fe model for deformation with twin nucleation in magnesium alloys," *International Journal of Plasticity*, vol. 67, pp. 148–170, 2015.

[50] J. D. Clayton and J. Knap, "A phase field model of deformation twinning: Nonlinear theory and numerical simulations," *Physica D: Nonlinear Phenomena*, vol. 240, no. 9-10, pp. 841–858, 2011.

[51] G. Proust *et al.*, "Modeling the effect of twinning and detwinning during strain-path changes of magnesium alloy az31," *International Journal of Plasticity*, vol. 25, no. 5, pp. 861–880, 2009.

[52] D. Grady, "Shock-wave compression of brittle solids," *Mechanics of Materials*, vol. 29, no. 3-4, pp. 181–203, 1998.

[53] F. Thevenot, "Boron carbide—a comprehensive review," *Journal of the European Ceramic society*, vol. 6, no. 4, pp. 205–225, 1990.

[54] M. Chen *et al.*, "Dynamic plasticity and failure of high-purity alumina under shock loading," *Nature materials*, vol. 5, no. 8, pp. 614–618, 2006.

[55] K. M. Reddy *et al.*, "Dislocation-mediated shear amorphization in boron carbide," *Science Advances*, vol. 7, no. 8, 2021. DOI: 10.1126/sciadv.abc6714. [Online]. Available: https://advances.sciencemag.org/content/7/8/eabc6714.

[56] G. Subhash *et al.*, "In search of amorphization-resistant boron carbide," *Scripta Materialia*, vol. 123, pp. 158–162, 2016, ISSN: 1359-6462. DOI: https://doi.org/10.1016/j.scriptamat.2016.06.012. [Online]. Available: https://www.sciencedirect.com/science/article/pii/S135964621630255X.

[57] M. Chen *et al.*, "Shock-induced localized amorphization in boron carbide," *Science*, vol. 299, no. 5612, pp. 1563–1566, 2003.

[58] K. M. Reddy *et al.*, "Atomic structure of amorphous shear bands in boron carbide," *Nature communications*, vol. 4, p. 2483, 2013.

[59] M. Chen *et al.*, "Deformation twinning in nanocrystalline aluminum," *Science*, vol. 300, no. 5623, pp. 1275–1277, 2003. DOI: 10.1126/science.1083727. [Online]. Available: https://science.sciencemag.org/content/300/5623/1275.

[60] Q. Yu *et al.*, "Strong crystal size effect on deformation twinning," *Nature*, vol. 463, no. 7279, pp. 335–338, 2010. DOI: https://doi.org/10.1038/nature08692.

[61] G. Chen *et al.*, "Polysynthetic twinned tial single crystals for high-temperature applications," vol. 15, no. 8, pp. 876–881, 2016. DOI: https://doi.org/10.1038/nmat4677.

[62] X. Zhang *et al.*, "Ultrafine-grained boron carbide ceramics fabricated via ultrafast sintering assisted by high-energy ball milling," *Ceramics International*, vol. 44, no. 6, pp. 7291–7295, 2018, ISSN: 0272-8842. DOI: https://doi.org/10.1016/j.ceramint.2018.01.011.

[63] B. M. Moshtaghioun *et al.*, "Does grain size have an influence on intrinsic mechanical properties and conduction mechanism of near fully-dense boron carbide ceramics?" *Journal of Alloys and Compounds*, vol. 795, pp. 408–415, 2019, ISSN: 0925-8388. DOI: https://doi.org/10.1016/j.jallcom.2019.05.037. [Online]. Available: https://www.sciencedirect.com/science/article/pii/S0925838819316950.

[64] M. DeVries, J. Pittari III, G. Subhash, K. Mills, C. Haines, and J. Q. Zheng, "Rate-dependent mechanical behavior and amorphization of ultrafine-grained boron carbide," *Journal of the American Ceramic Society*, vol. 99, no. 10, pp. 3398–3405, 2016.

[65] I. G. Crouch *et al.*, "A study of the penetration behaviour of mild-steel-cored ammunition against boron carbide ceramic armours," *International Journal of Impact Engineering*, vol. 80, pp. 203–211, 2015.

[66] J. D. Hogan *et al.*, "The effects of microstructure and confinement on the compressive fragmentation of an advanced ceramic," *Journal of the American Ceramic Society*, vol. 98, no. 3, pp. 902–912, 2015.

[67] I. J. Beyerlein *et al.*, "Statistical analyses of deformation twinning in magnesium," *Philosophical Magazine*, vol. 90, no. 16, pp. 2161–2190, 2010, ISSN: 1478-6435. DOI: 10.1080/14786431003630835. [Online]. Available: https://doi.org/10.1080/14786431003630835.

[68] Q. An and W. A. Goddard III, "Atomistic origin of brittle failure of boron carbide from large-scale reactive dynamics simulations: Suggestions toward improved ductility," *Physical review letters*, vol. 115, no. 10, p. 105 501, 2015.

[69] J. Clayton and A. Tonge, "A nonlinear anisotropic elastic-inelastic constitutive model for polycrystalline ceramics and minerals with application to boron carbide," *International Journal of Solids and Structures*, vol. 64, pp. 191–207, 2015.

[70] P. Korotaev *et al.*, "Quantum and classical molecular dynamics simulation of boron carbide behavior under pressure," *AIP Conference Proceedings*, vol. 1793, no. 1, p. 070 014, 2017. DOI: 10.1063/1.4971602. eprint: https://aip.scitation.org/doi/pdf/10.1063/1.4971602. [Online]. Available: https://aip.scitation.org/doi/abs/10.1063/1.4971602.

[71] J. Clayton and J Knap, "Continuum modeling of twinning, amorphization, and fracture: Theory and numerical simulations," *Continuum Mechanics and Thermodynamics*, vol. 30, no. 2, pp. 421–455, 2018.

[72] B Amirian *et al.*, "An experimental and numerical study of novel nano-grained (γ+ α2)-tial/al2o3 cermets," *Materials Science and Engineering: A*, 2018.

[73] B Amirian *et al.*, "The mechanical response of a α2 (ti3al)+ γ (tial)-submicron grained al2o3 cermet under dynamic compression: Modeling and experiment," *Acta Materialia*, vol. 181, pp. 291–308, 2019.

[74] L. L. Hench, "Bioceramics, a clinical success," *American Ceramic Society Bulletin*, vol. 77, no. 7, pp. 67–74, 1998.

[75] J Silvestre *et al.*, "An overview on the improvement of mechanical properties of ceramics nanocomposites," *Journal of Nanomaterials*, vol. 2015, p. 3, 2015.

[76] M. Estili *et al.*, "The homogeneous dispersion of surfactantless, slightly disordered, crystalline, multiwalled carbon nanotubes in α-alumina ceramics for structural reinforcement," *Acta Materialia*, vol. 56, no. 15, pp. 4070–4079, 2008.

[77] D Djenkal *et al.*, "Sic-reinforcement of an al2o3-γ alon composite," *Journal of the European Ceramic Society*, vol. 20, no. 14-15, pp. 2585–2590, 2000.

[78] D. Zhang *et al.*, "The current state and trend of metal matrix composites," *Materials China*, vol. 29, no. 4, pp. 1–7, 2010.

[79] B. Compton and F. Zok, "Impact resistance of tic-based cermets," *International Journal of Impact Engineering*, vol. 62, pp. 75–87, 2013.

[80] V. Verma and B. M. Kumar, "Processing of ticn–wc–ni/co cermets via conventional and spark plasma sintering technique," *Transactions of the Indian Institute of Metals*, vol. 70, no. 3, pp. 843–853, 2017.

[81] Y.-W. Kim and D. M. Dimiduk, "Progress in the understanding of gamma titanium aluminides," *JoM*, vol. 43, no. 8, pp. 40–47, 1991.

[82] C. M. Ward-Close *et al.*, "Intermetallic-matrix composites—-a review," *Intermetallics*, vol. 4, no. 3, pp. 217–229, 1996.

[83] T.-t. Ai *et al.*, "Oxidation behavior of in-situ al2o3/tial composites at 900c in static air," *International Journal of Minerals, Metallurgy and Materials*, vol. 16, no. 3, pp. 339–344, 2009.

[84] L. Y. Xiang *et al.*, "Microstructure and mechanical properties of al2o3/tial in situ composites doped with fe2o3," in *Materials Science Forum*, Trans Tech Publ, vol. 675, 2011, pp. 597–600.

[85] W.-H. Wei *et al.*, "Microstructure and mechanical properties of in situ formed tic-reinforced ti–6al–4v matrix composites," *Materials Science and Technology*, vol. 34, no. 2, pp. 191–198, 2018.

[86] L. Xiang *et al.*, "Mechanical properties and microstructure of al2o3/tial in situ composites doped with cr2o3," *Materials Science and Engineering: A*, vol. 528, no. 9, pp. 3337–3341, 2011.

[87] Z. Hashin and S. Shtrikman, "A variational approach to the theory of the elastic behaviour of multiphase materials," *Journal of the Mechanics and Physics of Solids*, vol. 11, no. 2, pp. 127–140, 1963.

[88] M. Starink and S Syngellakis, "Shear lag models for discontinuous composites: Fibre end stresses and weak interface layers," *Materials Science and Engineering: A*, vol. 270, no. 2, pp. 270–277, 1999.

[89] P. A. Cundall and O. D. Strack, "A discrete numerical model for granular assemblies," *Geotechnique*, vol. 29, no. 1, pp. 47–65, 1979.

[90] J. Pelletier *et al.*, "Microstructure and mechanical properties of some metal matrix composites produced on different materials by laser cladding," *Lasers in Engineering*, vol. 3, pp. 15–27, 1994.

[91] H Engqvist *et al.*, "A model for the hardness of cemented carbides," *Wear*, vol. 252, no. 5-6, pp. 384–393, 2002.

[92] N Shi *et al.*, "Phase-stress partition during uniaxial tensile loading of a tic–particulate-reinforced al composite," *Metallurgical and Materials Transactions A*, vol. 28, no. 12, pp. 2741–2753, 1997.

[93] T. Gustafson *et al.*, "Influence of microstructural scale on plastic flow behavior of metal matrix composites," *Acta Materialia*, vol. 45, no. 4, pp. 1633–1643, 1997.

[94] B. N. Legarth, "Plasticity dependent damage evolution in composites with strain-gradient effects," *International Journal of Solids and Structures*, vol. 63, pp. 1–10, 2015.

[95] G Bao *et al.*, "Particle reinforcement of ductile matrices against plastic flow and creep," *Acta Metallurgica et Materialia*, vol. 39, no. 8, pp. 1871–1882, 1991.

[96] R Hill, "A self-consistent mechanics of composite materials," *Journal of the Mechanics and Physics of Solids*, vol. 13, no. 4, pp. 213–222, 1965.

[97] C. Liu *et al.*, "Force fluctuations in bead packs," *Science*, vol. 269, no. 5223, pp. 513–515, 1995.

[98] E. Bele and V. S. Deshpande, "The compressive response of idealized cermetlike materials," *Journal of Applied Mechanics*, vol. 82, no. 4, p. 041 009, 2015.

[99] E. Bele *et al.*, "Deformation mechanisms of idealised cermets under multi-axial loading," *Journal of the Mechanics and Physics of Solids*, vol. 102, pp. 80–100, Jan. 2017. DOI: 10.1016/j.jmps.2017.01.002.

[100] J. D. Hogan *et al.*, "The effects of defects on the uniaxial compressive strength and failure of an advanced ceramic," *Acta Materialia*, vol. 102, pp. 263–272, 2016.

[101] "Astm c1425-15. standard test method for monotonic compressive strength of advanced ceramics at ambient temperature," *West Conshohocken (PA)*, 2015.

[102] Vic-2D, *Correlated solutions inc, irmo, south carolina*, version 2016.1.0, Jun. 21, 2016. [Online]. Available: http://correlatedsolutions.com/vic-2d/.

[103] B. Pan *et al.*, "Two-dimensional digital image correlation for in-plane displacement and strain measurement: A review," *Measurement Science and Technology*, vol. 20, no. 6, p. 062 001, 2009.

[104] S.-W. Khoo *et al.*, "A review of surface deformation and strain measurement using two-dimensional digital image correlation," *Metrology and Measurement Systems*, vol. 23, no. 3, pp. 461–480, 2016.

[105] M Jerabek *et al.*, "Strain determination of polymeric materials using digital image correlation," *Polymer Testing*, vol. 29, no. 3, pp. 407–416, 2010.

[106] M. J. Kerper *et al.*, "Evaluation of tensile, compressive, torsional, transverse, and impact tests and correlation of results for brittle cermets," *Journal of Research of the National Bureau of Standards*, vol. 61, no. 3, p. 149, 1958.

[107] A. R. Kamali *et al.*, "Production of tial (ti3al)/al2o3 nanocomposite," in *Journal of Nano Research*, Trans Tech Publ, vol. 3, 2008, pp. 7–14.

[CoorsTek Inc.] CoorsTek Inc., *Advanced alumina brochure*, http://www.coorstek.com/media/1715/advanced-alumina-brochure.pdf, 2016.

[108] Y He *et al.*, "Elastic constants of single crystal γ–tial," *Journal of Materials Research*, vol. 10, no. 5, pp. 1187–1195, 1995.

[109] K. Danas and N Aravas, "Numerical modeling of elasto-plastic porous materials with void shape effects at finite deformations," *Composites Part B: Engineering*, vol. 43, no. 6, pp. 2544–2559, 2012.

[110] N Aravas and P. P. Castaneda, "Numerical methods for porous metals with deformation-induced anisotropy," *Computer Methods in Applied Mechanics and Engineering*, vol. 193, no. 36-38, pp. 3767–3805, 2004.

[111] M Kailasam and P. P. Castaneda, "A general constitutive theory for linear and nonlinear particulate media with microstructure evolution," *Journal of the Mechanics and Physics of Solids*, vol. 46, no. 3, pp. 427–465, 1998.

[112] V. Tvergaard, "Material failure by void coalescence in localized shear bands," *International Journal of Solids and Structures*, vol. 18, no. 8, pp. 659–672, 1982.

[113] V. Tvergaard and A. Needleman, "Analysis of the cup-cone fracture in a round tensile bar," *Acta Metallurgica*, vol. 32, no. 1, pp. 157–169, 1984.

[114] R. Spriggs and L. Brissette, "Expressions for shear modulus and poisson's ratio of porous refractory oxides," *Journal of the American Ceramic Society*, vol. 45, no. 4, pp. 198–199, 1962.

[115] H. S. Kim and M. B. Bush, "The effects of grain size and porosity on the elastic modulus of nanocrystalline materials," *Nanostructured materials*, vol. 11, no. 3, pp. 361–367, 1999.

[116] R Chaim and M Hefetz, "Effect of grain size on elastic modulus and hardness of nanocrystalline zro2-3 wt% y2o3 ceramic," *Journal of materials science*, vol. 39, no. 9, pp. 3057–3061, 2004.

[117] Q. Mei *et al.*, "Grain size dependence of the elastic modulus in nanostructured niti," *Scripta Materialia*, vol. 63, no. 10, pp. 977–980, 2010.

[118] T.-Y. Kim *et al.*, "Numerical study of the grain-size dependent young's modulus and poisson's ratio of bulk nanocrystalline materials," *International Journal of Solids and Structures*, vol. 49, no. 26, pp. 3942–3952, 2012.

[119] S. Guicciardi *et al.*, "Nanoindentation characterization of submicro- and nano-sized liquid-phase-sintered sic ceramics," *Journal of the American Ceramic Society*, vol. 87, no. 11, pp. 2101–2107, 2004.

[120] F. Appel *et al.*, *Gamma titanium aluminide alloys: science and technology*. John Wiley & Sons, 2011.

[121] C. de Formanoir *et al.*, "A strategy to improve the work-hardening behavior of ti–6al–4v parts produced by additive manufacturing," *Materials Research Letters*, vol. 5, no. 3, pp. 201–208, 2017.

[122] H Yildiz *et al.*, "Effects of hardening parameter and strain hardening exponent on residual stress and plastic zone growth in aluminum metal–matrix composites under out-of-plane loading," *Journal of Reinforced Plastics and Composites*, vol. 23, no. 18, pp. 2065–2080, 2004.

[123] M. Malagu *et al.*, "Diameter-dependent elastic properties of carbon nanotube-polymer composites: Emergence of size effects from atomistic-scale simulations," *Composites Part B: Engineering*, vol. 131, pp. 260–281, 2017.

[124] V. Monchiet and D. Kondo, "Combined voids size and shape effects on the macroscopic criterion of ductile nanoporous materials," *International Journal of Plasticity*, vol. 43, pp. 20–41, 2013.

[125] T Goudarzi *et al.*, "Surface energy effects on the yield strength of nanoporous materials containing nanoscale cylindrical voids," *Mechanics of Materials*, vol. 42, no. 9, pp. 852–862, 2010.

[126] W. Zhang *et al.*, "Effect of surface/interface stress on the plastic deformation of nanoporous materials and nanocomposites," *International Journal of Plasticity*, vol. 26, no. 7, pp. 957–975, 2010.

[127] I. C. Getting *et al.*, "The strength and rheology of commercial tungsten carbide cermets used in high-pressure apparatus," in *Experimental Techniques in Mineral and Rock Physics*, Springer, 1993, pp. 545–577.

[128] E. Pickering *et al.*, "Multi-axial response of idealized cermets," *Acta Materialia*, vol. 116, pp. 281–289, 2016.

[129] P. P. Castaneda, "The effective mechanical properties of nonlinear isotropic composites," *Journal of the Mechanics and Physics of Solids*, vol. 39, no. 1, pp. 45–71, 1991.

[130] T. D. Huy *et al.*, "Microstructure and mechanical properties of tial3/al2o3 in situ composite by combustion process," *Materials Transactions*, vol. 55, no. 7, pp. 1091–1093, 2014.

[131] S Scudino *et al.*, "Mechanical properties of al-based metal matrix composites reinforced with zr-based glassy particles produced by powder metallurgy," *Acta Materialia*, vol. 57, no. 6, pp. 2029–2039, 2009.

[132] C. Feng and L. Froyen, "In-situ p/m al/(zrb2+ al2o3) mmcs: Processing, microstructure and mechanical characterization," *Acta Materialia*, vol. 47, no. 18, pp. 4571–4583, 1999.

[133] N. Chawla and Y.-L. Shen, "Mechanical behavior of particle reinforced metal matrix composites," *Advanced Engineering Materials*, vol. 3, no. 6, pp. 357–370, 2001.

[134] Y.-L. Shen *et al.*, "Effective plastic response of two-phase composites," *Acta Metallurgica et Materialia*, vol. 43, no. 4, pp. 1701–1722, 1995.

[135] L. Chingshen and F Ellyin, "Fatigue damage and its localization in particulate metal matrix composites," *Materials Science and Engineering: A*, vol. 214, no. 1-2, pp. 115–121, 1996.

[136] M Taya and H Lilholt, "Advances in composite materials and structures," *ASME*, pp. 21–27, 1986.

[137] B. Park *et al.*, "Material characterisation and mechanical properties of al2o3-al metal matrix composites," *Journal of Materials Science*, vol. 36, no. 10, pp. 2417–2426, 2001.

[138] K.-T. Park *et al.*, "High temperature creep of silicon carbide particulate reinforced aluminum," *Acta Metallurgica et Materialia*, vol. 38, no. 11, pp. 2149–2159, 1990.

[139] R. Imayev *et al.*, "Alloy design concepts for refined gamma titanium aluminide based alloys," *Intermetallics*, vol. 15, no. 4, pp. 451–460, 2007.

[140] A. Kelly, "Composites for the 1990s," *Phil. Trans. R. Soc. Lond. A*, vol. 322, no. 1567, pp. 409–423, 1987.

[141] G Sauthoff, "Multiphase intermetallic alloys for structural applications," *Intermetallics*, vol. 8, no. 9-11, pp. 1101–1109, 2000.

[142] A. Lasalmonie, "Intermetallics: Why is it so difficult to introduce them in gas turbine engines," *Intermetallics*, vol. 14, no. 10-11, pp. 1123–1129, 2006.

[143] J.-M. Yang *et al.*, "Development of tic particle-reinforced mosi2 composite," *Scripta metallurgica*, vol. 23, no. 11, pp. 1953–1958, 1989.

[144] K Morinaga *et al.*, "Fabrication of fine α-alumina powders by thermal decomposition of ammonium aluminum carbonate hydroxide (aach)," *Acta materialia*, vol. 48, no. 18-19, pp. 4735–4741, 2000.

[145] F. Wang *et al.*, "Microstructure and mechanical properties of al2o3/tial in situ composites doped with cr2o3," in *Advanced Materials Research*, Trans Tech Publ, vol. 194, 2011, pp. 1736–1739.

[146] A. Bartels *et al.*, "Strain rate dependence of the deformation mechanisms in a fully lamellar γ-tial-based alloy: Dedicated to professor dr. mont. karl leopold maurer on the occasion of his 75th birthday," *Zeitschrift fur Metallkunde*, vol. 93, no. 3, pp. 180–185, 2002.

[147] Z Jin *et al.*, "Mechanical behavior of a fine-grained duplex γ-tial alloy," *Metallurgical and Materials Transactions A*, vol. 31, no. 13, pp. 1007–1016, 2000.

[148] W. Kaplan *et al.*, "Static and dynamic mechanical damage mechanisms in tic-1080 steel cermets," *Scripta materialia*, vol. 51, no. 1, pp. 37–41, 2004.

[149] D Rittel *et al.*, "Dynamic mechanical and fracture properties of an infiltrated tic-1080 steel cermet," *International journal of solids and structures*, vol. 42, no. 2, pp. 697–715, 2005.

[150] Y. Li *et al.*, "Comparison of the plastic deformation and failure of a359/sic and 6061-t6/al2o3 metal matrix composites under dynamic tension," *Materials Science and Engineering: A*, vol. 371, no. 1-2, pp. 359–370, 2004.

[151] E. Pickering *et al.*, "Effect of confinement on the static and dynamic indentation response of model ceramic and cermet materials," *International Journal of Impact Engineering*, vol. 110, pp. 123–137, 2017.

[152] T Christman *et al.*, "An experimental and numerical study of deformation in metal-ceramic composites," *Acta Metallurgica*, vol. 37, 3029–3050, Nov. 1989. DOI: 10.1016/0001-6160(89)90339-8.

[153] K. Ramesh and G Ravichandran, "An ultrasonic evaluation of damage in cermets," in *Review of Progress in Quantitative Nondestructive Evaluation*, Springer, 1989, pp. 1841–1846.

[154] L. R. Deobald and A. S. Kobayashi, "Dynamic fracture characterization of al2o3 and sicw/al2o3," *Journal of the American Ceramic Society*, vol. 75, no. 10, pp. 2867–2870, 1992.

[155] Q. Zhuang *et al.*, "Influence of temperature on sintering behavior and properties of tic-fe-co-ni-cr-mo cermets," *Ceramics International*, vol. 43, no. 17, pp. 15 992–15 998, 2017.

[156] W. Chen and G Ravichandran, "Dynamic compressive failure of a glass ceramic under lateral confinement," *Journal of the Mechanics and Physics of Solids*, vol. 45, no. 8, pp. 1303–1328, 1997.

[157] W. W. Chen and B. Song, *Split Hopkinson (Kolsky) bar: design, testing and applications*. Springer Science & Business Media, 2010.

[158] K. Xia and W. Yao, "Dynamic rock tests using split hopkinson (kolsky) bar system–a review," *Journal of Rock Mechanics and Geotechnical Engineering*, vol. 7, no. 1, pp. 27–59, 2015.

[159] K. Ramesh and G Ravichandran, "Dynamic behavior of a boron carbide aluminum cermet: Experiments and observations," *Mechanics of Materials*, vol. 10, no. 1-2, pp. 19–29, 1990.

[160] H. li *et al.*, "Characterization and mechanical testing on novel (γ+ α_2) tial/ti3al/al2o3 cermet," *Materials Science and Engineering: A*, pp. 152–163, Feb. 2019. DOI: 10.1016/j.msea.2019.02.039.

[161] K. Ravichandran, "A simple model of deformation behavior of two phase composites," *Acta metallurgica et materialia*, vol. 42, no. 4, pp. 1113–1123, 1994.

[162] J. Lee *et al.*, "The influence of reinforced particle fracture on strengthening of spray formed cu-tib sub2 composite," *Scripta Materialia*, vol. 39, no. 8, 1998.

[163] W. Han *et al.*, "The effects of three-dimensional multi-particle arrangements on the mechanical behavior and damage initiation of particle-reinforced mmcs," *Composites science and technology*, vol. 61, no. 11, pp. 1581–1590, 2001.

[164] S. Torquato, *Random heterogeneous materials: microstructure and macroscopic properties*. Springer Science & Business Media, 2013, vol. 16.

[165] A. Mbiakop *et al.*, "An analytical model for porous single crystals with ellipsoidal voids," *Journal of the Mechanics and Physics of Solids*, vol. 84, pp. 436–467, 2015.

[166] J. D. Eshelby, "The determination of the elastic field of an ellipsoidal inclusion, and related problems," *Proceedings of the Royal Society of London. Series A. Mathematical and Physical Sciences*, vol. 241, no. 1226, pp. 376–396, 1957.

[167] K. Danas and P. P. Castaneda, "A finite-strain model for anisotropic viscoplastic porous media: I–theory," *European Journal of Mechanics-A/Solids*, vol. 28, no. 3, pp. 387–401, 2009.

[168] A Needleman, "On finite element formulations for large elastic–plastic deformations," in *Advances and Trends in Structures and Dynamics*, Elsevier, 1985, pp. 247–257.

[169] C. Chu and A Needleman, "Void nucleation effects in biaxially stretched sheets," *Journal of engineering materials and technology*, vol. 102, no. 3, pp. 249–256, 1980.

[170] V. Tvergaard and A. Needleman, "Three dimensional microstructural effects on plane strain ductile crack growth," *International journal of solids and structures*, vol. 43, no. 20, pp. 6165–6179, 2006.

[171] A. B. Richelsen and V. Tvergaard, "Dilatant plasticity or upper bound estimates for porous ductile solids," *Acta Metallurgica et Materialia*, vol. 42, no. 8, pp. 2561–2577, 1994.

[172] K. Jayaraman *et al.*, "Elastic and thermal effects in the interphase: Part ii. comments on modeling studies," *Journal of Composites, Technology and Research*, vol. 15, no. 1, pp. 14–22, 1993.

[173] J. Kim and Y.-W. Mai, "Effects of interfacial coating and temperature on the fracture behaviours of unidirectional kevlar and carbon fibre reinforced epoxy resin composites," *Journal of Materials Science*, vol. 26, no. 17, pp. 4702–4720, 1991.

[174] A Miserez *et al.*, "Fracture of aluminium reinforced with densely packed ceramic particles: Link between the local and the total work of fracture," *Acta Materialia*, vol. 52, no. 5, pp. 1337–1351, 2004.

[175] G. I. Barenblatt, "The mathematical theory of equilibrium cracks in brittle fracture," in *Advances in applied mechanics*, vol. 7, Elsevier, 1962, pp. 55–129.

[176] G. I. Barenblatt, "The formation of equilibrium cracks during brittle fracture. general ideas and hypotheses. axially-symmetric cracks," *Journal of applied mathematics and mechanics*, vol. 23, no. 3, pp. 622–636, 1959.

[177] N Chandra and H Ghonem, "Interfacial mechanics of push-out tests: Theory and experiments," *Composites Part A: Applied Science and Manufacturing*, vol. 32, no. 3-4, pp. 575–584, 2001.

[178] V. Tvergaard, "Effect of fibre debonding in a whisker-reinforced metal," *Materials Science and Engineering: A*, vol. 125, no. 2, pp. 203–213, 1990. DOI: 10.1016/0921-5093(90)90170-8.

[179] C. C. Holland and R. M. McMeeking, "The influence of mechanical and microstructural properties on the rate-dependent fracture strength of ceramics in uniaxial compression," *International Journal of Impact Engineering*, vol. 81, pp. 34–49, 2015.

[180] M. Handbook, "Metallic materials and elements for aerospace vehicle structures," *Military Handbook No. MIL-HDBK-5H, Section*, vol. 5, 1998.

[181] A. H. Tavakoli *et al.*, "Amorphous alumina nanoparticles: Structure, surface energy, and thermodynamic phase stability," *The Journal of Physical Chemistry C*, vol. 117, no. 33, pp. 17 123–17 130, 2013.

[182] A. Bartlett and A. Evans, "The effect of reaction products on the fracture resistance of a metal/ceramic interface," *Acta Metallurgica et Materialia*, vol. 41, pp. 497–504, Feb. 1993. DOI: 10.1016/0956-7151(93)90078-7.

[183] M. Guden *et al.*, "Effect of strain rate on the compressive mechanical behavior of a continuous alumina fiber reinforced ze41a magnesium alloy based composite," *Materials Science and Engineering: A*, vol. 425, no. 1-2, pp. 145–155, 2006.

[184] D. Zhu *et al.*, "Dynamic deformation behavior of a high reinforcement content tib2/al composite at high strain rates," *Materials Science and Engineering: A*, vol. 487, no. 1-2, pp. 536–540, 2008.

[185] J. Zhang *et al.*, "Constitutive analysis of the hot deformation behavior of fe–23mn–2al–0.2c twinning induced plasticity steel in consideration of strain," *Materials & Design*, vol. 44, pp. 354–364, 2013.

[186] G Bao and Z Lin, "High strain rate deformation in particle reinforced metal matrix composites," *Acta materialia*, vol. 44, no. 3, pp. 1011–1019, 1996.

[187] J. Lankford, "The influence of temperature and loading rate on flow and fracture of partially stabilized zirconia," *Journal of materials science*, vol. 20, no. 1, pp. 53–59, 1985.

[188] J Lankford, "Mechanisms responsible for strain-rate-dependent compressive strength in ceramic materials," *Journal of the American Ceramic Society*, vol. 64, no. 2, pp. C–33, 1981.

[189] S. Acharya *et al.*, "Deformation and failure of alumina under high strain rate compressive loading," *Ceramics International*, vol. 41, no. 5, pp. 6793–6801, 2015.

[190] H. Luo and W. Chen, "Dynamic compressive response of intact and damaged ad995 alumina," *International Journal of Applied Ceramic Technology*, vol. 1, no. 3, pp. 254–260, 2004.

[191] J. Pittari III *et al.*, "The rate-dependent fracture toughness of silicon carbide-and boron carbide-based ceramics," *Journal of the European Ceramic Society*, vol. 35, no. 16, pp. 4411–4422, 2015.

[192] H Pouraliakbar *et al.*, "Toughness prediction in functionally graded al6061/sicp composites produced by roll-bonding," *Ceramics International*, vol. 40, no. 6, pp. 8809–8825, 2014.

[193] S. Fida Hassan and M. Gupta, "Development of ductile magnesium composite materials using titanium as reinforcement," *Journal of Alloys and Compounds*, vol. 345, pp. 246–251, Oct. 2002. DOI: 10.1016/S0925-8388(02)00413-9.

[194] P Pérez *et al.*, "Mechanical properties of a mg–10 vol. ti composite," *Composites Science and Technology*, vol. 64, pp. 145–151, Jan. 2004. DOI: 10.1016/S0266-3538(03)00215-X.

[195] H Zhang *et al.*, "Effects of interfacial debonding on the rate-dependent response of metal matrix composites," *Acta materialia*, vol. 53, no. 17, pp. 4687–4700, 2005.

[196] M. Tarantino *et al.*, "Effect of hydrostatic pressure on flow and deformation in highly reinforced particulate composites," *Acta Materialia*, vol. 117, pp. 345–355, Jul. 2016. DOI: 10.1016/j.actamat.2016.06.052.

[197] D. Zhou *et al.*, "The nano-sized tic particle reinforced al–cu matrix composite with superior tensile ductility," *Materials Science and Engineering: A*, vol. 622, pp. 189–193, 2015.

[198] F Longy and J Cagnoux, "Plasticity and microcracking in shock-loaded alumina," *Journal of the American Ceramic Society*, vol. 72, no. 6, pp. 971–979, 1989.

[199] M. Mataya and V. Sackschewsky, "Effect of internal heating during hot compression on the stress-strain behavior of alloy 304l," *Metallurgical and Materials Transactions A*, vol. 25, no. 12, p. 2737, 1994.

[200] C San Marchi *et al.*, "Quasistatic and dynamic compression of aluminum-oxide particle reinforced pure aluminum," *Materials Science and Engineering: A*, vol. 337, no. 1-2, pp. 202–211, 2002.

[201] Z. Tan *et al.*, "The compressive properties of 2024al matrix composites reinforced with high content sic particles at various strain rates," *Materials Science and Engineering: A*, vol. 489, no. 1-2, pp. 302–309, 2008.

[202] J. Lankford, "The failure of fiber-reinforced ceramic-matrix composites under dynamic loading," *JOM*, vol. 47, no. 5, pp. 64–68, 1995.

[203] S Nemat-Nasser and H Deng, "Strain-rate effect on brittle failure in compression," *Acta metallurgica et materialia*, vol. 42, no. 3, pp. 1013–1024, 1994.

[204] B Paliwal and K. Ramesh, "An interacting micro-crack damage model for failure of brittle materials under compression," *Journal of the Mechanics and Physics of Solids*, vol. 56, no. 3, pp. 896–923, 2008.

[205] J Kimberley *et al.*, "A scaling law for the dynamic strength of brittle solids," *Acta Materialia*, vol. 61, no. 9, pp. 3509–3521, 2013.

[206] J. Lankford, "Dynamic compressive fracture in fiber-reinforced ceramic matrix composites," *Materials Science and Engineering: A*, vol. 107, pp. 261–268, 1989.

[207] J Lankford, "High strain rate compression and plastic flow of ceramics," *Journal of materials science letters*, vol. 15, no. 9, pp. 745–750, 1996.

[208] J. Lankford Jr, "The role of dynamic material properties in the performance of ceramic armor," *International Journal of Applied Ceramic Technology*, vol. 1, no. 3, pp. 205–210, 2004.

[209] C.-C. Perng *et al.*, "High strain rate tensile properties of an (al2o3 particles)-(al alloy 6061-t6) metal matrix composite," *Materials Science and Engineering: A*, vol. 171, no. 1-2, pp. 213–221, 1993.

[210] B. Liu *et al.*, "Size-dependent compression deformation behaviors of high particle content b4c/al composites," *Materials Science and Engineering: A*, vol. 534, pp. 530–535, 2012.

[211] S. Liu *et al.*, "Effect of deformation temperature, strain rate and strain on the strain hardening exponent of copper/aluminum laminated composites," *Advanced Composites Letters*, vol. 27, no. 4, 2018.

[212] S. Hong and G. Gray, "Dynamic mechanical response of a 1060 al/al2o3 composite," *Journal of materials science*, vol. 29, no. 11, pp. 2987–2992, 1994.

[213] Z. Zhang and D. Chen, "Consideration of orowan strengthening effect in particulate-reinforced metal matrix nanocomposites: A model for predicting their yield strength," *Scripta Materialia*, vol. 54, no. 7, pp. 1321–1326, 2006.

[214] S. Hong *et al.*, "Dynamic deformation behavior of al-zn-mg-cu alloy matrix composites reinforced with 20 vol. % sic," *Acta metallurgica et materialia*, vol. 41, no. 8, pp. 2337–2351, 1993.

[215] L. Bin *et al.*, "Compressive behavior of high particle content b4c/al composite at elevated temperature," *Transactions of Nonferrous Metals Society of China*, vol. 23, no. 10, pp. 2826–2832, 2013.

[216] Z. Tan *et al.*, "The dynamic mechanical response of sic particulate reinforced 2024 aluminum matrix composites," *Materials Letters*, vol. 61, no. 23-24, pp. 4606–4609, 2007.

[217] Z. Song and Y. Lu, "Mesoscopic analysis of concrete under excessively high strain rate compression and implications on interpretation of test data," *International Journal of Impact Engineering*, vol. 46, pp. 41–55, 2012.

[218] Y. Zhou and Y. Xia, "Experimental study of the rate-sensitivity of sicp/al composites and the establishment of a dynamic constitutive equation," *Composites Science and Technology*, vol. 60, pp. 403–410, Feb. 2000. DOI: 10.1016/S0266-3538(99)00136-0.

[219] I. Tirtom *et al.*, "Simulation of the strain rate sensitive flow behavior of sic-particulate reinforced aluminum metal matrix composites," *Computational Materials Science*, vol. 42, pp. 570–578, Jun. 2008. DOI: 10.1016/j.commatsci.2007.09.005.

[220] L. Guoju *et al.*, "Simulation of damage and failure processes of interpenetrating sic/al composites subjected to dynamic compressive loading," *Acta Materialia*, vol. 78, 190–202, Oct. 2014. DOI: 10.1016/j.actamat.2014.06.045.

[221] X C. Tong and A K. Ghosh, "Fabrication of in situ tic reinforced aluminum matrix composites," *Journal of Materials Science*, vol. 36, pp. 4059–4069, Aug. 2001. DOI: 10.1023/A:1017946927566.

[222] A. Miserez *et al.*, "Investigation of crack-tip plasticity in high volume fraction particulate metal matrix composites," *Engineering Fracture Mechanics*, vol. 71, pp. 2385–2406, Nov. 2004. DOI: 10.1016/j.engfracmech.2004.01.006.

[223] M Kouzeli *et al.*, "Influence of damage on the tensile behaviour of pure aluminium reinforced with $\geq$ 40 vol. pct alumina particles," *Acta Materialia*, vol. 49, pp. 3699–3709, Oct. 2001. DOI: 10.1016/S1359-6454(01)00279-8.

[224] D. Lloyd, "Aspects of fracture in particulate reinforced metal matrix composites," *Acta metallurgica et materialia*, vol. 39, no. 1, pp. 59–71, 1991.

[225] J. Hirsch and T. Al-Samman, "Superior light metals by texture engineering: Optimized aluminum and magnesium alloys for automotive applications," *Acta Materialia*, vol. 61, no. 3, pp. 818–843, 2013, The Diamond Jubilee Issue, ISSN: 1359-6454. DOI: https://doi.org/10.1016/j.actamat.2012.10.044. [Online]. Available: https://www.sciencedirect.com/science/article/pii/S1359645412007914.

[226] X. Z. Liao *et al.*, "Deformation twinning in nanocrystalline copper at room temperature and low strain rate," *Applied Physics Letters*, vol. 84, no. 4, pp. 592–594, 2004. DOI: 10.1063/1.1644051. eprint: https://doi.org/10.1063/1.1644051. [Online]. Available: https://doi.org/10.1063/1.1644051.

[227] X. Y. Zhang *et al.*, "Growth of deformation twins in room-temperature rolled nanocrystalline nickel," *Applied Physics Letters*, vol. 94, no. 12, p. 121 907, 2009, ISSN: 0003-6951. DOI: 10.1063/1.3104858. [Online]. Available: https://doi.org/10.1063/1.3104858.

[228] R. J. McCabe *et al.*, "Quantitative analysis of deformation twinning in zirconium," *International Journal of Plasticity*, vol. 25, no. 3, pp. 454–472, 2009, ISSN: 0749-6419. DOI: https://doi.org/10.1016/j.ijplas.2008.03.010. [Online]. Available: https://www.sciencedirect.com/science/article/pii/S0749641908000569.

[229] R. J. McCabe *et al.*, "Deformation of wrought uranium: Experiments and modeling," *Acta Materialia*, vol. 58, no. 16, pp. 5447–5459, 2010, ISSN: 1359-6454. DOI: https://doi.org/10.1016/j.actamat.2010.06.021. [Online]. Available: https://www.sciencedirect.com/science/article/pii/S1359645410003757.

[230] T. Guo *et al.*, "Analysing single twinning events in mg-6zn using nanoindentation," *Journal of Alloys and Compounds*, vol. 768, pp. 510–516, 2018, ISSN: 0925-8388. DOI: https://doi.org/10.1016/j.jallcom.2018.07.033. [Online]. Available: https://www.sciencedirect.com/science/article/pii/S0925838818325337.

[231] Z. Wu *et al.*, "Mechanistic origin and prediction of enhanced ductility in magnesium alloys," *Science*, vol. 359, no. 6374, p. 447, 2018. DOI: 10.1126/science.aap8716. [Online]. Available: https://doi.org/10.1126/science.aap8716.

[232] K. Dang, C. N. Tomé, and L. Capolungo, "The $\{10\bar{1}2\}$ non-cozone twin-twin interactions in mg: A stability and mobility study using 3-d atomistic simulations," *Scripta Materialia*, vol. 200, p. 113 913, 2021.

[233]M. Lentz *et al.*, "In situ x-ray diffraction and crystal plasticity modeling of the deformation behavior of extruded mg–li–(al) alloys: An uncommon tension–compression asymmetry," *Acta Materialia*, vol. 86, pp. 254–268, 2015, ISSN: 1359-6454. DOI: https://doi.org/10.1016/j.actamat.2014.12.003. [Online]. Available: https://www.sciencedirect.com/science/article/pii/S1359645414009112.

[234]L. Capolungo *et al.*, "Slip-assisted twin growth in hexagonal close-packed metals," *Scripta Materialia*, vol. 60, no. 1, pp. 32–35, 2009, ISSN: 1359-6462. DOI: https://doi.org/10.1016/j.scriptamat.2008.08.044. [Online]. Available: https://www.sciencedirect.com/science/article/pii/S1359646208006374.

[235]J. W. Christian and S. Mahajan, "Deformation twinning," *Progress in materials science*, vol. 39, no. 1-2, pp. 1–157, 1995.

[236]M. Arul Kumar *et al.*, "Deformation twinning and grain partitioning in a hexagonal close-packed magnesium alloy," *Nature Communications*, vol. 9, no. 1, p. 4761, 2018. DOI: 10.1038/s41467-018-07028-w. [Online]. Available: https://doi.org/10.1038/s41467-018-07028-w.

[237]F. Yang *et al.*, "Crack initiation mechanism of extruded az31 magnesium alloy in the very high cycle fatigue regime," *Materials Science and Engineering: A*, vol. 491, no. 1, pp. 131–136, 2008, ISSN: 0921-5093. DOI: https://doi.org/10.1016/j.msea.2008.02.003. [Online]. Available: https://www.sciencedirect.com/science/article/pii/S0921509308002074.

[238]J. Tang *et al.*, "Interactions between twin boundary and point defects in magnesium at low temperature," *Journal of Materials Research*, pp. 1–12, 2021. DOI: https://doi.org/10.1557/s43578-021-00120-w.

[239]H. Abdolvand *et al.*, "Strong grain neighbour effects in polycrystals," *Nature Communications*, vol. 9, no. 1, p. 171, 2018. DOI: 10.1038/s41467-017-02213-9. [Online]. Available: https://doi.org/10.1038/s41467-017-02213-9.

[240]H. Fan *et al.*, "Precipitation hardening effects on extension twinning in magnesium alloys," *International Journal of Plasticity*, vol. 106, pp. 186–202, 2018, ISSN: 0749-6419. DOI: https://doi.org/10.1016/j.ijplas.2018.03.008. [Online]. Available: https://www.sciencedirect.com/science/article/pii/S0749641917306721.

[241]Y. Hu *et al.*, "Embracing the chaos: Alloying adds stochasticity to twin embryo growth," *Physical Review Letters*, vol. 125, no. 20, p. 205 503, 2020.

[242] J. Wang *et al.*, "$(\bar{1}012)$ twinning nucleation mechanisms in hexagonal-close-packed crystals," *Acta Materialia*, vol. 57, no. 18, pp. 5521–5530, 2009, ISSN: 1359-6454. DOI: https://doi.org/10.1016/j.actamat.2009.07.047. [Online]. Available: https://www.sciencedirect.com/science/article/pii/S1359645409004832.

[243] Y. Cao *et al.*, "Twinning interactions induced amorphisation in ultrafine silicon grains," *Materials Science and Engineering: A*, vol. 658, pp. 321–325, 2016, ISSN: 0921-5093. DOI: https://doi.org/10.1016/j.msea.2016.02.014. [Online]. Available: https://www.sciencedirect.com/science/article/pii/S0921509316301307.

[244] V. Kannan, K. Hazeli, and K. Ramesh, "The mechanics of dynamic twinning in single crystal magnesium," *Journal of the Mechanics and Physics of Solids*, vol. 120, pp. 154–178, 2018.

[245] B. Li and E. Ma, "Atomic shuffling dominated mechanism for deformation twinning in magnesium," *Phys. Rev. Lett.*, vol. 103, p. 035 503, 3 2009. DOI: 10.1103/PhysRevLett.103.035503. [Online]. Available: https://link.aps.org/doi/10.1103/PhysRevLett.103.035503.

[246] J. Hirth *et al.*, "Disconnections and other defects associated with twin interfaces," *Progress in Materials Science*, vol. 83, pp. 417–471, 2016, ISSN: 0079-6425. DOI: https://doi.org/10.1016/j.pmatsci.2016.07.003. [Online]. Available: https://www.sciencedirect.com/science/article/pii/S0079642516300329.

[247] J. Zhang *et al.*, "The dislocation-twin interaction and evolution of twin boundary in az31 mg alloy," *Acta Materialia*, vol. 133, pp. 208–216, 2017, ISSN: 1359-6454. DOI: https://doi.org/10.1016/j.actamat.2017.05.034. [Online]. Available: https://www.sciencedirect.com/science/article/pii/S1359645417304214.

[248] Z Wu *et al.*, "Magnesium interatomic potential for simulating plasticity and fracture phenomena," vol. 23, no. 1, p. 015 004, 2014. DOI: 10.1088/0965-0393/23/1/015004. [Online]. Available: https://doi.org/10.1088/0965-0393/23/1/015004.

[249] A. A. Benzerga *et al.*, "Plastic flow anisotropy drives shear fracture," *Scientific Reports*, vol. 9, no. 1, p. 1425, 2019, ISSN: 2045-2322. DOI: 10.1038/s41598-018-38437-y. [Online]. Available: https://doi.org/10.1038/s41598-018-38437-y.

[250] C. L. Kelchner *et al.*, "Dislocation nucleation and defect structure during surface indentation," *Phys. Rev. B*, vol. 58, pp. 11 085–11 088, 17 1998. DOI: 10.1103/PhysRevB.58.11085. [Online]. Available: https://link.aps.org/doi/10.1103/PhysRevB.58.11085.

[251] G. J. Ackland and A. P. Jones, "Applications of local crystal structure measures in experiment and simulation," *Phys. Rev. B*, vol. 73, p. 054 104, 5 2006. DOI: 10.1103/PhysRevB.73.054104. [Online]. Available: https://link.aps.org/doi/10.1103/PhysRevB.73.054104.

[252] G. Agarwal and A. M. Dongare, "Deformation twinning in polycrystalline mg microstructures at high strain rates at the atomic scales," *Scientific Reports*, vol. 9, no. 1, p. 3550, 2019. DOI: 10.1038/s41598-019-39958-w. [Online]. Available: https://doi.org/10.1038/s41598-019-39958-w.

[253] R. Gluge *et al.*, "A pseudoelastic model for mechanical twinning on the microscale," *ZAMM - Journal of Applied Mathematics and Mechanics / Zeitschrift fur Angewandte Mathematik und Mechanik*, vol. 90, no. 7-8, pp. 565–594, 2010. DOI: https://doi.org/10.1002/zamm.200900339. eprint: https://onlinelibrary.wiley.com/doi/pdf/10.1002/zamm.200900339. [Online]. Available: https://onlinelibrary.wiley.com/doi/abs/10.1002/zamm.200900339.

[254] V. Kolupaev *et al.*, "Yield criteria of hexagonal symmetry in the π-plane," *Acta Mechanica*, vol. 224, no. 7, pp. 1527–1540, 2013. DOI: https://doi.org/10.1007/s00707-013-0830-5.

[255] M. Gong, J Graham, V. Taupin, and L. Capolungo, "The effects of stress, temperature and facet structure on growth of $\{10\bar{1}2\}$ twins in mg: A molecular dynamics and phase field study," *Acta Materialia*, vol. 208, p. 116 603, 2021.

[256] C. Liu *et al.*, "An integrated crystal plasticity–phase field model for spatially resolved twin nucleation, propagation, and growth in hexagonal materials," *International Journal of Plasticity*, vol. 106, pp. 203–227, 2018, ISSN: 0749-6419. DOI: https://doi.org/10.1016/j.ijplas.2018.03.009. [Online]. Available: https://www.sciencedirect.com/science/article/pii/S0749641917307209.

[257] R Kondo, Y Tadano, and K. Shizawa, "A phase-field model of twinning and detwinning coupled with dislocation-based crystal plasticity for hcp metals," *Computational materials science*, vol. 95, pp. 672–683, 2014.

[258] R. Y. Zhang *et al.*, "Parametric study of stress state development during twinning using 3d finite element modeling," *Materials Science and Engineering: A*, vol. 528, no. 6, pp. 2725–2735, 2011, ISSN: 0921-5093. DOI: https://doi.org/10.1016/j.msea.2010.12.062. [Online]. Available: https://www.sciencedirect.com/science/article/pii/S0921509310014693.

[259] M. A. Kumar *et al.*, "Effect of local stress fields on twin characteristics in hcp metals," *Acta Materialia*, vol. 116, pp. 143–154, 2016, ISSN: 1359-6454. DOI: https://doi.org/10.1016/j.actamat.2016.06.042. [Online]. Available: https://www.sciencedirect.com/science/article/pii/S1359645416304621.

[260] Y. Hu *et al.*, "Disconnection-mediated twin embryo growth in mg," *Acta Materialia*, vol. 194, pp. 437–451, 2020, ISSN: 1359-6454. DOI: https://doi.org/10.1016/j.actamat.2020.04.010. [Online]. Available: https://www.sciencedirect.com/science/article/pii/S1359645420302676.

[261] G. H. Farrahi *et al.*, "On the phase field modeling of crack growth and analytical treatment on the parameters," *Continuum Mechanics and Thermodynamics*, vol. 32, no. 3, pp. 589–606, 2020. DOI: https://doi.org/10.1007/s00161-018-0685-z.

[262] L. Farbaniec *et al.*, "Spall response and failure mechanisms associated with a hot-extruded amx602 mg alloy," *Materials Science and Engineering: A*, vol. 707, pp. 725–731, 2017, ISSN: 0921-5093. DOI: https://doi.org/10.1016/j.msea.2017.09.105. [Online]. Available: https://www.sciencedirect.com/science/article/pii/S0921509317312753.

[263] R. D. James, "Finite deformation by mechanical twinning," *Archive for Rational Mechanics and Analysis*, vol. 77, no. 2, pp. 143–176, 1981. DOI: https://doi.org/10.1007/BF00250621.

[264] V. I. Levitas and D. L. Preston, "Three-dimensional landau theory for multivariant stress-induced martensitic phase transformations. i. austenite martensite," *Physical review B*, vol. 66, no. 13, p. 134 206, 2002.

[265] V. I. Levitas and D. L. Preston, "Thermomechanical lattice instability and phase field theory of martensitic phase transformations, twinning and dislocations at large strains," *Physics Letters A*, vol. 343, no. 1-3, pp. 32–39, 2005.

[266] J. Clayton, "A continuum description of nonlinear elasticity, slip and twinning, with application to sapphire," *Proceedings of the Royal Society A: Mathematical, Physical and Engineering Sciences*, vol. 465, no. 2101, pp. 307–334, 2008.

[267] J. Bonet and R. D. Wood, *Nonlinear Continuum Mechanics for Finite Element Analysis*, 2nd ed. Cambridge University Press, 2008. DOI: 10.1017/CBO9780511755446.

[268] V. I. Levitas, V. A. Levin, K. M. Zingerman, and E. I. Freiman, "Displacive phase transitions at large strains: Phase-field theory and simulations," *Physical Review Letters*, vol. 103, no. 2, p. 025 702, 2009.

[269] V. I. Levitas, "Phase field approach to martensitic phase transformations with large strains and interface stresses," *Journal of the Mechanics and Physics of Solids*, vol. 70, pp. 154–189, 2014.

[270] J. Lee and M. Yoo, "Elastic strain energy of deformation twinning in tetragonal crystals," *Metallurgical Transactions A*, vol. 21, no. 9, pp. 2521–2530, 1990. DOI: https://doi.org/10.1007/BF02646997.

[271] A. Staroselsky and L. Anand, "A constitutive model for hcp materials deforming by slip and twinning: Application to magnesium alloy az31b," *International Journal of Plasticity*, vol. 19, no. 10, pp. 1843–1864, 2003, ISSN: 0749-6419. DOI: https://doi.org/10.1016/S0749-6419(03)00039-1. [Online]. Available: https://www.sciencedirect.com/science/article/pii/S0749641903000391.

[272] H. El Kadiri *et al.*, "The candidacy of shuffle and shear during compound twinning in hexagonal close-packed structures," *Acta materialia*, vol. 61, no. 20, pp. 7646–7659, 2013.

[273] A. M. Kosevich and V. S. Bouko, "Dislocation theory of the elastic twinning of crystals," *Soviet Physics Uspekhi*, vol. 14, no. 3, pp. 286–316, 1971.

[274] J. Wang *et al.*, "Detwinning mechanisms for growth twins in face-centered cubic metals," *Acta Materialia*, vol. 58, no. 6, pp. 2262–2270, 2010, ISSN: 1359-6454. DOI: https://doi.org/10.1016/j.actamat.2009.12.013. [Online]. Available: https://www.sciencedirect.com/science/article/pii/S1359645409008556.

[275] S. Lee *et al.*, "Reversible cyclic deformation mechanism of gold nanowires by twinning–detwinning transition evidenced from in situ tem," *Nature communications*, vol. 5, no. 1, pp. 1–10, 2014. DOI: 10.1038/ncomms4033.

[276] B. Morrow *et al.*, "Toward understanding twin–twin interactions in hcp metals: Utilizing multiscale techniques to characterize deformation mechanisms in magnesium," *Materials Science and Engineering: A*, vol. 613, pp. 365–371, 2014, ISSN: 0921-5093. DOI: https://doi.org/10.1016/j.msea.2014.06.062. [Online]. Available: https://www.sciencedirect.com/science/article/pii/S0921509314007795.

[277] K. Mathis *et al.*, "On the dynamics of twinning in magnesium micropillars," *Materials & Design*, vol. 203, p. 109 563, 2021, ISSN: 0264-1275. DOI: https://doi.org/10.1016/j.matdes.2021.109563. [Online]. Available: https://www.sciencedirect.com/science/article/pii/S0264127521001167.

[278]B. Clausen *et al.*, "Reorientation and stress relaxation due to twinning: Modeling and experimental characterization for mg," *Acta Materialia*, vol. 56, no. 11, pp. 2456–2468, 2008, ISSN: 1359-6454. DOI: https://doi.org/10.1016/j.actamat.2008.01.057. [Online]. Available: https://www.sciencedirect.com/science/article/pii/S1359645408000724.

[279]C. Mareau and M. R. Daymond, "Micromechanical modelling of twinning in polycrystalline materials: Application to magnesium," *International Journal of Plasticity*, vol. 85, pp. 156–171, 2016, ISSN: 0749-6419. DOI: https://doi.org/10.1016/j.ijplas.2016.07.007. [Online]. Available: https://www.sciencedirect.com/science/article/pii/S0749641916301140.

[280]A. Hürkamp *et al.*, "Combining simulation and machine learning as digital twin for the manufacturing of overmolded thermoplastic composites," *Journal of Manufacturing and Materials Processing*, vol. 4, no. 3, 2020, ISSN: 2504-4494. DOI: 10.3390/jmmp4030092. [Online]. Available: https://www.mdpi.com/2504-4494/4/3/92.

[281]E. Barchiesi *et al.*, "Mechanical metamaterials: A state of the art," *Mathematics and Mechanics of Solids*, vol. 24, no. 1, pp. 212–234, 2019.

[282]R. Liu *et al.*, "A predictive machine learning approach for microstructure optimization and materials design," *Scientific reports*, vol. 5, no. 1, pp. 1–12, 2015. DOI: https://doi.org/10.1038/srep11551.

[283]S. R. Yeratapally *et al.*, "Microstructure based fatigue life prediction framework for polycrystalline nickel-base superalloys with emphasis on the role played by twin boundaries in crack initiation," *Acta Materialia*, vol. 107, pp. 152–167, 2016, ISSN: 1359-6454. DOI: https://doi.org/10.1016/j.actamat.2016.01.038. [Online]. Available: https://www.sciencedirect.com/science/article/pii/S1359645416300374.

[284]J.-M. Hu *et al.*, "Understanding and designing magnetoelectric heterostructures guided by computation: Progresses, remaining questions, and perspectives," *npj Computational Materials*, vol. 3, no. 1, pp. 1–21, 2017. DOI: https://doi.org/10.1038/s41524-017-0020-4.

[285]Q. Sun *et al.*, "Investigation of twin–twin interaction in deformed magnesium alloy," *Philosophical Magazine*, vol. 98, no. 9, pp. 741–751, 2018. DOI: 10.1080/14786435.2017.1417648. eprint: https://doi.org/10.1080/14786435.2017.1417648. [Online]. Available: https://doi.org/10.1080/14786435.2017.1417648.

[286]G.-D. Sim *et al.*, "Anomalous hardening in magnesium driven by a size-dependent transition in deformation modes," *Acta Materialia*, vol. 144, pp. 11–20, 2018, ISSN: 1359-6454. DOI: https://doi.org/

10.1016/j.actamat.2017.10.033. [Online]. Available: https://www.sciencedirect.com/science/article/pii/S1359645417308911.

[287]M. Bönisch *et al.*, "Hardening by slip-twin and twin-twin interactions in femnnicocr," *Acta Materialia*, vol. 153, pp. 391–403, 2018, ISSN: 1359-6454. DOI: https://doi.org/10.1016/j.actamat.2018.04.054. [Online]. Available: https://www.sciencedirect.com/science/article/pii/S1359645418303318.

[288]J. Cheng and S. Ghosh, "Crystal plasticity finite element modeling of discrete twin evolution in polycrystalline magnesium," *Journal of the Mechanics and Physics of Solids*, vol. 99, pp. 512–538, 2017, ISSN: 0022-5096. DOI: https://doi.org/10.1016/j.jmps.2016.12.008. [Online]. Available: https://www.sciencedirect.com/science/article/pii/S0022509616304641.

[289]H. Jafarzadeh, V. I. Levitas, G. H. Farrahi, and M. Javanbakht, "Phase field approach for nanoscale interactions between crack propagation and phase transformation," *Nanoscale*, vol. 11, no. 46, pp. 22 243–22 247, 2019.

[290]B. E. Abali, *Computational Reality, Solving Nonlinear and Coupled Problems in Continuum Mechanics*, ser. Advanced Structured Materials. Springer Nature, Singapore, 2017, vol. 55, ISBN: 978-981-10-2443-6.

[291]Y. Liu *et al.*, "Experimentally quantifying critical stresses associated with basal slip and twinning in magnesium using micropillars," *Acta Materialia*, vol. 135, pp. 411–421, 2017, ISSN: 1359-6454. DOI: https://doi.org/10.1016/j.actamat.2017.06.008. [Online]. Available: https://www.sciencedirect.com/science/article/pii/S1359645417304792.

[292]M. Gong *et al.*, "Atomistic simulations of interaction between basal <a> dislocations and three-dimensional twins in magnesium," *Acta Materialia*, vol. 155, pp. 187–198, 2018, ISSN: 1359-6454. DOI: https://doi.org/10.1016/j.actamat.2018.05.066. [Online]. Available: https://www.sciencedirect.com/science/article/pii/S1359645418304579.

[293]V. I. Levitas, "Phase-field theory for martensitic phase transformations at large strains," *International Journal of Plasticity*, vol. 49, pp. 85–118, 2013.

[294]K. Momeni and V. I. Levitas, "A phase-field approach to solid–solid phase transformations via intermediate interfacial phases under stress tensor," *International Journal of Solids and Structures*, vol. 71, pp. 39–56, 2015, ISSN: 0020-7683. DOI: https://doi.org/10.1016/j.ijsolstr.2015.05.027. [Online]. Available: https://www.sciencedirect.com/science/article/pii/S0020768315002450.

[295]J. Robson, "The effect of internal stresses due to precipitates on twin growth in magnesium," *Acta Materialia*, vol. 121, pp. 277–287, 2016, ISSN: 1359-6454. DOI: https://doi.org/10.1016/j.actamat.2016.09.022. [Online]. Available: https://www.sciencedirect.com/science/article/pii/S1359645416307108.

[296]D. Jang *et al.*, "Deformation mechanisms in nanotwinned metal nanopillars," *Nature nanotechnology*, vol. 7, no. 9, p. 594, 2012. DOI: https://doi.org/10.1038/nnano.2012.116.

[297]W. Hutchinson and M. Barnett, "Effective values of critical resolved shear stress for slip in polycrystalline magnesium and other hcp metals," *Scripta Materialia*, vol. 63, no. 7, pp. 737–740, 2010, ISSN: 1359-6462. DOI: https://doi.org/10.1016/j.scriptamat.2010.05.047. [Online]. Available: https://www.sciencedirect.com/science/article/pii/S1359646210003726.

[298]J. Jung *et al.*, "Continuum understanding of twin formation near grain boundaries of fcc metals with low stacking fault energy," *npj Computational Materials*, vol. 3, no. 1, pp. 1–9, 2017. DOI: https://doi.org/10.1038/s41524-017-0023-1.

[299]A. Logg and G. N. Wells, "Dolfin: Automated finite element computing," *ACM Transactions on Mathematical Software (TOMS)*, vol. 37, no. 2, pp. 1–28, 2010.

[300]K. B. Ølgaard, A. Logg, and G. N. Wells, "Automated code generation for discontinuous galerkin methods," *SIAM Journal on Scientific Computing*, vol. 31, no. 2, pp. 849–864, 2009.

[301]S. Balay *et al.*, "PETSc users manual," Argonne National Laboratory, Tech. Rep. ANL-95/11 - Revision 3.15, 2021. DOI: https://www.mcs.anl.gov/petsc.

[302]B. E. Abali, *Supply code for computations*, 2020. DOI: http://bilenemek.abali.org/.

[303]GNU Public, *Gnu general public license*, Jun. 2007. DOI: http://www.gnu.org/copyleft/gpl.html.

[304]J. D. Clayton, *Nonlinear mechanics of crystals*. Springer Science & Business Media, 2010, vol. 177.

[305]L. J. Slutsky and C. W. Garland, "Elastic constants of magnesium from 4.2°K to 300°K," *Phys. Rev.*, vol. 107, pp. 972–976, 4 1957. DOI: 10.1103/PhysRev.107.972. [Online]. Available: https://link.aps.org/doi/10.1103/PhysRev.107.972.

[306]B. P. Flannery, H. W. Deckman, W. G. Roberge, and K. L. D'AMICO, "Three-dimensional x-ray microtomography," *Science*, vol. 237, no. 4821, pp. 1439–1444, 1987.

[307]M. Wang *et al.*, "In-situ sem observation of phase transformation and twinning mechanisms in an interstitial high-entropy alloy," *Acta Materialia*, vol. 147, pp. 236–246, 2018.

[308]G. Dehm *et al.*, "Overview on micro-and nanomechanical testing: New insights in interface plasticity and fracture at small length scales," *Acta Materialia*, vol. 142, pp. 248–282, 2018.

[309]C. L. Rountree, R. K. Kalia, E. Lidorikis, A. Nakano, L. Van Brutzel, and P. Vashishta, "Atomistic aspects of crack propagation in brittle materials: Multimillion atom molecular dynamics simulations," *Annual Review of Materials Research*, vol. 32, no. 1, pp. 377–400, 2002.

[310]B. B. Sharma and A. Parashar, "Inter-granular fracture behaviour in bicrystalline boron nitride nanosheets using atomistic and continuum mechanics-based approaches," *Journal of Materials Science*, pp. 1–16,

[311]R. Thomson, S. Zhou, A. Carlsson, and V. Tewary, "Lattice imperfections studied by use of lattice green's functions," *Physical Review B*, vol. 46, no. 17, p. 10 613, 1992.

[312]S. F. Ferdous and A. Adnan, "Mode-i fracture toughness prediction of diamond at the nanoscale," *Journal of Nanomechanics and Micromechanics*, vol. 7, no. 3, p. 04 017 010, 2017.

[313]S. P. Patil, Y. Heider, C. A. H. Padilla, E. R. Cruz-Chú, and B. Markert, "A comparative molecular dynamics-phase-field modeling approach to brittle fracture," *Computer Methods in Applied Mechanics and Engineering*, vol. 312, pp. 117–129, 2016.

[314]H. Chen, Y. Jiao, and Y. Liu, "A nonlocal lattice particle model for fracture simulation of anisotropic materials," *Composites Part B: Engineering*, vol. 90, pp. 141–151, 2016.

[315]L. Scholtès and F.-V. Donzé, "Modelling progressive failure in fractured rock masses using a 3d discrete element method," *International Journal of Rock Mechanics and Mining Sciences*, vol. 52, pp. 18–30, 2012.

[316]S. Sinaie, T. D. Ngo, and V. P. Nguyen, "A discrete element model of concrete for cyclic loading," *Computers & structures*, vol. 196, pp. 173–185, 2018.

[317]N. Moës, J. Dolbow, and T. Belytschko, "A finite element method for crack growth without remeshing," *International journal for numerical methods in engineering*, vol. 46, no. 1, pp. 131–150, 1999.

[318]X.-P. Xu and A. Needleman, "Numerical simulations of fast crack growth in brittle solids," *Journal of the Mechanics and Physics of Solids*, vol. 42, no. 9, pp. 1397–1434, 1994.

[319] J. J. Remmers, R. de Borst, and A. Needleman, "A cohesive segments method for the simulation of crack growth," *Computational mechanics*, vol. 31, no. 1-2, pp. 69–77, 2003.

[320] G. Pijaudier-Cabot and Z. P. Bažant, "Nonlocal damage theory," *Journal of engineering mechanics*, vol. 113, no. 10, pp. 1512–1533, 1987.

[321] V. Hakim and A. Karma, "Laws of crack motion and phase-field models of fracture," *Journal of the Mechanics and Physics of Solids*, vol. 57, no. 2, pp. 342–368, 2009.

[322] C. Linder and A. Raina, "A strong discontinuity approach on multiple levels to model solids at failure," *Computer Methods in Applied Mechanics and Engineering*, vol. 253, pp. 558–583, 2013.

[323] M Baydoun and T. Fries, "Crack propagation criteria in three dimensions using the xfem and an explicit–implicit crack description," *International journal of fracture*, vol. 178, no. 1-2, pp. 51–70, 2012.

[324] T. Belytschko, H. Chen, J. Xu, and G. Zi, "Dynamic crack propagation based on loss of hyperbolicity and a new discontinuous enrichment," *International journal for numerical methods in engineering*, vol. 58, no. 12, pp. 1873–1905, 2003.

[325] I. Babuška and J. M. Melenk, "The partition of unity method," *International journal for numerical methods in engineering*, vol. 40, no. 4, pp. 727–758, 1997.

[326] A. R. Ingraffea and V. Saouma, "Numerical modeling of discrete crack propagation in reinforced and plain concrete," in *Fracture mechanics of concrete: structural application and numerical calculation*, Springer, 1985, pp. 171–225.

[327] D. Sutula, P. Kerfriden, T. Van Dam, and S. P. Bordas, "Minimum energy multiple crack propagation. part i: Theory and state of the art review," *Engineering Fracture Mechanics*, vol. 191, pp. 205–224, 2018.

[328] E. Lorentz and S Andrieux, "Analysis of non-local models through energetic formulations," *International Journal of Solids and Structures*, vol. 40, no. 12, pp. 2905–2936, 2003.

[329] K. Pham and J.-J. Marigo, "Approche variationnelle de l'endommagement: Ii. les modčles ą gradient," *Comptes Rendus Mécanique*, vol. 338, no. 4, pp. 199–206, 2010.

[330] A. Karma, D. A. Kessler, and H. Levine, "Phase-field model of mode iii dynamic fracture," *Physical Review Letters*, vol. 87, no. 4, p. 045 501, 2001.

[331] M. Hofacker and C. Miehe, "Continuum phase field modeling of dynamic fracture: Variational principles and staggered fe implementation," *International Journal of Fracture*, vol. 178, no. 1-2, pp. 113–129, 2012.

[332] M. J. Borden, C. V. Verhoosel, M. A. Scott, T. J. Hughes, and C. M. Landis, "A phase-field description of dynamic brittle fracture," *Computer Methods in Applied Mechanics and Engineering*, vol. 217, pp. 77–95, 2012.

[333] A. A. Griffith, "Vi. the phenomena of rupture and flow in solids," *Philosophical transactions of the royal society of london. Series A, containing papers of a mathematical or physical character*, vol. 221, no. 582-593, pp. 163–198, 1921.

[334] S. A. Silling, "Reformulation of elasticity theory for discontinuities and long-range forces," *Journal of the Mechanics and Physics of Solids*, vol. 48, no. 1, pp. 175–209, 2000.

[335] P. Roy, A. Pathrikar, S. Deepu, and D. Roy, "Peridynamics damage model through phase field theory," *International Journal of Mechanical Sciences*, vol. 128, pp. 181–193, 2017.

[336] J.-H. Song, H. Wang, and T. Belytschko, "A comparative study on finite element methods for dynamic fracture," *Computational Mechanics*, vol. 42, no. 2, pp. 239–250, 2008.

[337] R. d. Borst, J. J. Remmers, A. Needleman, and M.-A. Abellan, "Discrete vs smeared crack models for concrete fracture: Bridging the gap," *International journal for numerical and analytical methods in geomechanics*, vol. 28, no. 7-8, pp. 583–607, 2004.

[338] P.-E. Bernard, N. Moës, and N. Chevaugeon, "Damage growth modeling using the thick level set (tls) approach: Efficient discretization for quasi-static loadings," *Computer Methods in Applied Mechanics and Engineering*, vol. 233, pp. 11–27, 2012.

[339] K. Moreau, N. Moës, D. Picart, and L. Stainier, "Explicit dynamics with a non-local damage model using the thick level set approach," *International Journal for Numerical Methods in Engineering*, vol. 102, no. 3-4, pp. 808–838, 2015.

[340] S. Mariani and U. Perego, "Extended finite element method for quasi-brittle fracture," *International Journal for Numerical Methods in Engineering*, vol. 58, no. 1, pp. 103–126, 2003.

[341] W. J. Boettinger *et al.*, "Phase-field simulation of solidification," *Annual review of materials research*, vol. 32, no. 1, pp. 163–194, 2002.

[342] R Schmitt, C Kuhn, R Müller, and K Bhattacharya, "Crystal plasticity and martensitic transformations," *Technische Mechanik. Scientific Journal for Fundamentals and Applications of Engineering Mechanics*, vol. 34, no. 1, pp. 23–38, 2014.

[343] D Schrade, R Mueller, B. Xu, and D Gross, "Domain evolution in ferroelectric materials: A continuum phase field model and finite element implementation," *Computer methods in applied mechanics and engineering*, vol. 196, no. 41-44, pp. 4365–4374, 2007.

[344] C. Denoual, A. M. Caucci, L. Soulard, and Y.-P. Pellegrini, "Phase-field reaction-pathway kinetics of martensitic transformations in a model fe 3 ni alloy," *Physical review letters*, vol. 105, no. 3, p. 035 703, 2010.

[345] J. Slutsker, K Thornton, A. Roytburd, J. A. Warren, and G. B. McFadden, "Phase field modeling of solidification under stress," *Physical Review B*, vol. 74, no. 1, p. 014 103, 2006.

[346] C Albrecht, A Hunter, A Kumar, and I. Beyerlein, "A phase field model for dislocations in hexagonal close packed crystals," *Journal of the Mechanics and Physics of Solids*, vol. 137, p. 103 823, 2020.

[347] P. J. Loew, B. Peters, and L. A. Beex, "Rate-dependent phase-field damage modeling of rubber and its experimental parameter identification," *Journal of the Mechanics and Physics of Solids*, vol. 127, pp. 266–294, 2019.

[348] A. Ruffini and A. Finel, "Phase-field model coupling cracks and dislocations at finite strain," *Acta Materialia*, vol. 92, pp. 197–208, 2015.

[349] N. Mozaffari and G. Z. Voyiadjis, "Coupled gradient damage–viscoplasticty model for ductile materials: Phase field approach," *International Journal of Plasticity*, vol. 83, pp. 55–73, 2016.

[350] R. Schmitt, C. Kuhn, R. Skorupski, M. Smaga, D. Eifler, and R. Müller, "A combined phase field approach for martensitic transformations and damage," *Archive of Applied Mechanics*, vol. 85, no. 9-10, pp. 1459–1468, 2015.

[351] G. A. Francfort and J.-J. Marigo, "Revisiting brittle fracture as an energy minimization problem," *Journal of the Mechanics and Physics of Solids*, vol. 46, no. 8, pp. 1319–1342, 1998.

[352] B. Bourdin, G. A. Francfort, and J.-J. Marigo, "Numerical experiments in revisited brittle fracture," *Journal of the Mechanics and Physics of Solids*, vol. 48, no. 4, pp. 797–826, 2000.

[353] B. Bourdin, G. A. Francfort, and J.-J. Marigo, "The variational approach to fracture," *Journal of elasticity*, vol. 91, no. 1-3, pp. 5–148, 2008.

[354] V. I. Levitas, H. Jafarzadeh, G. H. Farrahi, and M. Javanbakht, "Thermodynamically consistent and scale-dependent phase field approach for crack propagation allowing for surface stresses," *International Journal of Plasticity*, vol. 111, pp. 1–35, 2018.

[355] C. Kuhn and R. Müller, "A continuum phase field model for fracture," *Engineering Fracture Mechanics*, vol. 77, no. 18, pp. 3625–3634, 2010.

[356] J. M. Sargado, E. Keilegavlen, I. Berre, and J. M. Nordbotten, "High-accuracy phase-field models for brittle fracture based on a new family of degradation functions," *Journal of the Mechanics and Physics of Solids*, vol. 111, pp. 458–489, 2018.

[357] E. Eid, R. Seghir, and J. Réthoré, "Multiscale analysis of brittle failure in heterogeneous materials," *Journal of the Mechanics and Physics of Solids*, vol. 146, p. 104 204, 2021.

[358] M. A. Msekh, J. M. Sargado, M. Jamshidian, P. M. Areias, and T. Rabczuk, "Abaqus implementation of phase-field model for brittle fracture," *Computational Materials Science*, vol. 96, pp. 472–484, 2015.

[359] P. Shanthraj, B. Svendsen, L. Sharma, F. Roters, and D. Raabe, "Elasto-viscoplastic phase field modelling of anisotropic cleavage fracture," *Journal of the Mechanics and Physics of Solids*, vol. 99, pp. 19–34, 2017.

[360] J.-Y. Wu, V. P. Nguyen, C. T. Nguyen, D. Sutula, S. Bordas, and S. Sinaie, "Phase field modeling of fracture," *Advances in applied mechancis: multi-scale theory and computation*, vol. 52, 2018.

[361] C. Cui, R. Ma, and E. Martínez-Pañeda, "A phase field formulation for dissolution-driven stress corrosion cracking," *Journal of the Mechanics and Physics of Solids*, vol. 147, p. 104 254, 2021.

[362] J. Clayton and J Knap, "Phase field modeling and simulation of coupled fracture and twinning in single crystals and polycrystals," *Computer Methods in Applied Mechanics and Engineering*, vol. 312, pp. 447–467, 2016.

[363] A. Emdadi and M. A. Zaeem, "Phase-field modeling of crack propagation in polycrystalline materials," *Computational Materials Science*, vol. 186, p. 110 057, 2021.

[364] Y. Chen, D. Vasiukov, L. Gélébart, and C. H. Park, "A fft solver for variational phase-field modeling of brittle fracture," *Computer Methods in Applied Mechanics and Engineering*, vol. 349, pp. 167–190, 2019.

[365] P. Yue, C. Zhou, J. J. Feng, C. F. Ollivier-Gooch, and H. H. Hu, "Phase-field simulations of interfacial dynamics in viscoelastic fluids using finite elements with adaptive meshing," *Journal of Computational Physics*, vol. 219, no. 1, pp. 47–67, 2006.

[366] P Kasirajan, S Bhattacharya, A Rajagopal, and J. Reddy, "Phase field modeling of fracture in quasi-brittle materials using natural neighbor galerkin method," *Computer Methods in Applied Mechanics and Engineering*, vol. 366, p. 113 019, 2020.

[367] P Carrara, M Ambati, R Alessi, and L De Lorenzis, "A framework to model the fatigue behavior of brittle materials based on a variational phase-field approach," *Computer Methods in Applied Mechanics and Engineering*, vol. 361, p. 112 731, 2020.

[368] P Raghu, A. Rajagopal, and J. Reddy, "Thermodynamically consistent variational approach for modeling brittle fracture in thick plates by a hybrid phase field model," *Journal of Applied Mechanics*, vol. 87, no. 2, 2020.

[369] J. Kiendl, M. Ambati, L. De Lorenzis, H. Gomez, and A. Reali, "Phase-field description of brittle fracture in plates and shells," *Computer Methods in Applied Mechanics and Engineering*, vol. 312, pp. 374–394, 2016.

[370] T. Wang, X. Ye, Z. Liu, X. Liu, D. Chu, and Z. Zhuang, "A phase-field model of thermo-elastic coupled brittle fracture with explicit time integration," *Computational Mechanics*, pp. 1–17, 2020.

[371] Y. Wang *et al.*, "Stressnet: Deep learning to predict stress with fracture propagation in brittle materials," *arXiv preprint arXiv:2011.10227*, 2020.

[372] S. Xie and J. Shao, "Experimental investigation and poroplastic modelling of saturated porous geomaterials," *International journal of plasticity*, vol. 39, pp. 27–45, 2012.

[373] J.-Y. Wu, "A unified phase-field theory for the mechanics of damage and quasi-brittle failure," *Journal of the Mechanics and Physics of Solids*, vol. 103, pp. 72–99, 2017.

[374] H. M. Hilber, T. J. Hughes, and R. L. Taylor, "Improved numerical dissipation for time integration algorithms in structural dynamics," *Earthquake Engineering & Structural Dynamics*, vol. 5, no. 3, pp. 283–292, 1977.

[375] L. Landau and E. Lifshitz, "Statistical physics. vol. 5 . pergamon press. oxford-new york," 1980.

[376] I. Aranson, V. Kalatsky, and V. Vinokur, "Continuum field description of crack propagation," *Physical review letters*, vol. 85, no. 1, p. 118, 2000.

[377] C. Miehe, F. Welschinger, and M. Hofacker, "Thermodynamically consistent phase-field models of fracture: Variational principles and multi-field fe implementations," *International journal for numerical methods in engineering*, vol. 83, no. 10, pp. 1273–1311, 2010.

[378] C. Miehe, M. Hofacker, and F. Welschinger, "A phase field model for rate-independent crack propagation: Robust algorithmic implementation based on operator splits," *Computer Methods in Applied Mechanics and Engineering*, vol. 199, no. 45-48, pp. 2765–2778, 2010.

[379] N Singh, C. Verhoosel, R De Borst, and E. Van Brummelen, "A fracture-controlled path-following technique for phase-field modeling of brittle fracture," *Finite Elements in Analysis and Design*, vol. 113, pp. 14–29, 2016.

[380] T. Heister, M. F. Wheeler, and T. Wick, "A primal-dual active set method and predictor-corrector mesh adaptivity for computing fracture propagation using a phase-field approach," *Computer Methods in Applied Mechanics and Engineering*, vol. 290, pp. 466–495, 2015.

[381] M. Ambati, T. Gerasimov, and L. De Lorenzis, "A review on phase-field models of brittle fracture and a new fast hybrid formulation," *Computational Mechanics*, vol. 55, no. 2, pp. 383–405, 2015.

[382] J. Kim, X. Gao, and T. Srivatsan, "Modeling of crack growth in ductile solids: A three-dimensional analysis," *International journal of solids and structures*, vol. 40, no. 26, pp. 7357–7374, 2003.

[383] Z. S. Hosseini, M. Dadfarnia, B. P. Somerday, P. Sofronis, and R. O. Ritchie, "On the theoretical modeling of fatigue crack growth," *Journal of the Mechanics and Physics of Solids*, vol. 121, pp. 341–362, 2018.

[384] M. Ayatollahi, M. Aliha, and M. Hassani, "Mixed mode brittle fracture in pmma—an experimental study using scb specimens," *Materials Science and Engineering: A*, vol. 417, no. 1-2, pp. 348–356, 2006.

[385] H Andersson, C Persson, and T Hansson, "Crack growth in in718 at high temperature," *International Journal of Fatigue*, vol. 23, no. 9, pp. 817–827, 2001.

[386] H. Richard, M Fulland, and M Sander, "Theoretical crack path prediction," *Fatigue & fracture of engineering materials & structures*, vol. 28, no. 1-2, pp. 3–12, 2005.

[387] H. Amor *et al.*, "Regularized formulation of the variational brittle fracture with unilateral contact: Numerical experiments," *Journal of the Mechanics and Physics of Solids*, vol. 57, no. 8, pp. 1209–1229, 2009.

[388] S. Melin, "When does a crack grow under mode ii conditions?" *International Journal of fracture*, vol. 30, no. 2, pp. 103–114, 1986.

[389] S. Melin, "Fracture from a straight crack subjected to mixed mode loading," *International journal of fracture*, vol. 32, no. 4, pp. 257–263, 1986.

[390] T. Cajuhi, L Sanavia, and L. De Lorenzis, "Phase-field modeling of fracture in variably saturated porous media," *Computational Mechanics*, vol. 61, no. 3, pp. 299–318, 2018.

[391] N. P. van Dijk, J. J. Espadas-Escalante, and P. Isaksson, "Strain energy density decompositions in phase-field fracture theories for orthotropy and anisotropy," *International Journal of Solids and Structures*, vol. 196, pp. 140–153, 2020.

[392] T. Li, "Gradient-damage modeling of dynamic brittle fracture: Variational principles and numerical simulations," Ph.D. dissertation, Université Paris-Saclay (ComUE), 2016.

[393] M. Alnæs *et al.*, "The fenics project version 1.5," *Archive of Numerical Software*, vol. 3, no. 100, 2015.

[394] J. Clayton, "Modeling finite deformations in trigonal ceramic crystals with lattice defects," *International journal of plasticity*, vol. 26, no. 9, pp. 1357–1386, 2010.

[395] K. Edalati, S. Toh, Y. Ikoma, and Z. Horita, "Plastic deformation and allotropic phase transformations in zirconia ceramics during high-pressure torsion," *Scripta Materialia*, vol. 65, no. 11, pp. 974–977, 2011.

[396] G Arlt, "Twinning in ferroelectric and ferroelastic ceramics: Stress relief," *Journal of materials Science*, vol. 25, no. 6, pp. 2655–2666, 1990.

[397] H. Conrad, "Electroplasticity in metals and ceramics," *Materials Science and Engineering: A*, vol. 287, no. 2, pp. 276–287, 2000.

[398] K. U. Kainer and B. L. Mordike, *Magnesium alloys and their applications*. Wiley-VCH Weinheim, 2000.

[399] B. Mordike and T. Ebert, "Magnesium: Properties—applications—potential," *Materials Science and Engineering: A*, vol. 302, no. 1, pp. 37–45, 2001.

[400] G. S. Rohrer, *Structure and bonding in crystalline materials*. Cambridge University Press, 2001.

[401] B. Morrow *et al.*, "Characterization and modeling of mechanical behavior of single crystal titanium deformed by split-hopkinson pressure bar," *International Journal of Plasticity*, vol. 82, pp. 225–240, 2016.

[402] D. Brown *et al.*, "Role of twinning and slip during compressive deformation of beryllium as a function of strain rate," *International Journal of Plasticity*, vol. 29, pp. 120–135, 2012.

[403] J. Gong *et al.*, "< a> prismatic,< a> basal, and< c+ a> slip strengths of commercially pure zr by micro-cantilever tests," *Acta Materialia*, vol. 96, pp. 249–257, 2015.

[404] M Lentz *et al.*, "Strength and ductility with $10-11$ - $10-12$ double twinning in a magnesium alloy," *Nature communications*, vol. 7, no. 1, pp. 1–7, 2016.

[405] R. A. Lebensohn *et al.*, "A self-consistent anisotropic approach for the simulation of plastic deformation and texture development of polycrystals: Application to zirconium alloys," *Acta metallurgica et materialia*, vol. 41, no. 9, pp. 2611–2624, 1993.

[406] P. Turner *et al.*, "A study of residual stresses in zircaloy-2 with rod texture," *Acta metallurgica et Materialia*, vol. 42, no. 12, pp. 4143–4153, 1994.

[407] M. Lindroos *et al.*, "On the effect of deformation twinning and microstructure to strain hardening of high manganese austenitic steel 3d microstructure aggregates at large strains," *International Journal of Solids and Structures*, vol. 125, pp. 68–76, 2017.

[408] P. Karandikar, G Evans, S Wong, M. Aghajanian, and M Sennett, "A review of ceramics for armor applications," *Advances in Ceramic Armor IV*, vol. 29, pp. 163–175, 2009.

[409] V. I. Matkovich, G. .-. Samsonov, and P. Hagenmuller, *Boron and refractory borides*. Springer, 1977.

[410] C Subramanian, A. Suri, and T. Murthy, "Development of boron-based materials for nuclear applications," *Barc Newsletter*, vol. 313, p. 14, 2010.

[411] Y Li *et al.*, "Deformation twinning in boron carbide particles within nanostructured al 5083/b4c metal matrix composites," *Philosophical Magazine*, vol. 90, no. 6, pp. 783–792, 2010.

[412] Q. An, W. A. Goddard III, and T. Cheng, "Atomistic explanation of shear-induced amorphous band formation in boron carbide," *Physical review letters*, vol. 113, no. 9, p. 095 501, 2014.

[413] S. Zhao *et al.*, "Directional amorphization of boron carbide subjected to laser shock compression," *Proceedings of the National Academy of Sciences*, vol. 113, no. 43, pp. 12 088–12 093, 2016.

[414] X. Yan *et al.*, "Depressurization amorphization of single-crystal boron carbide," *Physical review letters*, vol. 102, no. 7, p. 075 505, 2009.

[415] G. Fanchini *et al.*, "Behavior of disordered boron carbide under stress," *Physical review letters*, vol. 97, no. 3, 2006.

[416] D. E. Taylor, J. W. McCauley, and T. Wright, "The effects of stoichiometry on the mechanical properties of icosahedral boron carbide under loading," *Journal of Physics: Condensed Matter*, vol. 24, no. 50, p. 505402, 2012.

[417] J. Clayton, "Dynamic plasticity and fracture in high density polycrystals: Constitutive modeling and numerical simulation," *Journal of the Mechanics and Physics of Solids*, vol. 53, no. 2, pp. 261–301, 2005.

[418] C. A. H. Padilla and B. Markert, "A coupled ductile fracture phase-field model for crystal plasticity," *Continuum Mechanics and Thermodynamics*, vol. 29, no. 4, pp. 1017–1026, 2017.

[419] J. Clayton and J Knap, "Phase-field analysis of fracture-induced twinning in single crystals," *Acta Materialia*, vol. 61, no. 14, pp. 5341–5353, 2013.

[420] J. Clayton and J Knap, "Phase field modeling of directional fracture in anisotropic polycrystals," *Computational Materials Science*, vol. 98, pp. 158–169, 2015.

[421] J. W. Cahn and J. E. Hilliard, "Free energy of a nonuniform system. i. interfacial free energy," *The Journal of chemical physics*, vol. 28, no. 2, pp. 258–267, 1958.

[422] S. M. Allen and J. W. Cahn, "A microscopic theory for antiphase boundary motion and its application to antiphase domain coarsening," *Acta metallurgica*, vol. 27, no. 6, pp. 1085–1095, 1979.

[423] B. A. Bilby, R Bullough, and E. Smith, "Continuous distributions of dislocations: A new application of the methods of non-riemannian geometry," *Proceedings of the Royal Society of London. Series A. Mathematical and Physical Sciences*, vol. 231, no. 1185, pp. 263–273, 1955.

[424] J. D. Clayton, D. Bammann, and D. McDowell, "Anholonomic configuration spaces and metric tensors in finite elastoplasticity," *International Journal of Non-Linear Mechanics*, vol. 39, no. 6, pp. 1039–1049, 2004.

[425] J. D. Clayton, "A non-linear model for elastic dielectric crystals with mobile vacancies," *International Journal of Non-Linear Mechanics*, vol. 44, no. 6, pp. 675–688, 2009.

[426] J. Bleyer and R. Alessi, "Phase-field modeling of anisotropic brittle fracture including several damage mechanisms," *Computer Methods in Applied Mechanics and Engineering*, vol. 336, pp. 213–236, 2018.

[427] K. Pham, H. Amor, J.-J. Marigo, and C. Maurini, "Gradient damage models and their use to approximate brittle fracture," *International Journal of Damage Mechanics*, vol. 20, no. 4, pp. 618–652, 2011.

[428] P. Farrell and C. Maurini, "Linear and nonlinear solvers for variational phase-field models of brittle fracture," *International Journal for Numerical Methods in Engineering*, vol. 109, no. 5, pp. 648–667, 2017.

[429] J. Clayton, "Finsler-geometric continuum mechanics and the micromechanics of fracture in crystals," *Journal of Micromechanics and Molecular Physics*, vol. 1, no. 03n04, p. 1 640 003, 2016.

[430] G. N. Greaves, A. Greer, R. S. Lakes, and T. Rouxel, "Poisson's ratio and modern materials," *Nature materials*, vol. 10, no. 11, pp. 823–837, 2011.

[431] G. Oleinik and T. Ostapchuk, "Effect of pores on the cleavage of twinned boron carbide crystals," *Powder Metallurgy and Metal Ceramics*, vol. 34, no. 9, pp. 500–504, 1996.

[432] G. Del Piero, G. Lancioni, and R. March, "A variational model for fracture mechanics: Numerical experiments," *Journal of the Mechanics and Physics of Solids*, vol. 55, no. 12, pp. 2513–2537, 2007.

[433] J. Chung and G. Hulbert, "A time integration algorithm for structural dynamics with improved numerical dissipation: The generalized-α method," 1993.

[434] P. Wriggers, *Nonlinear finite element methods*. Springer Science & Business Media, 2008.

[435] D. Taylor *et al.*, "First principles calculation of stress induced amorphization in armor ceramics," ARMY RESEARCH LAB ABERDEEN PROVING GROUND MD, Tech. Rep., 2011.

[436] J. Clayton, "Towards a nonlinear elastic representation of finite compression and instability of boron carbide ceramic," *Philosophical Magazine*, vol. 92, no. 23, pp. 2860–2893, 2012.

[437] J. Wang, J. Hirth, and C. Tomé, "$(1^{-}\ 012)$ twinning nucleation mechanisms in hexagonal-close-packed crystals," *Acta Materialia*, vol. 57, no. 18, pp. 5521–5530, 2009.

[438] K. B. Ølgaard and G. N. Wells, "Optimizations for quadrature representations of finite element tensors through automated code generation," *ACM Transactions on Mathematical Software (TOMS)*, vol. 37, no. 1, pp. 1–23, 2010.

[439] A. Awasthi and G. Subhash, "Deformation behavior and amorphization in icosahedral boron-rich ceramics," *Progress in Materials Science*, vol. 112, p. 100 664, 2020.

[440] H. Zhang, H Gu, J Jetter, E Quandt, R. James, and J. R. Greer, "Size-dependence of zirconia-based ceramics via deformation twinning," *Extreme Mechanics Letters*, vol. 42, p. 101 124, 2021.

[441] I. D. Mackinnon, T. Aselage, and S. B. Van Deusen, "High resolution imaging of boron carbide microstructures," in *AIP Conference Proceedings*, American Institute of Physics, vol. 140, 1986, pp. 114–120.

[442] B. C. Mutsuddy, "Mechanical properties of injection molded ceramics," *Powder Metall. Int.;(Germany, Federal Republic of)*, vol. 19, no. 2, 1987.

[443] E. Heian *et al.*, "Synthesis of dense, high-defect-concentration b4c through mechanical activation and field-assisted combustion," *Journal of the American Ceramic Society*, vol. 87, no. 5, pp. 779–783, 2004.

[444] Q. An *et al.*, "Superstrength through nanotwinning," *Nano letters*, vol. 16, no. 12, pp. 7573–7579, 2016.

[445] E Orowan *et al.*, "Dislocations in metals," *AIME, New York*, vol. 131, 1954. DOI: https://www.tms.org/pubs/Books/PDFs/09-1003-e/09-1003-0.pdf.

[446] M. S. Hooshmand, *Atomic-Scale Modeling of Twinning in Titanium and Other HCP Alloys*. The Ohio State University, 2019. DOI: https://gradsch.osu.edu/calendar/events/atomic-scale-modeling-twinning-titanium-and-other-hcp-alloys.

[447] U. Anselmi-Tamburini *et al.*, "Modeling studies of the effect of twins on the x-ray diffraction patterns of boron carbide," *Chemistry of Materials*, vol. 16, no. 22, pp. 4347–4351, 2004.

[448] B. Xu, L. Capolungo, and D. Rodney, "On the importance of prismatic/basal interfaces in the growth of (1^{-} 012) twins in hexagonal close packed crystals," *Scripta Materialia*, vol. 68, no. 11, pp. 901–904, 2013.

[449] H. Kaga and J. J. Gilman, "Twinning and detwinning in calcite," *Journal of Applied Physics*, vol. 40, no. 8, pp. 3196–3207, 1969. DOI: 10.1063/1.1658166. eprint: https://doi.org/10.1063/1.1658166. [Online]. Available: https://doi.org/10.1063/1.1658166.

[450] B. Yangui *et al.*, "High-resolution study of incoherent twin boundaries and of isolated wedge microtwins in rare-earth monoclinic sesquioxides (ln2o3-b)," *Philosophical Magazine A*, vol. 45, no. 3, pp. 443–454, 1982. DOI: 10.1080/01418618208236181. eprint: https://doi.org/10.1080/01418618208236181. [Online]. Available: https://doi.org/10.1080/01418618208236181.

[451] T Nakamura and D. Parks, "Antisymmetrical 3-d stress field near the crack front of a thin elastic plate," *International Journal of Solids and Structures*, vol. 25, no. 12, pp. 1411–1426, 1989.

[452] J. R. Rice *et al.*, "Mathematical analysis in the mechanics of fracture," *Fracture: an advanced treatise*, vol. 2, pp. 191–311, 1968.

[453] T. Tang, S. Kim, M. Horstemeyer, and P. Wang, "Atomistic modeling of crack growth in magnesium single crystal," *Engineering fracture mechanics*, vol. 78, no. 1, pp. 191–201, 2011.

[454] M. Barnett, "Twinning and the ductility of magnesium alloys: Part ii."contraction" twins," *Materials Science and Engineering: A*, vol. 464, no. 1-2, pp. 8–16, 2007.

[455] K. Broberg, "On crack paths," *Engineering Fracture Mechanics*, vol. 28, no. 5-6, pp. 663–679, 1987.

[456] K Hayashi and S Nemat-Nasser, "Energy-release rate and crack kinking under combined loading," 1981.

[457] A. Bobet and H. Einstein, "Fracture coalescence in rock-type materials under uniaxial and biaxial compression," *International Journal of Rock Mechanics and Mining Sciences*, vol. 35, no. 7, pp. 863–888, 1998.

[458] S. Jung *et al.*, "The study of fracture of brittle rock under pure shear loading," in *Fractured and jointed rock masses*, 1995, pp. 457–463.

[459] K. McClellan *et al.*, "Room temperature single crystal elastic constants of boron carbide," *Journal of materials science*, vol. 36, no. 14, pp. 3403–3407, 2001.

[460] T. D. Beaudet, J. R. Smith, and J. W. Adams, "Surface energy and relaxation in boron carbide (1011) from first principles," *Solid State Communications*, vol. 219, pp. 43–47, 2015.

[461] J.-B. Leblond and J. Frelat, "Crack kinking from an initially closed crack," *International journal of solids and structures*, vol. 37, no. 11, pp. 1595–1614, 2000.

[462] A. Bobet, "The initiation of secondary cracks in compression," *Engineering Fracture Mechanics*, vol. 66, no. 2, pp. 187–219, 2000.

[463] P. Isaksson and P. Staahle, "Mode ii crack paths under compression in brittle solids–a theory and experimental comparison," *International Journal of Solids and Structures*, vol. 39, no. 8, pp. 2281–2297, 2002.

[464] L. Vásárhelyi *et al.*, "Microcomputed tomography–based characterization of advanced materials: A review," *Materials Today Advances*, vol. 8, p. 100 084, 2020.

[465] Q. Yang *et al.*, "A variational formulation of the coupled thermo-mechanical boundary-value problem for general dissipative solids," *Journal of the Mechanics and Physics of Solids*, vol. 54, no. 2, pp. 401–424, 2006.

[466] M. E. Gurtin and L. Anand, "A gradient theory for single-crystal plasticity," *Modelling and Simulation in Materials Science and Engineering*, vol. 15, no. 1, S263, 2006.

[467] L. Li and C. Ortiz, "Pervasive nanoscale deformation twinning as a catalyst for efficient energy dissipation in a bioceramic armour," *Nature materials*, vol. 13, no. 5, pp. 501–507, 2014.

[468] A. Chauhan *et al.*, "Experimental observations of amorphization in stoichiometric and boron-rich boron carbide," *Acta Materialia*, vol. 181, pp. 207–215, 2019.

[469] G. Ma *et al.*, "Numerical simulation of compressive failure of heterogeneous rock-like materials using sph method," *International Journal of Rock Mechanics and Mining Sciences*, vol. 48, no. 3, pp. 353–363, 2011.

[470] L Farbaniec *et al.*, "Damage evolution of hot-pressed boron carbide under confined dynamic compression," *International Journal of Impact Engineering*, vol. 99, pp. 75–84, 2017.

[471] Z. Zhang *et al.*, "Microstructures and mechanical properties of b4c–sic intergranular/intragranular nanocomposite ceramics fabricated from b4c, si, and graphite powders," *Journal of the European Ceramic Society*, vol. 34, no. 10, pp. 2153–2161, 2014.

[472] G. Li *et al.*, "Development of a parallel fe simulator for modeling the whole trans-scale failure process of rock from meso-to engineering-scale," *Computers & Geosciences*, vol. 98, pp. 73–86, 2017.

[473] S. Zhou *et al.*, "Phase field modeling of quasi-static and dynamic crack propagation: Comsol implementation and case studies," *Advances in Engineering Software*, vol. 122, pp. 31–49, 2018.

[474] E. Roubin *et al.*, "Multi-scale failure of heterogeneous materials: A double kinematics enhancement for embedded finite element method," *International Journal of Solids and Structures*, vol. 52, pp. 180–196, 2015.

[475] V. I. Levitas *et al.*, "Triaxial-stress-induced homogeneous hysteresis-free first-order phase transformations with stable intermediate phases," *Physical review letters*, vol. 118, no. 2, p. 025 701, 2017.